Computational modelling of fluid-structure interaction at nano-scale boundaries.

Hafezi, Farzaneh

Computational Modelling Of Fluid-Structure Interaction At Nano-Scale Boundaries

Farzaneh Hafezi

College of Engineering
Swansea University

Swansea University
Prifysgol Abertawe

Submitted to Swansea University in fulfilment of the requirements for the degree of Doctor of Philosophy

March 2014

Declaration

This work has not previously been accepted in substance for any degree and is not being concurrently submitted in candidature for any degree.

Signed ..... (candidate)

Date ..... 12/09/2014 .....

STATEMENT 1

This thesis is the result of my own investigations, except where otherwise stated. Where correction services have been used, the extent and nature of the correction is clearly marked in a footnote(s).

Other sources are acknowledged by footnotes giving explicit references. A bibliography is appended.

Signed ..... (candidate)

Date ..... 12/09/2014 .....

STATEMENT 2

I hereby give consent for my thesis, if accepted, to be available for photocopying and for inter-library loan, and for the title and summary to be made available to outside organisations.

Signed ..... (candidate)

Date ..... 12/09/2014 .....

Acknowledgments

My acknowledgments to those helped me towards my thesis are heartfelt. I have come to realize I will never be able to adequately thank those that I am most grateful to.

First, I would like to express my deepest gratitude to Dr Rajesh Ransing, my supervisor, for his invaluable guidance, who enthusiastically and patiently guided me throughout all stages of this research.

A special thanks to my parents, for their support and encouragement my loving brother and sister, my best friend Mariam and all of my good friends.

I would like to thank all the staff of the College of Engineering at Swansea University (spatially the IT support staffs for helping me to run more than 2000 simulations) for creating very friendly and supportive research environment in which to work.

Last and foremost, I want to thank someone who shows to me the meaning of unconditional love, my friend, my love, my husband, my Pooya.

Summary

With the emergence of nano-devices and nano-scale research, gaining further understanding of the evolution of drag forces exerted by molecular flows, at low Knudsen numbers (~0.1-0.5), over nano-scaled objects with 20-100 nm size is a realistic expectation. The proposed research examines the fluid-structure interaction at nano-scales from first principles. It has also critically evaluated, and if necessary modified, the assumptions made during the development of a computational model. The research has provided new insights in modelling molecular interaction with continuum as well as molecular walls and calculation procedures for predicting macroscopic properties such as velocity, pressure and drag coefficients. The proposed formulation has been compared with the state of the art formulations as published in recent journals and verified on number numerical and molecular tests as experimental and analytical results are unavailable at this scale. The effect of various geometry configurations (slit pore, inclined and stepped wall) to model the pressure driven molecular flow through confined walls is studied for number of surface roughness and driving force values given by adjusting molecular accelerations. The molecular flow over diamond, circular and square shaped cylinders confined within parallel walls has also been modelled at various input conditions.

It is expected that the proposed research will have impact in developing future nano-scale applications, in the field of drug delivery, surface cleaning and protein movement, where adsorption, drag resistance or, in general, understanding of the knowledge of fluid-structure interaction at 50-100nm scale is important. Some of the future research areas resulting from this research have also been identified.

TABLE OF CONTENTS

List of Figures

List of Tables

Chapter 1 Introduction

1.1 Introduction

The word 'nano' is probably becoming one of the most frequently 'abused word' by the media and commercial world. Almost all agree that 'nano' means small. However, how small the scale needs to be before the word 'nano' is used is subjective. The world's cheapest car, with length 3,099,000,000 nm, is referred to as 'Nano' (TATA-MOTORS) where as a 5,000,000 nm long and 3,500,000 nm wide wireless controlled machine[1] that can navigate through human blood and hence potentially through human blood vessels is also identified as a nano-robot or nano-device by the media[2]. To put into context, a human hair has diameter between 17,000 – 180,000 nm (Ley, 1999), the red blood cells in human blood have diameter around 6200-8200 nm (Turgeon, 2005) and a rod shaped *Escherichia coli* bacterium has a length 2500nm and diameter 800nm (Berg, 2004). Individual atoms are typically fraction of a nano-meter and a human DNA molecule is 2.2-2.6nm wide (Mandelkern et al., 1981).

The research presented in this thesis is a curiosity driven fundamental research investigating computational modelling of molecular fluid-structure interaction for pressure driven flows in channels at scales around 50-500 nm length. Due to the limitations of the available computational power, the algorithms developed in this thesis are tested on a slit pore (nano-channel) geometry of dimensions 8nm high and 20nm length. When engineering becomes practical at 50-500nm length, predicting continuum information such as drag force, drag coefficient, velocity and pressure profiles will become necessary. Currently, this length scale has its own challenges. The 50-500nm scale is also small enough so that the molecular effects cannot be ignored but not large enough for continuum assumptions to be valid and experimental results are only available at the micron scale.

---

[1]https://engineering.stanford.edu/news/implantable-wirelessly-powered-self-propelled-medical-device

[2]http://www.imedicalapps.com/2012/03/robotic-medical-devices-controlled-wireless-technology-nanotechnology

Nano-scale particles also have much larger surface area than similar masses of large scale materials. As a result, surface forces such as adhesion, friction, meniscus forces, viscous drag forces and surface tension that are proportional to area, become a thousand times larger than the forces proportional to the volume, such as inertial and electromagnetic forces. In addition to the consequence of a large surface-to-volume ratio as observed in Table 1.1, these devices are designed for small tolerances, which makes them particularly vulnerable to adhesion between adjacent components. Slight particulate or chemical contamination present at the interface can be detrimental (Bhushan, 2007).

Millimeter Scale (for a sphere with 1mm radius)	Nanometer Scale (for a sphere with 1 nanometer radius)
$a_1=1mm=10^{-3}m$	$a_2=1nm=10^{-9}m$
$A_1=4\pi a^2=(10^{-3})^2=12.566\times10^{-6}m$	$A_2=4\pi a_2^2=(10^{-9})^2=12.566\times10^{-18}m$
$V_1=4/3\pi a^3=(10^{-3})^3=4.188\times10^{-9}m$	$V_2=4/3\pi a_2^3=(10^{-9})^3=4.188\times10^{-27}m$
surface-to-volume ratio: $\frac{A_1}{V_1}=3\times10^3\ m^{-1}$	surface-to-volume ratio: $\frac{A_2}{V_2}=3\times10^9\ m^{-1}$

Table 1.1. Surface to volume ratio for a sphere with unit radius increases by a factor of 10^6 as the scale is reduced from millimeter to nanometer.

For a nano-scale molecular flow at the slit pore, the inertial forces are much smaller than the viscous forces there by making the Reynolds number (Re) value much less than unity and the results are occasionally 'counter intuitive' (Purcell, 1977, Squires and Quake, 2005). Lauga, Brenner and Stone (Eric Lauga, 2005) argue that the continuum concept of no-slip boundary condition at the solid-liquid interface cannot be derived from sound first principles and at nano-scales this concept is not valid. Molecular dynamics code have predicted slip at the liquid solid boundary, however, the slip behaviour at solid liquid interface is much more complex and depends on number of factors such as wetting conditions, shear rate, pressure, surface energy, surface roughness, dissolved gas, molecular shape and size, probe size and viscosity. The authors anticipate that with further insights into experiments, one day it may be possible to design a desired slip value at the nano-scale boundary as viscous

dominated motion can lead to larger pressure drops. However, predicting viscous forces at this scale is not trivial, and perhaps, difficult to predict.

The research algorithms presented in this thesis are generic. However, the gas used for modelling purpose in this thesis is methane gas at 300K and 40MPa as it is commonly used in the literature (Dyson et. al. 2008 and Sokhan et. al. 2001). The average molecular speed of colliding molecules with methane gas at rest is high - 300 m/s for methane at 300 K and 40MPa. However, the molecular inertial forces are tiny as the molecular mass is exceptionally low (e.g. the mass of methane molecule is 266.65×10^{-28} kg). Understanding the interaction of methane molecules with graphite, and in particular, with reference to its adsorption and storage in nano-channels and groove sites of two carbon nano-tubes (Adisa, 2012) is a relevant application. The high pressures (e.g. 40 MPa) normally exist at deep ocean beds and also have been reported for methane adsorption and storage in carbon nano-tubes (Volkova et al., 2009).

1.2 Scope and objective of the work

The main research objective is to gain an insight in the fluid structure interaction at nano-scale for gas flows just outside the continuum limit where the molecular contribution is important. The other objectives are as follows:

1. Examine assumptions that are normally taken for granted by the molecular dynamics community for modelling the fluid structure interaction at nano-scales using first principles; as at this scale, it is difficult to validate results with experiments.
2. Extend the previous work (Dyson et al., 2008) undertaken in the group to further understand molecular contribution in pressure driven flows at nano-channels in order to predict macroscopic distributions of properties such as velocity and pressure (e.g. Poiseuille flow) and drag forces.
3. Study the effect of geometric changes, surface roughness and external forces on velocity and pressure profiles as well as drag coefficients.
4. Evaluate the assumption of using a continuum wall to replace molecular wall

It is believed that the research undertaken in this thesis is fundamental, novel and original. The algorithms presented in this thesis are not yet available in the commonly used molecular dynamics codes LAMMPS[1] and DL_POLY[2].

These open source codes have become very large to make fundamental changes and at the beginning of the research, it was decided to extend the code developed in the previous work (Dyson et al., 2008) so that it was easy to change, modify, extend and evaluate the proposed algorithms. The work has contributed to the following two journal publications and, as discussed in the conclusions and future work chapter, has opened doors to many more.

(i) F Hafezi and RS Ransing, Computational Modelling of fluid structure interaction at nano-scale boundaries with modified Maxwellian velocity. *Applied Mathematical Modelling,* 37, 14-15, 7504-7520, 2013

(ii) F Hafezi and RS Ransing, Numerical prediction of drag forces on nano-cylinders, under preparation.

1.3 Layout of the thesis

The thesis is organized in five chapters. Every main chapter has its own literature review to compare the approach presented with the state-of-the-art. The purpose and objectives of each chapter are described below.

Chapter 1: Introduction: This chapter has introduced research objectives, put the nano-scale into context and identified the layout of the thesis.

Chapter 2: Literature Review: This Chapter is divided into three parts. The first part reviews some of the potential applications where the knowledge of drag coefficients for molecular flows at nano-scales (50-500 nm) could be useful.

The second part describes various computational approaches for modelling nano/meso scale problems and the choice of using molecular dynamics simulations is justified.

---

[1] http://lammps.sandia.gov

[2] http://www.stfc.ac.uk/cse/25526.aspx

In the third part, the basic concepts of continuum limit, Knudsen number, mean free path, ideal gas law, compressibility limit, molecular diameter, Avogadro's number, Boltzmann constant, mean molecular speed, speed of sound at nano-scale are revisited to (i) visualize the applicability of the continuum limit and (ii) accurately calculate the molecular volume and number density for a methane molecule at 300 K and 40MPa.

Chapter 3: Fluid-structure interaction at nano-scale boundaries: This chapter begins with the review of assumptions made in a molecular dynamics simulation and has been followed by explanation of the novelty of the work describing a new algorithm that modifies the Maxwell condition for thermalized molecules by the wall and uses a Moving Least Square method for predicting macroscopic properties of flow. A number of case studies and numerical tests have been performed to gain insight in the development of macroscopic velocities.

Chapter 4: Numerical prediction of drag forces on nano-cylinders: Calculation of drag coefficients is a focus of this Chapter. The Irvin Kirkwood equation for calculation of stress tensor has been revisited and the algorithms proposed in Chapter 3 extended to calculate equivalent terms in the Irwin-Kirkwood stress tensor and the corresponding macroscopic properties. Drag coefficients for confined molecular flows over circular, diamond and square shaped nano-cylinders at various Reynolds numbers are studied using both continuum and molecular wall assumptions.

Chapter 5: Conclusions and future work:

Every chapter has its own conclusions, however, the overall conclusions of this research are highlighted in this chapter and future research tasks and challenges are also discussed

Chapter 2 Literature Review

2.1 Introduction

This Chapter is divided into the following three parts:

Part I: Potential applications requiring prediction of drag forces at nano-scales

Part II: Review of computational approaches at nano-meso scale

Part III: Continuum limit and calculation of molecular volume for methane at 40MPa and 300K from first principles.

The first part describes the relevance and need, in form of potential applications, for calculating drag forces at nano-scales. The second part reviews various nano/meso scale computational approaches used in the literature and justifies the choice of molecular dynamics method used in this research. The modelling of molecular flow of methane gas at 40MPa and 300K is taken as an example in this research. With reference to this example, the third part describes the characterisation of the continuum limit concept and uses thermodynamic principles to calculate the volume occupied by each methane molecule. This value of molecular volume is used in Chapters 3 and 4.

2.2 Part I: Potential applications requiring prediction of drag forces at nano-scales

Molecular biomechanics principles are used to design nano and micro scale devices which generally are less than 100 nm in one dimension at least. Nano-scale devices or nano-particles are made of different materials such as lipids, metals and natural or synthetic polymers. Nano-particles have been employed for therapeutic and diagnostic purposes during the last two decades (Bawa, 2008).

Bao et al. (2010) presented that understanding mechanical forces in molecular scale can be used in current medical and technological problems. Studying the mechanical force provides more insight to diseases and alternative treatments for medical conditions such as asthma, polycystic kidney and cancer. For instance, World et al. (2006) presented that atherosclerotic plaques form in areas which have less wall shear stress.

In this section the following applications of mechanical forces at the nano-scale have been reviewed to understand the importance of studying molecular dynamics:

- Drug and gene delivery applications
- Nano-surface cleaning applications
- Protein movement

2.2.1 Drug and gene delivery applications

Molecular machines can be used as a drug delivery device to transport drugs through the blood stream, lungs and intestines to target specific cancer cells with minimal side effect (Kipp, 2004, Ould-Ouali et al., 2005, Suri et al., 2007). Figure 2.1 describes untargeted and targeted drug delivery systems. Drugs can either be integrated in the matrix of the particle or attached to the particle surface. Efficient targeting of molecules and cells in cancer and inflammation can be achieved by understanding the interactions of nano-materials with the biological environment, targeting cell-surface receptors (Groneberg et al., 2006), targeting cell population, drug release, changes in cell receptors that occur with progression of disease, multiple drug administration, mechanism and site of drug action, drug retention, stability of therapeutic agents and molecular mechanisms of cell signalling involved in pathobiology of the disease under consideration (Suri et al., 2007). Tan et al. (2013) studied the motion of spherical and rod-shaped nano-particles as shown in Figure 2.2 by the combined effects of drag forces from fluid flow, adhesion force from ligand-receptor binding, and Brownian motion. For example, a rod with a point contact with the wall results in a smaller adhesion force and larger drag force, and is washed away easily.

Brownian motion is the random motion of small particles immersed in fluids resulting from the random collisions from the surrounding liquid molecules (Ermak and McCammon, 1978, Li and Ahmadi, 1992). It is also observed that nano-particles with rod shape and smaller size have higher binding capabilities due to larger contact area and smaller drag force (Tan et al., 2013).

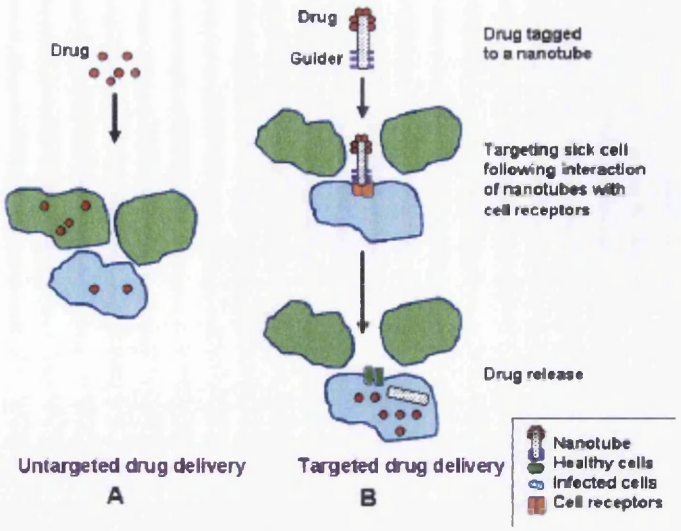

Figure 2.1. A schematic comparison of untargeted and targeted drug delivery systems (Suri et al., 2007).

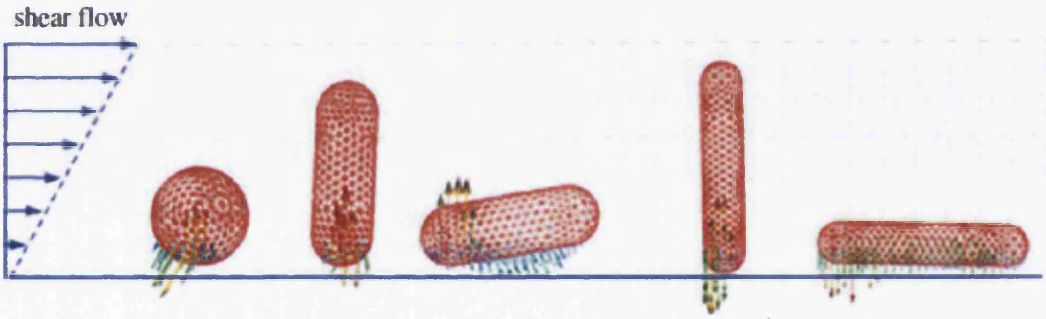

Figure 2.2. Sphere and rod particle with different orientation. The drag force decreases as the nano-rode lays down and the contact area increases (Tan et al., 2013).

In spite of recent progress in nanoscale platforms, nanodevices still have poor targeting capabilities (Kingsley et al., 2006, Uhrich et al., 1999). Guidance techniques have been proposed to increase the targeting capabilities of the nano-particles and to enhance their therapeutic and diagnostic efficacy by integrating sensing and actuation mechanisms on the nano-carrier. In order to improve the mechanisms, many researchers have been developing and investigating applications of magnetic nano-particles (Arruebo et al., 2007, Dobson, 2006, Misra, 2008).

Magnetic Resonance Imaging (MRI) guided nano-robotic drug delivery systems are used to localize drug delivery in the human body at the cellular and sub-cellular level by producing the required external driving forces to guide magnetic nano-capsules to

a specific target that could perform diagnostic, curative and reconstructive treatments in the human body (Vartholomeos and Mavroidis, 2010). Gupta and Kompella (2006) presented that only particles with the size of 30-300 nm are able to move through the thinnest sections of the vasculature system and can target and interact with cells. Such nano-robotic devices will hopefully be part of the arsenal of future medical devices and instruments that will: (1) perform operations, inspections, and treatments of diseases inside the body, and (2) achieve ultra-high accuracy and localization in drug delivery, thus minimizing side effects.

One of the advantages of using the MRI platform is that it is a non-invasive method and it allows for simultaneous actuation and tracking of the nano-particles. It is also capable of providing very accurate localization of the magnetic particles, and commercial MRI devices are readily available at most hospitals (Martel et al., 2008, Mathieu and Martel, 2007).

An ability to determine drag forces using molecular dynamics simulations can also be used to design pathogen biosensors (Sirk, 2006). Gijs (2004) studied the behaviour of magnetic nano-particles at the molecular scale and their applications in magnetic separation, immune-assays, magnetic resonance imaging, drug delivery and hyperthermia.

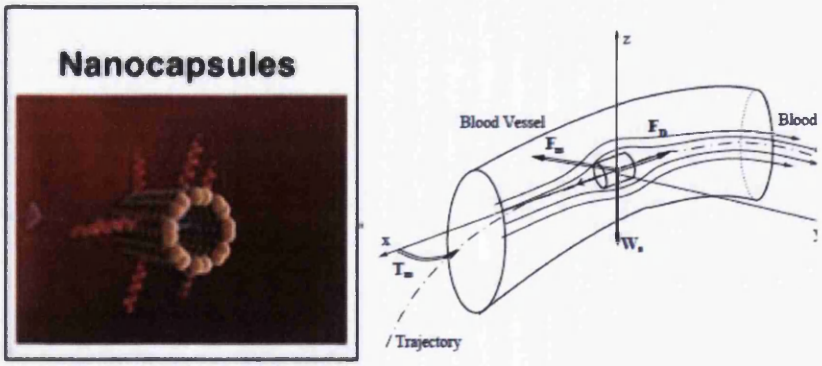

Figure 2.3. Navigation of nano-capsule through the blood vessel (Vartholomeos et al., 2011).

2.2.2 Nano-surface cleaning applications

The cleaning of structured nano-surfaces is a challenging task that has many applications in industry such as in semiconductor, pharmaceutical and xerographic (Ahmadi and Guo, 2007). The removal of nano-scale particles from a surface with holes is even more challenging as particles get trapped in these structures.

The drag force has been used to remove particles in order clean the structured surface (Huang et al., 2011). Particles adhesion and removal have been studied by many researchers (Goddard et al., 2007, Krupp, 1967, Bowling, 1985). Under dry conditions the van der Waals force is the main factor for adhesion of particle to surfaces (Quesnel et al., 2002). Busnaina and Elsawy (2000), Podczeck et al. (1997) studied the effect of relative humidity on detachment and adhesion of particle. Ahmadi and Guo (2007) reported the result of their study on the effect of the capillary force on the minimum critical shear velocities needed for removing different size spherical particles from surfaces. High frequency acoustic streaming is a promising technique for nano-scale particle removal from both flat and structured surface.

Despite the hard particles, soft particles can deform due to van der Waals forces so that when a soft sphere particle and a flat surface come into contact with each other, the Vander Waals (adhesion) force deforms the interface as shown in Figure 2.4. Deformation of the particle leads to larger adhesion force and less drag force so that larger acoustic energy, shorter aging time and the use of proper chemistry is required to remove the nano-scale particles from the surface (Busnaina and Hong, 2002).

Gale and Busnaina (1999) present that high intensity sound waves generate pressure fluctuations and acoustic streaming which provide sufficient hydrodynamic drag force to detach the particles from the both flat and structured surfaces. Busnaina and Hong (2002) reported that by increasing the frequency of sound waves, the acoustic boundary layer thickness decreases and the streaming velocity increases. This increases the drag force and hence, the corresponding removal moment on the particle Figure 2.4. In spite of all the advantages of ultrasonic and megasonic cleaning approaches, they may cause substrate damage because of cavitation (Mertens and Parton, 2002). Kim et al. (2012) studied a physical scalable Wet Laser Shockwave Cleaning (WLSC) for the removal of nanoscale by taking advantage of a

very thin water film on the surface to reduce the adhesion force and increase the drag force.

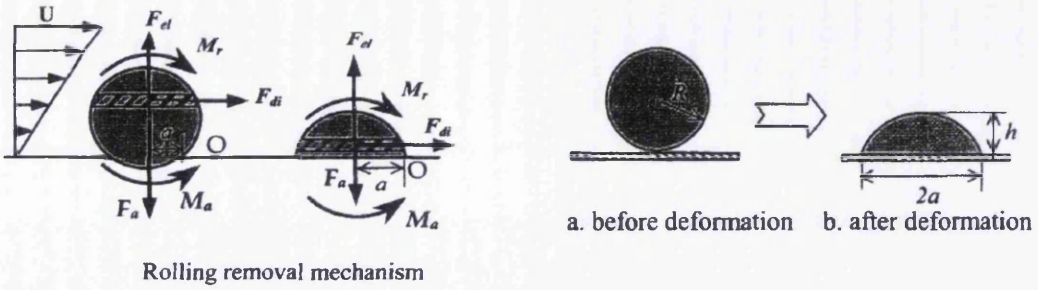

Figure 2.4. Deformation of spherical nano-particle with constant volume (Busnaina and Hong, 2002).

2.2.3 Proteins movement

Modelling the protein movement e.g. a DNA or RNA in 3D helps to understand their interactions and to study how they control their deformation under various forces conditions such as shear and bending, stretching and twisting (Brower-Toland et al., 2002, Bao, 2009, Kolahi and Mofrad, 2008, Santangelo et al., 2006). Molecular mechanics can describe the process of protein trafficking through the use of active transport and vesicle movement (Bean, 2006). The forces sensed by molecules must be understood to study molecular movement. The most important forces at molecular scale are mechanical, chemical and thermal.

Mechanical (viscous) forces are of fundamental importance to diffusion. The drag force which is sensed by a molecule through stationary fluid depends on viscosity of the fluid, the velocity of the molecule and a drag coefficient that is a function of the shape and size of the molecule.

Thermal (collisional) forces are defined as forces that take place when molecules collide with each other, and unlike the mechanical forces that retard molecular movement, thermal forces drive movement (Howard, 2001). The amount of the force due to the collision depends on the momentum of the molecule that is a function of the mass and velocity of the molecule.

Hess and Vogel (2001) studied the active transport of molecular shuttles in synthetic environments based on motor proteins. They present that the flow fields are able to exert substantial drag forces that is a function of flow velocity and viscosity of the solution.

2.3 Part II: Review of computational approaches at nano-meso scale

Variety of computational approaches have been proposed by many researchers to study physical phenomena as the appropriate computational approaches for a given phenomenon depend on the length and time scales of the system. As a result, a single model cannot represent all physical phenomena efficiently.

Molecular contributions become significant when the mean free path i.e. the average distance before molecules collide with each other is comparable with the characteristic length of the problem. This concept is discussed in detail in Part III of this Chapter. In general, the continuum Computational Fluid Dynamics (CFD) techniques are used at micron scale and Molecular Dynamics (MD) methods that model the collisions of molecules are employed at molecular scales (~< 50 nm). Molecular dynamics simulations become computationally prohibitive at scales between 100nm to few microns, normally referred to as the mescoscopic scales. Several approaches to mesoscopic modeling are currently available, the most common being: Brownian Dynamics (BD), the Lattice Boltzmann Method (LBM), and Dissipative Particle Dynamics (DPD). In this section these methods are reviewed briefly and the choice of using molecular dynamics method is justified.

2.3.1 The Brownian dynamics (BD)

Mathematical formulation based on the Brownian dynamics (BD) formulation is often employed for representing the physics at the micro-meso scale (1 nm–10 μm). Robert Brown observed the Brownian motion at the first time in 1827 when he found that pollen particles moved through the water randomly (Fanun, 2010). The Robert Brown's publications based on his observations became the motivation to develop the Brownian dynamics framework. The random motion of a particle in a liquid was explained afterwards as the result of random thermal collisions of the particle with the liquid molecules surrounding it.

In order to simulate the molecular dynamics, the time step is an important factor. A smaller time step is better in terms of accuracy but can only describe the motion trajectory of a limited proportion of the phase space. A large time step may lead to instabilities in the integration algorithm and as a result of the high energy overlaps between atoms it may even result in failure of a program (Lopez, 2007).

The Brownian dynamics (BD) simulation technique is described as a mesoscopic method to reduce the dimensional of the dynamics in which specific detailed interactions of each particle with the other particles are replaced by a stochastic force (Doyle and Underhill, 2005, Ivancevic and Ivancevic, 2006). In the simulation of solute-solvent systems, the time scales between the fast processes such as movements of solvent molecules and the more sluggish motion of solute molecules such as colloids or polymers are different and can be separated from each other. The Brownian dynamics simulation takes advantage of incorporating the effects of solvent without requiring any solvent molecules to be present that makes the time step adjustable within a wide range to optimise accuracy and speed without changing the mechanism of the process (Larson, 2005). Brownian dynamics technique is very useful to investigate the rheology and structure of complex fluids hydrodynamic flows and other nonequilibrium situations. However, BD technique is limited to systems with small mass of particles and inertia (Doyle and Underhill, 2005).

2.3 Lattice Boltzmann Method (LBM)

Lattice Boltzmann Method is a class of computational fluid dynamics simulations that was proposed in 1980 as a way to enhance the method of lattice gas automata. The lattice gas method models the motion of single particle in a fluid while Lattice Boltzmann Method allows particles to move on a discrete lattice mesh and treat collision in a different manner than lattice gas automata (Wagner, 2008). The lattice gas method has limitations such as occurrence of statistical noise and the difficulty to model three-dimensional problems (Succi, 2001). The Lattice Boltzmann method is able to overcome these limitations by pre-averaging the lattice gas and considering particle distributions that exist on the lattice nodes rather than single particles. The Lattice Boltzmann Method is easy to implement and parallelisation of the code is straightforward.

In Lattice Boltzmann Method, particles at a lattice node move to the neighbouring node according to their lattice velocity. This motion is called the propagation or streaming phase. If after propagation phase, two or more particles arrives at the same node then the particles collision occur and each particle get a new velocity. This process is called the collision phase. Therefore particles perform consecutive propagation and collision phases during the simulation. Figure 2.5 describes the propagation and collision phase which occur from (a) to (b) and (b) to (c) respectively (Rothman and Zaleski, 1997).

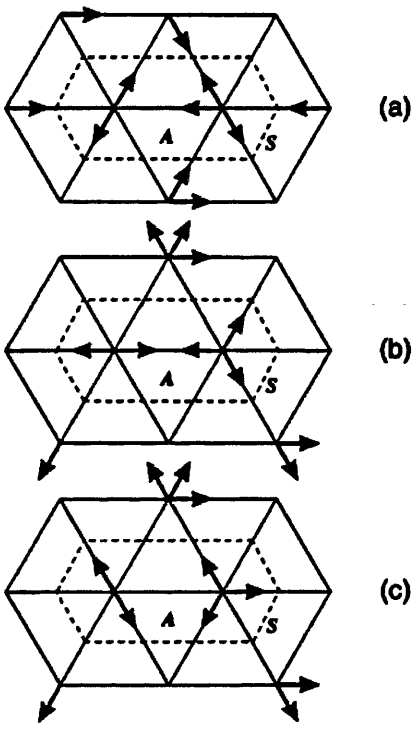

Figure 2.5. The transition from (a) to (b) and (b) to (c) represents propagation and collision phases respectively (Rothman and Zaleski, 1997).

2.3.4 Molecular Dynamics Method (MD)

Molecular dynamics method has been used to study the structure of molecules and the interactions between them. The length and time scale of molecular dynamics is between the quantum mechanics and mesoscale dynamics as shown in Figure 2.6. In a real system, movement of a molecule can't be calculated solely using classical mechanics as molecules interact with each other and the interactions are numerous (Satoh, 2010). Therefore, in order to analysis molecular dynamics, computer simulations are essential.

Alder and Wainwright performed the first molecular dynamics simulation using simple models in the late 1950's to study the interaction of hard spheres (Alder and Wainwright, 1957). In this model, the velocity of the spheres was assumed to be constant and they move in straight lines between collisions that assumed to be perfectly elastic. The velocity of each molecule after collision was calculated using conservation of linear momentum. Rahman (1964) proposed more realistic models of intermolecular interactions by determining amount of force acting on each molecule according to the position of the molecule with respect to others. (Stillinger and Rahman (1974) performed one of the first molecular dynamics simulations of a realistic system by simulating the liquid water in 1974.

Generally molecular dynamics simulations consist of three stages Jabbarzadeh and Tanner (2006): developing a molecular model, calculating the molecular position, velocities and trajectories, and finally collecting the desired properties from the molecular trajectories. In molecular dynamics the position, velocity and forces of molecules are computed for a position at small time intervals using the Newtonian equation of motion where the molecules are allowed to interact. Therefore, new molecular positions are determined and the system is moved one step forward in time and this cycle repeats throughout the simulation until terminated by the user (Sirk, 2006).

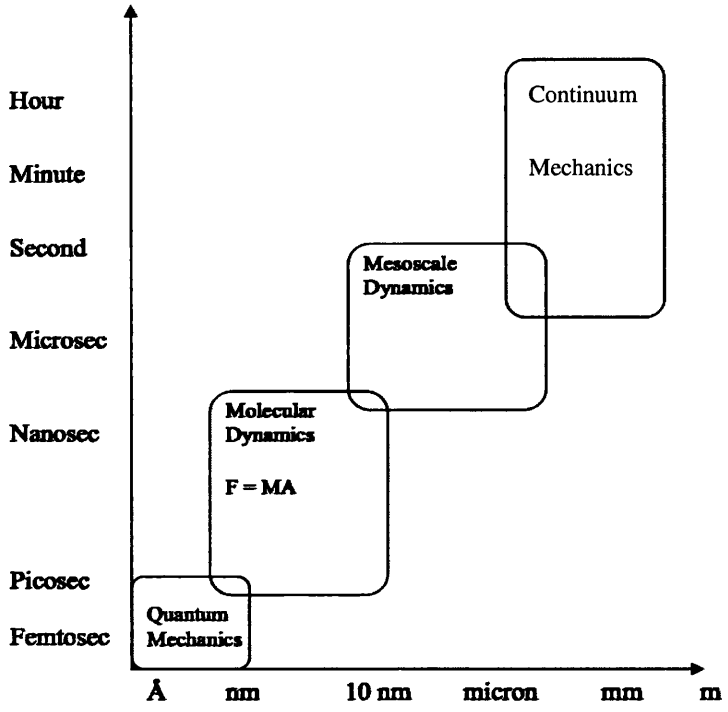

Figure 2.6. Modeling methods for very small scales to very large scales (Sirk, 2006).

2.3.5 The Dissipative particle dynamics method

Dissipative particle dynamics (DPD) is an approach devised by Koelman and Hoogerbrugge (1993) for simulating systems of particles in simple and complex fluid. The simulation technique in DPD is similar to MD as each particle moves according to Newton's second law. However, DPD model consists of particles which correspond to coarse-grained entities (Keaveny et al., 2005). Figure 2.7 describes interactions between molecules in MD and clusters in DPD. Therefore, DPD represents molecular clusters which are in mesoscale rather than individual atoms. Mesoscale structures cannot be model by continuum computational fluid dynamics (CFD) methods duo to their complexity and also MD method is not an appropriate method for scales much beyond the atomistic (Pan, 2010). According to Tosenberger et al. (2011) another difference between DPD and MD methods is in the form of forces acting between the particles. In MD method, it is a pairwise potential force which depends on the distance between each pair of molecules while in DPD method there are two additional forces namely random and dissipative forces. The dissipative forces reduce the relative velocity between the molecules and together with random forces form DPD thermostat that keeps the mean temperature of the system constant.

The speed at which the system reacts to temperature variations is directly proportional to the random force so that by increasing the random force the speed is increased (Groot and Warren, 1997).

The DPD method applied to model complex media, for example constructing polymers, colloids, amphiphiles, and mixtures and in particular blood flows.

However, the DPD method has its own limitations for describing cell-cell interaction in the flow or cell-vessel wall (Tosenberger et al., 2011).

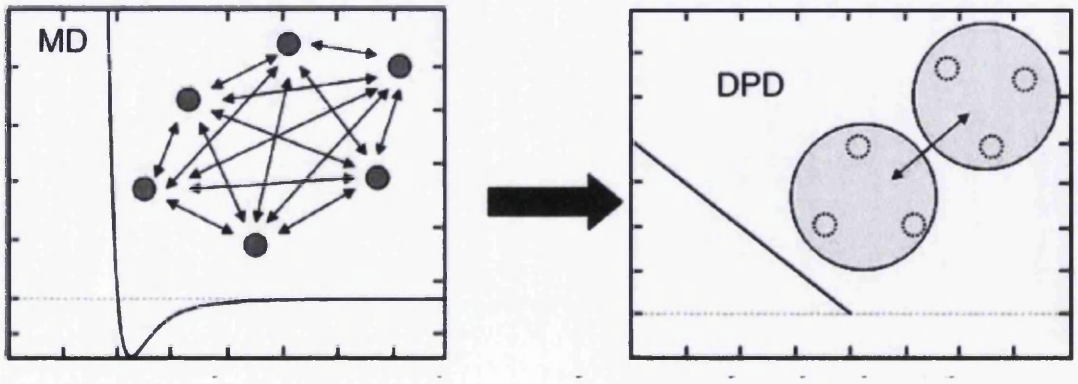

Figure 2.7. Interaction between molecules in MD and clusters in DPD (Lipkowitz, 2010).

2.3.6 Justification for the choice of the molecular dynamics method:

As described in the Chapter 1, one of the main research objectives of this research is to use first principles for exploring the fluid-structure interaction with the view of calculating drag forces at nano-scale. Experimental results on drag coefficients at less than 100nm objects are not reported in the literature. However, as described in the part I of this Chapter, potential applications that require calculation of drag coefficients are appearing in the literature. As discussed in the literature review for Chapter 4, various approaches are being reported in the literature to calculate pressure values using molecular dynamics models. However, the calculation of nano-scale drag coefficients on various geometries, to the authors' knowledge, has not been reported in the literature.

In the absence of experimental results, it was decided to gain an insight into the molecular interaction with the wall (e.g. with reference to the roughness of the wall, external force applied to the fluid and geometry of the wall) with minimum number of external assumptions that can influence the results. Molecular dynamics model conserve the kinetic energy of individual molecules and it was decided to use this method. It was also decided to include the wall and all geometric variations within one periodic cell thus not requiring the Lees-Edwards (Lees and Edwards, 1972) adjustment at boundaries to superimpose any velocity gradient. The periodic cell was chosen long enough to justify the application of periodic boundary conditions.

2.4 Part III: Continuum limit and calculation of molecular volume for methane at 40MPa and 300K from first principles.

Kinetic theory is a mathematical framework intended to relate directly the most relevant characteristics of the molecular structure to the rheological behaviour of the bulk system. At molecular scales, molecules continuously exchange energy via collisions. The total kinetic energy of colliding molecules within a control volume is conserved. When the molecules collide with a wall, their momentum is changed, and the average rate at which they exchange momentum with the walls corresponds to the pressure force. The pressure depends only on the translational motion of molecules. A temperature value, measured in Kelvin, is proportional to the average kinetic energy of a molecule. The distance travelled by molecules between collisions is

referred to as the mean free path. In an inhomogeneous gas, molecules move between different regions, smoothing out the inhomogeneities. The rate at which molecules transport kinetic energy from high temperature regions to low temperature regions relates to the thermal conductivity, the rate at which molecules transport momentum determines the viscosity, and the rate at which they transport different forms of matter determines the diffusion constant. Each of these transport coefficients is proportional both to the mean free path of the molecules and to their typical speeds.

The mean free path is also used in the characterization whether continuum assumptions are valid or not. A dimensionless parameter, referred to as the Knudsen number, defined as the ratio of the mean free path between molecular collisions with the macroscopic or characteristic length ($Kn = \lambda / L$, λ is mean free path and L is a characteristic length) of often used to describe the continuum limit.

Using kinetic theory of gases, the mean free path for methane gas is proportional to $1/na^2$ where n is the number density of molecules with radius 'a' (Squires and Quake, 2005). Squires and Quake (2005) have reported mean free path for air molecules as 70 nm at 1atm and 25°C. This means that for understanding interaction of air with a boundary at dimensions around 70nm, the contributions from molecular dynamics cannot be ignored. Schaaf and Chambre (1961) classified different flow regimes based on the Knudsen number. Fluid is considered as continuum for Kn <= 0.01 and the assumption of a no-slip boundary condition at the fluid-wall interface remains valid. The flow between Kn >0.01 and Kn < 0.1 is categorized as slip flow and then it becomes transitional flow up to Kn =10. For Kn > 10 the flow is considered as a free molecular flow. Karniadakis et al. (2005) have further classified this range and introduced further regions (Figure 2.8) where statistical fluctuations due to molecular contributions are assumed to be greater than 1% when the characteristic length L drops is approximately 20 times the average molecular spacing δ. The gas is characterized as dilute gas if $\delta / d \gg 1$, where d is the molecular diameter.

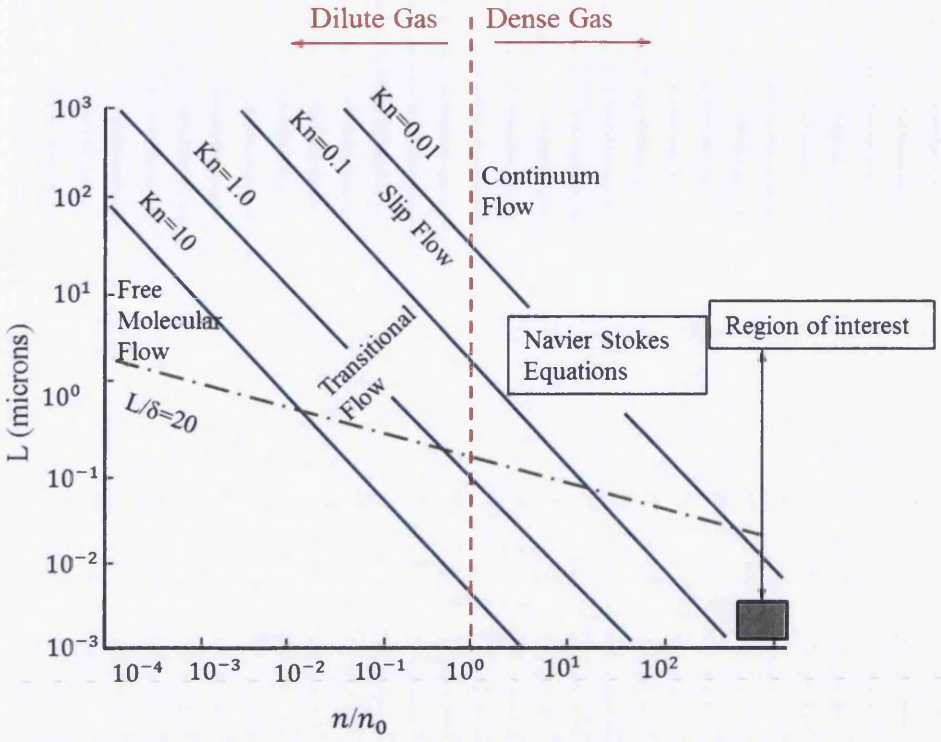

Figure 2.8. Limits of approximations in modelling gas microflows (Karniadakis et al., 2005). n/n_0 is the number density normalized with corresponding atmospheric conditions.

L is the characteristic length. Kn is Knudsen number and δ is the mean molecular spacing

For methane gas at 40MPa and 300K, the number density is calculated using the perfect gas equation:

$$\frac{1}{V} = \frac{P}{zR_uT} = \frac{P}{zN_AK_BT} = \frac{n}{N_A} \qquad (2.1)$$

$$n = \frac{P}{zK_BT} \quad (A^\circ)^3 \qquad (2.2)$$

Where:

P: Gas pressure (Pa)

z : Compressibility factor

T: Temperature (K)

N_A: Avogadro's number

R_u: Universal gas constant

K_B: Boltzmann constant

n: Number density

The compressibility factor for methane at 40MPa and 300K is determined using compressibility charts (Figure 2.9a and b). This requires calculation of reduced pressure P_R and temperature T_R values that are based on the critical pressure P_{cr} and temperature T_{cr} values.

$$P_R = \frac{P}{P_{cr}} = \frac{400}{45.99} \approx 8.77 \qquad (2.3)$$

$$T_R = \frac{T}{T_{cr}} = \frac{300}{274.14 - 82.59} = 1.566 \qquad (2.4)$$

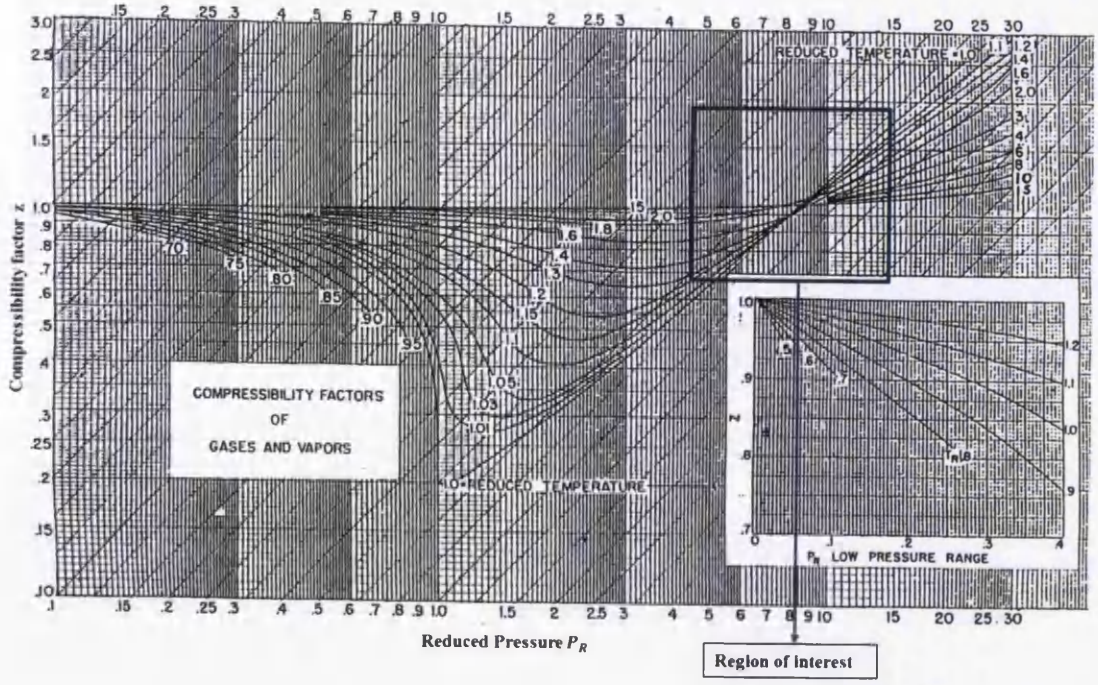

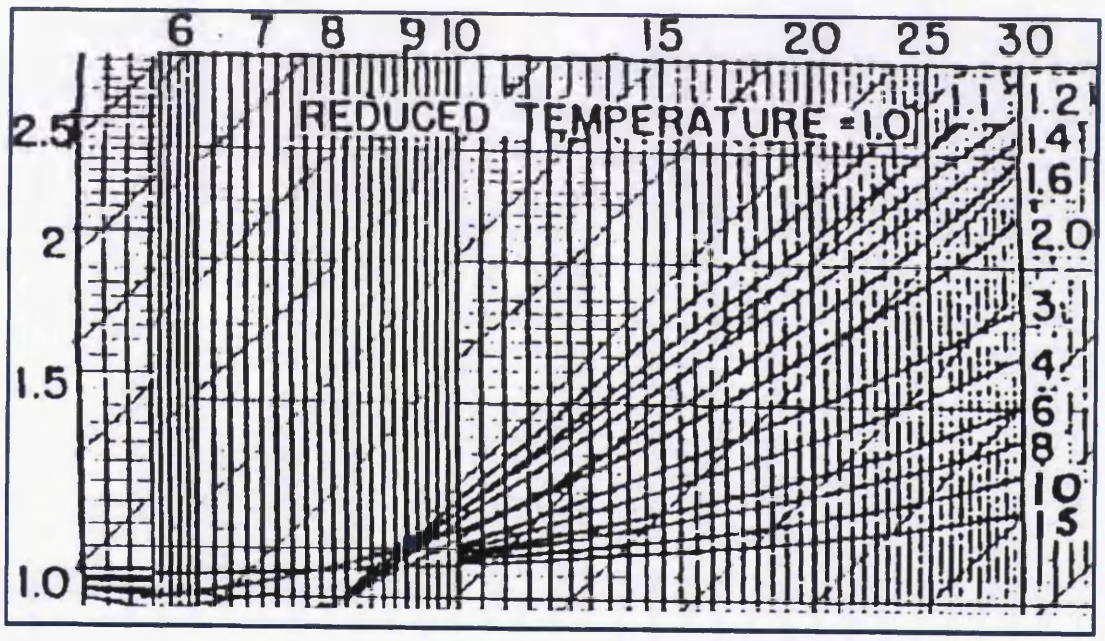

Figure 2.9. (a) Compressibility chart for Methane (b) the region of interest. The blue dot shows the corresponding point for 300K and 40MPa[1].

[1]http://www.reviewpe.net/penotes/thermo/fig_2.01.jpg

Using Figure 2.9b the compressibility factor z is assumed as 1.06

Using Equation 2.2, the number density n is calculated as follows:

$$n = \frac{P}{zK_BT} = \frac{40\times10^6}{1.06\times1.38\times10^{-23}\times300} = 9.11926\times10^{27}\ (A^\circ)^3$$

The volume occupied by each methane molecule is 1/n and a value of 109.66 $(A^\circ)^{-3}$ has been used in Chapters 3 and 4 to correspond with a temperature and pressure value of 300K and 40MPa.

The location of the region of interest, shown as a square in Figure 2.9a, is calculated as follows:

Hence,

$$n_0 = \frac{P_0}{zK_BT_0}\ (A^\circ)^3$$

$$\frac{n}{n_0} = \frac{9.1192\times10^{27}}{2.69\times10^{25}} \approx 339$$

The width L of the slit pore is $L = 8.24\times10^{-9}$ (m)

The Knudsen number is calculated as follows:

The molecular diameter (d) of methane is calculated using a critical volume value for methane as 99 (cc/mol) (Dutta, 2009) using the following equation

$$d = 0.8094\mathrm{V_c^{1/3}} \qquad (2.5)$$

$$d = 3.742\times10^{-10}\,(\mathrm{m})$$

$$L = 8.24\times10^{-9}\,(\mathrm{m})$$

The mean free path λ is given by:

$$\lambda = \frac{1}{\sqrt{2}\pi d^2 n} = \frac{1}{\sqrt{2}\times\pi\times(3.742\times10^{-10})^2\times9.11926\times10^{27}} = 1.7627\times10^{-10}\,(\mathrm{m}) \qquad (2.6)$$

And, hence the Knudsen number is given by:

$$K_n = \frac{\lambda}{L} = \frac{1.7627 \times 10^{-10}}{8.24 \times \times 10^{-9}} = 0.0214 \qquad (2.7)$$

The L/ δ ratio, where $\delta \propto \frac{1}{\sqrt[3]{n}}$ this ratio is less than 20 and hence, as shown in Figure 2.8, it is expected that molecular contributions should be significant even if the Knudsen number close to the continuum limit of 0.01. This curiosity driven research hypothesis is effectively tested in this thesis and it is shown in Chapter 4 that drag coefficients predicted from molecular dynamics code at these conditions are significantly higher than values predicted based on analytical continuum based assumptions.

Chapter 3 Modelling of fluid structure interaction at nano-scale boundaries

3.1 Introduction

The soft collisions among fluid-fluid and fluid-wall molecules are modelled from first principles. In particular, the assumption of Maxwellian distribution of velocities for thermalized molecules, in both parallel and perpendicular directions to the wall, has been re-evaluated with supporting experimental and/or numerical evidence.

It is proposed that the normal component of molecular velocity post collision is conserved for all fluid molecules. The slip effect at the wall boundary, introduced by the surface roughness, is accounted by an accommodation coefficient (or sometimes referred to as Maxwell coefficient) f. A moving least square method is used to calculate macroscopic velocity values. The influence of molecular interaction on the macroscopic velocity distribution is investigated at 40MPa and 300K for slit pore, inclined and stepped wall configurations. The accommodation coefficient values f = 0, 0.07, 0.257, 0.45, 0.681 and 1; and acceleration values ranging from zero to 1 $\times 10^{11}\ m/s^2$ and $250\times 10^{11}\ m/s^2$ are used for comparison.

The distribution of macroscopic velocity parallel to the wall is studied to observe the effect of the slip behavior. The detailed study of average of velocity values at various magnitudes of acceleration has shown an evidence of charactersitic low and high speed of molecular flows that is considered as significant and a comparison is sought with an equivalent laminar and turbulent flow style behavior.

3.1.1 Background research and proposed assumptions for modelling fluid-wall interactions

Understanding fluid properties at nano-meso scales is becoming increasingly important from engineering perspective, even though there are many research challenges including interaction of molecules with continuum walls (Dyson et al., 2008). The effect of slip and wall surface roughness, on the macroscopic velocity distribution of molecular flow in nano/micro channels, are areas of active research (Mickel et al., 2011, Basagaoglu and Succi, 2010, Zhang et al., 2011, Li et al., 2010)

Idealized molecular walls to capture surface roughness or molecular corrugation by introducing different types of molecular obstructions to the wall have been used in the literature (Yang, 2006, Sofos et al., 2012, Sun et al., 2012). However, with recent advances in the Atomic Force Microscopy (AFM) it is possible to study of high resolution solid-liquid interfaces under real conditions. These surfaces taken at Angstrom scale are also referred to as atomically smooth, freshly cleaved mica surfaces. Liang et al. (2007) have shown an AFM image of such a surface at the Angstrom scale. The image illustrated the existence of roughness at molecular scales; however, the roughness shown in the image is not similar to the molecular approximation of rough walls generally used in the literature.

Sokhan et al. (2001) proposed a solid wall with a slip condition at the boundary to simulate the steady state Poiseuille flow. A fraction of the molecules, categorized by Maxwell's coefficient *f*, were thermalized using Equations 3.1 and 3.2 (Maxwell, 1878). Maxwell's law defines velocity distributions for evaporated molecules in the normal (Equation 3.1) and parallel (Equation 3.2) directions as follows. The experimental evidence for the Maxwellian distribution of velocities is given by Loeb (2004). Equation 3.1 represents the distribution of electrons emitted by a thermal wall in the normal direction.

$$g(v)_{\perp} = \frac{m}{K_b T} \; v \; e^{\left(\frac{-mv^2}{2K_b T}\right)} \tag{3.1}$$

$$g(v)_{\parallel} = \sqrt{\frac{m}{2\pi K_b T}} \; e^{\left(\frac{-mv^2}{2K_b T}\right)} \tag{3.2}$$

Maxwell's coefficient *f*, also referred to as the accommodation coefficient in the literature, is a convenient way to model the effect of surface roughness and the resulting slip or no-slip boundary condition at the wall. f=1 corresponds to no-slip boundary condition, where every molecule that interacts with the wall is thermalized. Arya et al. (2003) demonstrated that the accommodation coefficient f is strongly dependent on the physical roughness of the wall (proportional to σ_{wg}/L) and the

attractiveness of the wall to the fluid (proportional to ε_{wg}/k_BT) where σ_{wg} and ε_{wg} are the Lennard-Jones interaction parameters of the wall and fluid molecules and L is the lattice unit length. The wall becomes rough as L increases from 0.1 nm value. It is also shown that the coefficient *f* is independent of tangential drift velocity and the inertial mass of fluid/gas molecules. Arya et al. (2003) studied a fully molecular boundary and plotted values for a wide range of *f*. Sokhan et al. (2001) also confirmed the work and have reported similar values (approximately 0.029 for rigid graphite wall) for the flow between parallel plates.

Sokhan et al. (2001) checked the accuracy of Maxwell's theory of slip by analyzing velocity distributions of particles colliding with the wall immediately before and after the collision and did not find any noticeable deviation from the Maxwellian distribution for the tangential component. However, non-Maxwellian behavior was observed for the normal distribution even though it did not induce non-uniformity in the temperature profile. It should be noted that the coefficient *f* used in their simulation was very small (<= 0.029).

Molecular velocities given by Equation 3.1 do not follow Gaussian distribution for a given temperature value (Figure 3.1). As a result for large *f* values, a significant number of molecules receive exceptionally high velocities in the normal direction, thereby making thermostats ineffective and irreversibly damaging velocity and temperature distributions. The use of velocity rescaling techniques (Toghraie Semiromi and Azimian, 2010) to maintain constant temperature in the production phase is an over simplification and may not be suitable for accurate prediction of velocity gradients near wall.

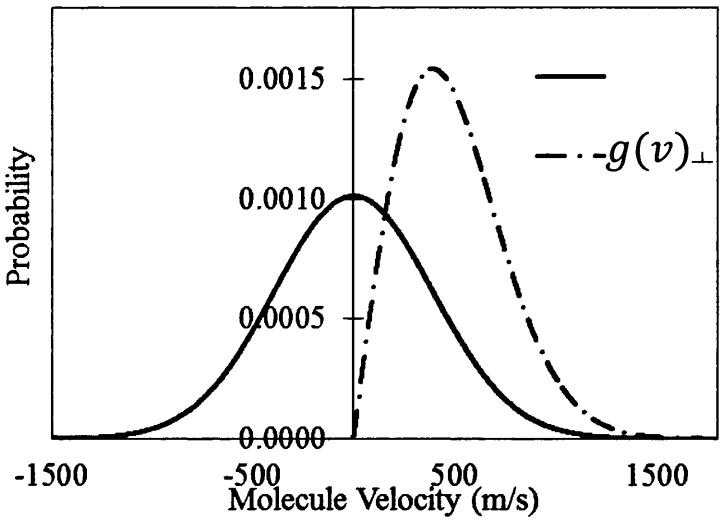

Figure 3.1. Maxwell's velocity distributions for thermal wall model. The solid line illustrates the distribution of thermalized molecules with velocity component parallel to the wall and the second distribution (dash and dot line) represents the velocity component perpendicular to the wall.

In this chapter, it is proposed that for soft sphere models, the Equation 3.1 is not used to replace normal component of velocities for thermalised molecules. Molecular dynamics simulation codes that use the accommodation coefficient f to model the collision effect of a molecule (sphere) with a wall are based on the Maxwell's (Maxwell, 1878) assumption designed for a hard sphere model where molecular collisions with a wall are not modelled as reflective collisions. The molecular wall was assumed as a layer of spheres touching each other. "The condition of the molecules that collided with the wall was assumed to be intermediate between that of evaporated gas and that of reflected gas approaching most nearly to evaporated gas at normal incidence and most nearly to reflected gas at grazing incidence". This assumption led to Maxwell's theory of slip in which a fraction f of all incident molecules was evaporated.

With velocities corresponding to those in still gas at the temperature of the solid (Equation 3.1 and 3.2) and the portion $(1-f)$ is reflected.

However, this interpretation is not true for a soft sphere model where molecules interact by exerting a force on each other relative to the distance between them.

These interactions occur continually and every molecule influences all other molecules within its cut off zone. Maxwell further interpreted that "if the spheres, instead of being hard elastic bodies, are supposed to act on the molecules at finite, though small, distances and if they are so close together that their spheres of action intersect, then the gas which leaves the surface will be still more like reflected gas, and less like evaporated gas. The concept of 'evaporated gas' in a direction parallel to the wall is made analogous to the degree of surface roughness that induces 'slip' and 'no slip' effects at the surface and is concept is being interpreted as favouring conservation the normal component of velocity during the collision. The sphere of action for a molecule is interpreted as being similar to the cut off radius for a molecule.

With this interpretation and background, the following assumptions for modelling soft sphere based molecular interactions are proposed:

i. A molecule is assumed to be collided with a wall if it is within the cut off radius of the wall molecule and has changed the direction of normal component of velocity from approaching to the wall to moving away from it within two consecutive time steps.

ii. The magnitude of the normal component of velocity of a molecule is conserved for all molecules during the thermalization process i.e. Equation 3.1 is not used to replace the normal component of velocity for thermalized molecules categorized by fraction *f*.(A similar approach has been proposed by Dyson et. al. (2008) Fig 3.4 page 75)

iii. For the thermalized molecules, the parallel component of velocity of a molecule post collision follows the Maxwellian's distribution corresponding to the wall temperature given by Equation 3.2. This assumption forms the basis of modelling the slip and surface roughness effects as discussed below.

iv. In a soft sphere model, the effect of the wall molecule is modelled by a single wall molecule that is nearest to the colliding gas molecule. The force and potential exerted by the wall on the molecule is calculated for a predefined section of molecular wall and results are stored, as function of distance of the molecule from the wall, in the form a look up table.

The advantage of using these assumptions is that they can be applied to model the molecular interaction of different types of molecules with a wall. It is shown in this work that the proposed approach does not disturb the Gaussian distribution corresponding to the simulation temperature for all three velocity components. The interaction with the wall is modelled by using a single wall molecule with derived properties and a single accommodation coefficient f to introduce slip and account for surface roughness.

It should be noted that the wall roughness only influences the parallel component of molecular velocity for the fraction of molecules chosen for the thermalization process. In other words, it is assumed that the wall roughness does not influence the normal component of colliding molecule. As discussed earlier, the thermostats and/or velocity rescaling methods have dampened the adverse effects of not conserving post collision normal velocity in a soft sphere model. The Maxwell's assumption (Maxwell, 1878) to model the collision of fluid molecules with the wall is based on a hard sphere model. Physically, the assumption allowed to model post collision velocities using the Maxwellian distribution of velocities in the tangential and normal direction as given by Equations 3.1 and 3.2. The proposed model is based on the soft sphere collision model and it is argued that the positions of all neighbouring fluid molecules and wall molecules have influence on the post collision velocity of a colliding molecule. As a result, it is proposed that the post collision velocity in the normal direction is conserved for all colliding molecules. In the proposed model, the atomic scale asperities of the larger wall roughness are modelled using high 'f' values thereby thermalizing larger fraction of fluid molecules that undergo collision. The soft collision model accounts for the inter-molecular forces between the fluid-fluid and fluid-wall molecules using the Lennard-Jones potential. The proposed formulation is original, novel and is not currently available in one of the most popular open source software for molecular dynamics code, LAMMPS.

The proposed assumptions i-iv are implemented in a soft sphere molecular dynamics code with Lennard Jones (12-6) potential to model the molecular interaction with a solid wall. The mathematical formulation is described in the next Section.

3.2 Mathematical Formulation

In order to evaluate the effect of our assumptions, the mathematical formulation for modelling pair wise interaction among 'fluid-fluid' and 'fluid-wall' molecules is derived using a simple and most commonly used form of the pair wise Lennard-Jones 12-6 potential, U(r) as described below:

$$U_{ij} = 4\varepsilon\left[\left(\frac{\sigma}{r_{ij}}\right)^{12} - \left(\frac{\sigma}{r_{ij}}\right)^{6}\right] \qquad r_{ij} < r_C \qquad (3.3)$$

Where subscripts *i, j* corresponding to molecules *i* and *f* represents fluid. r_{ij} is the distance between two molecules. The subscripts *w* and *f* are used to categories properties for the wall and fluid molecules. Methane is modelled as fluid and the solid wall is assumed to be made of carbon molecules. σ represents the collision radius (σ_f for methane is 0.381 nm and σ_w for carbon is 0.34 nm). The standard Lorenz-Barthelot mixing rule is used to calculate σ_{fw} as 0.3605 nm. ε is the well depth (strength of interaction) and is commonly referred to in the form ε / k_b (k_b is the Boltzmann constant). The corresponding values for methane, carbon and methane-carbon wall, ε_f / k_b, ε_w / k_b and ε_{fw} / k_b are 148.1 K, 28 K and 64.39 K. r_c is the cut off radius and is taken is 2.75 σ. The lattice constant with value of 3.808A is used to construct a graphite molecular wall with FCC (Face Cantered Cubic) structure.

The Lennard-Jones force *F* is the force acting between the two molecules (positive for molecule *i* and negative for molecule *j*) is given by:

$$F_{ij} = -\frac{\partial U(r_{ij})}{\partial r} \qquad (3.4)$$

The long range correction term for the fluid-fluid molecular potential energy expression is:

$$U_{lrc} = \frac{8}{3}\pi\rho\varepsilon_f\sigma_f^3\left[\frac{1}{3}\left(\frac{\sigma_f}{r_c}\right)^9 - \left(\frac{\sigma_f}{r_c}\right)^3\right] \qquad r_{ij} > r_C \tag{3.5}$$

Using fluid-fluid specific properties (σ_f and ε_f) in Equation 3.3 and combining it with Equation 3.5 results in the expression for the total fluid-fluid potential as:

$$U_{f-f} = U_{ij,f-f} + U_{lrc} \tag{3.6}$$

3.2.1 Short and long range contributions from wall molecules (assumption iv)

In an earlier work (Dyson et al., 2008), the effect of the molecular wall was modelled by an equivalent continuum wall by increasing the well depth corresponding to the molecular layers in the wall. The effect of increasing the well depth on the force distance curve is shown in Figure 3.2. A parametric study on various well depth values is undertaken to understand whether there any relationship between the well depth value and the average macroscopic velocity profile. The results, as shown in Figure 3.3, indicate no direct relationship with the well depth value.

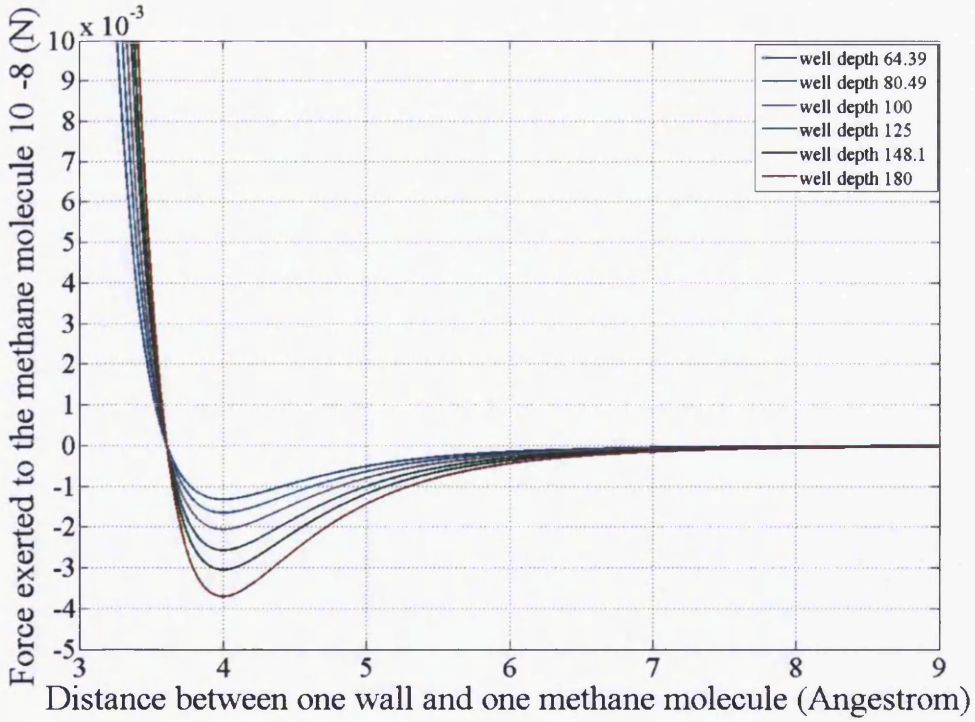

Figure 3.2. Effect of different well depth on Lenard Jones force.

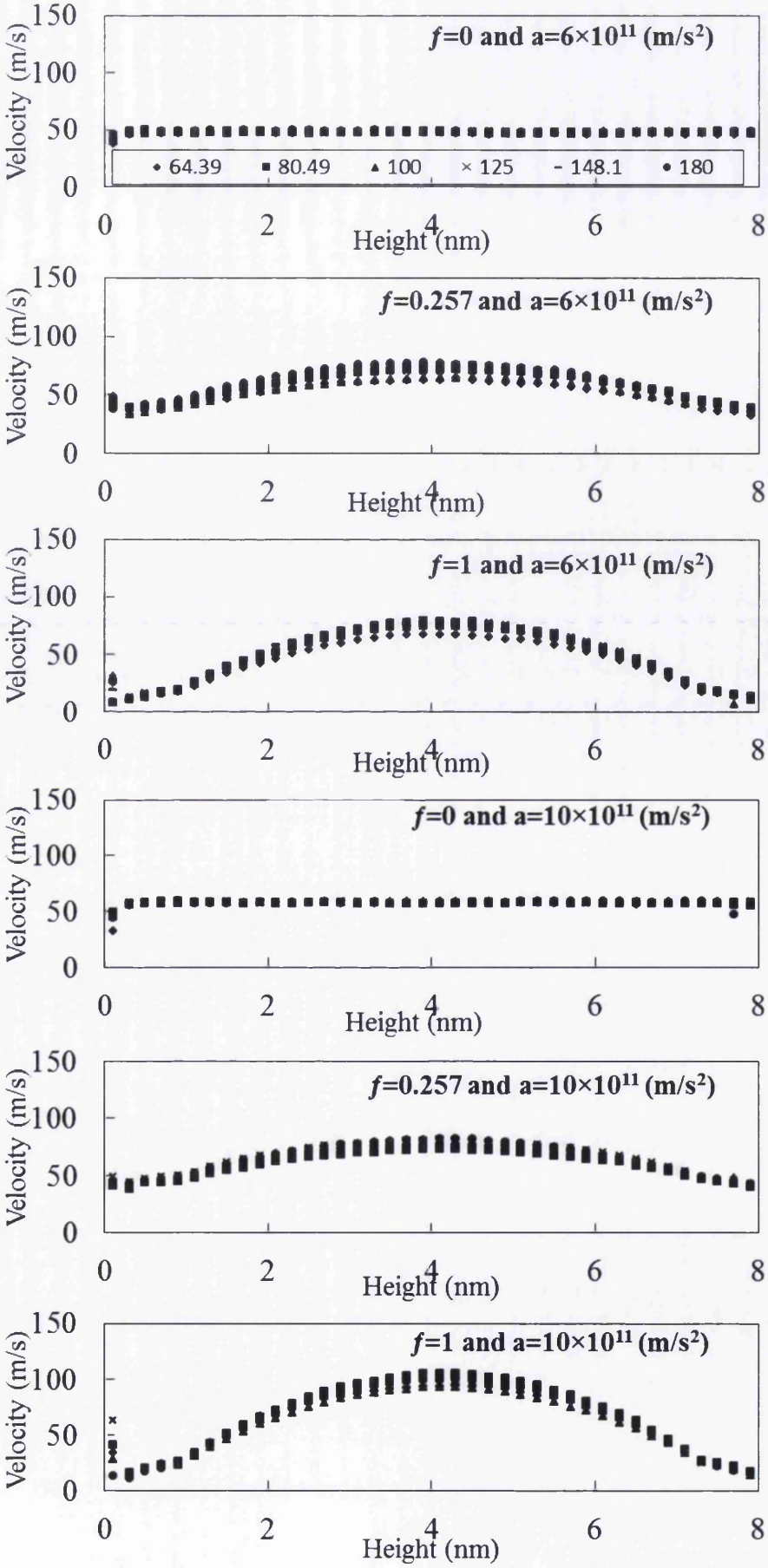
f=0 and a=6×10^11 (m/s^2)
64.39
80.49
100
125
148.1
180
Velocity (m/s)
Height (nm)
f=0.257 and a=6×10^11 (m/s^2)
f=1 and a=6×10^11 (m/s^2)
f=0 and a=10×10^11 (m/s^2)
f=0.257 and a=10×10^11 (m/s^2)
f=1 and a=10×10^11 (m/s^2)

Figure 3.3. The effect of six well depth values (64.39, 80.49, 100, 125, 148.1, 180) is shown on velocity profiles for various surface roughness and acceleration values. The legend is shown in the first graph. It is observed that the changes in well depth values do not have direct influence on the average velocity profile.

As the accommodation coefficient and/or acceleration value was increased, random variation in the predicted average velocity values was observed with respect to well depth changes. As a result, the well depth parameter was not considered as design parameter during the parametric study and the model was modified to include a look up table concept as described next in this section. Also, non-symmetrical variation was also observed near the lower boundary wall. The data shown is actual simulation data without undertaking any smoothing procedures near wall. The results of the modified model are discussed in Section 3.3

One of the main objectives of replacing a molecular wall with an equivalent continuum wall is the computational efficiency. The accuracy of the simulation with a continuum wall is normally assessed by comparing results with an equivalent molecular wall. Hence, it was decided to approximate the molecular wall by calculating the resulting force-distance curves between a fluid molecule and the wall by moving the fluid molecule towards the wall (Figure 3.5) and use this information in the form of a look up table for approximating the molecular wall effects using a continuum wall. The resulting force distance curves for different types of wall molecules are shown in Figure 3.4.

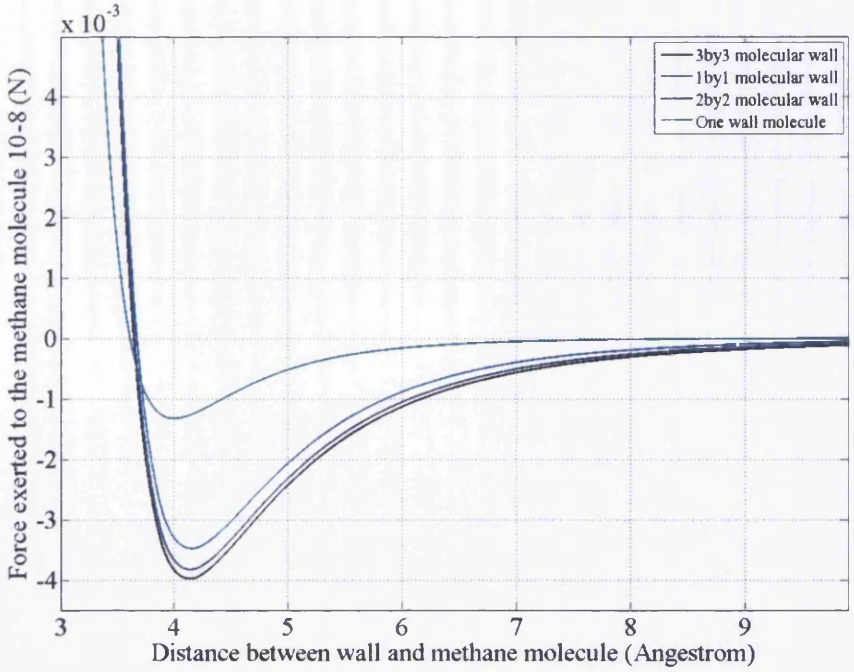

Figure 3.4. The effect of different wall arrangements on the force-distance curve for a fluid molecule approaching the molecular wall.

The influence of wall molecules is characterised by including both short range and long range potentials. The molecules shown within the circle in Figure 3.5 are modelled separately using a four layered molecular wall with a given lattice structure (e.g. FCC lattice for a carbon/graphite wall). The corresponding potential and forces components in x, y and z directions are stored in a lookup table format for various distance values 'z' between the fluid and nearest wall molecule. Additional lookup tables are designed for special cases when the wall molecule that is closest to the fluid molecule is at the corner of the molecular wall. In such cases, the neighbouring wall molecules may not be symmetrically arranged.

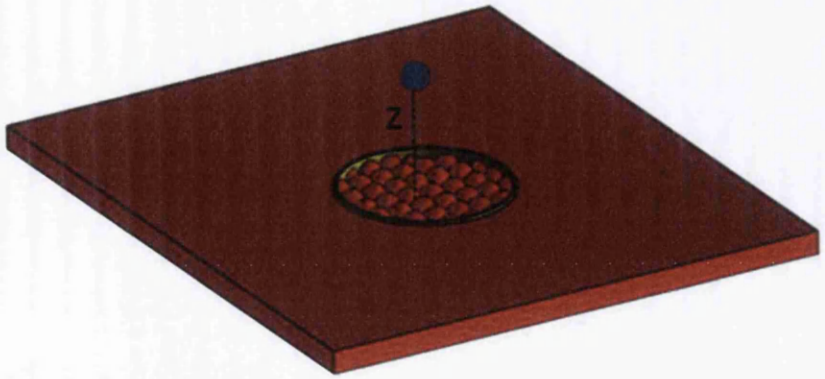

Figure 3.5. Schematic representation of short and long range contributions from wall molecules within the surface layer needs to be considered. z is the shortest distance between a fluid molecule and the wall and is within the cut off radius. The interaction among fluid molecules is modelled separately.

The long range contribution of wall molecules is modeled using a cylindrical cut off radius $r_{c,w}$ as given by the following expression (Siperstein et al., 2002):

$$U_{Wlrc} = 4\pi\rho_w \varepsilon_{fw} \sigma_{fw}^2 \left[\frac{1}{5} \left(\frac{\sigma_{fw}^{10}}{(z^2 + r_{c,w}^{\ 2})^5} \right) - \frac{1}{2} \left(\frac{\sigma_{fw}^4}{(z^2 + r_{c,w}^2)^2} \right) \right] \tag{3.8}$$

The total fluid-wall molecule potential is given by the following equation.

$$U_{f-w} = U_{wf} + U_{Wlrc} \tag{3.9}$$

Equation 3.4 is generalized to give an expression for the total force as:

$$F_{Total} = -\left(\frac{\partial U_{f-w}}{\partial r} + \frac{\partial U_{f-f}}{\partial r} \right) + F_{External} \tag{3.10}$$

where, $F_{External}$ is the external force applied to molecules.

The lookup tables significantly enhance the computational efficiency (Table 3.1) however; the potential loss of accuracy needs to be compared by modelling an equivalent molecular wall. The force (expressed in ε/σ units) exerted by a molecular wall on the fluid molecule at distance z=2 A° and z=1.8 A° Angstrom (Figure 3.5) is plotted in Figure 3.6 respectively. Figure 3.6a plots three dimensional contours of force exerted by the molecular wall with FCC lattice structure. The peaks denote the force exerted when the fluid molecule is directly above a spherical wall molecule. As the fluid molecule is moved around the spherical wall molecule by maintaining the distance from the wall, the force value drops from the peak value of 1×10^{-8} N to just under 0.4×10^{-8} N (Figures 3.6a and b). When the fluid molecule moves 0.2 Angstrom towards the wall, i.e. at a distance of 1.8 Angstrom from the wall the force experienced by the fluid molecule increases exponentially. The corresponding increase in the force is shown in Figures 3.6b and c. It should be noted that the force value shown as the value between two peaks in Figure 3.6c is 1×10^{-8} N. In other words, as a result of assumption (iv), the fluid molecule in Figure 3.6a will be within 0.2 Angstrom distance from the wall to experience the same magnitude of force (e.g. 1×10^{-8} N). The effect of assumption (iv) on overall macroscopic velocity and force values is insignificant. This is illustrated further in Section 3.1.

Number of fluid molecules	Simulation model (as shown in Figure 4.11)	Running time on one cluster node: 2.5 GHz processor and 4GB Ram
12448	Actual molecular wall	600 hours
12448	Continuum wall: using look up table concept	120 hours

Table 3.1. Increased in the computational efficiency resulting from the look table model.

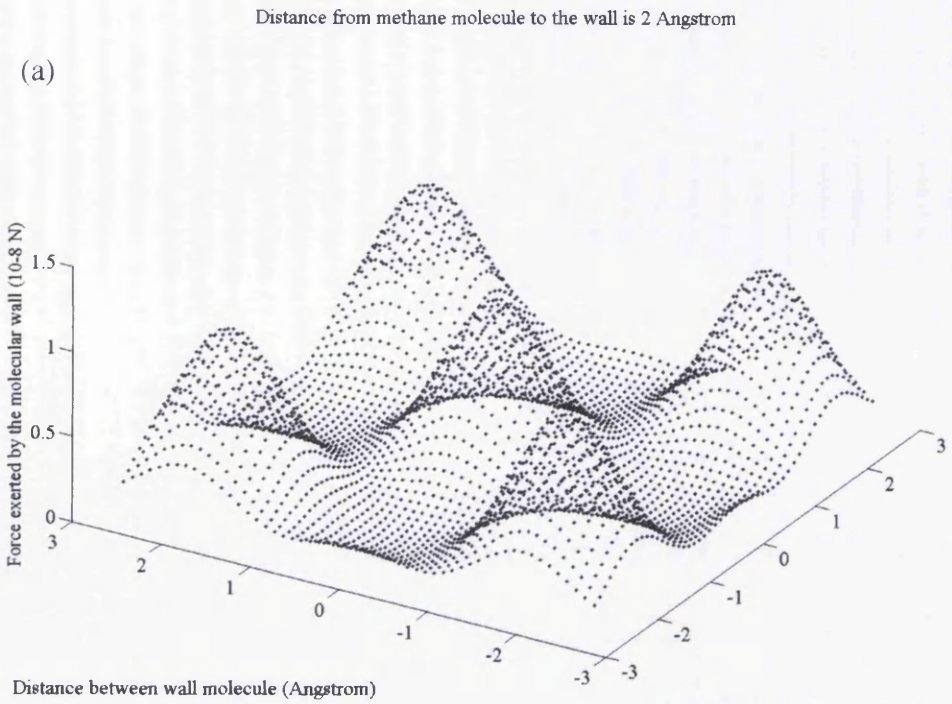
Distance from methane molecule to the wall is 2 Angstrom
(a)
Force exerted by the molecular wall (10-8 N)
1.5
1
0.5
0
3
2
1
0
-1
-2
-3
-3
-2
-1
0
1
2
3
Distance between wall molecule (Angstrom)

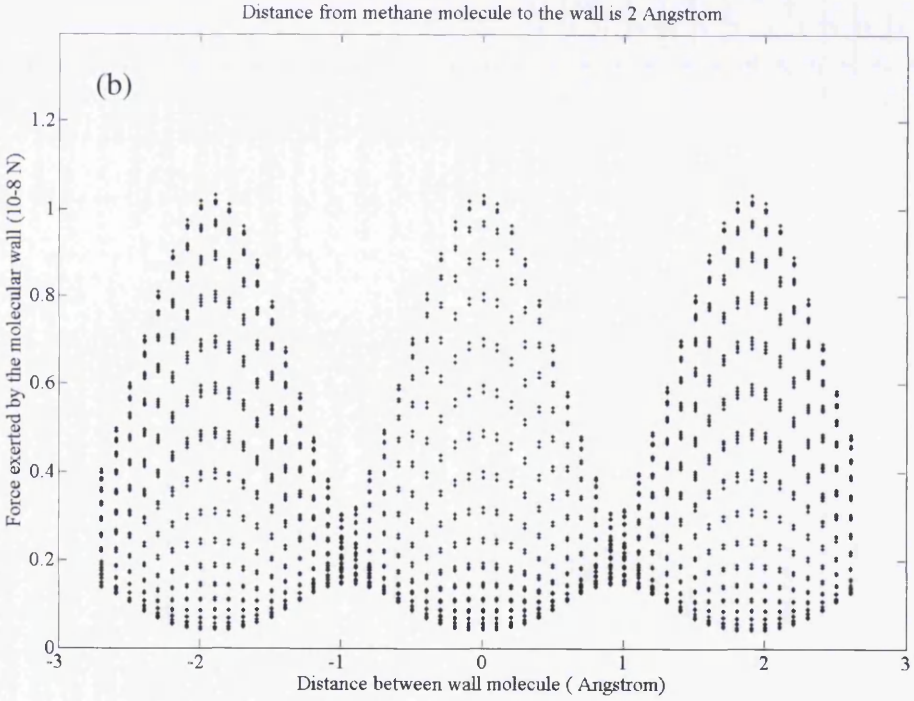
Distance from methane molecule to the wall is 2 Angstrom
(b)
Force exerted by the molecular wall (10-8 N)
1.2
1
0.8
0.6
0.4
0.2
0
-3
-2
-1
0
1
2
3
Distance between wall molecule (Angstrom)

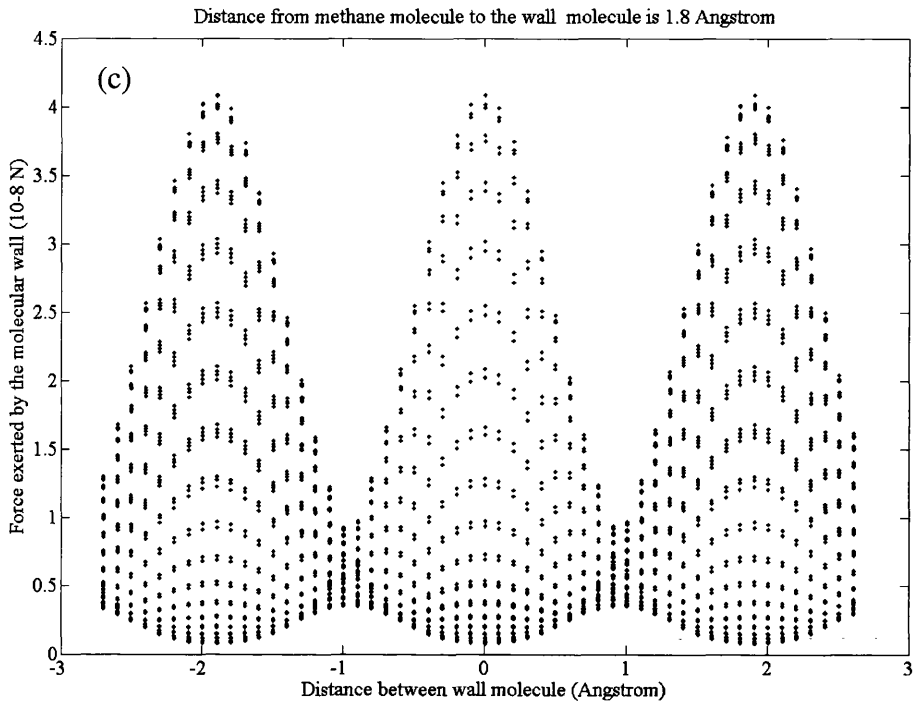

Figure 3.6. Contours of force experience by a fluid molecule as it moves around a spherical wall molecule at a distance of (a,b) 2 Angstrom and (c) 1.8 Angstrom from the wall. Maximum force (at the peak) is experienced when the fluid molecule is at the top of the wall molecule and the minimum force (valley between the peaks) occurs when the fluid molecule is between two spherical wall molecules.

3.2.2 Diffuse boundary conditions (assumptions i-iii)

The soft sphere nature of the simulation means there are no instantaneous collisions with the wall. The molecules that are interacting with the wall and are assumed to have collided with the wall satisfy the condition given in the first assumption. This requires calculation of the following two quantities:

1. Perpendicular distance between the fluid particle and the wall (distance z) as shown in Figure 3.5.
2. Direction of the outward normal from the wall surface to the fluid particle (e.g. $z_{C1}, z_{C2}, z_{C3}, z_{C4}$ in Figure 3.7).

A proportion of fluid molecules that have assumed to be collided with the wall, as defined by the accommodation coefficient *f*, is randomly chosen for thermalisation. For the thermalised molecules, the local co-ordinate system is rotated so that the y axis aligns with the outward normal direction as calculated above (x', y' as shown in Figure 3.7). The velocity vector for the molecule, as calculated from the molecular interactions, is projected onto the rotated co-ordinate system and the components of velocity in the local x and z directions are replaced as per Equation 3.2. Once the molecule is thermalised, the local co-ordinate system and hence the velocity vector is rotated back to the global co-ordinate system (x, y). This generalized formulation allows interaction of fluid molecules with inclined wall surfaces.

For simulating pressure driven molecular flow within nano-channels, the boundary wall can be described by one or more line segments. The proposed formulation assumes that there is no variation in the channel geometry in the z direction (Figures 3.11 and 3.16) for examples on sample nano-channel geometries). With reference to a boundary wall segment represented as a line segment AB, a fluid molecule can occupy four positions (c_1, c_2, c_3 and c_4) relative to the line segment and is represented by point C with co-ordinates x_C, y_C (Figure 3.7). The position vectors of the end points of the line segment A(x_A, y_A)and B(x_B, y_B) are known and hence the distance between the wall and the molecule, $z_{C1}, z_{C2}, z_{C3}, z_{C4}$ corresponding to the four possible positions, is calculated using geometry.

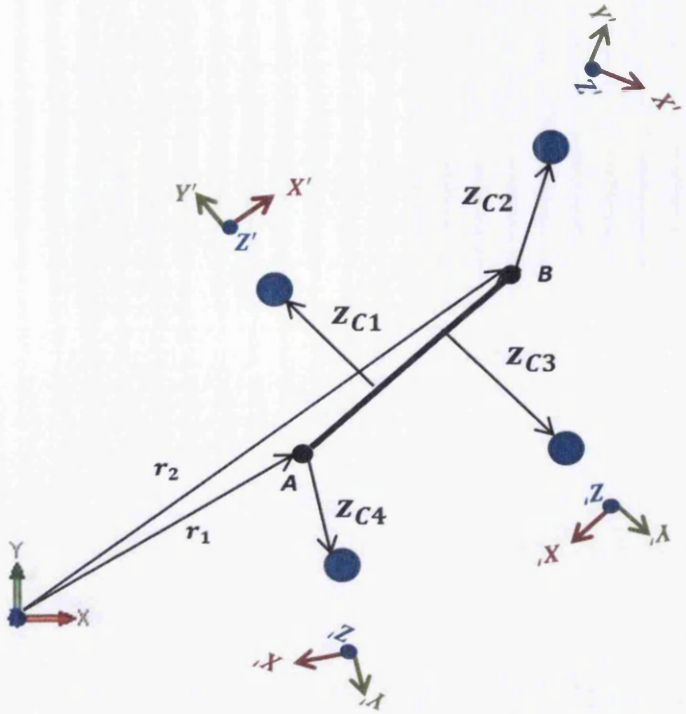

Figure 3.7. Distance of the fluid molecule from a boundary segment is calculated using geometry.

Let point p be the point on line AB which also on the perpendicular projection of C on AB. Its position on line AB is computed by the following equation.

$$p = \frac{AC.AB}{\|AB\|^2} \tag{3.11}$$

where p has the following meaning:

- p=0 p is on point A
- p=1 p is on point B
- p < 0 p is on the backward extension of AB (for example point C_4)
- p >1 p is on the forward extension of AB (for example point C_2)
- 0 < p <1 p is interior to AB (for example points C_1 C_1, and C_3)

If point p is not on the interior to AB then the distance between the point C and the line segment is either |AC| and |BC| and the normal direction is along vector AC or BC. Else, it is necessary to determine whether point C is on the left or right of AB. This is determined by calculating a factor *s*

$$S = \frac{(y_A - y_C)(x_B - x_A) - (x_A - x_C)(y_B - y_A)}{L^2} \tag{3.12}$$

where $L = \sqrt{(x_B - x_A)^2 + (y_B - y_A)^2}$ (3.13)

If S = 0 then C is on AB, if S < 0 then C is the left of AB else C is the right of AB. This information is used in calculating the normal direction and the distance of the point C from the line segment is $z = |S| \times L$ (3.14)

3.2.3 Gaussian Thermostat and Velocity Verlet Algorithm

For NVT (Number of Molecules Volume and Temperature) systems the number of molecules, volume and temperature is assumed to remain constant. The application of external force, in the form of uniform acceleration to all molecules in the system, and interaction of fluid molecules with the boundary alter the energy levels of the molecular system. The energy that is added to the system should influence the proportions of energy within the system but not change its global value. A thermostat is necessary to maintain the temperature of the system so that the dynamic behaviour of the system is unaffected. The simple velocity rescaling techniques to maintain Gaussian distributions for velocity in each direction are far too crude for this application. A Gaussian thermostat is used that uses a thermostat variable $\dot{\xi}(t)$ by scaling the molecular momentum (Equation 3.15). The Gaussian thermostat controls the temperature of the system by using Gauss's principle of least constraint (Edberg et al., 1986, Evans et al., 1983). The Gauss's principle ensures that the constrained trajectories deviate as little as possible from the unconstrained equations of motion.
The total force given by Equation 3.10 is converted into units of acceleration. It is expected that the streaming velocity is subtracted from the molecular velocity in order to pass the random molecular velocity to a thermostat. However, it appears in the literature that an uncorrected velocity vector value is passed to a thermostat

(Kamali and Kharazmi, 2011, Li et al., 2010, Toghraie Semiromi and Azimian, 2010, Yang and Zheng, 2010, Hanasaki et al., 2003). This assumption may be valid for low streaming velocity conditions. The initial focus in the research was to establish a novel algorithm for predicting streaming velocities at low acceleration values. Hence, the results in this chapter are based on this assumption. It is acknowledged that the results are valid for low acceleration values and the next step of research needs to extend the algorithm to undertake the necessary velocity correction. The Gaussian thermostat is combined with the velocity Verlet integrator to predict the positions and velocities of molecules at the next time step and the computational procedure at time t and time step δt is as follows:

1) Calculate the thermostat variable at time t:

$$\dot{\xi}(t)=\left[\sum_{i=1}^{N} m_i a_i(t)\cdot v_i(t) / \sum_{i=1}^{N} m_i v_i^2(t)\right] \tag{3.15}$$

2) Evolve velocities at time $t+\delta t/2$:

$$v_i(t+\delta t/2)=v_i(t)+\left[a_i(t)-v_i(t)\,\dot{\xi}(t)\right]\delta t/2 \tag{3.16}$$

3) Evolve positions at time $t+\delta t$: $r_i(t+\delta t)=r_i(t)+v_i(t+\delta t/2)\delta t$ (3.17)

4) Calculate acceleration at $t+\delta t$ by evaluating the total force: $a_i(t+\delta t)=F_i(t+\delta t)/m_i$

5) Replace the molecular velocity $v_i(t+\delta t/2)$ for thermalized molecules according to assumptions i-iii and Section 2.3.

6) Evolve velocities at time $t+\delta t$ by recalculating the thermostat variable at time $t+\delta t$.

$$\dot{\xi}(t+\delta t)=\left[\sum_{i=1}^{N} m_i a_i(t+\delta t) v_i(t+\delta t) / \sum_{i=1}^{N} m_i v_i^2(t+\delta t)\right] \tag{3.18}$$

$$v_i(t+\delta t)=v_i(t+\delta t/2)+\left[a_i(t+\delta t)-v_i(t+\delta t)\,\dot{\xi}(t+\delta t)\right]\delta t/2 \tag{3.19}$$

The particles velocities $v_i(t+\delta t)$ are calculated iteratively within a Newton-Raphson procedure by solving until the difference $v_i(t+\delta t)_k - v_i(t+\delta t)_{k-1}$ is sufficiently small.

$$v_i(t+\delta t)_k = v_i(t+\delta t)_{k-1} - \frac{h_i(v_i,\dot{\xi})}{J_{ii}} \tag{3.20}$$

$$h_i(v_i,\dot{\xi}) = v_i(t+\delta t/2) + \left[a_i(t+\delta t) - v_i(t+\delta t)\,\dot{\xi}(t+\delta t)\right]\delta t/2 - v_i(t+\delta t) \tag{3.21}$$

$$J_{ii} = \frac{\partial h_i(v_i,\dot{\xi})}{\partial v_i} = -\left[\dot{\xi}(t+\delta t) + v_i\frac{\partial \dot{\xi}}{\partial v_i}\right]\delta t/2 - 1 \tag{3.22}$$

Where,

$$\frac{\partial \dot{\xi}}{\partial v_i} = \frac{\partial}{\partial v_i}\left[\frac{\sum_{i=1}^{N} F v_i}{\sum_{i=1}^{N} F v_i^2}\right] = \frac{\partial}{\partial v_i}\left[\sum_{i=1}^{N} F v_i \left(\sum_{i=1}^{N} F v_i^2\right)^{-1}\right] =$$

$$\left(\sum_{i=1}^{N} F v_i\right)\left(-2m_i v_i\left(\sum_{i=1}^{N} m_i v_i^2\right)^{-2} + \left(\sum_{i=1}^{N} m_i v_i^2\right)^{-1}\left(\sum_{i=1}^{N} F\right)\right) =$$

$$\left(-\frac{2\dot{\xi} m_i v_i}{\sum_{i=1}^{N} m_i v_i^2} + \frac{\sum_{i=1}^{N} F}{\sum_{i=1}^{N} m_i v_i^2}\right)$$

An optimal time step should conserve both kinetic and potential energy. It is shown that a time step of 2fs maintains energy levels within 0.02% for kinetic energy and ±0.5% for potential energy without significantly compromising simulation time (Dyson et al., 2008) and hence is used in this work.

3.2.4 Capturing macroscopic velocity at a fixed location using Moving Least Squares method.

At each instance all molecules need to follow Gaussian distribution, as given by Equation 3.2 (and shown in Figure 3.1), in each direction so that the resulting three dimensional distribution of speed is as per the Maxwell Boltzmann distribution. Although the molecules are initialized with corresponding distributions, they are not directly constrained or rescaled to follow the distributions at each time step. The Gaussian thermostat as described in the subsection 3.2.3 maintains the overall kinetic energy. The external force or acceleration and the boundary wall geometry influence the probability that high or low velocity molecules occur at given point. E.g. for

rough surfaces with high value of *f*, the average macroscopic velocity parallel to the wall is much lower than in the centre of the flow regime. In order to examine bulk properties, the ensemble properties are assembled from local values sampled at discrete time steps through the simulation. An average of all ensemble averages is taken as a bulk/macroscopic value at a given point.

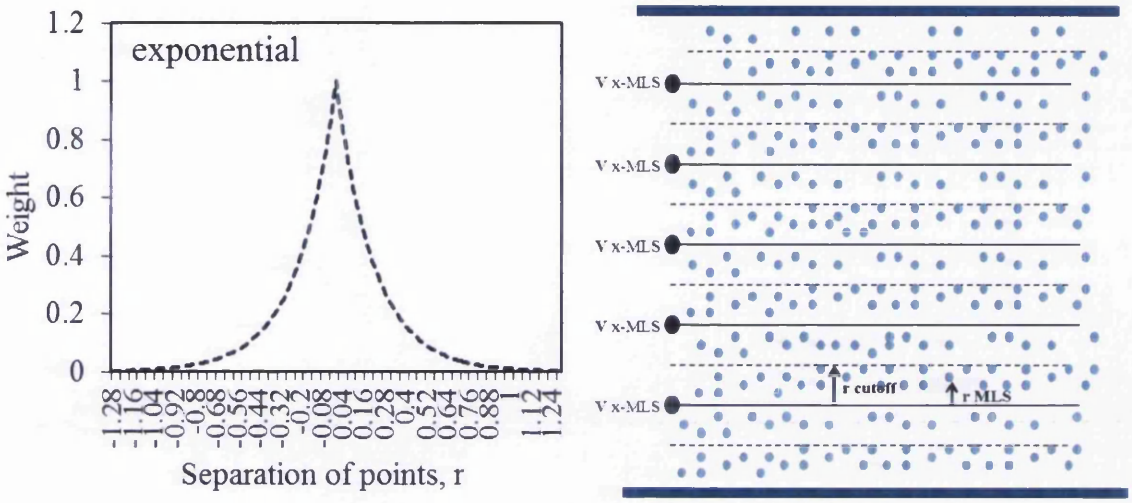

Figure 3.8. Weighting function used for the moving least square method in left. Sample ensemble with moving least square (MLS) nodes to average molecular properties within a layer defined by distance in right.

For a set of *N* molecules within a sample ensemble (Figure 3.8), the individual positions *xi*, *yi* and *zi* and molecular property values (e.g. velocity in *x* direction) *Vi* for $i = 1$ to *N* is known. The distance *r* (Equation 3.24) from fixed points ($V_{x\text{-}MLS}$) is used for calculating weights as defined by the graph (Figure 3.8) and Equation 3.23:

$$W(r) = \frac{1}{100^{\,r}} \tag{3.23}$$

$$r = \frac{r_{MLS}}{r_{cutoff}} \tag{3.24}$$

The average value at a given least square node ($V_{x\text{-}MLS}$) for the ensemble is determined by minimizing the error function $J_{LS} = \sum_{i=1}^{N} W(r)(V(r) - V_i)$ where $V(r)$ is

a local polynomial function that approximates given scalar values V_i within the layer defined by r_{cutoff} at the least square node with the weighting function $W(r)$.

3.3 Verification of the Simulation Model

The proposed model is verified by comparing results with the molecular wall (Section 3.3.1) as well as published results (Section 3.3.2).

The conformance of velocity distribution at each dimension is checked with the corresponding Gaussian distribution at the appropriate temperature and the resulting distribution for speed verified with the Maxwell Boltzman distribution. Figure 3.9 shows excellent agreement with the exact versions of the distribution for slit pore geometry at 300K with significantly rough walls (f = 0.681) and very high acceleration values ($1\times10^{13}\ m/s^2$).

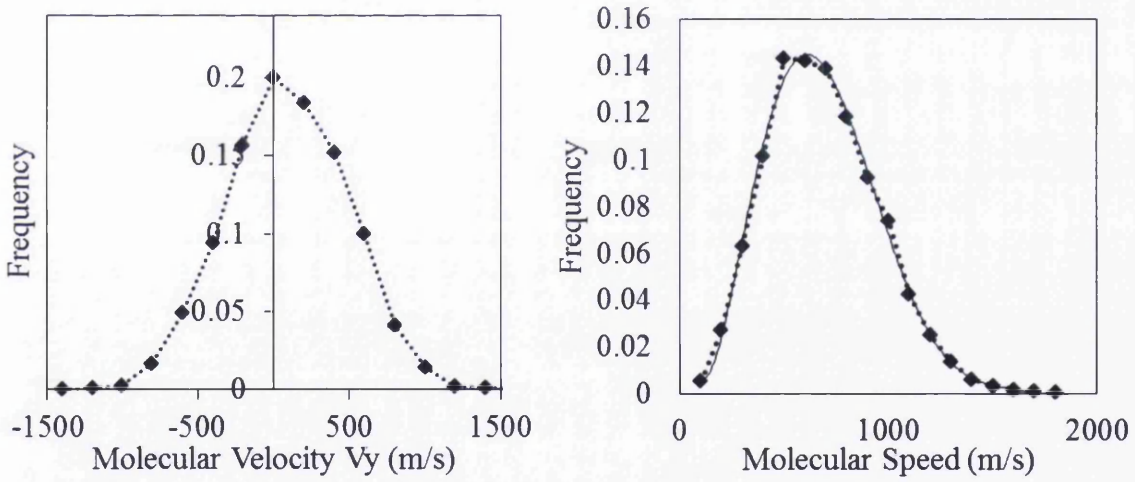

Figure 3.9. Distribution of y component of molecular velocity in left. Distributions for x and z components are also very similar to the y component. The resultant distribution for the molecular speed is shown on the right

Figure 3.9 demonstrates that the fluid molecules conform to the correct thermodynamic state and that the thermostat is not having adverse effects on the velocity distribution. Sokhan *et al.* have reported deviation from the exact velocity distributions for much smaller accomodation coefficient values (f = 0.029) and the acceleration values $5\times10^{11}\ m/s^2$. Figure 3.10 illustrates the effect of replacing

molecular velocities perpendicular to the wall using Equation 3.1. Significantly higher molecular speeds and molecular velocities in y direction are observed. As a result Gaussian thermostat fails to conserve kinetic energy unless velocity rescaling techniques are employed to impose Gaussian distributions. Velocity rescaling techniques adversly influence velocity patterns and are not recommended.

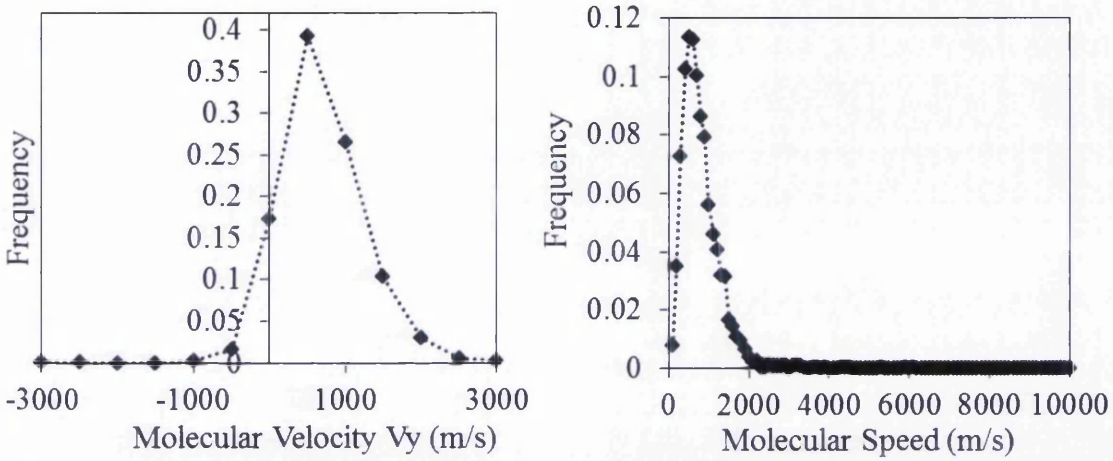

Figure 3.10. Distribution of y component of molecular velocity (in left) and molecular speed (in right) when velocity perpendicular to the wall is replaced by Equation 3.1 for thermalized molecules.

3.3.1 Comparison with an equivalent molecular wall

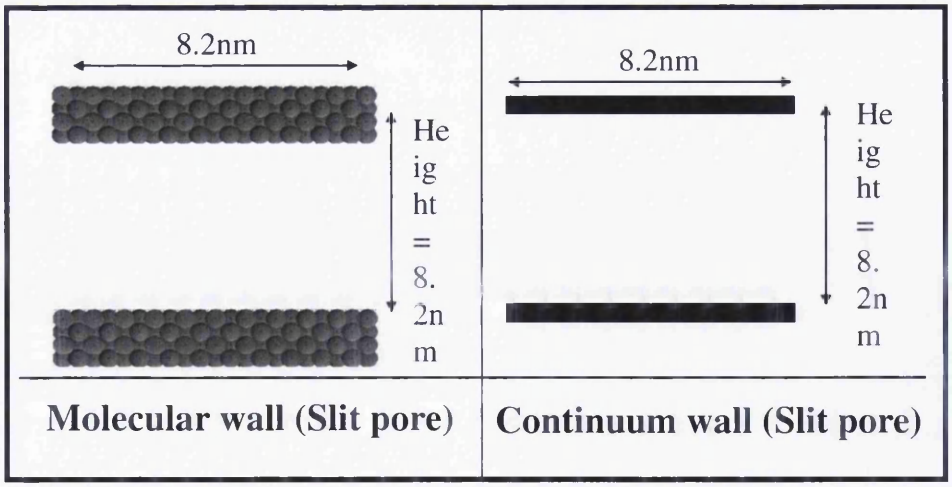

Figure 3.11. Molecular and the equivalent continuum graphite wall for slit pore geometry.

The proposed model is compared with an equivalent molecular wall. The dimensions given for the slit pore geometry (Figure 3.11) correspond to 5104

methane molecules at 40MPa and 300K with the specific volume of 109.66 $\mathring{A}^3$ per molecule. Values for material constants used in the simulation model are given in Section 3.2. As described in Section 3.2.4 and Figure 3.8, the macroscopic velocity at corresponding 'MLS' nodes, captured at various time steps, is shown in Figure 3.12 as dotted curves along with the overall average value calculated at each MLS node (continuous curve). The accommodation coefficient values are calculated using the tabulated data given by Arya et al. (2003) corresponding to the reduced energy parameter (ε_{fw}/k_bT) and the roughness parameter (σ_{wg}/L) with L equal to 3, 4, 5, 6 $\mathring{A}$. The corresponding values of f are 0.07, 0.256, 0.45 and 0.681. These values correspond to surface roughness with higher f values indicating higher surface roughness. The influence of all f values on velocity distributions is discussed in Section 4.3. In this example, three f values are chosen: smooth wall (f = 0), intermediate roughness (f = 0.257) and theoretical maximum with f = 1. An uniform acceleration of $6\times10^{11} m/s^2$ is applied to all fluid molecules. The corresponding results (Figure 3.12a) show that the assumption (iv) does not adversely affect the overall velocity distributions. Figure 3.12b compares the average velocity profiles given by the molecular and continuum wall assumptions respectively.

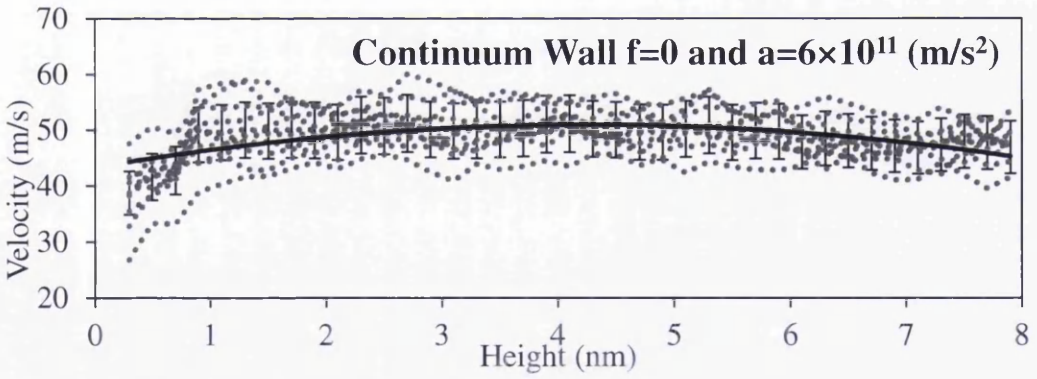

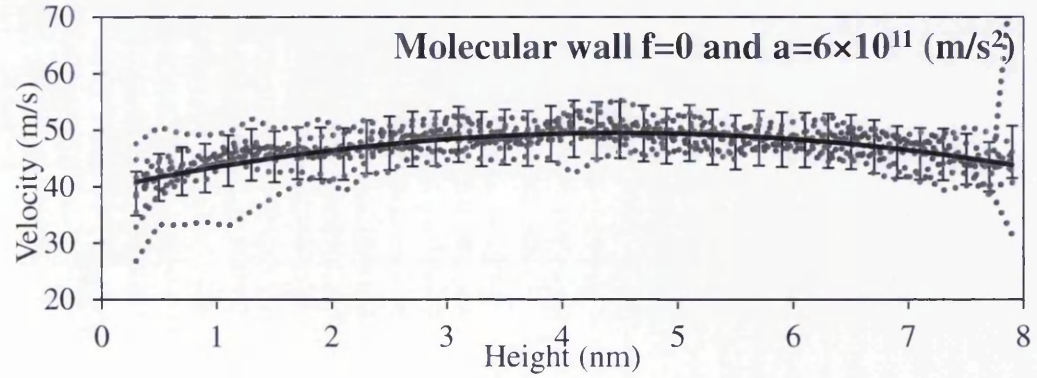

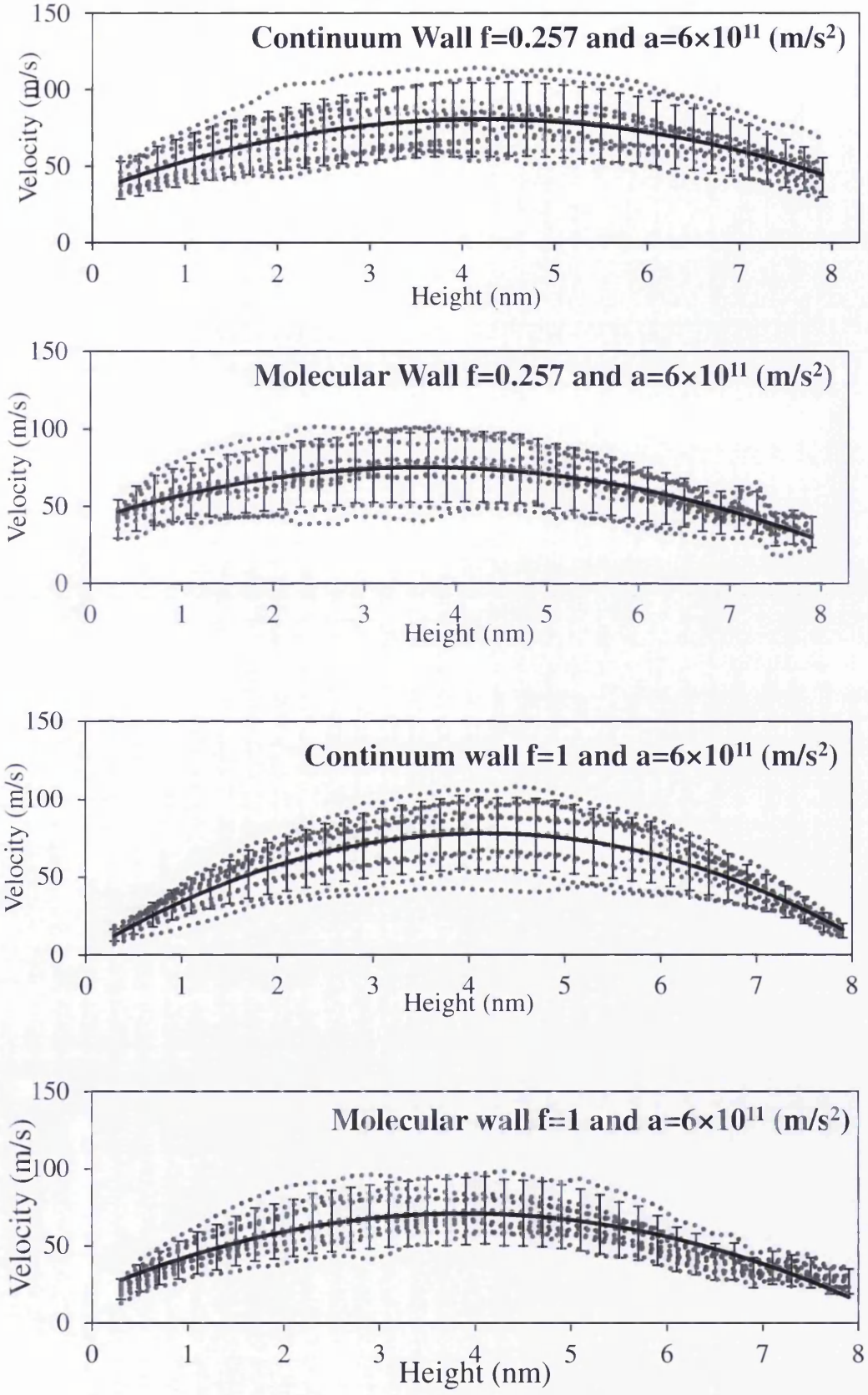

Figure 3.12a. Comparison of average velocity profiles with continuum and molecular walls.

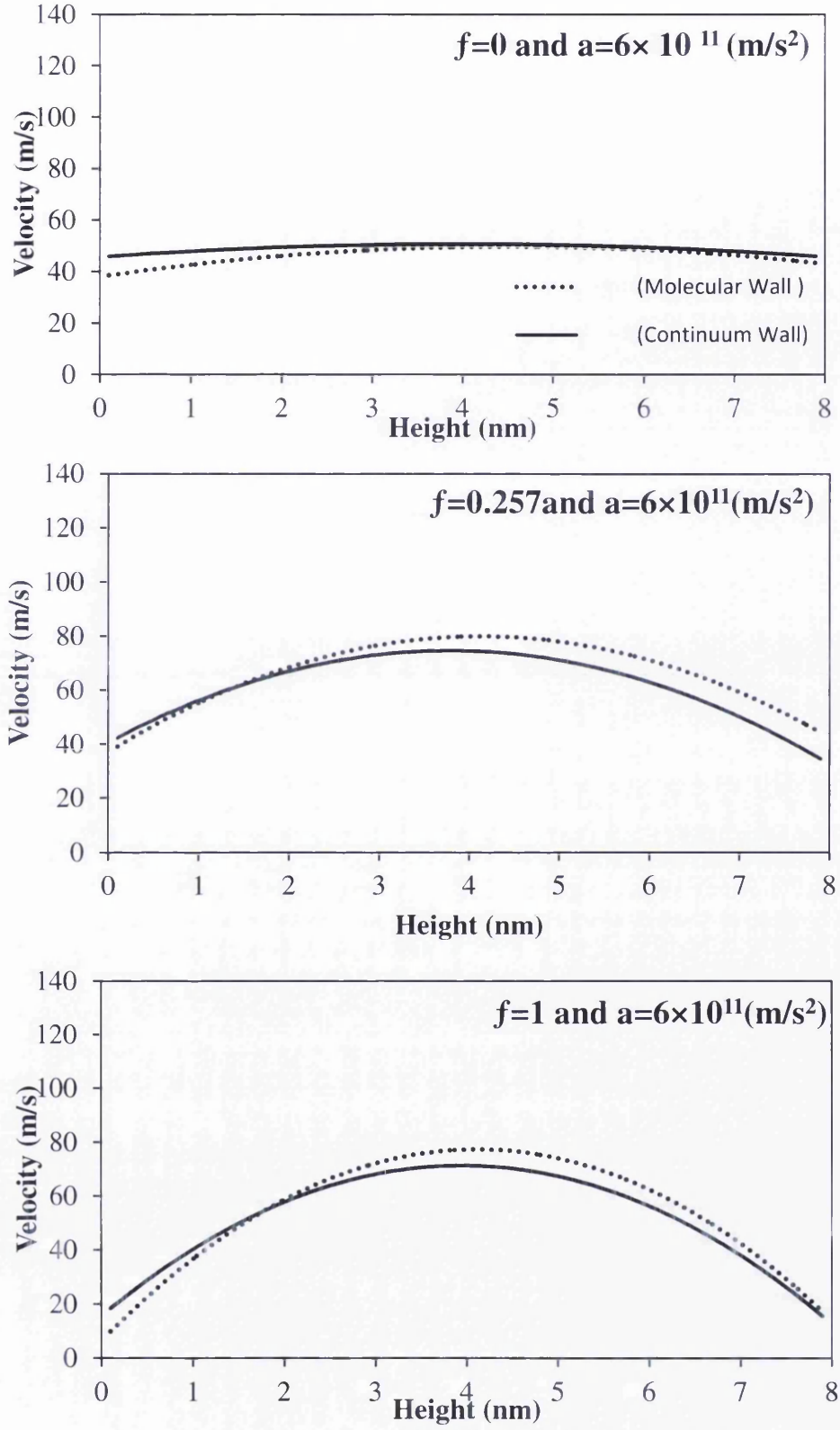

Figure 3.12b. Comparison of average velocity profiles with continuum and molecular walls.

3.3.2 Comparison of the results with published literature

The results of the proposed model were compared with the molecular simulation results published by Sokhan et al. (2001). Both simulations assumed continuum wall and methane as working fluid at 300K temperature. The slit pore geometry was similar to the one shown Figure 3.11, except that the graphite plates were separated by 7.1nm and the corresponding width and breadth values were 7.715 nm and 8.368 nm respectively. The numbers of methane molecules used were 5104 with a reduced density value of 0.61. The accommodation coefficient value was 0.029 and the uniform acceleration applied to all molecules. The Lennard Jones parameters were same as used in this Chapter.

The velocity profiles parallel to the slit pore are compared. The average velocity values (shown by the dotted curve) are found to be comparable to results shown by Sokhan et al. (2001) (continuous curve) (Figure 3.13). However, the velocity at the center is predicted to be lower than the one calculated by Sokhan. This is certainly not a benchmark comparison. However, it does give confidence that the results are comparable to the published results. It should be noted that the accommodation coefficient value is very low (0.029). This means that the wall only thermalizes 2.9% of molecules that collide with the wall. Hence, the effect of wall interaction is relatively small. The difference in results could also be due to the way diffuse boundary conditions are implemented in the proposed algorithm (assumptions i-iii).

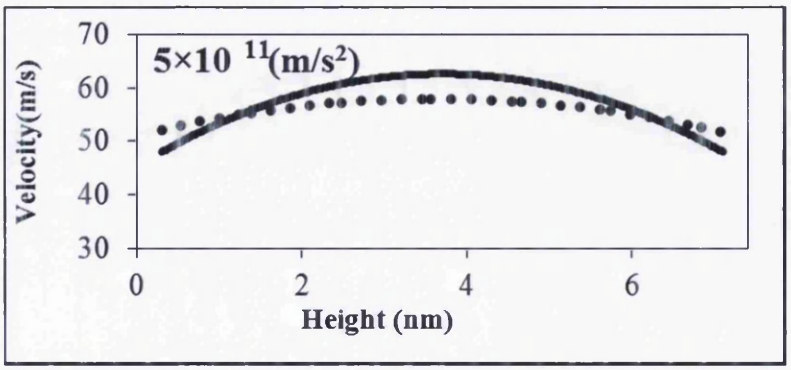

Figure 3.13. Comparison of average velocity profiles predicted by the proposed model (dotted curve) and Sokhan et al. (2001) (continuous curve).

3.3.3 Effect of interaction with wall

The accommodation coefficient f determines the fraction of molecules thermalised by the wall. The accuracy of the simulation is checked by solving a molecular flow problem in a slit pore with initial temperature of 300K at different acceleration and accommodation coefficient values. However, the temperature of the walls is maintained at 250K and 350K. At $f = 0$ when none of the wall molecules are thermalised, as shown in Figure 3.14 and Figure 3.15, the temperature of the fluid remained unchanged at all acceleration values (6, 10, 50, 100 (m/s^2)). As the f value increased, a gradient is formed with molecules closer to the wall retaining wall temperature. For $f = 1$, the molecules near wall are in thermal equilibrium with the wall as all of the colliding molecules were thermalised by the wall. With NVT assumptions, the overall kinetic energy of the molecules was conserved at 300K with a linear temperature gradient between 250K and 350K wall. It is observed that the pattern is independent of the acceleration applied to the molecules.

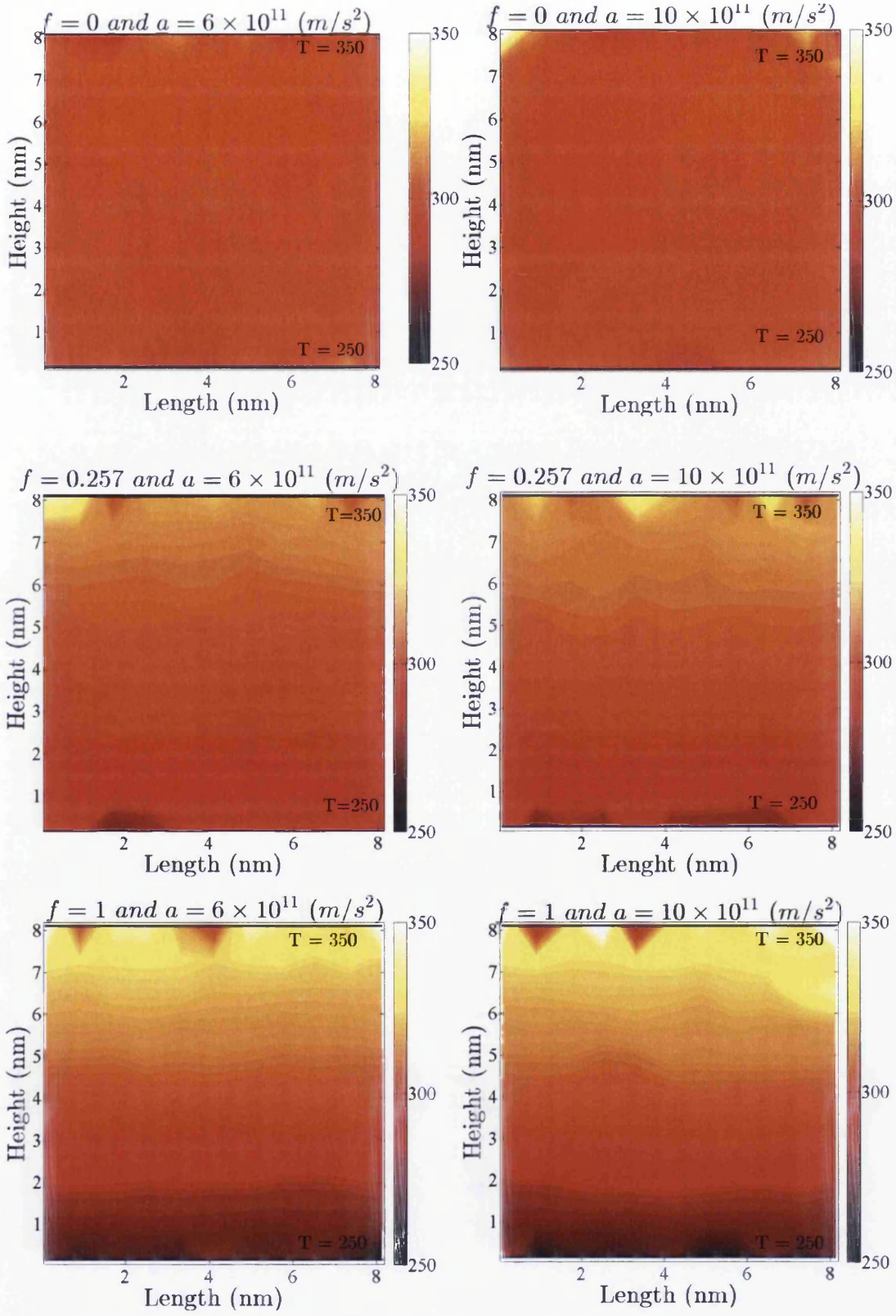

Figure 3.14. Thermalisation of fluid molecules with wall temperatures at 250K and 300K at different accommodation coefficient values and acceleration values.

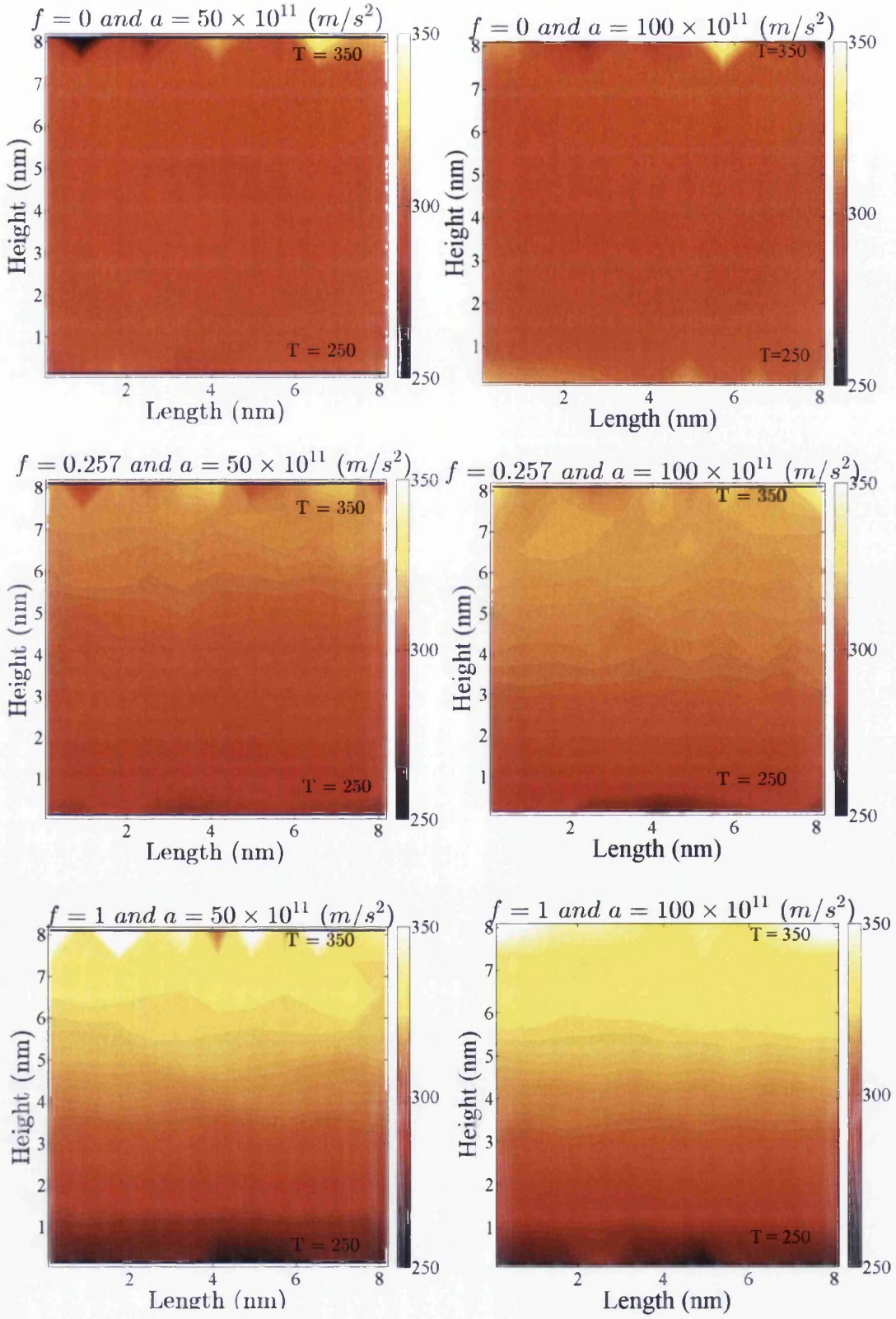

Figure 3.15. Thermalisation of fluid molecules with wall temperatures at 250K and 300K at different accommodation coefficient values and acceleration values.

3.4 Discussion of Results

The simulation is run for three wall geometries as tabulated in Figure 3.16. The depth in z direction is 8.2 nm for all geometry configurations. The effect of wall geometry (Section 3.4.1) and surface roughness characterized by accommodation coefficient f (Section 3.4.2) for various acceleration values is discussed. A non-linear variation between overall macroscopic average velocity value and the driving force expressed in terms of acceleration values that was observed is discussed in Section 3.4.1. The one dimensional arrangement of MLS nodes shown in Figure 3.8 is extended into grid of two dimensional MLS nodes to derive macroscopic two dimensional velocity distributions for stepped and inclined geometry. The results for acceleration value of $50\times10^{11}\ m/s^2$ and accommodation coefficient f values of 0.07, 0.257, 0.45, 0.681 and 1 are discussed in Section 3.4.2.

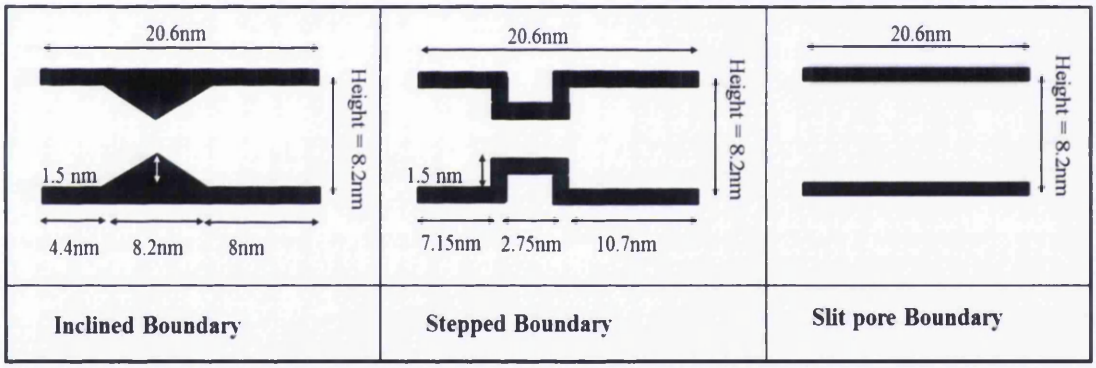

Figure 3.16. Specification of continuum wall geometries used in the simulation

The number of molecules and dimensions of the geometry are chosen so that the specific volume for a molecule at 40MPa and 300K is 109.66 $Å^3$ per molecule.

As shown in Figure 3.17, in the absence of external force the range for molecular acceleration is between 1×10^{14} and $1\times10^{15}\ (m/s^2)$ with very few molecules at 1×10^{12} and $1\times10^{16}\ (m/s^2)$. In order to ensure that the external force does not disturb the molecular interaction the external uniform acceleration value applied does not exceed $5\times10^{13}\ (m/s^2)$. At higher accelerations molecular motion becomes unstable with a tendency to form molecular clusters. The system becomes overconstraint and

adversly affects subsequent molecular collisons. It is noted that the acceleration values are applied at the molecular scales and hence are compared with the acceleration values resulting from the molecular interaction (Figure 3.17). The microscopic acceleration of fluid particles in micro-channels is a continuum concept. In this research the continuum velocities are extracted from molecular velocities.

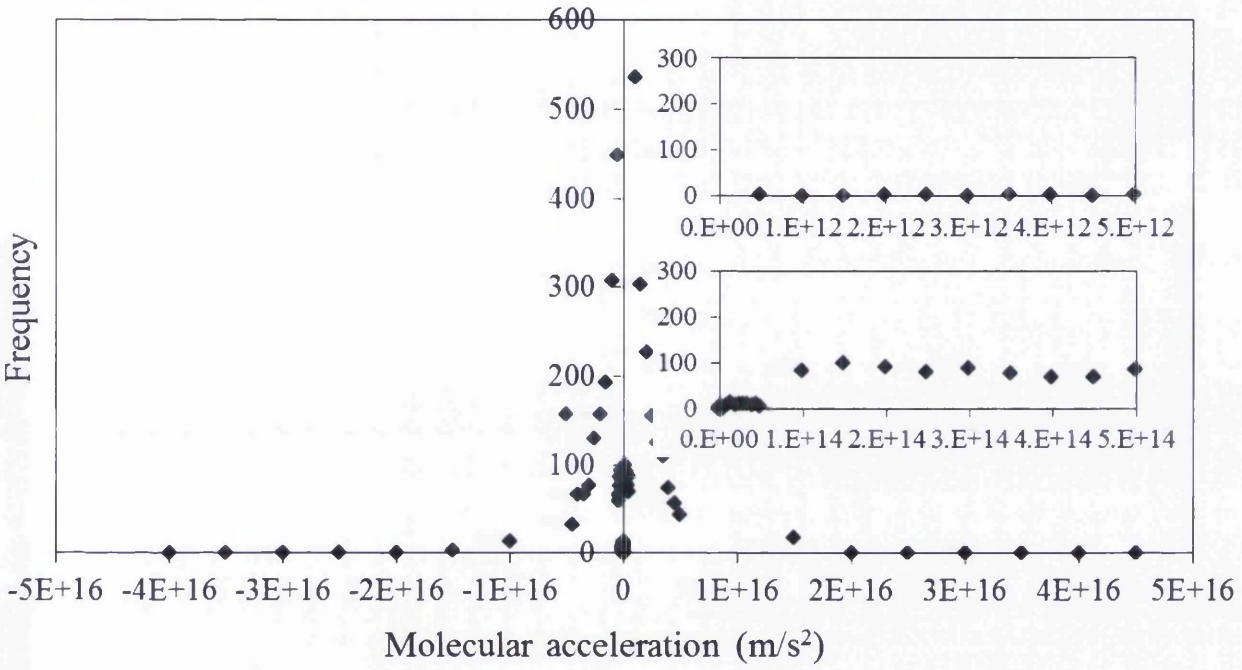

Figure 3.17. Typical frequency distribution of molecular acceleration values in the absence of external force.

3.4.1 Influence of wall geometry on the macroscopic velocity distribution

The effect of acceleration values (6×10^{11}, 10×10^{11}, 50×10^{11} and 100×10^{11} (m/s^2)) on three wall geometries as described in Figure 3.11 is shown in Figure 3.18. The accommodation coefficient value f is 0.257. The macroscopic velocity parallel to the wall is calculated at fixed MLS nodes as shown in Figure 3.8. It is observed that the stepped geometry has the minimum velocity near the wall and maximum velocity at the centre for all acceleration values. The result for the slit pore geometry is same as the one shown in Figure 3.12 and is included in Figure 3.18 for comparison. The inclined wall appears to encourage molecular interactions in such a way that the velocity pattern is similar to the slit pore however at high acceleration values the velocity at the center is slightly higher for the inclined geometry. Detailed

discussion on possible reasons for the changes in velocity profiles between inclined, step and slit pore boundaries is undertaken in Section 3.4.2 after Figure 3.26.

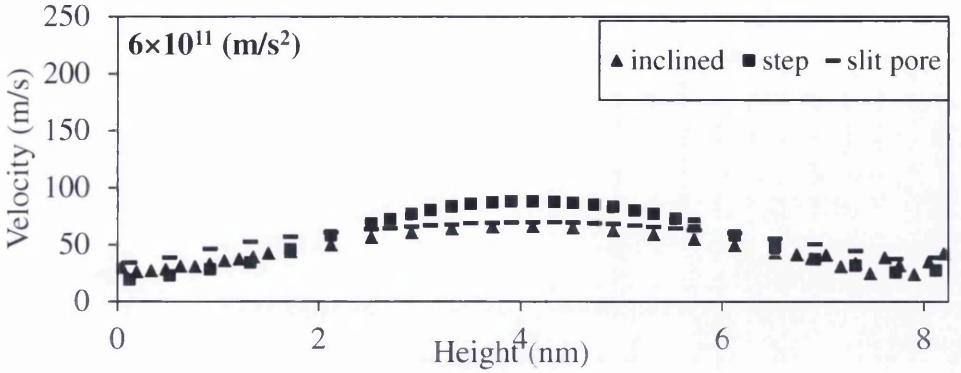

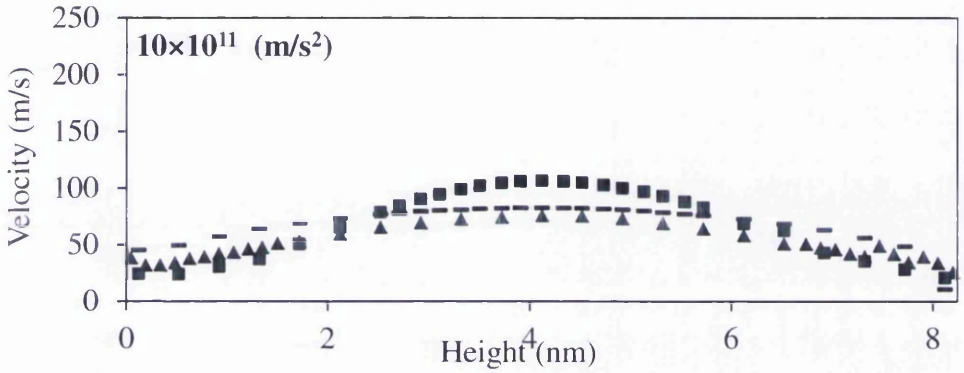

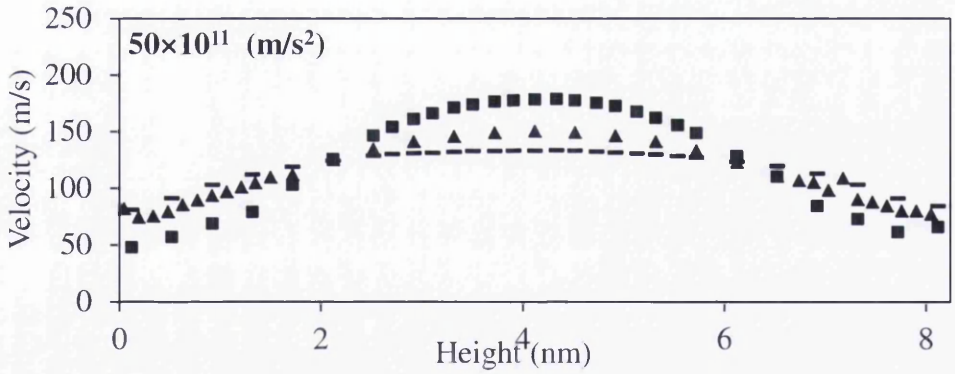

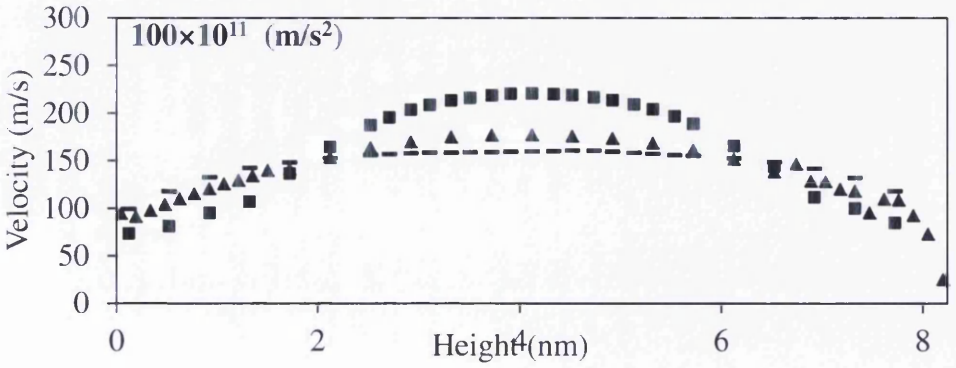

Figure 3.18. Effect of wall geometries on the macroscopic velocity distribution parallel to the wall at four acceleration values.

Interesting flow patterns emerge if an average of macroscopic velocity values parallel to the wall at all MLS nodes (Figure 3.8) is plotted for various acceleration values. Figures 3.19-3.3.23 show dependence of average velocity with the acceleration applied for different temperature, pressure, accommodation coefficient values or wall geometry types. The error bars on average velocity values are shown in Figure 3.22 where the effect of geometry types is studied. Similar error bars were observed for all graphs, however for the sake of clarity, the error bars are shown for Figure 3.22 only. The graphs show a distinctive shape suggesting that at low acceleration values, the average velocity increases rapidly for a small change in the acceleration values. In contrast, at high acceleration values the increase in average velocity is relatively small even for significantly high acceleration values.

Figures 3.19 and 3.20 highlight that the average velocity is higher at higher temperature values, however the effect is more significant at higher pressure values.

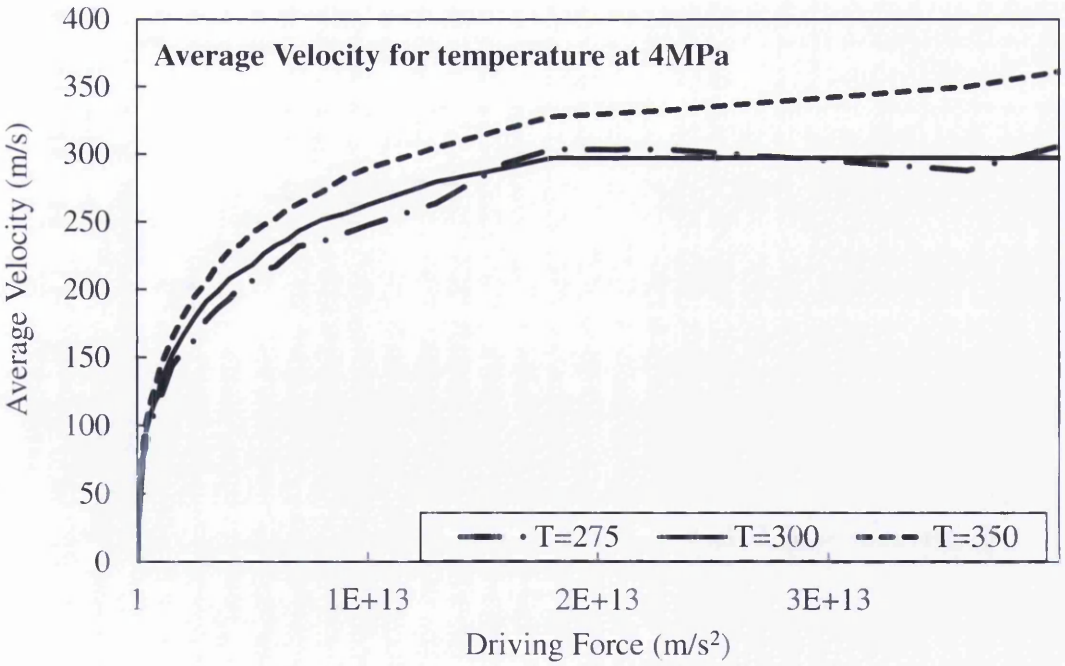

Figure 3.19. Average velocity plotted against the driving force (or acceleration) for slit pore geometry for 3 different temperature values at 4 MPa.

As seen in Figure 3.19 and 3.20, the velocity increase after the driving force value of $2\times10^{12}(m/s^2)$ is much smaller for 4MPa as compared to the simulation for 40MPa pressure. In this comparative study, the number of molecules were same however,

the dimensional size was not same as it accounted for the differences in the molecular densities at both pressures. It is possible that the molecular density may have influenced this observation. This effect needs to be investigated further.

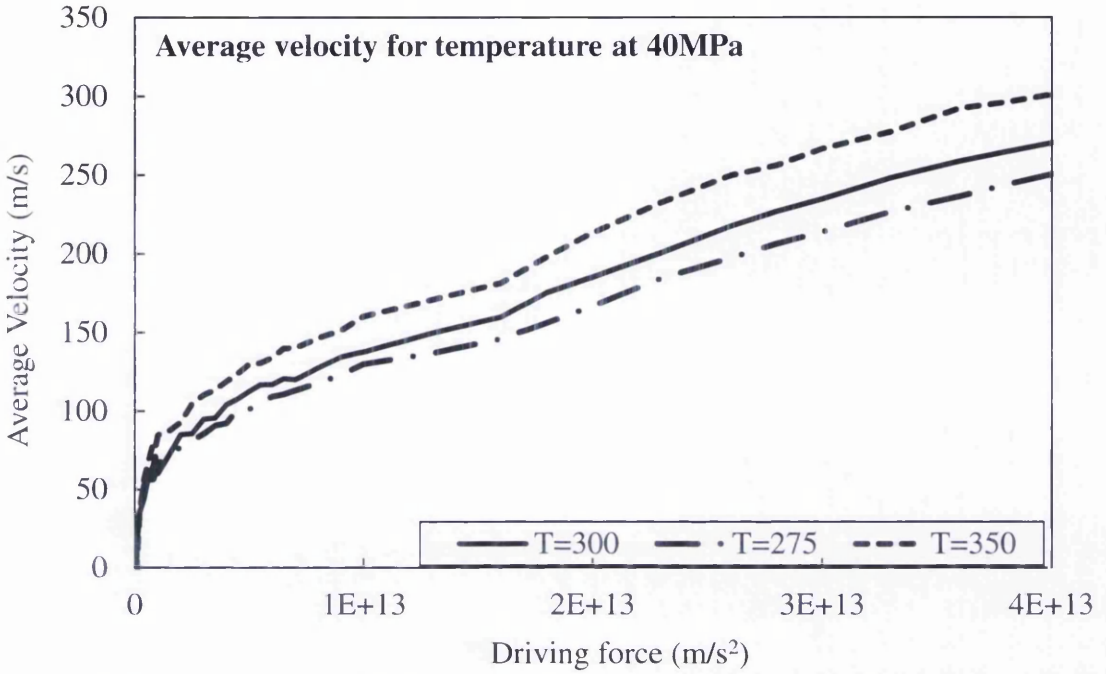

Figure 3.20. Average velocity plotted against the driving force (or acceleration) for slit pore geometry for 3 different temperature values at 40 MP.

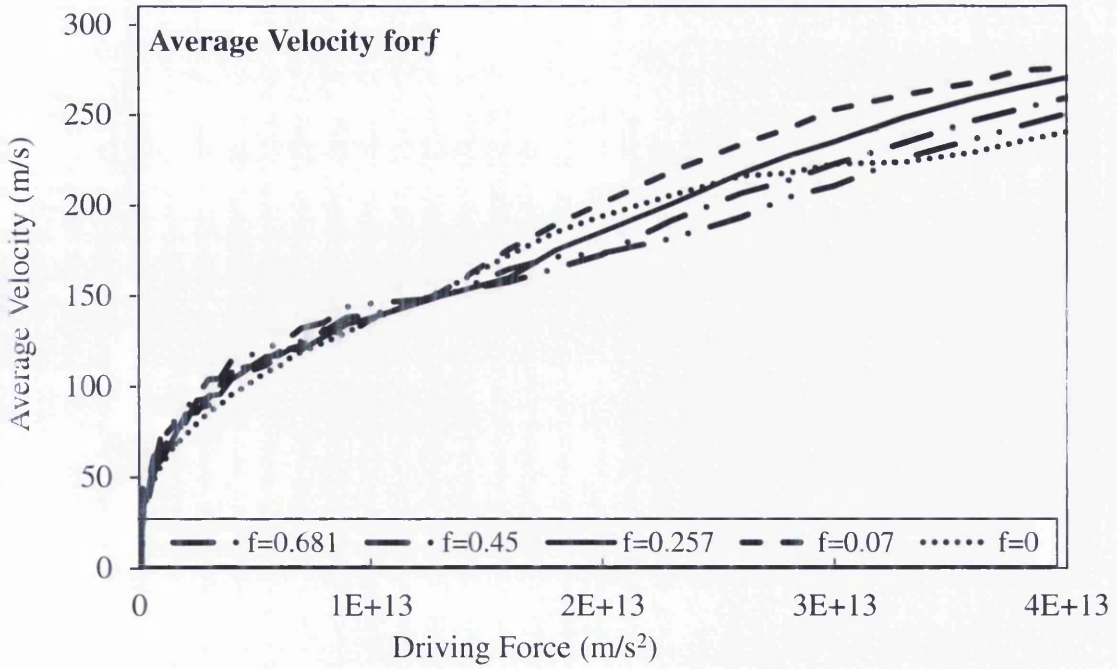

Figure 3.21. Average velocity plotted against the driving force (or acceleration) for slit pore geometry for 5 different roughness values at 300K and 40 MPa.

The surface roughness is expected to have more influence on the evolution of the boundary layer and on molecules closer to the wall. It is observed in Figure 3.21 that increasing or decreasing surface roughness value has no meaningful influence on the overall average velocity.

Figure 3.22 shows the variation for slit pore, stepped and inclined wall. Stepped wall has largest average velocity values and the inclined wall has lowest average velocity values. It is also observed that for acceleration values less than $1\times10^{12}\,(m/s^2)$the increase in the velocity is linear. The slop is much higher as compared to high acceleration values (e.g. > $5\times10^{12}\,(m/s^2)$). The low speed flow is characterized similar to laminar flow where losses are less (unit increase in the acceleration values causes higher changes in velocity values) and the high speed flow is made analogous to the flow. The losses are high as the unit change in the a[illegible] in this regime caues much lower change in the velocity value.

The molecular velocity is higher at low pressures as seen in [illegible] noted that when the simulation was run on different pressure and [illegible]s than 300K and 40MPa, the corresponding value of number d[illegible] in the simulation.

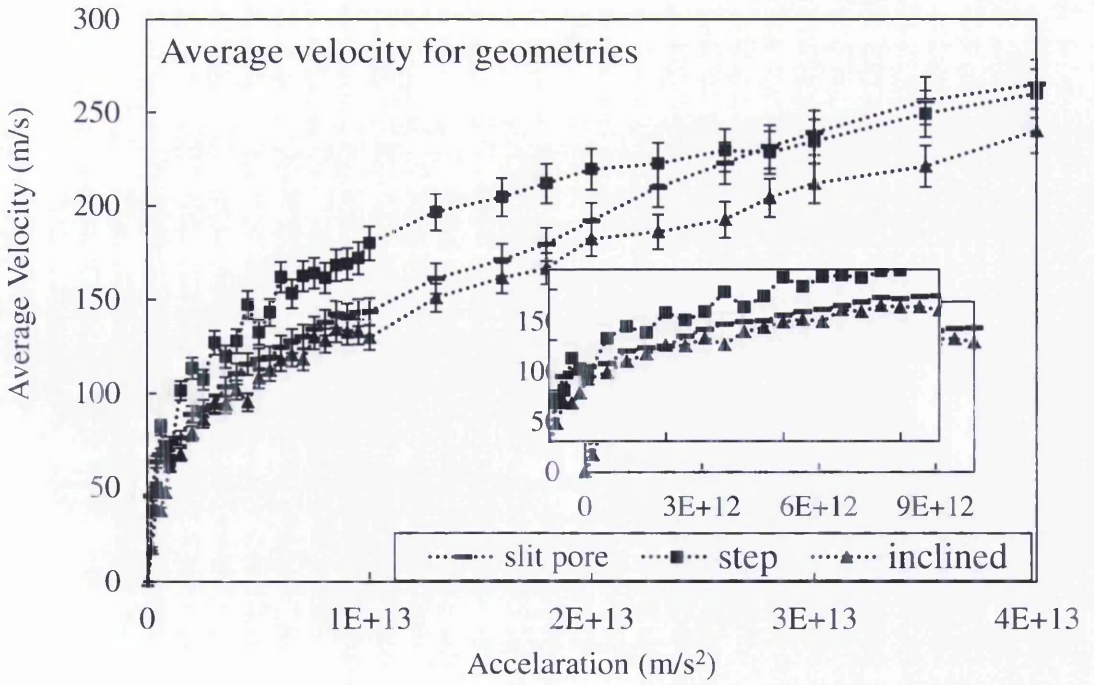

Figure 3.22. Average velocity plotted against the driving force (or acceleration) for inclined, slit pore, and stepped wall at 300K and 40MPa.

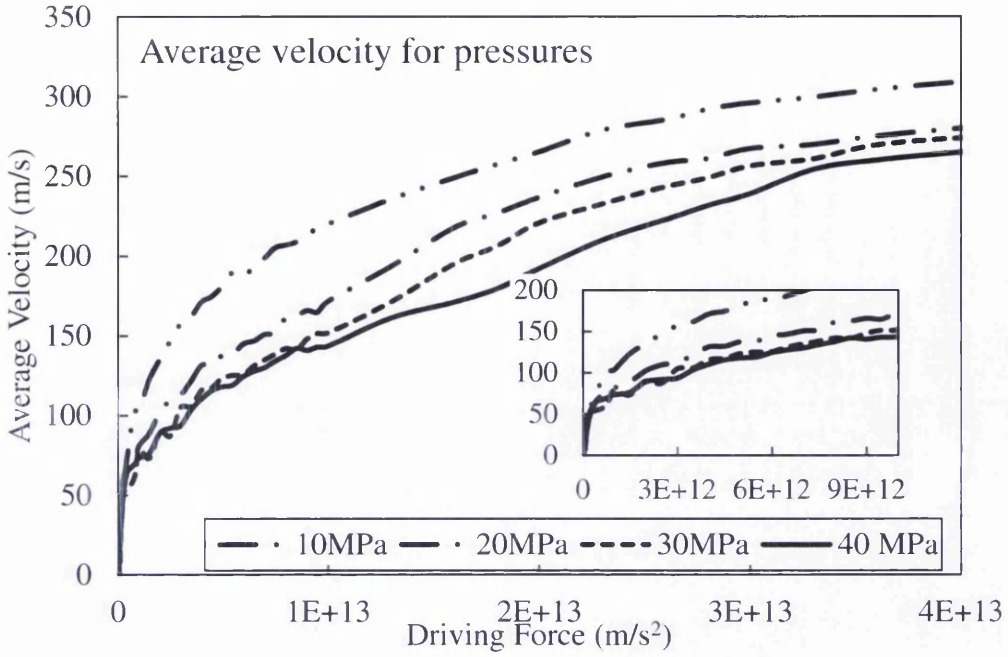

Figure 3.23. Average velocity plotted against the driving force (or acceleration) for slit pore geometry for 4 different pressure values at 300K.

3.4.2 Influence of surface roughness on the macroscopic velocity distribution for slit pore, stepped and inclined wall boundaries

The effect of increasing surface roughness on average x velocities for the slit pore wall geometry is studied for acceleration values 6×10^{11}, 10×10^{11}, 50×10^{11} and $100\times10^{11}(m/s^2)$(

Figure 3.24). It should be noted that for all simulations undertaken, the Gaussian distribution is maintained for x, y and z components of molecular velocities corresponding to a 300K temperature value at every time step. For the slit pore geometry, as the accommodation coefficient f increases, the velocity component parallel to the wall reduces near the wall and approaches a no-slip condition. It is noted that the velocity at the wall and in the centre is constant for $f=0$ whereas the parabolic velocity profile at high f values is evident for all acceleration values. Each plot in Figures 3.24, 3.25 or 3.26 is prepared in the same way as shown in Figures 3.12, Figures 3.25 and 3.26 show the effect of inclined and stepped geometries respectively. It is observed that for inclined geometry (Figure 3.25) the effect of

surface roughness is negligible for lower acceleration values ($6\times10^{11}$and 10×10^{11}(m/s^2)). At high acceleration values the effect of surface roughness is clear and is in line with the pattern observed with the slit pore geometry. For the stepped geometry (Figure 3.26), very low velocity regions are observed in the wall with a higher average velocity in the centre. The overall influence of surface roughness is consistent with the patterns observed in the slit pore and the effect of surface roughness is clearly seen even at low acceleration values.

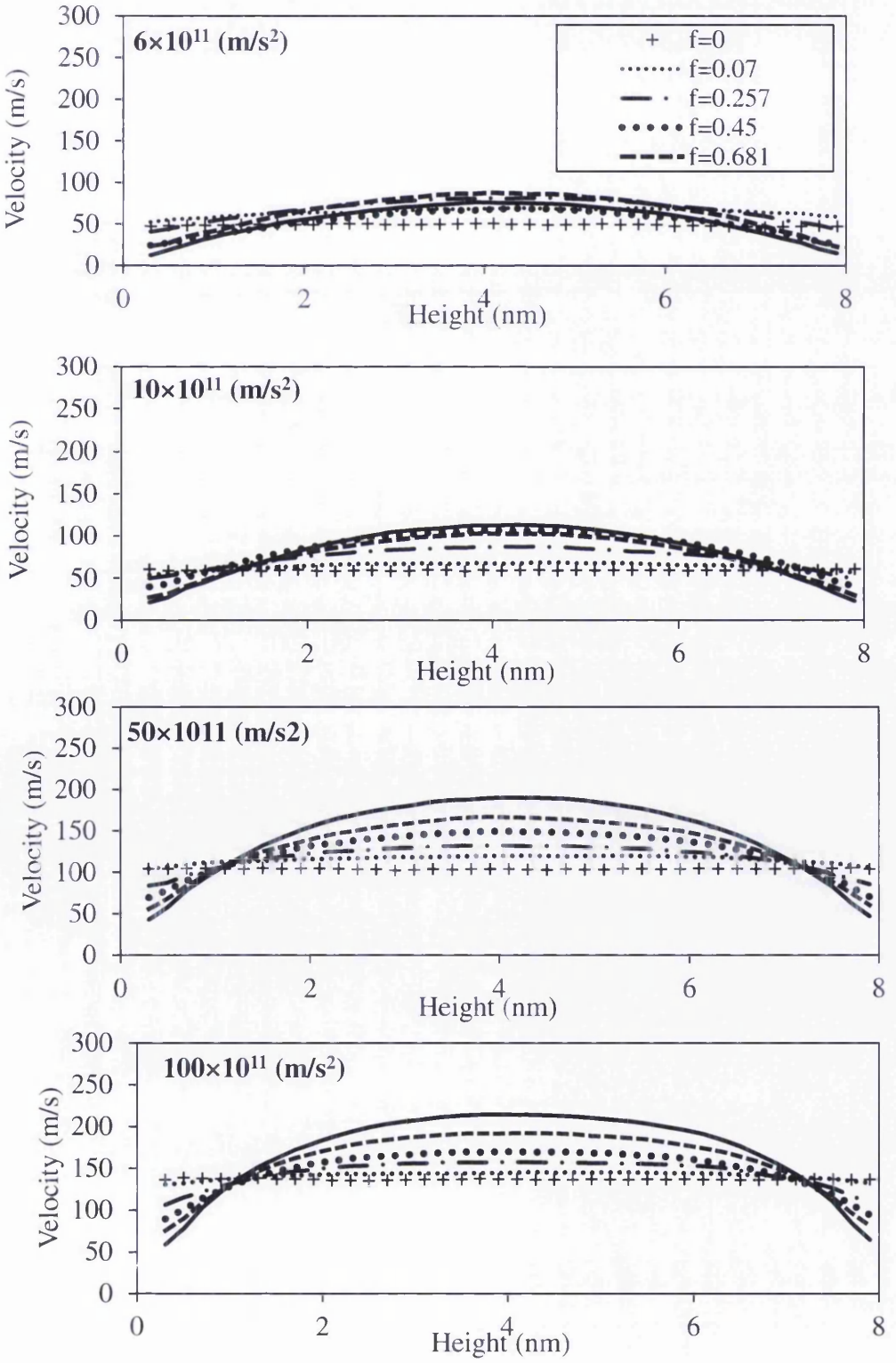

Figure 3.24. The effect of surface roughness on slit pore boundary.

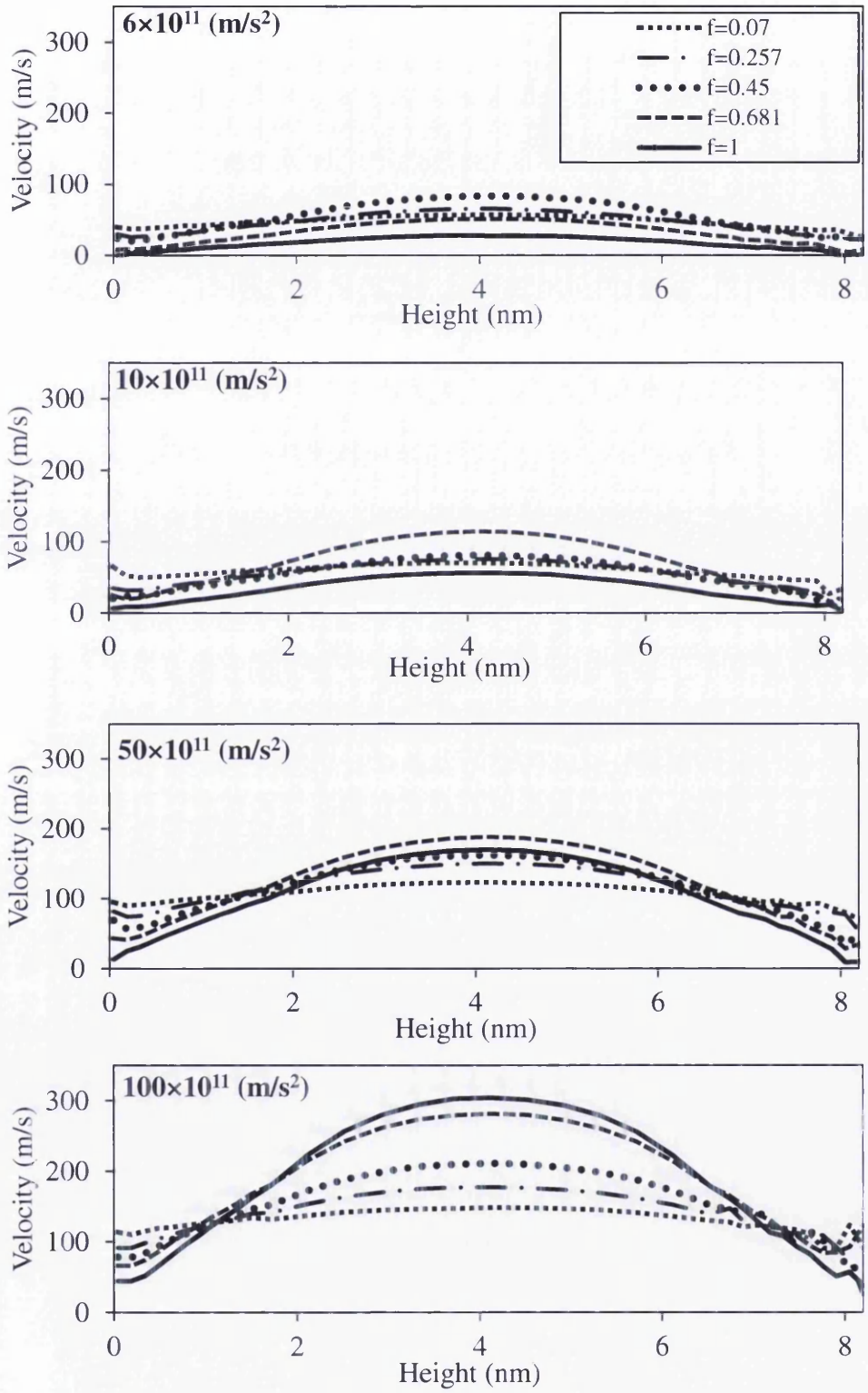

Figure 3.25. Two dimensional average velocity vectors and contours for inclined wall corresponding to three accommodation coefficient values (f=0, 0.257 and 1)

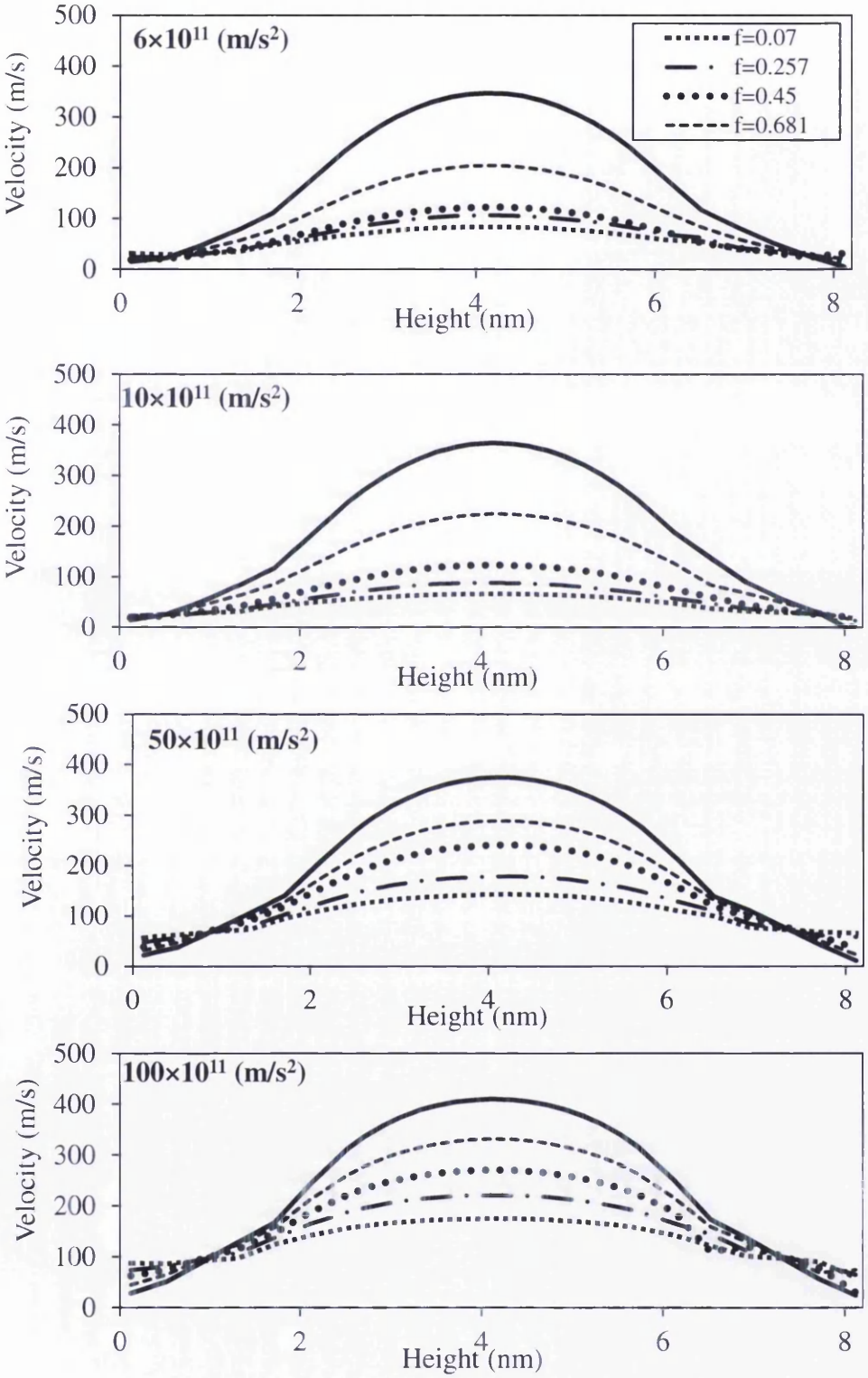

Figure 3.26. Two dimensional average velocity vectors and contours for stepped wall corresponding to three accommodation coefficient values (f=0, 0.257 and 1)

The one dimensional array of MLS nodes shown in Figure 3.8 is extended to two dimensional grid by defining r_{cutoff} in both x and y directions. Average velocities in both x and y direction are calculated at each MLS node. The resulting two dimensional velocity vectors and contours are shown in Figures 3.28- 31 for both inclined and stepped wall configurations. These contours are steady state and averaged over time steps as shown in Figure 3.12. The periodic boundary condition has significant influence on re-circulation zones and the velocity patterns as the periodic boundary condition ensures that the molecule leaving the exit boundary re-enters the computational domain with the same velocity vectors and maintains its distances from the walls.

For periodic boundary conditions, the results are sensitive to the length of the slit pore used. As shown in Figure 3.27, a length of 8.2 nm was not sufficiently long as there was not enough space to recover the velocity direction after the interaction with stepped or inclined wall. This changes the equilibrium flow conditions as the periodic conditions force the molecules to return with a same velocity vector.

The length of the inclined and stepped wall geometries is chosen so that the two dimensional exit velocity vectors are in the x direction. As shown in Figure 3.28, a length of 20nm ensured that the exit velocity vectors were parallel to the wall. The acceleration value of 50×10^{11} (m/s^2) is applied in x direction only and the accommodation coefficient value of 0.07, 0.257, 0.45, 0.681 and 1 is used respectively. For inclined wall, the average molecular velocity at the wall is much smaller and the velocity at the center much higher as compared to corresponding values with lower f. It is also seen that there is virtually no flow separation even at the high acceleration value of 50×10^{11} (m/s^2). One reason could be the application of the periodic boundary condition. As a result of the condition, the magnitude of the macroscopic velocity at the inlet is not same at all points. It is also noted in Figure 3.28 that as the accommodation coefficient value is increased from zero, the average velocity at the centre of the inclined wall is increased until f is equal to 0.45. The further increase in the accommodation coefficient value reduced the velocity differential in the flow domain making the velocity profile almost same everywhere at f=1. Similar trend is also observed at high acceleration values (Figure 3.29) where the highest velocity values in the centre are reduced as f is increased from 0.681 to 1.

This counter intuitive observation may be explained as follows. The normal velocity component remains same for every molecule after the collision for all f values. However, at f =1 all molecules receive a thermalized velocity for the velocity component parallel to the wall that is averaged at zero. Thus, effectively aligning the total velocity towards the normal component of the velocity. The subsequent interactions with other molecules may have resulted in better mixing of molecules thereby reducing velocity gradients and resulting into a uniform flow profile as seen in Figures 3.28 and 3.29. Clearly, the dependence of inclined geometry on various acceleration and accommodation coefficient values requires further investigation.

Stepped wall boundary has generated maximum velocity values at the centre as compared to inclined or slit pore wall configuration (Figure 3.18). The results shown are steady state velocity profiles. It should be noted that these are also influenced by the periodic boundary condition. In case of a stepped wall boundary (Figure 3.31), it is seen that the periodic boundary velocity near walls is much smaller as compared to the velocity value near centre. This may have created a zone of low average (streaming) velocity near walls with a high average velocity at the centre.

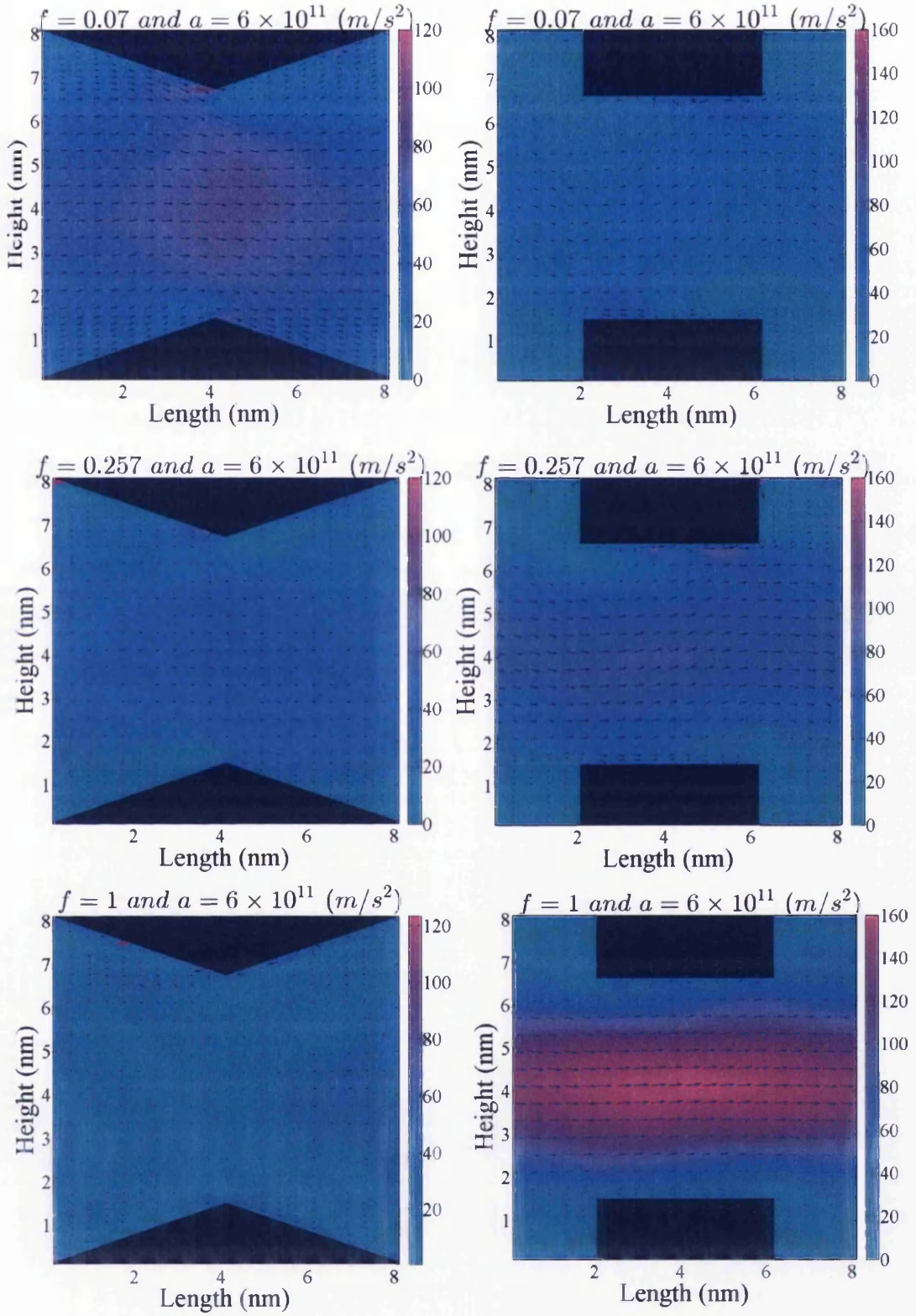

Figure 3.27. Velocity contours for 8.2nm long inclined and stepped geometry.

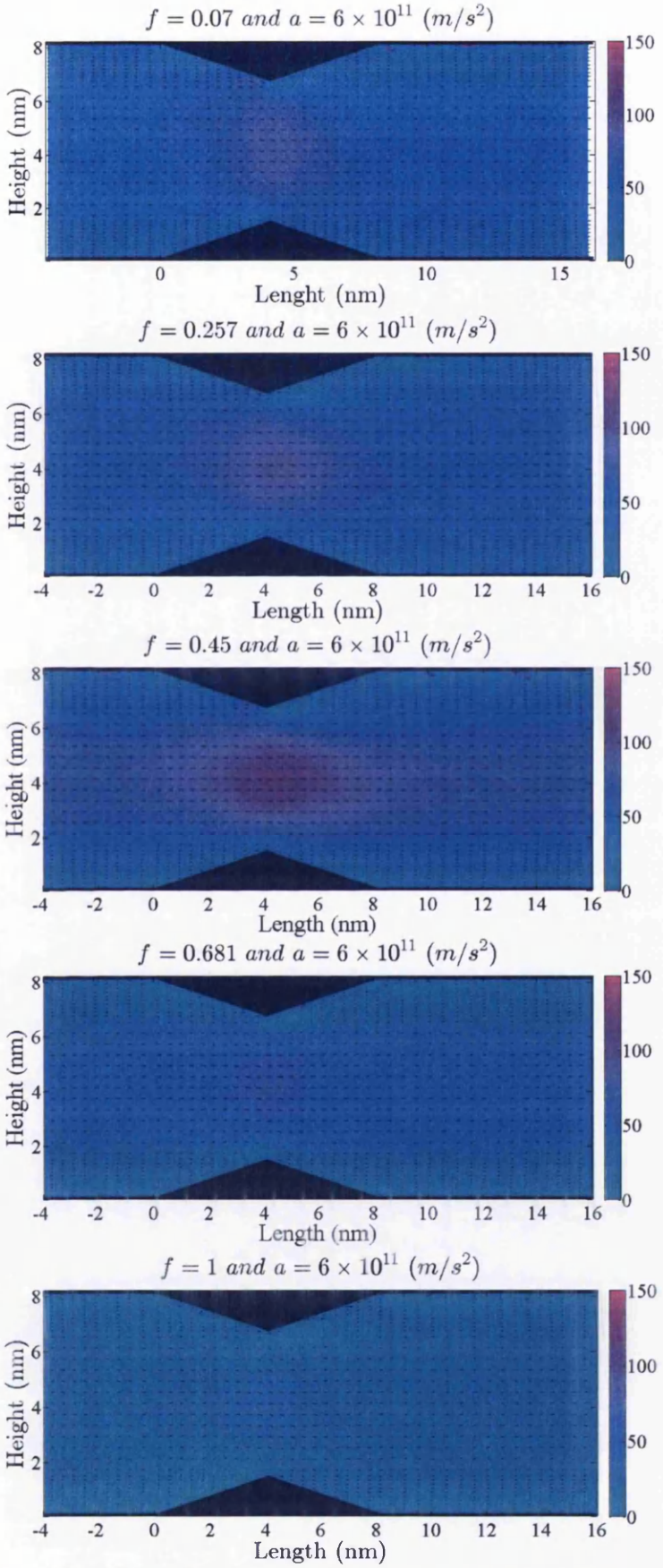

Figure 3.28. Velocity contours for inclined boundary for f= 0.07, 0.257, 0.45, 0.681, 1 and a= 6(m/s^2).

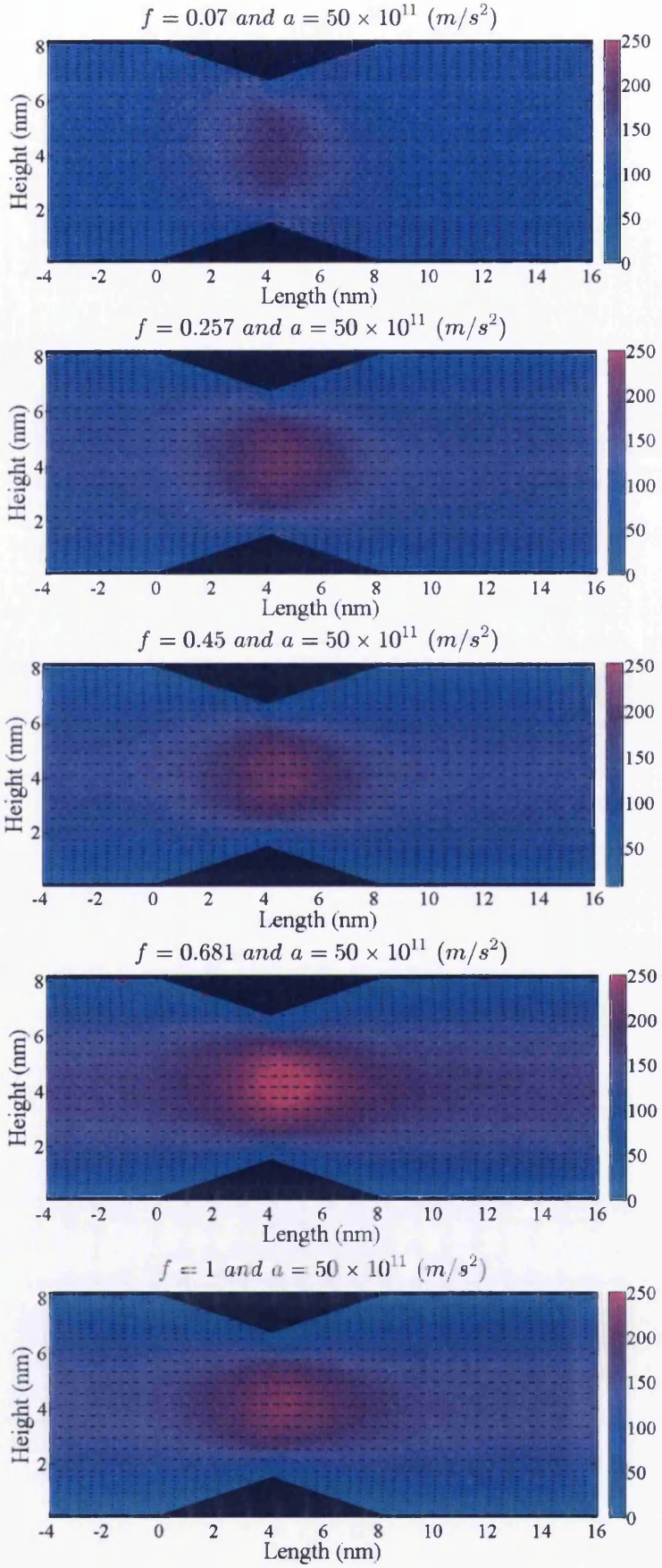

Figure 3.29. Velocity contours for inclined boundary for f= 0.07, 0.257, 0.45, 0.681, 1 and a= 50(m/s^2).

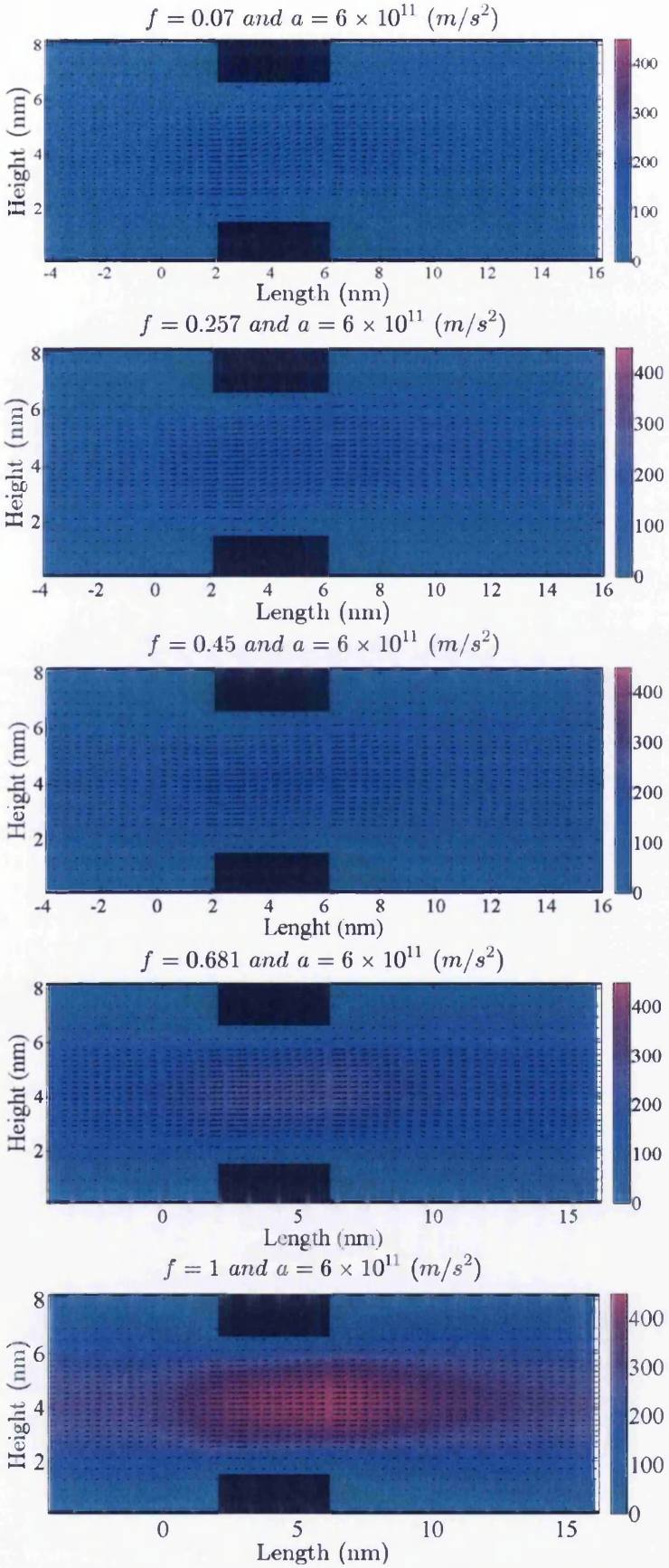

Figure 3.30. Velocity contours for stepped boundary for f= 0.07, 0.257, 0.45, 0.681, 1 and a= 6(m/s^2).

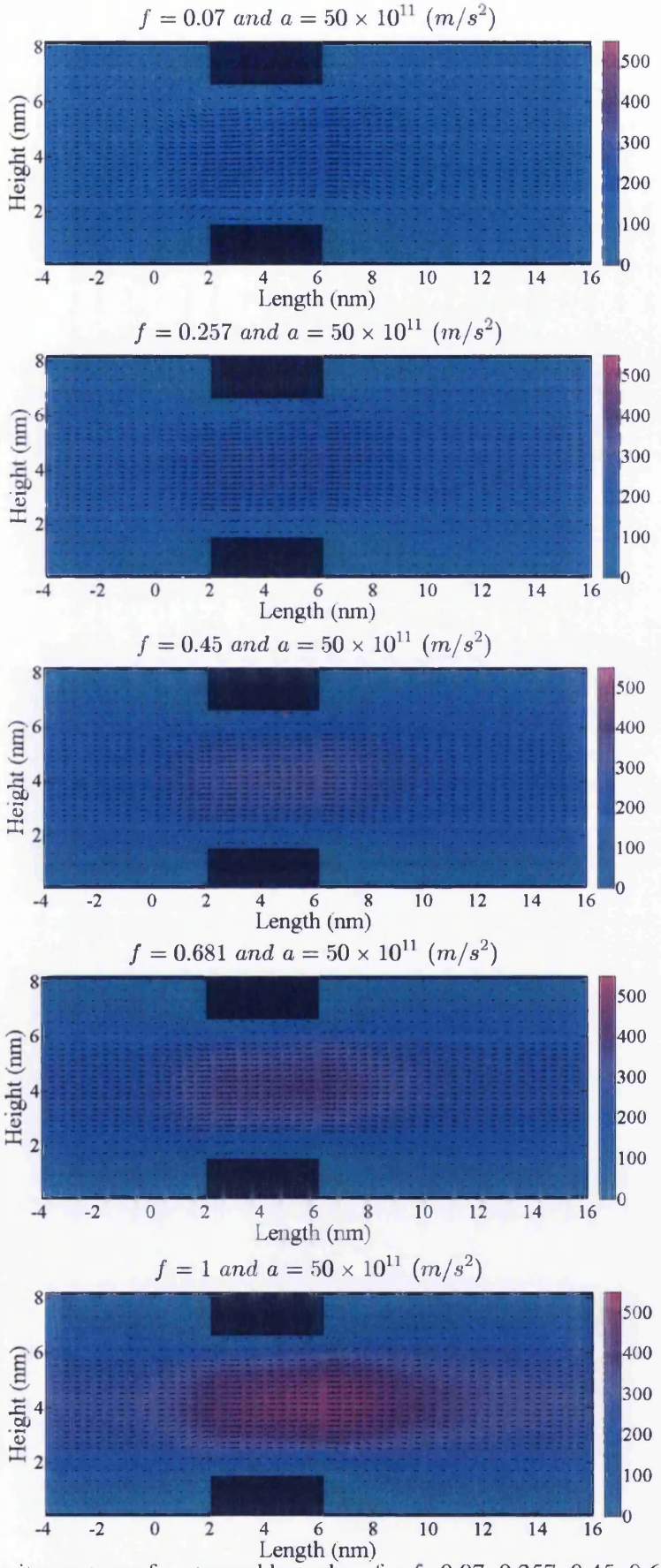

Figure 3.31. Velocity contours for stepped boundary for f= 0.07, 0.257, 0.45, 0.681, 1 and a= 50(m/s^2).

3.5 Conclusions

A soft sphere molecular dynamics model has been proposed to understand the interaction of fluid molecules with continuum wall. A collision criterion has been defined to estimate whether the collision has occurred with the wall. A fraction of all molecules that collide with the wall are randomly chosen and their tangential momentum is replaced by randomly picked values that correspond to the Maxwell velocity distribution associated with the wall temperature. The fraction is referred to as accommodation coefficient and is interpreted as a measure of the surface roughness of the wall. The normal component of velocity is conserved for all molecules. A Gaussian thermostat is implemented with the velocity Verlet algorithm and macroscopic velocity values at fixed points are derived using a moving least square method. The use look up table is proposed to calculate the potential and force contributions from the wall. It is shown that the resulting error as a result of the lookup table assumption is equivalent to small variation in the location of molecules and the comparison with the molecular wall showed that the assumption does not affect macroscopic velocity values. The Maxwell Boltzmann distribution of velocity is also followed for a significantly rough wall with high acceleration values and the results of the proposed model are compared with a case study published in the literature (Sokhan et al., 2001).

The effect of stepped, inclined and slit pore wall geometries on two and one dimensional macroscopic velocity distributions have been studied at various surface roughness and acceleration values. Increasing the surface roughness will approach a no slip boundary condition with velocity profiles following parabolic distributions. It was observed that the wall geometry has significant influence on the velocity profile. However, it was also discovered that the implementation of the periodic boundary condition is a limiting factor for gaining deeper insights into nanoscale flows.

The overall average velocity values are plotted against acceleration values to discover characteristic slow and high speed molecular flow regimes. For a given increase in the acceleration value, the rate of increase of velocity remains constant and it is found to be much higher for acceleration values less than $1\times10^{12}\ m/s^2$ as compared to values greater than $5\times10^{12}\ m/s^2$. It is inferred that in the low accelertion regime the corresponding losses are lower and the increase in the external

force results into much greater increase in the velocity values. The low speed molecular flows are made analogous to laminar flows and high speed molecular flows are interpreted as similar to turbulent flows. The next stage of the research will be to study the effect of various paramenters (e.g. surface roughness, temperature, pressure, non-uniform boundary condition etc) on the low-high speed flow transition.

It is expected that the proposed computational model and results shown in this chapter will enhance our understanding of the interaction of fluid molecules with continuum walls, drive experimental research forward and assist in the design of future atomic and colloidal systems. Further experimental research is necessary to link surface roughness, accomodation coefficient and macroscopic velocity profiles at 200-500 nm scale where molecular dynamics simulations can continue to influence the continuum concepts of fluid particles.

Chapter 4 Numerical prediction of drag forces on nano-cylinders

4.1 Introduction

The potential nano scale flow applications, e.g. removing nano-scale particles or transportation of nanotubes in a blood for drug delivery, as described in Chapter 2, require calculation of drag forces F_d exerted by the molecular flow on the solid wall. The drag force is calculated by integrating the component of stress (pressure) tensor σ parallel to the direction of the flow along the surface.

$$\vec{F} = \iint_s f_s \, ds = \iint_s \sigma \cdot \hat{n} \, ds \tag{4.1}$$

$$f_s = \begin{bmatrix} f_x \\ f_y \end{bmatrix}_s = \begin{bmatrix} \sigma_{xx} & \tau_{xy} \\ \tau_{yx} & \sigma_{yy} \end{bmatrix} \begin{bmatrix} n_x \\ n_y \end{bmatrix} = \begin{bmatrix} \sigma_{xx} n_x + \tau_{xy} n_y \\ \tau_{yx} n_x + \sigma_{yy} n_y \end{bmatrix} \tag{4.2}$$

Where σ is the stress tensor and n is the normal to the surface ds.

The drag coefficient C_d relates the drag force with the average macroscopic kinetic energy of the flow.

$$C_d = \frac{2F_d}{\rho A V_i^2} \tag{4.3}$$

F_d is drag force, ρ is the density of system , A is the area of object in flow and V_i is the average macroscopic velocity of fluid.

This Chapter extends the mathematical formulation for calculating local macroscopic velocity values at given continuum points, as proposed in Chapter 3, to incorporate pressure calculations near molecular wall and calculates drag coefficients for molecular flow over rough and smooth circular, diamond and square shaped cylinders at various molecular accelerations.

4.2 Pressure at nano-scale

The pressure is a state variable of a gas, like the temperature and the density. The change in pressure during any process is governed by the laws of thermodynamics. At molecular scales for an NVT system, the pressure value resulting from molecule's kinetic energy is given by nK_bT, where n is the number density, K_b Boltzmann constant and T is the overall absolute temperature value. At small scales, the

contribution from intermolecular forces also needs to be considered. The widely used Irwin-Kirkwood expression Equation (Barisik and Beskok, 2011, To et al., 2012, Huang et al., 2008, Kasiteropoulou et al., 2011, Kasiteropoulou et al., 2012, Hilbers et al., 2008, Jabbarzadeh, 2010, Fan et al., 2002) for calculating pressure values at molecular scales refers to the formal term as 'kinetic contribution' (due to motion of molecules) and the later term as 'configurational contribution' (due to intermolecular forces). It is assumed that molecular interactions are pairwise additive and molecules are nonreactive and structureless. The wall molecules are assumed to be at a constant temperature and the fluid molecules are not allowed to penetrate the wall. The fluid-wall interaction model as described in Chapter 3 has been used in this Chapter.

For homogeneous fluid, the pressure is hydrostatic and is a scalar quantity. However, the interaction of molecular flow with a wall makes the fluid inhomogeneous and the pressure becomes a second rank tensor as it depends on both the orientation of the wall surface and the direction relative to the wall surface. This is represented as a stress tensor $\sigma_{\alpha\beta}$ with the scalar pressure value given by its trace

$$P = \frac{1}{3} tr\sigma_{\alpha\beta} . \tag{4.4}$$

The subscript β denotes the stress direction on a surface pointing in the α direction. In the Cartesian co-ordinate system $\sigma_{\alpha\beta}$ is represented as

$$\sigma_{\alpha\beta} = \begin{bmatrix} \sigma_{xx} & \sigma_{xy} & \sigma_{xz} \\ \sigma_{yx} & \sigma_{yy} & \sigma_{yz} \\ \sigma_{zx} & \sigma_{zy} & \sigma_{zz} \end{bmatrix} \tag{4.5}$$

The stress tensor $\sigma_{\alpha\beta}$ is decomposed in the kinetic $\sigma_{\alpha\beta}^{K}$ and configurational $\sigma_{\alpha\beta}^{U}$ part as follows:

$$\sigma_{\alpha\beta} = \sigma_{\alpha\beta}^{K} + \sigma_{\alpha\beta}^{U} \tag{4.6}$$

As described in Chapter 3, at each time step every molecule is assigned an equal unidirectional force as described by an acceleration value. This method directly adjusts the molecular velocity. As discussed in Chapter 3 Figure 3.17 the assigned

acceleration value needs to be a small fraction of the average molecular acceleration value. As a result some of the random components of molecular velocity are changed in favour of the directed motion. This directed motion is referred to as "ordered" motion as opposed to the disordered random motion. At the macroscopic scale, pressure associated with the momentum of the ordered motion of the gas is termed as the dynamic pressure. However, at the molecular level, distinction is not made between random and ordered motion. Each molecule has a velocity in some direction until it collides with another molecule and the velocity is changed.

As discussed in Chapter 3, the applied acceleration is constrained to a small fraction of total molecular acceleration. The molecular velocity is also adjusted for a rough wall. A fraction of molecules that have collided with the wall replace the tangential component of its velocity with the thermal velocity associated with the wall. The molecular velocity is assumed to follow the Maxwell Boltzmann distribution using a Gaussian thermostat.

4.2.1 Review of Mathematical formulations for calculating the pressure tensor

Pressure (*P*) is the force per unit area acting on a surface element (Equation 4.4) and is the sum of a kinetic contribution which arises from the convective momentum transport of molecules and a configurational contribution which arises from interactions among molecules (Equation 4.6).

The expression of macroscopic stress tensor $\sigma_{\alpha\beta}$ in a fluid is originally from the microscopic law of momentum conservation at some point *r* in the fluid at time *t*.

The commonly used formulation for $\sigma_{\alpha\beta}^{K}$ and $\sigma_{\alpha\beta}^{U}$ is given by the Irving-Kirkwood method (Irving and Kirkwood, 1950). The $\sigma_{\alpha\beta}^{K}$ and $\sigma_{\alpha\beta}^{U}$ terms are defined as follows:

$$\sigma_{\alpha\beta} = -\frac{1}{V}\left[m\sum_{i}(\vec{v}_{i\alpha} - \vec{v}_{\alpha})(\vec{v}_{i\beta} - \vec{v}_{\beta}) + \frac{1}{2}\sum_{i}\sum_{i\neq j}\vec{r}_{ij\alpha}\,\vec{F}_{ij\beta} \right] \tag{4.7}$$

$$\sigma_{\alpha\beta}{}^{K} = -\frac{1}{V}m\sum_{i}(\vec{v}_{i\alpha} - \vec{v}_{\alpha})(\vec{v}_{i\beta} - \vec{v}_{\beta}), \quad \sigma_{\alpha\beta}{}^{U} = -\frac{1}{2V}\sum_{i}\sum_{i\neq j}\vec{r}_{ij\alpha}\,\vec{F}_{ij\beta} \tag{4.8}$$

m_i: is the mass of particle i

V: volume

Where α *and* β are the axes of the Cartesian coordinate system.

$\vec{v}_{i\alpha}$ *and* $\vec{v}_{i\beta}$ are the velocity component of particle *i* in α *and* β direction

$\vec{v}_{\alpha}$ *and* $\vec{v}_{\beta}$ are streaming velocities for molecules *i* and *j*.

$r_{ij\alpha}$: α component of the distance vector between particle *i* and *j*

$F_{ij\beta}$: β component of the force exerted on particle *i* by particle *j*

Note that $\vec{F}_{ij} = \frac{\partial u_{ij}}{\partial r_i} = -\frac{\partial u_{ij}}{\partial r_j}$ where r_i and r_j is the position vector of molecules *i* and *j*

where as u_{ij} is the intermolecular potential between molecules *i* and *j*. Depending on sign convention used authors have used positive or negative signs for $\sigma^{U}_{\alpha\beta}$ (Sofos et al., 2010, Nagayama and Cheng, 2004). It was observed that there is no unique method to calculate $\sigma^{K}_{\alpha\beta}$ and $\sigma^{U}_{\alpha\beta}$. Various authors have suggested alternative formulations (Barisik and Beskok, 2011, To et al., 2012, Huang et al., 2008, Kasiteropoulou et al., 2011, Kasiteropoulou et al., 2012, Hilbers et al., 2008, Jabbarzadeh, 2010, Fan et al., 2002) for calculating these contributions. Some of the recent advancements have been summarised in Table 4.1 (row(1): (Jabbarzadeh, 2010), row (2): row (3) :(Lion and Allen, 2012) and row (4): (Hartkamp et al., 2012)). The major differences in the formulations are in the calculation of streaming velocity, choice of the cut off region of molecules around a given point of interest and the molecules that are chosen for contribution to the intermolecular force term. The models reviewed in the literature also had a simplistic approach for modelling fluid-structure interaction and averaging macroscopic properties as described in the literature review of Chapter 3.

Table 4.1. Review of various approaches for calculating the kinetic and configurational part of the Irwin-Kirkwood expression.

Kinetic part: $\sigma_{\alpha\beta}{}^{K}(r)$		Configuration part: $\sigma_{\alpha\beta}{}^{U}(r)$	Streaming Velocity
(1)	$\frac{1}{V}\sum_{i}^{N} m_i u_{i\alpha} u_{i\beta}$ m_i : atomic mass α and β: coordination system axes which for Cartesian system can be simply X,Y and Z $u_{i\alpha}, u_{i\beta}$: the peculiar velocity components of particle i in α and β direction	$\frac{1}{V}\sum_{i}^{N}\sum_{j>i}^{N} r_{ij\alpha} F_{ij\beta}$ $r_{ij\alpha}$: α component of the distance vector between particle i and j $F_{ij\beta}$: β component of the force exerted on particle i by particle j	$U_{x,b} = \frac{\sum_{i=1}^{N_b} m_i v_{i,x}}{\sum_{i=1}^{N_b} m_i}$ m_i, v_i: mass and velocity of atom i inside the bin N_b: number of atoms inside the bin
(2)	$\frac{1}{3\Omega}\frac{\lvert p_i\rvert^2}{m_i}\Lambda_i$ Ω : volume of the region of interest Λ_i: unity if particle i lies within the volume Ω, and zero otherwise	$\frac{1}{3\Omega}\cdot\sum_{i=1}^{N-1}\sum_{j>i}(\vec{r_i}\cdot\vec{F_{ij}})l_{ij}$ $\vec{r_i}$ and $\vec{r_j}$: positions of particles i and j $\vec{r_{ij}} = \vec{r_i} - \vec{r_j}$ $\vec{F_{ij}}$: force exerted on particle i by particle j l_{ij} : fraction ($0 < l_{ij} < 1$) of the line, joining particles i and j that lies within Ω	
(3)	$\frac{Nk_bT}{V}$ N: number of particles V: volume T: temperature	$\frac{1}{3V}\sum_{i=1}^{N-1}\sum_{j>i}\vec{r_{ij}}\cdot\vec{F_{ij}}$ $\vec{r_i}$ and $\vec{r_j}$: positions of particles i and j $\vec{r_{ij}} = \vec{r_i} - \vec{r_j}$ $\vec{F_{ij}}$: force exerted on particle i by particle j	
(4)	$\sum_{i=1}^{N} m_i v_i' v_i' \Phi(r - r_i)$ $\Phi(r - r_i)$:Gaussian kernel to spatially smoothen the microscopic data m_i: mass of particle v_i': fluctuating (or thermal) velocity of atom i,	$-\frac{1}{2}\sum_{i=1}^{N}\sum_{j\neq i} r_{ij} F_{ij}\int_0^1 d\lambda\,\Phi(r - r_i - \lambda r_{ij})$ F_{ij}, r_{ij}: magnitude of force and distance between particle i and j $\Phi(r) = \frac{1}{(\sqrt{2\pi w^2})^D} e^{-\frac{\lvert r\rvert^2}{2w^2}}$ D: dimension of the system ω^2:variance: determines the	$u(r) = \frac{J(r)}{\rho(r)}$ $\rho(r)$: reduced mass density $J(r)$: reduced momentum density

	$v_i' = v_i - u(r)$ and defined as the difference between the laboratory velocity v_i and streaming velocity u at the location of the function evaluation r	amount of smoothing, while preserving the shape and the area under the curve $\left(\int \Phi(r)dr = 1\right)$	

4.2.2 Calculation of the pressure tensor at MLS nodes

As shown in the second row of Table 4.1, Lion and Allen (2012) proposed a l_{ij} term, in the configurational part of the stress tensor $\sigma^{U}_{\alpha\beta}$. The contribution of the intermolecular force to the configuration part was proportional to the part of the line segment contained in the cut off square

Figure 4.1a. In this work an approximate but computationally efficient technique has been proposed. As shown in

Figure 4.1b, l_{ij} is equal to one, 0.5 or zero depending upon whether the segment joining the two molecules is fully, partially and not contained within the cut off square corresponding to the MLS node. The proposed approximation is computationally simple. However, it is likely to introduce error in the final computation where l_{ij} is equal to 0.5 or zero. It is anticipated that the overall error will not be significant as some of the positive and negative contributions may cancel with each other. However, the future work needs to be undertaken with a detailed comparative analysis to justify this assumption.

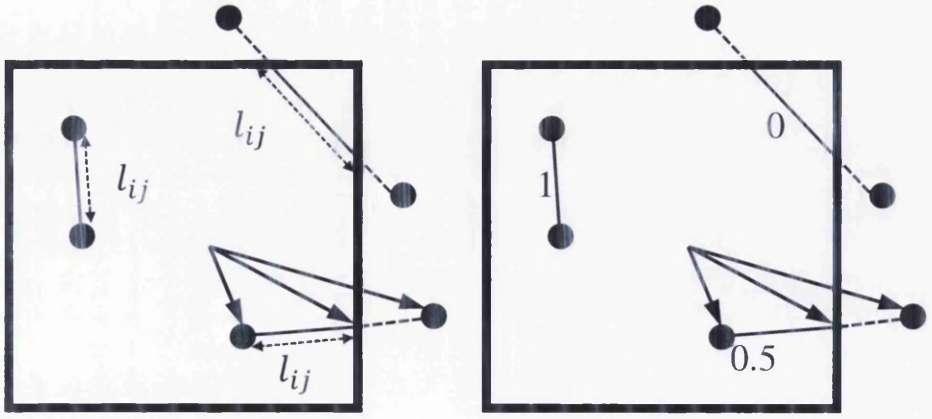

(a) (b)

Figure 4.1. (a) Molecules contribute to the configuration part of the stress tensor $\sigma_{\alpha\beta}^{U}$ depending upon the proportion of the segment l_{ij} contained in the cut off square (b) proposed approximation to l_{ij} values.

The streaming velocity at each MLS node is calculated with the Moving Least Square (MLS) method proposed in Chapter 3 which is extended to two dimensions as shown in Figure 4.2.

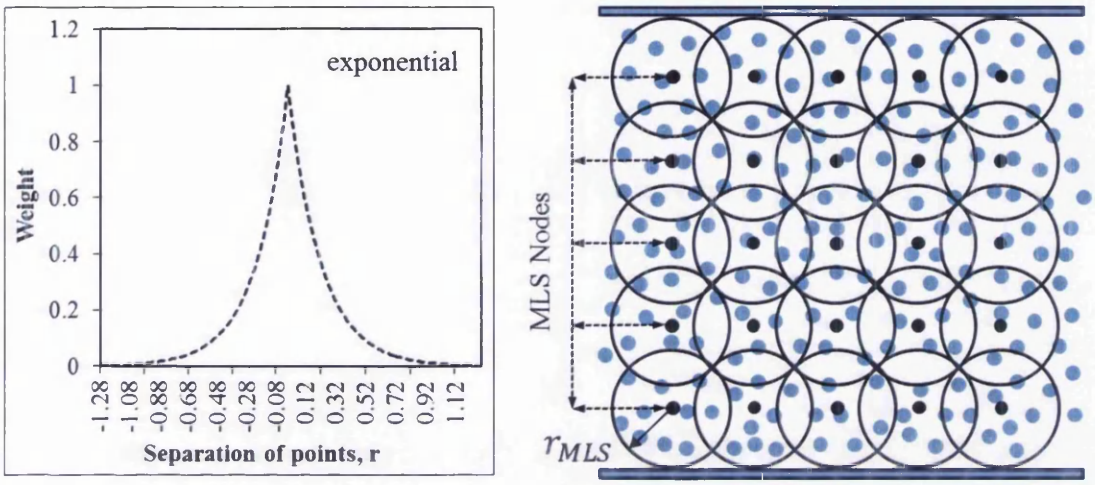

Figure 4.2. Left Weighting function with a unit value at the MLS node and zero after the cut off radius. Right A two dimensional array of MLS nodes with cut off circles are shown over schematic molecules in the background.

Equation 4.7 is used to calculate pressure values at each MLS nodes at a given time step. The cut off circle, shown around each MLS node, determines the number of molecules chosen for calculating macroscopic properties, such as velocity and pressure, at the corresponding MLS nodes. This strategy compares well the Gaussian kernel (Φ) used to spatially smoothen the microscopic data (Hartkamp et al., 2012).The current MLS nodal velocity value is used as the streaming velocity value in Equation 4.7. As discussed in Chapter 3, each time step for the molecular dynamics simulation is 2 fs. The molecular data (molecular positions and velocity vectors) is collected at every 0.0003 ns and used to calculate average MLS nodal values using a weighting function as described in Figure 4.2. MLS nodal values (macroscopic velocity vectors and stress tensors) are updated at every 0.05ns. The simulation is run for 2.8ns and the average of all MLS nodal values is used in results

(

Figure 4.3) as well as calculation of drag forces.

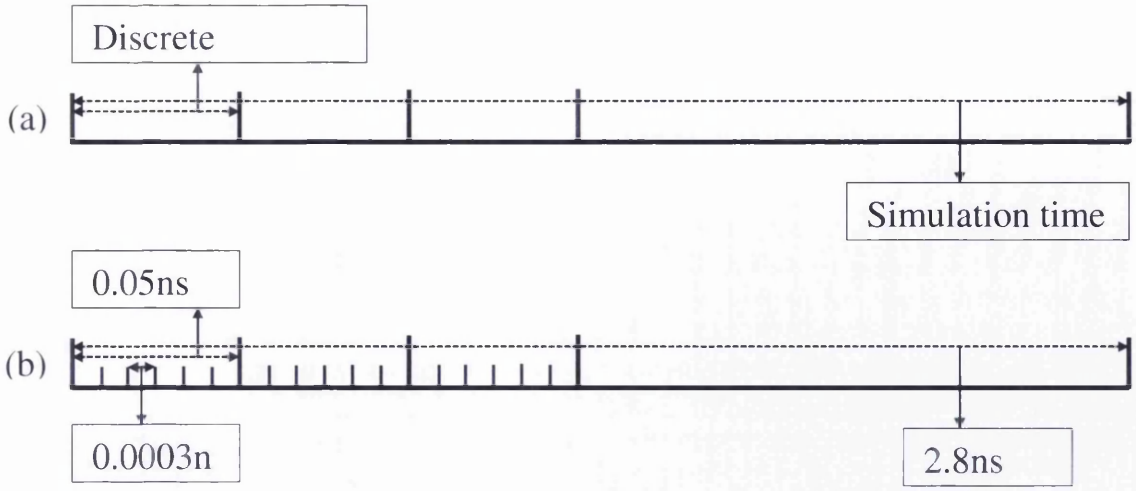

Figure 4.3. The MLS nodal values are calculated at every 0.05 ns using molecular data captured at every 0.0003 ns. The time step used in the molecular dynamics simulation is 2 fs. The equilibrium properties are averaged in the production stage between 1.12ns ns and 2.8 ns.

4.2.3 Calculation of the Drag Force

The pressure tensor calculated at every MLS node is further averaged using information of neighbouring nodes near the boundary. As shown in Figure 4.4, an average of stress tensor values at three MLS nodes is used for drag force calculations. The numerical integration, as used in Equation 4.9, assumes linear variation between two consecutive MLS nodes along the surface. This assumption is computationally efficient but may require higher density of MLS nodes in areas of higher stress gradients. Figure 4.5 describes forces on an element with length L between two MLS nodes. The width in z direction given by W. A periodic boundary condition is assumed in z direction; for the given geometries, the normal to the wall is always in the xy plane; the macroscopic velocity in z direction is zero and hence the stress contribution in z direction is small and is neglected. The i^{th} line segment joining two MLS nodes (MLS^1 and MLS^2) is inclined at an angle θ. Equations 4.17-4.22 calculate the elemental forces in x and y directions. The stress values are parameterised on variable 't' with t equal to zero 0 at node MLS^1 and t with a unit value at node MLS^2. The resultant drag or lift force is calculated by integrating the elemental forces over all line segments (Equations 4.23).

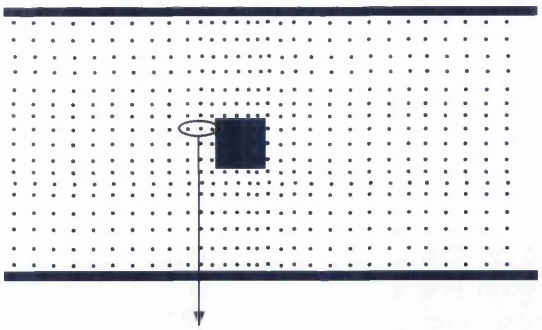

Figure 4.4. Two dimensional arrangement of MLS nodes.

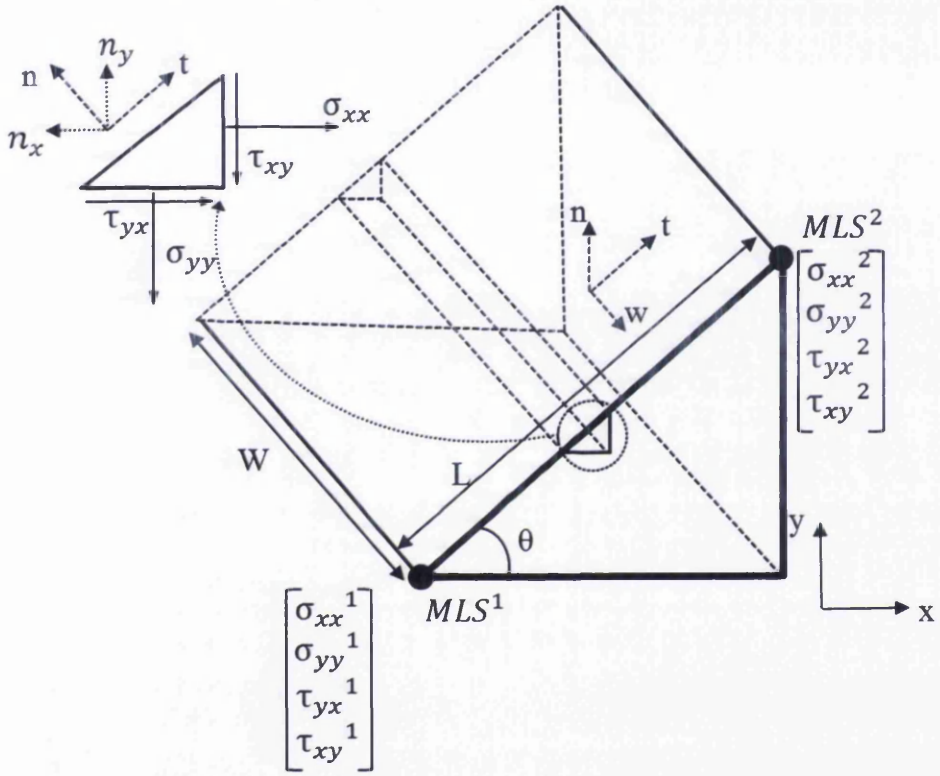

Figure 4.5. Elemental forces on an i^{th} line segment with length L and width W of a boundary inclined at an angle $\theta$and defined by MLS nodes 1 and 2 (MLS^1 and MLS^2).

$$\vec{F} = \iint_A f \, dA = \iint_A \sigma \cdot \hat{n} \, dA \tag{4.9}$$

$$f = \begin{bmatrix} f_x \\ f_y \end{bmatrix}_s = \begin{bmatrix} \sigma_{xx} & \tau_{xy} \\ \tau_{yx} & \sigma_{yy} \end{bmatrix} \begin{bmatrix} n_x \\ n_y \end{bmatrix} = \begin{bmatrix} \sigma_{xx} n_x + \tau_{xy} n_y \\ \tau_{yx} n_x + \sigma_{yy} n_y \end{bmatrix} \tag{4.10}$$

$$df_x = \sigma_{xx}(t) dt \sin(\theta) + \tau_{yx}(t) dt \cos(\theta) \tag{4.11}$$

$$df_y = \sigma_{yy}(t) dt \cos(\theta) + \tau_{xy}(t) dt \sin(\theta) \tag{4.12}$$

$$\sigma_{xx}(t)=\frac{\sigma_{xx}^2-\sigma_{xx}^1}{L}t+\sigma_{xx}^1 \tag{4.13}$$

$$\sigma_{yy}(t)=\frac{\sigma_{yy}^2-\sigma_{yy}^1}{L}t+\sigma_{yy}^1 \tag{4.14}$$

$$\tau_{xy}(t)=\frac{\tau_{xy}^2-\tau_{xy}^1}{L}t+\tau_{xy}^1 \tag{4.15}$$

$$\tau_{yx}(t)=\frac{\tau_{yx}^2-\tau_{yx}^1}{L}t+\tau_{yx}^1 \tag{4.16}$$

The force acting over the i^{th} line segment of the boundary is:

$$F_x^i=\int_0^W\int_0^L\left(\sigma_{xx}(t)\sin(\theta)+\tau_{yx}(t)\cos(\theta)\right)dt\,dw \tag{4.17}$$

$$F_y^i=\int_0^W\int_0^L\left(\sigma_{yy}(t)\cos(\theta)+\tau_{xy}(t)\sin(\theta)\right)dl\,dw \tag{4.18}$$

$$F_x^i=\int_0^W\left(\frac{\sigma_{xx}^2-\sigma_{xx}^1}{2L}t^2+\sigma_{xx}^1t\right)\sin(\theta)+\left(\frac{\tau_{yx}^2-\tau_{yx}^1}{2L}t^2+\tau_{yx}^1t\right)\cos(\theta)\Bigg|_0^L dw \tag{4.19}$$

$$F_y^i=\int_0^W\left(\frac{\sigma_{yy}^2-\sigma_{yy}^1}{2L}t^2+\sigma_{yy}^1t\right)\cos(\theta)+\left(\frac{\tau_{xy}^2-\tau_{xy}^1}{2L}t^2+\tau_{xy}^1t\right)\sin(\theta)\Bigg|_0^L dw \tag{4.20}$$

$$F_x^i=W\left(\left(\frac{\sigma_{xx}^1+\sigma_{xx}^2}{2}\right)L\sin(\theta)+\left(\frac{\tau_{yx}^1+\tau_{yx}^2}{2}\right)L\cos(\theta)\right) \tag{4.21}$$

$$F_y^i=W\left(\left(\frac{\sigma_{yy}^1+\sigma_{yy}^2}{2}\right)L\cos(\theta)+\left(\frac{\tau_{xy}^1+\tau_{xy}^2}{2}\right)L\sin(\theta)\right) \tag{4.22}$$

The drag and lift forces (F_D and F_L) are obtained by adding forces over all line segments defining the boundary or the geometry.

$$F_D=\sum_{i=1}^{k}F_x^i \qquad F_L=\sum_{i=1}^{k}F_y^i \tag{4.23}$$

4.3 Verification of the proposed model

The accuracy of the proposed formulation is verified with the following two tests. The third test compared the velocity and pressure contours calculated with molecular and continuum wall.

1. Verification of instantaneous molecular velocity distributions in x, y and z directions with Gaussian distributions corresponding to its temperature value.
2. Verification of the predicted pressure value at a point with periodic boundary conditions with all three directions and with no walls.
3. Comparison of velocity and pressure contours with and without molecular wall.

4.3.1 Test1: Verification of velocity distributions

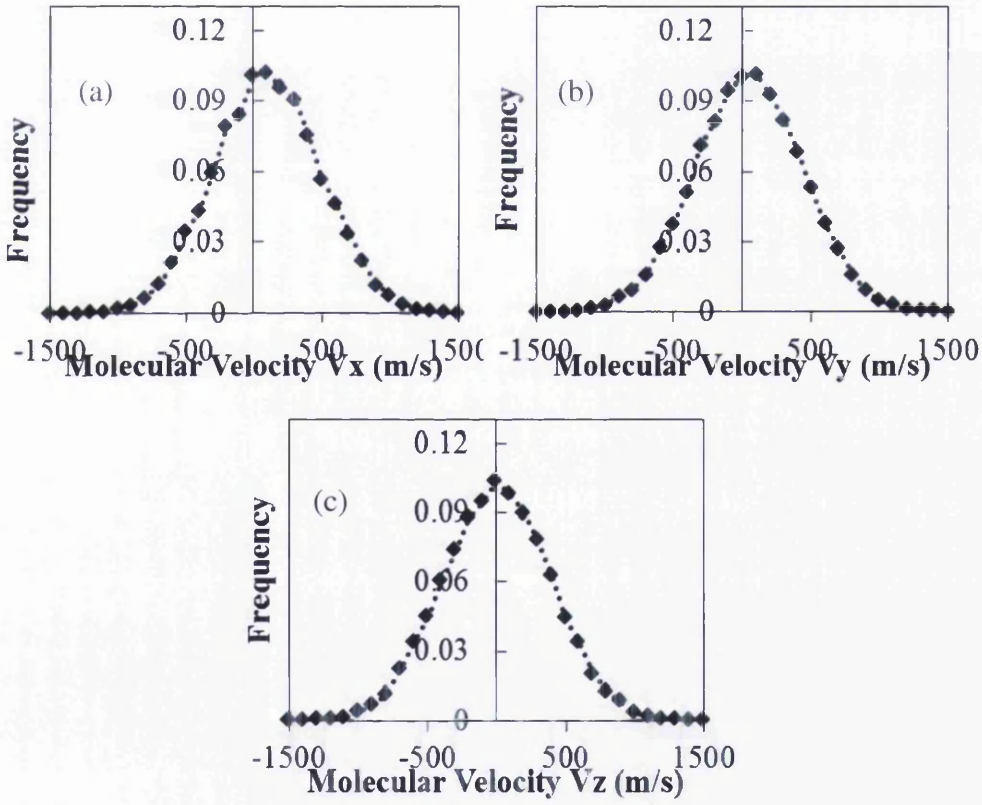

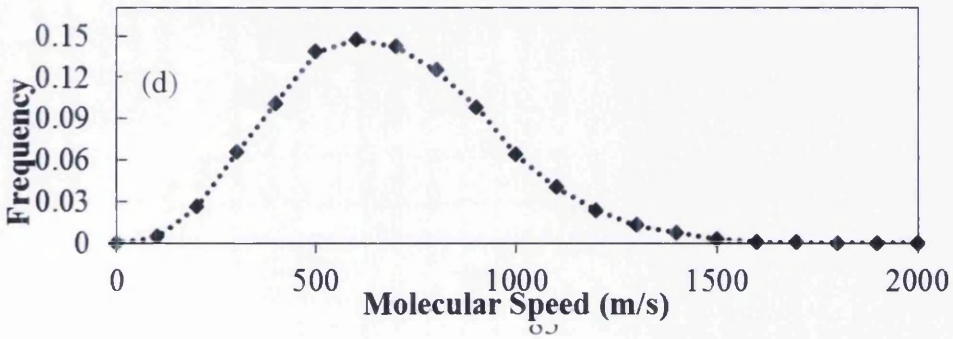

Figure 4.6. Distribution of x, y and z components of molecular velocity. The resulting distribution of molecular speeds is shown in (d).

Similar to Figure 3.9 in Chapter 3, the resulting velocity distributions in x, y and z directions followed the corresponding Gaussian distribution at the appropriate temperature and the resulting distribution for speed is verified with the Maxwell Boltzmann distribution. Figure 4.6 shows excellent agreement with the exact versions of the distribution for slit pore geometry (12755 molecules) at 300K with a rough wall ($f = 0.257$) and acceleration value ($10\,m/s^2$). This test is considered important as the thermostat in the proposed algorithm is not a simple velocity rescaling thermostat. The Gaussian thermostat as discussed in Section 3.2.3 in Chapter 3 will not conserve the temperature and hence the kinetic energy of molecules if there are any mistakes in the code or logic including any irregularities in the implementation of the formulation for modelling the interaction of fluid molecules with the wall.

4.3.2 Test2: Verification of the Pressure value

As discussed in Chapter 2, the number density of molecules is calculated for a temperature and pressure value of 300K and 40MPa respectively. Using this density a simulation with 5140 molecules was undertaken for a period boundary condition in all three directions with no walls and the pressure was calculated using the formulation described in this Chapter for the MLS nodes. However, instead of calculating the pressure value as described in Section 4.2.2, the following approximate equations were used as the local variation in pressure value was expected.

The Irwin-Kirkwood method (Equation 4.7) ignores the long correction W_{LR}. The long range correction to the pressure value is constant for given cut off radius, fluid molecules and number of molecules (Frenkel and Smit, 2001) and is given by Equation 4.26. The non-inclusions of the long range correction factor for calculating forces around an object may be justified as its effect will get cancelled during the cyclic integral of the stress tensor. The kinetic part is calculated using the average temperature and the configurational part ignored the correction term l_{ij} as discussed in the previous section but instead used the neighbourhood list for each molecule to decide the contribution from intermolecular forces.

$$P = \rho\left(K_b T - \frac{W}{3N}\right) = \rho\left(K_b T - \frac{W_{SR}}{3N} - \frac{W_{LR}}{3N}\right) \tag{4.24}$$

$$W_{SR} = \sum_{i=1}^{N-1}\sum_{j>i}^{N}\left[F_{LJ,ij}\cdot\left(\frac{r_{ij}^2}{r_{ij}}\right)\right] \tag{4.25}$$

$$W_{LR} = -\frac{1}{2}\frac{N^2}{V}\left[\frac{96\pi\varepsilon}{9}\left(2\frac{\sigma^{12}}{r_{cut}^9} - 3\frac{\sigma^6}{r_{cut}^3}\right)\right] \tag{4.26}$$

The average pressure at all MLS nodes in the domain was calculated as 39.23 MPa with less than 2% error.

4.3.3 Test3: Comparison of velocity and pressure contours with and without molecular wall

Comparison of average velocity

As shown in Chapter 3, Section 3.3.1 (Figures 3.11 and 3.12), the average molecular velocity is recalculated for the same slit pore geometry at local MLS nodes with a configuration as shown in Figure 4.2 The difference between two configurations is in the cut off regions. Chapter 3 (Figure 3.11) used a rectangular layered region as compared to the circular region (Figure 4.2) in this chapter. The recalculated average velocity profile is shown as dotted curve and is superimposed on each plot in Figure 3.12 and shown in Figure 4.7 for both molecular and continuum walls. The steady state velocity profile for a slit pore geometry is not expected to change along the slit pore length and hence the average velocities match very closely with velocity profiles shown in Figure 3.12.

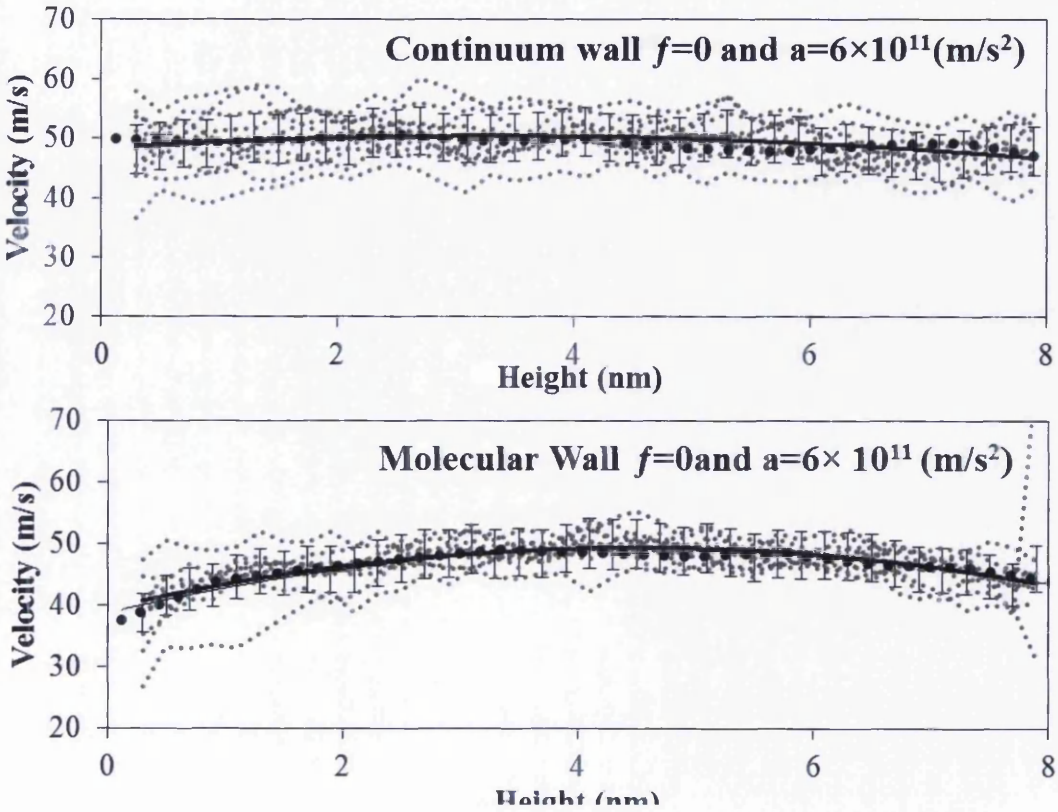

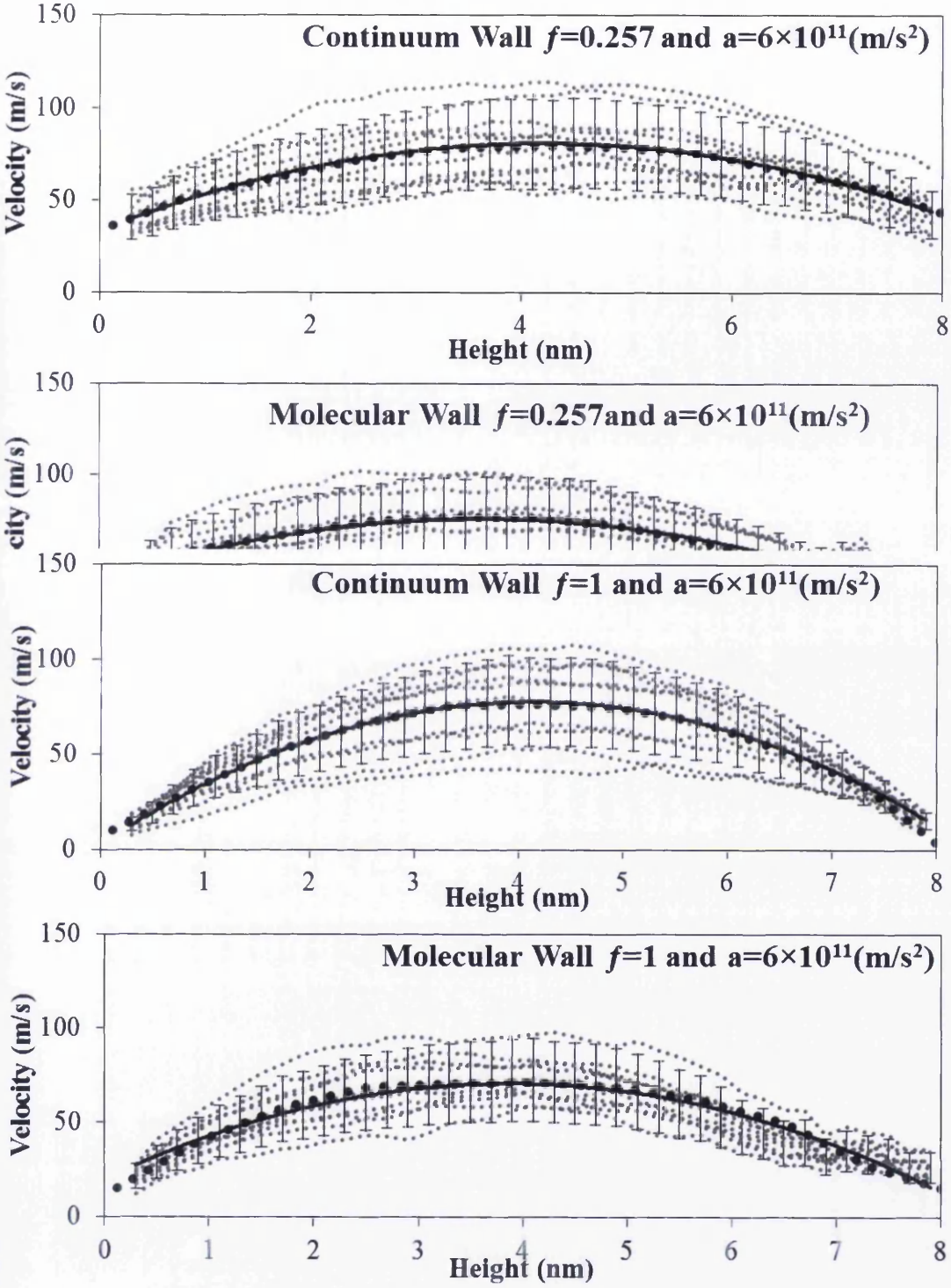

Figure 4.7. Comparison of average velocity for slit wall pore geometry with continuum and molecular wall for a = 6×10^{11} m/s^2 and f = 0, 0.257 and 1

Comparison of pressure and velocity contours with continuum and molecular walls

As shown in Figure 3.6 (Section 3.2.1) in Chapter 3, the position of molecules around the molecular and an equivalent continuum wall are not identical. The calculations illustrated that the molecules could be up to 0.2 Angstrom closer to the molecular wall than the equivalent continuum wall. The impact on the average velocity distribution was small as shown in Section 3.2.1. As discussed in Section 4.2.3, the velocity in z direction is ignored from calculations for the average two dimensional velocity at MLS nodes, is shown in Figure 4.2, for both the continuum and molecular walls for a slit pore geometry with a = 10 (m/s^2) and f =0.257. As expected the velocity vectors are very similar however, the resulting pressure contours were found to be significantly different for the molecular and continuum wall (Figure 4.8). The advantage of using the continuum wall was in the computational efficiency. The use of look-up tables (as discussed in Section 3.2.1, Chapter 3) also opened the possibility of inputting experimentally determined force-distance curves into the calculations. However, is it noted that the pressure values are sensitive to the wall configuration and the assumptions used in inputting force-distance curves. Fortunately, the difference in values was observed to be a constant value and hence, it was assumed that it may not influence the calculation of drag forces around the geometries under consideration. Rest of the simulations are undertaken for a continuum wall as a result of its computational efficiency.

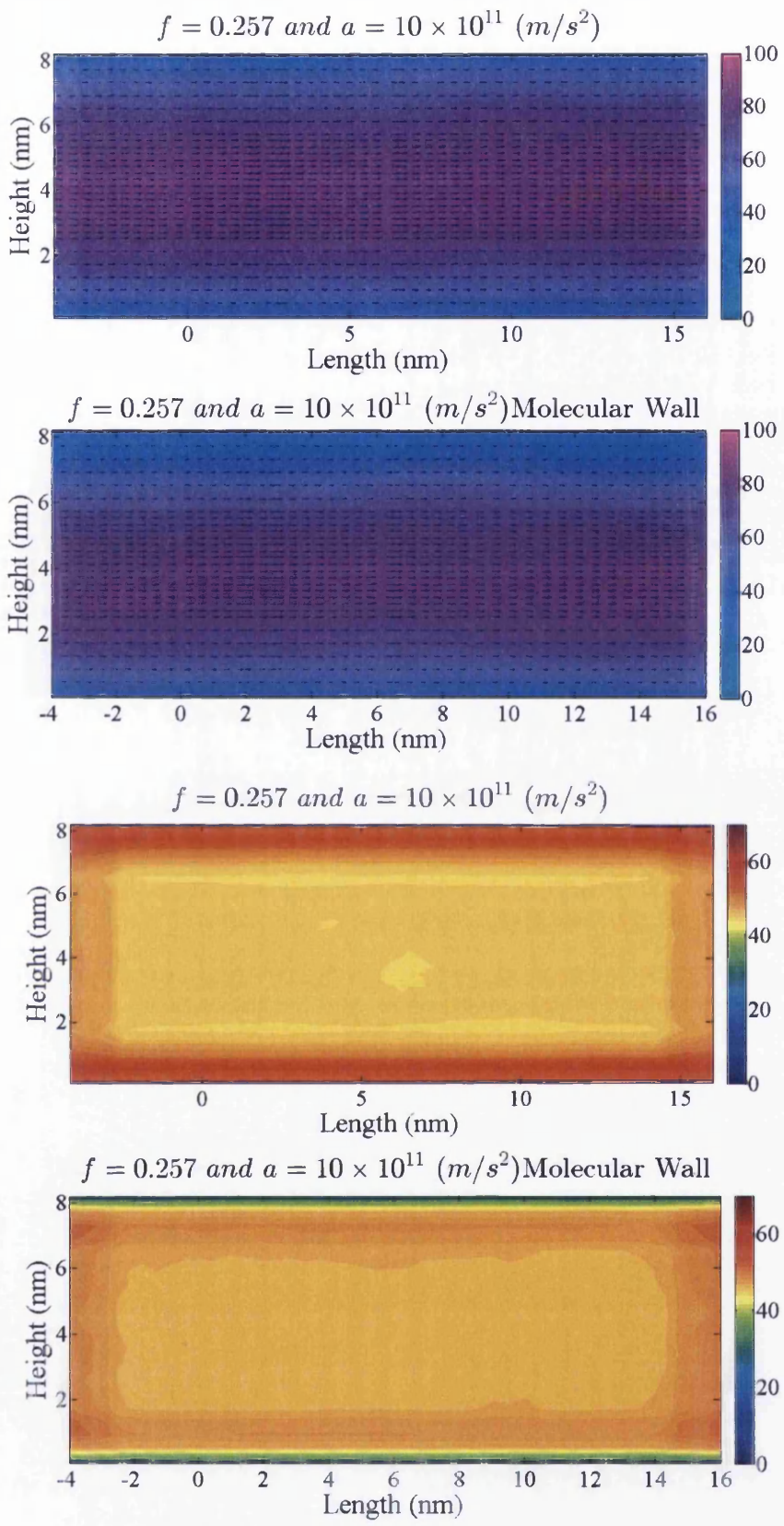

Figure 4.8. Macroscopic velocity and pressure contours calculated at MLS nodes for the continuum and molecular walls at f =0.257 and a = 10 (m/s^2).

4.4 Discussion of results

The simulation is run for three wall geometries (circle, square and diamond shaped cylinders placed inside a slit pore) as tabulated in Figure 4.9. The depth in z direction is 8.2 nm for all geometry configurations. The effect of surface roughness characterized by accommodation coefficient f (0.07, 0.257, 0.45, 0.681 and 1) for various acceleration values (0, 6×10^{11} and $10\times10^{11}(m/s^2)$) is discussed for all three geometries. Other values used in the simulation are as described in Chapter 3.

Section 4.4.1 highlights a comparison of flow past a square cylinder through a slit pore for molecular and continuum walls. The velocity and pressure contours for the three acceleration values at each f value are shown in the Appendix for this Chapter: Appendix A4.1, A4.2 and A4.3 for diamond, circle and square cylinder geometries respectively. It needs to be highlighted that the symmetry in results for all contour plots is an additional indication of the accuracy of the code and the implementation of the proposed algorithm. All contour plots are included in this thesis as supporting evidence to the discussion of results and the subsequent graphs illustrating drag coefficient variation across Reynolds numbers and corresponding to different f values for each geometry. Each simulation has taken couple of days on the cluster to complete. The results are summarised in Section 4.4.2.

For molecular flow over a circular shaped cylindrical confined between parallel walls (Figure 4.9) with a surface roughness value, f=1, and the acceleration value a=10(m/s^2) and using the proposed mathematical formulation, the average macroscopic velocity is calculated as 74 (m/s). Assuming the kinematic viscosity of methane as 1.1868E^{-9}(m^2/s) and using the diameter of the cylinder as characteristic length, the Reynolds number for flow over the cylinder 1.25. The Reynolds number for the slit pore flow over a cylinder can thus be calculated from the average velocity for the given surface roughness and acceleration value.

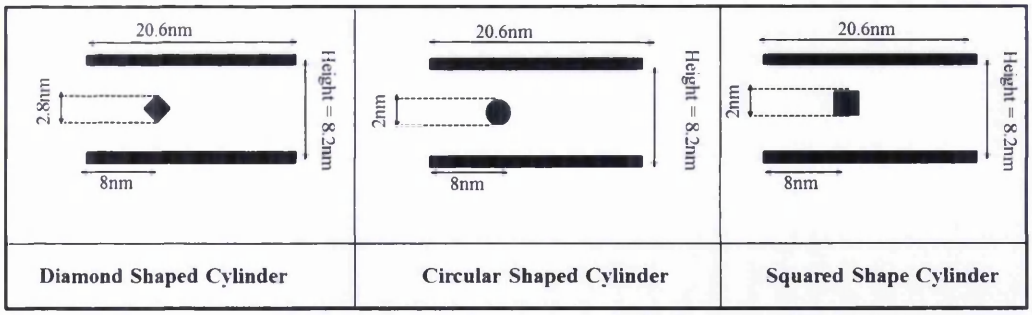

Figure 4.9. Schematic geometries for modelling molecular flow over diamond, circular and square shaped cylinders confined within parallel walls.

4.4.1 Flow past a square cylinder for continuum and molecular walls

Further to the difference in the predicted pressure values using continuum and molecular walls as discussed in Section 4.3.3, simulations were undertaken for a molecular square cylinder in a molecular slit pore and compared with an equivalent continuum wall. It was found that the continuum wall predicted pressure values that are around 10 -15 MPa higher than the molecular wall for an acceleration value of $10(m/s^2)$ which represents an increase of around 20%. However, the resulting drag coefficient variations with respect to Reynolds number are very similar (Figure 4.10). The simulation time required for the continuum wall was at least four times smaller than the equivalent molecular walls. As a result, rest of the simulations were undertaken on using continuum walls for the cylinder and the slit pore. The velocity and pressure contours for various f and acceleration values are shown in Figures 4.11-4.18.

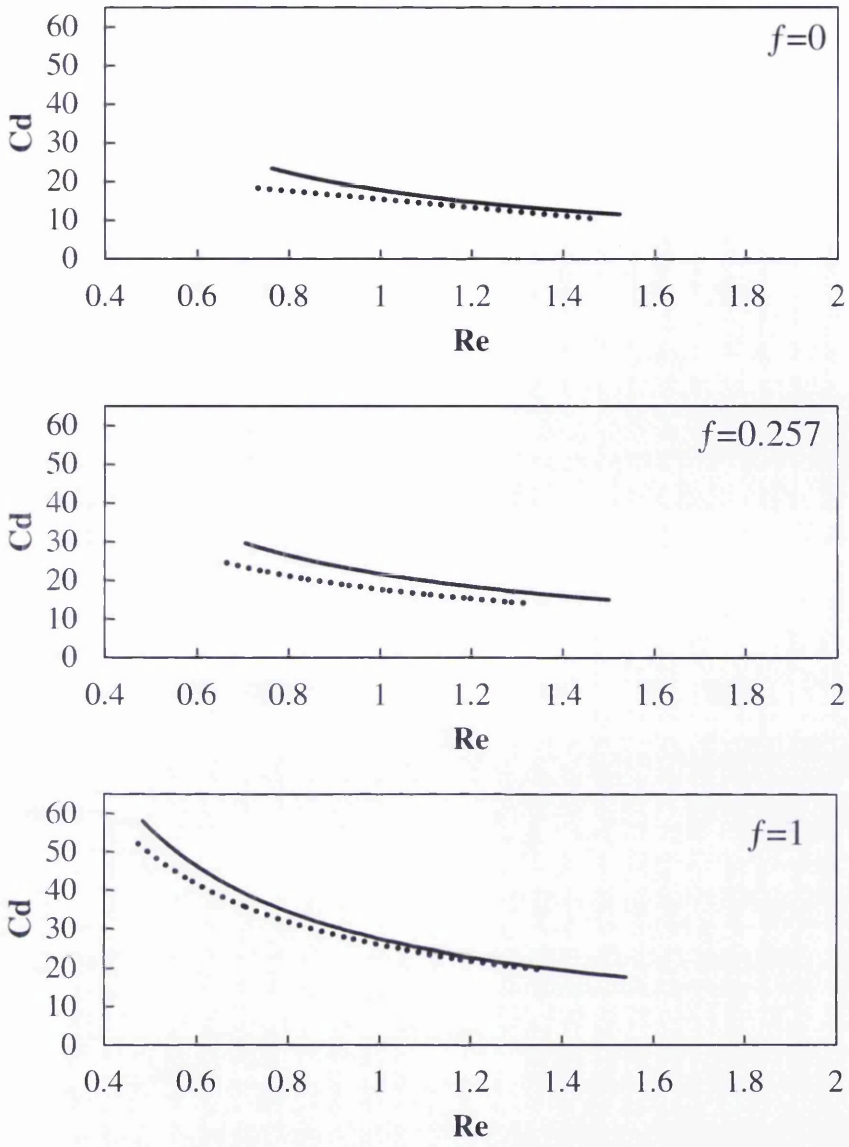

Figure 4.10. Comparison of drag coefficient variation with respect to Reynolds numbers using molecular and continuum wall assumptions.

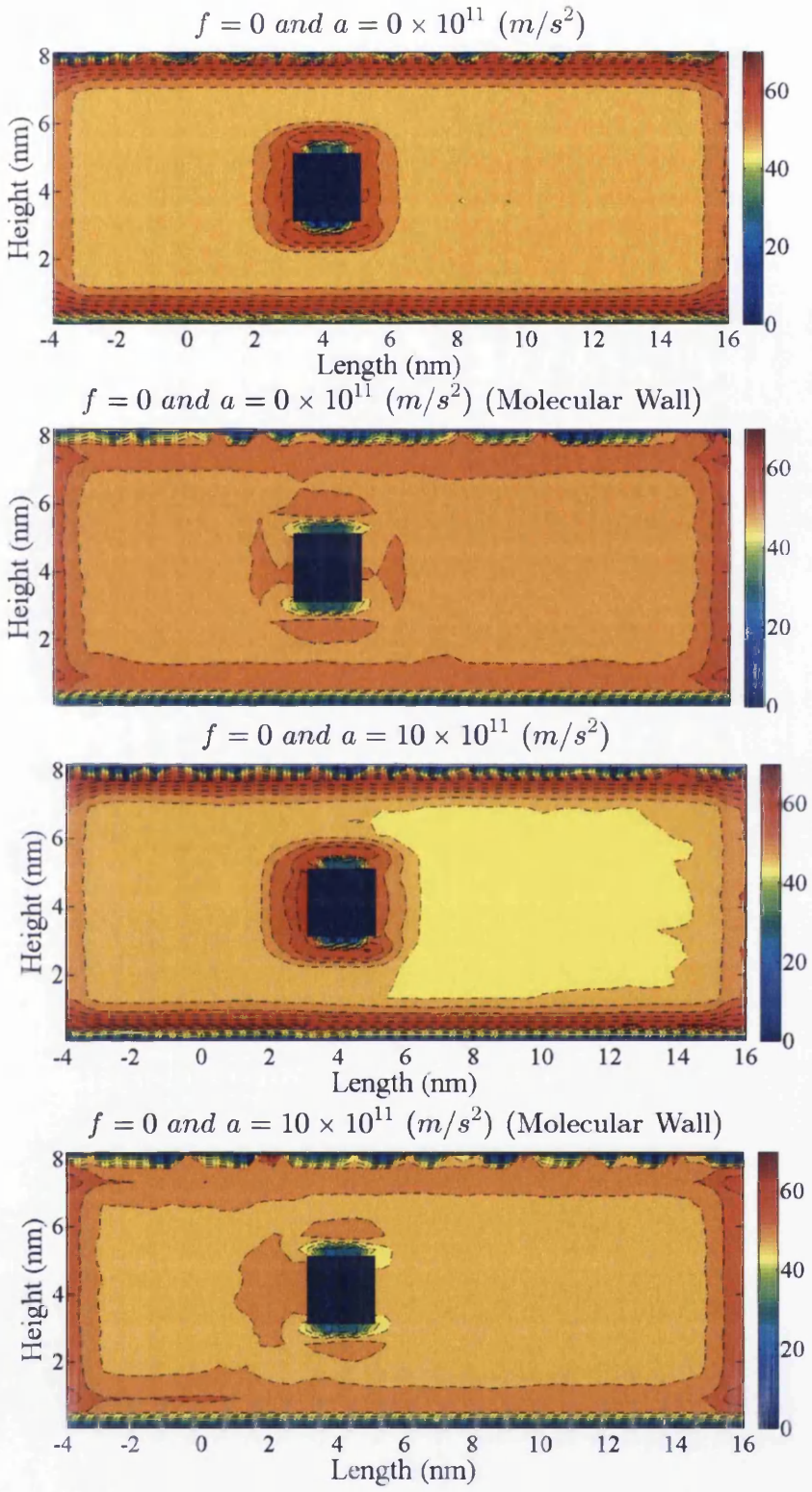

Figure 4.11. Pressure contours for f =0 and accelerations 0 and 10(m/s^2) around molecular and continuum square shaped cylinder

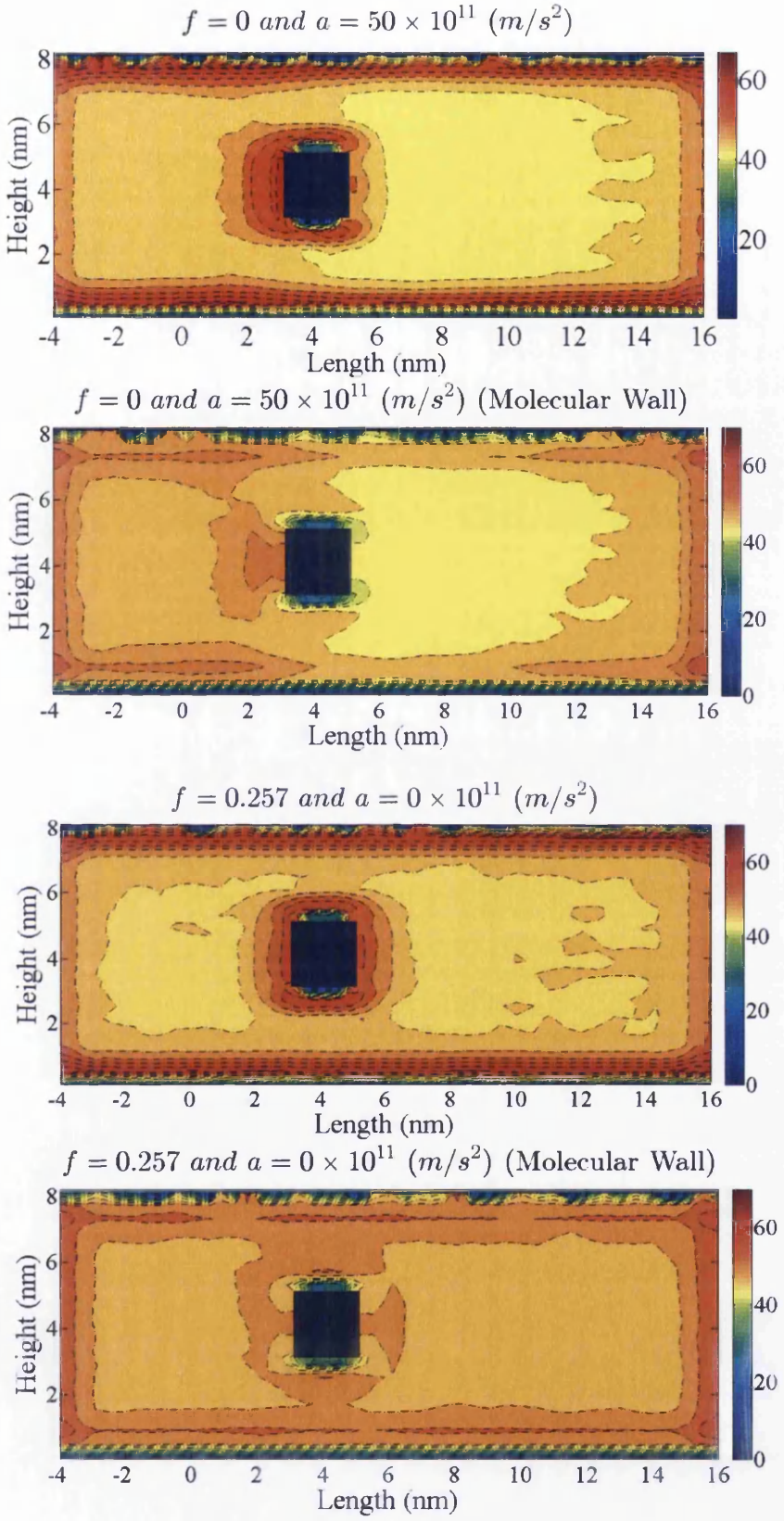

Figure 4.12. Pressure contours for f =0 and 0.257 and accelerations 0 and 50(m/s^2) around molecular and continuum square shaped cylinder

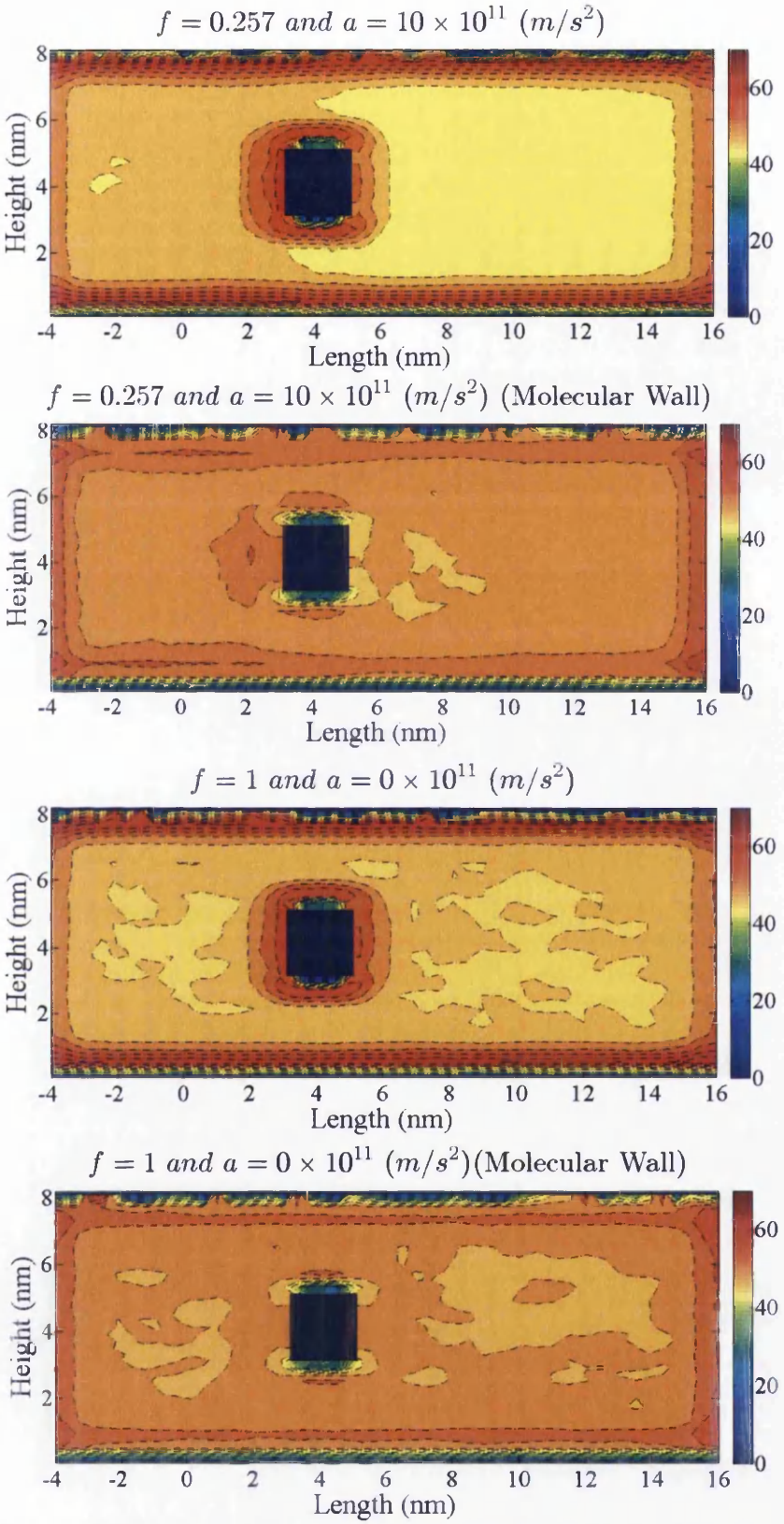

Figure 4.13. Pressure contours for f =1 and 0.257 and accelerations 0 and 10(m/s^2) around molecular and continuum square shaped cylinder

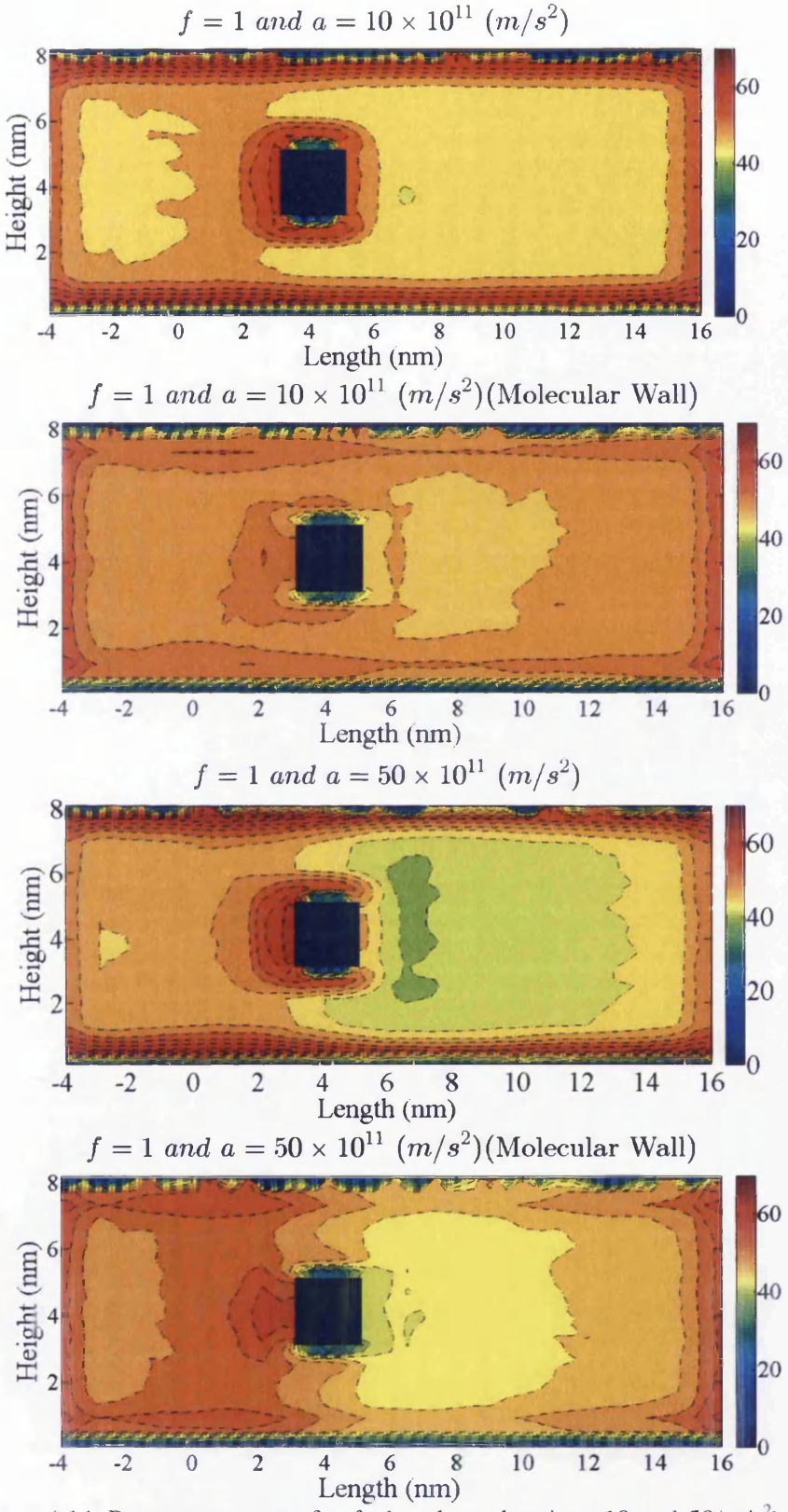

Figure 4.14. Pressure contours for f =1 and accelerations 10 and 50(m/s^2) around molecular and continuum square shaped cylinder

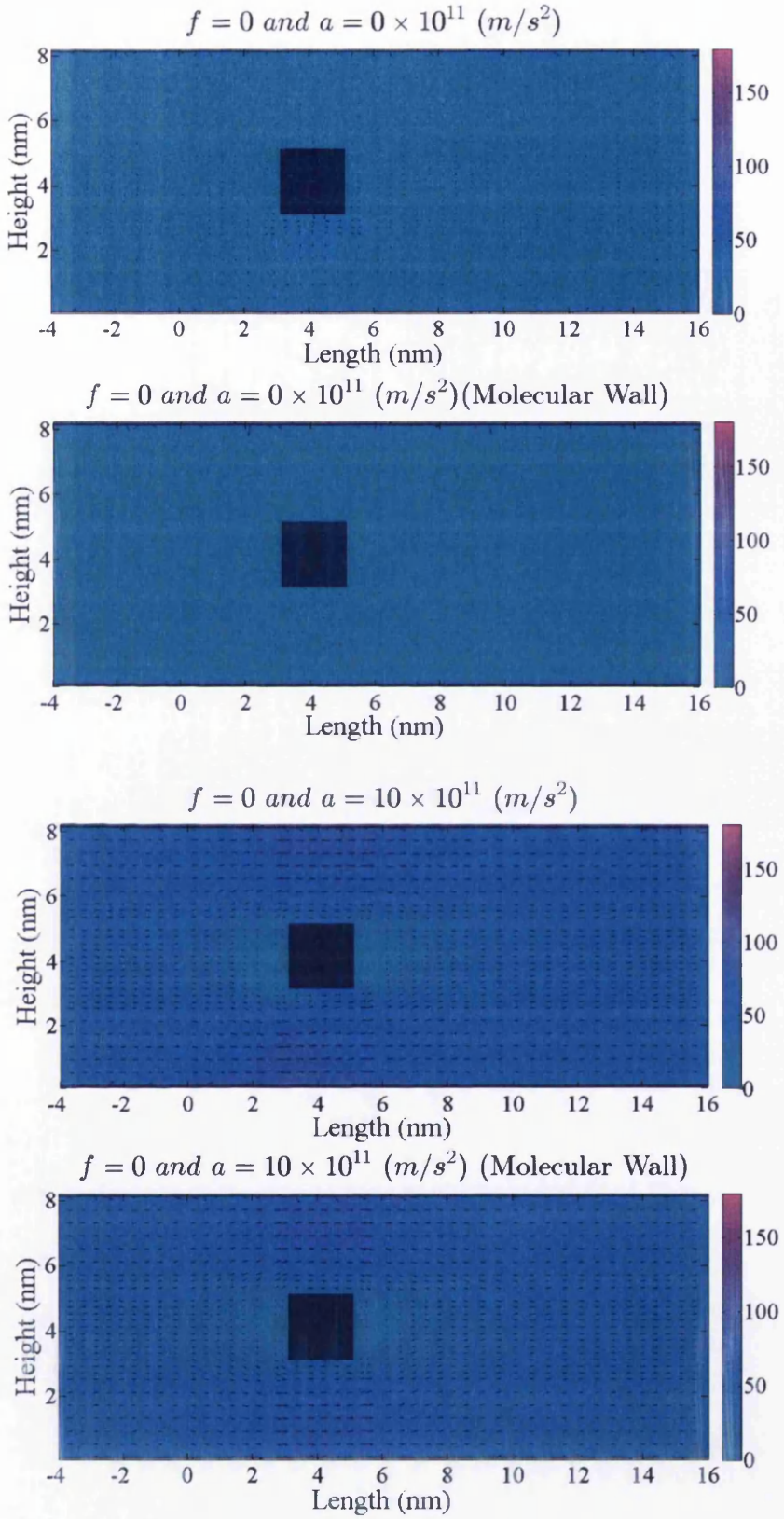

Figure 4.15. Velocity contours for f =0 and a= 0 and 10(m/s^2) around molecular and continuum square shaped cylinder

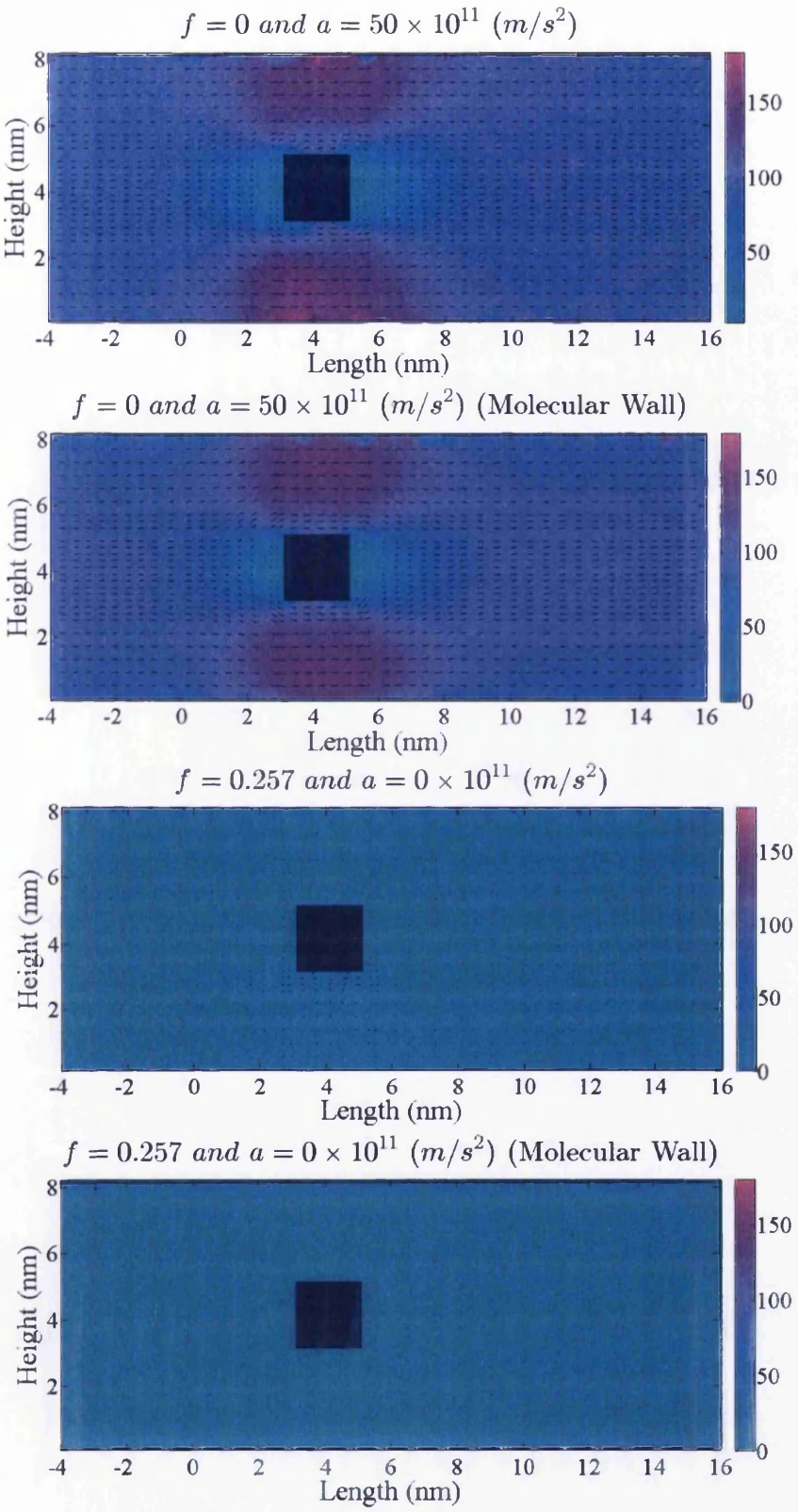

Figure 4.16. Velocity contours for f =0 and 0.257 and a= 0 and 50(m/s^2) around molecular and continuum square shaped cylinder

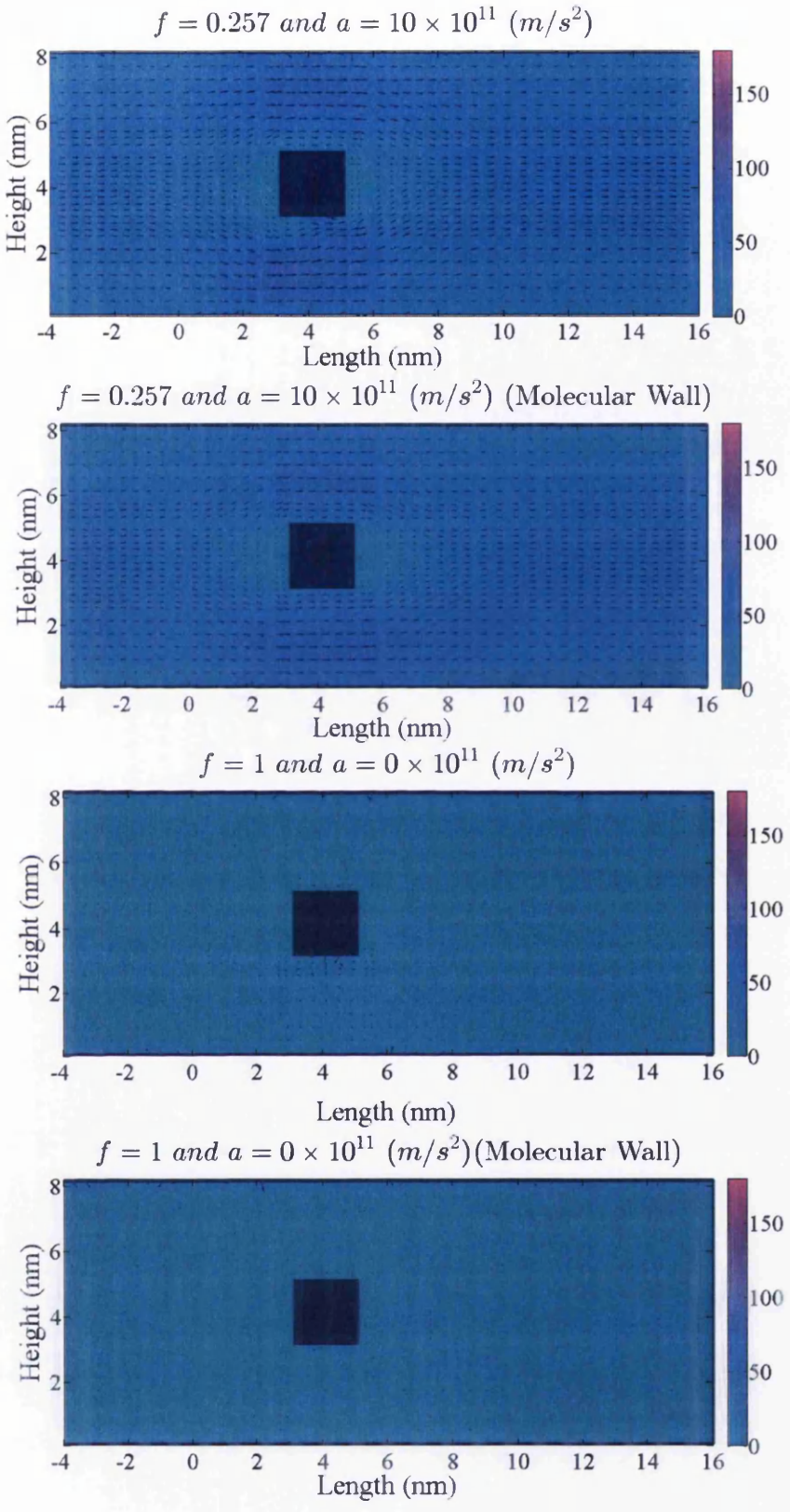

Figure 4.17. Velocity contours for f =0.257 and 1 and a= 0 and 10(m/s^2) around molecular and continuum square shaped cylinder

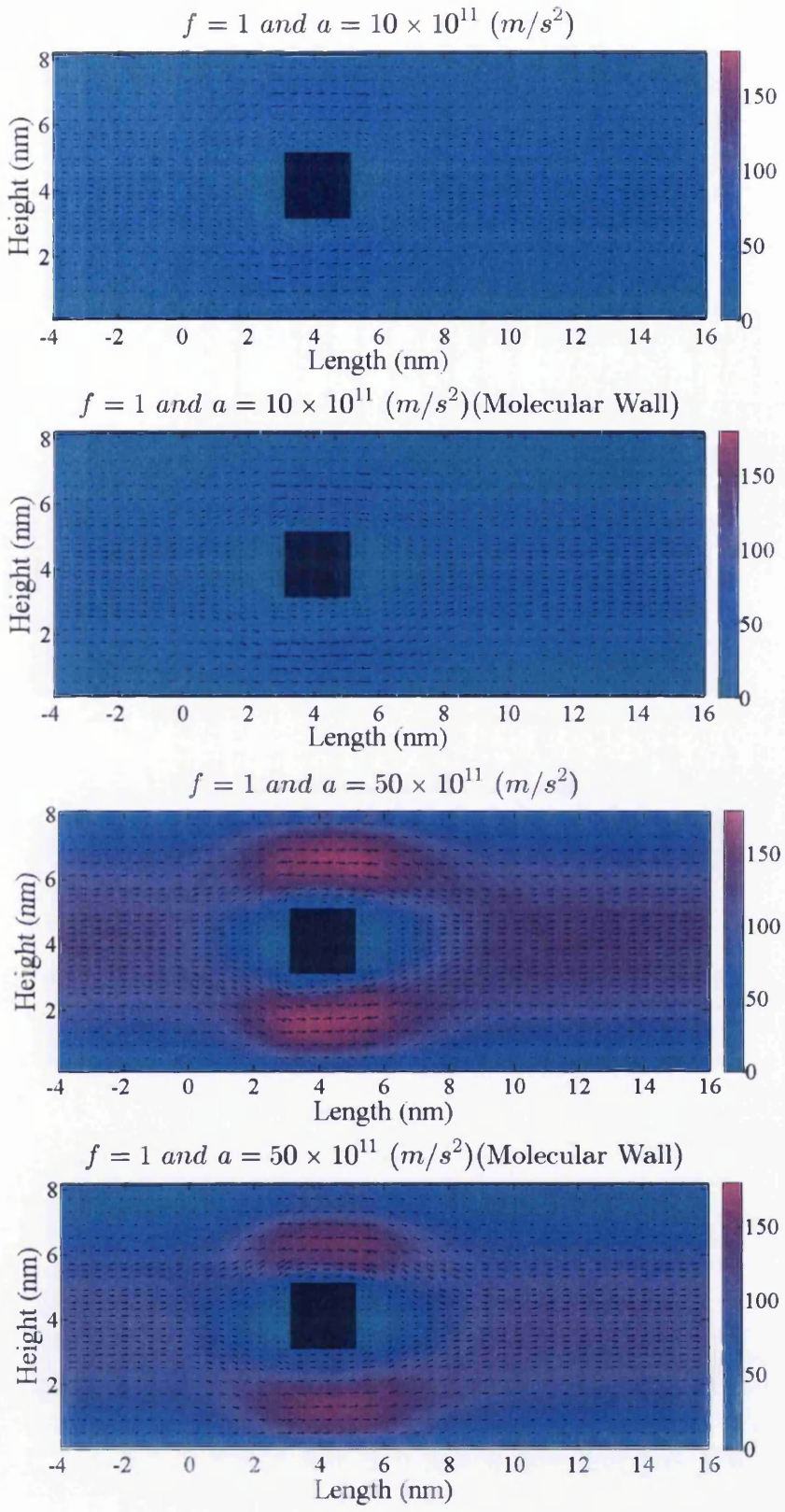

Figure 4.18. Velocity contours for f =1 and a=10(m/s^2) and 50(m/s^2) around molecular and continuum square shaped cylinder

4.4.2 Summary of Results

Pressure and velocity contours for acceleration 0, 10, 50 and 100 (m/s^2) for surface roughness value f = 0, 0.07, 0.257, 0.45, 0.681 and 1 are shown continuum diamond, square and circular cylinder respectively in Appendix A4.1, A4.2 and A4.3.

As discussed in Section 3.4.2 (Figures 3.28 and 3.29), the interaction of molecular flow with an inclined wall produced unexpected or counter intuitive results. Similar patterns are also observed in Figures 4.32 and 4.34 as the molecular flow is separated by an inclined wall. The same explanation given in Section 3.4.2 relating to Figures 3.28 and 3.29 may be extended to explain the reduction of average velocities in the region before the inclined the wall (Figures 4.32 and 4.32). As a result the flow is seen symmetric about x axis but not about y axis.

The corresponding graphs describing the variation of drag coefficient with respect to Reynolds number for various surface roughness values is shown in Figure 4.19, 4.20 and 4.21 for diamond, cylinder and square cylinders respectively. It is shown that for a given Reynolds number, the drag coefficient increases with surface roughness for all cylindrical geometries and it reduces with increase in the Reynolds number value for all cases.

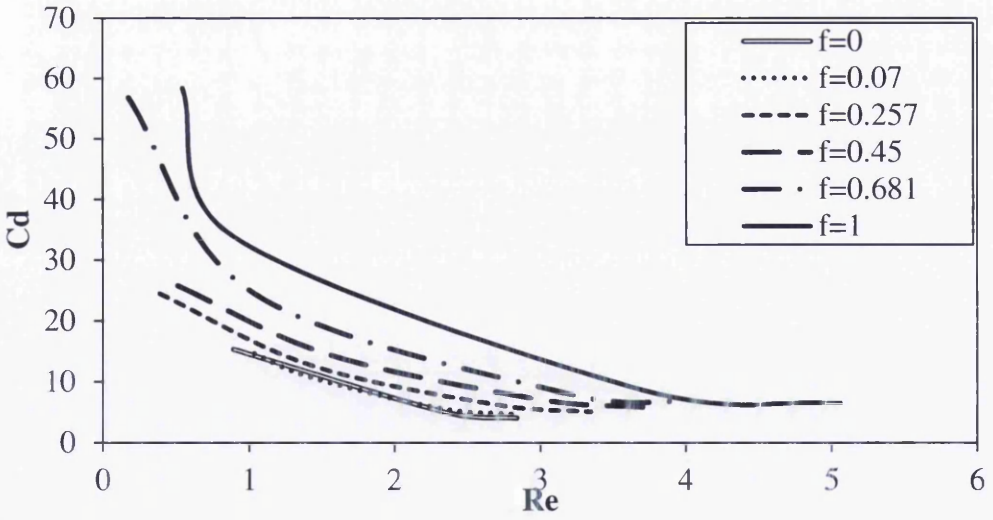

Figure 4.19. Drag coefficient variation with respect to Reynolds number for different roughness values for molecular flow over a diamond shaped cylinder within a slit pore with continuum wall assumptions.

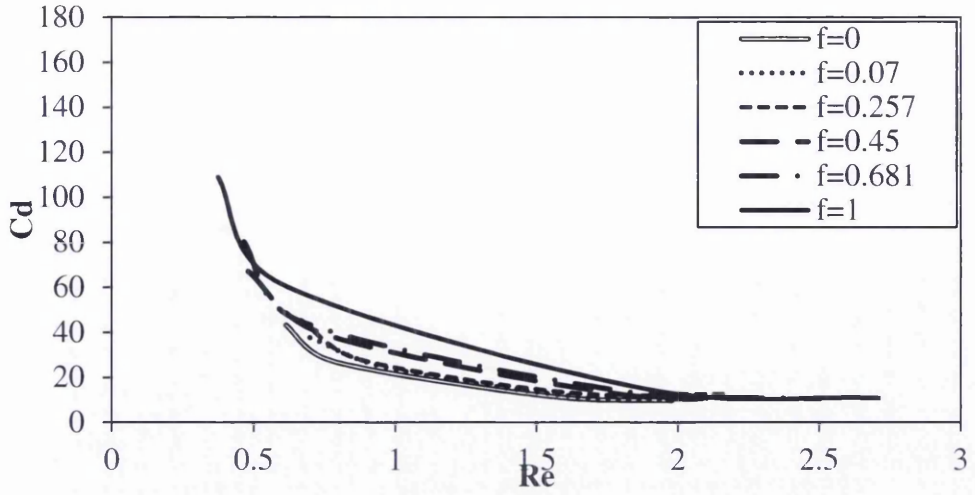

Figure 4.20. Drag coefficient variation with respect to Reynolds number for different roughness values for molecular flow over a circular shaped cylinder within a slit pore with continuum wall assumptions.

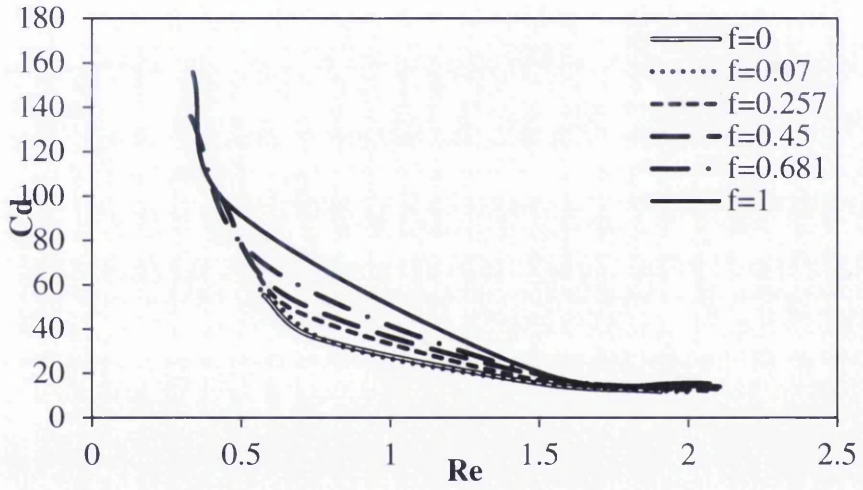

Figure 4.21. Drag coefficient variation with respect to Reynolds number for different roughness values for molecular flow over a square cylinder within a slit pore with continuum wall assumptions.

Figure 4.22 groups the variation of drag coefficients with respect to Reynolds number for the three cylindrical shapes and plots the corresponding graphs for each surface roughness value. It is observed that the drag is minimum for the flow over a diamond shaped cylinder and maximum for the square shaped cylinder. It is also seen that the drag coefficient increases as the surface roughness value increases.

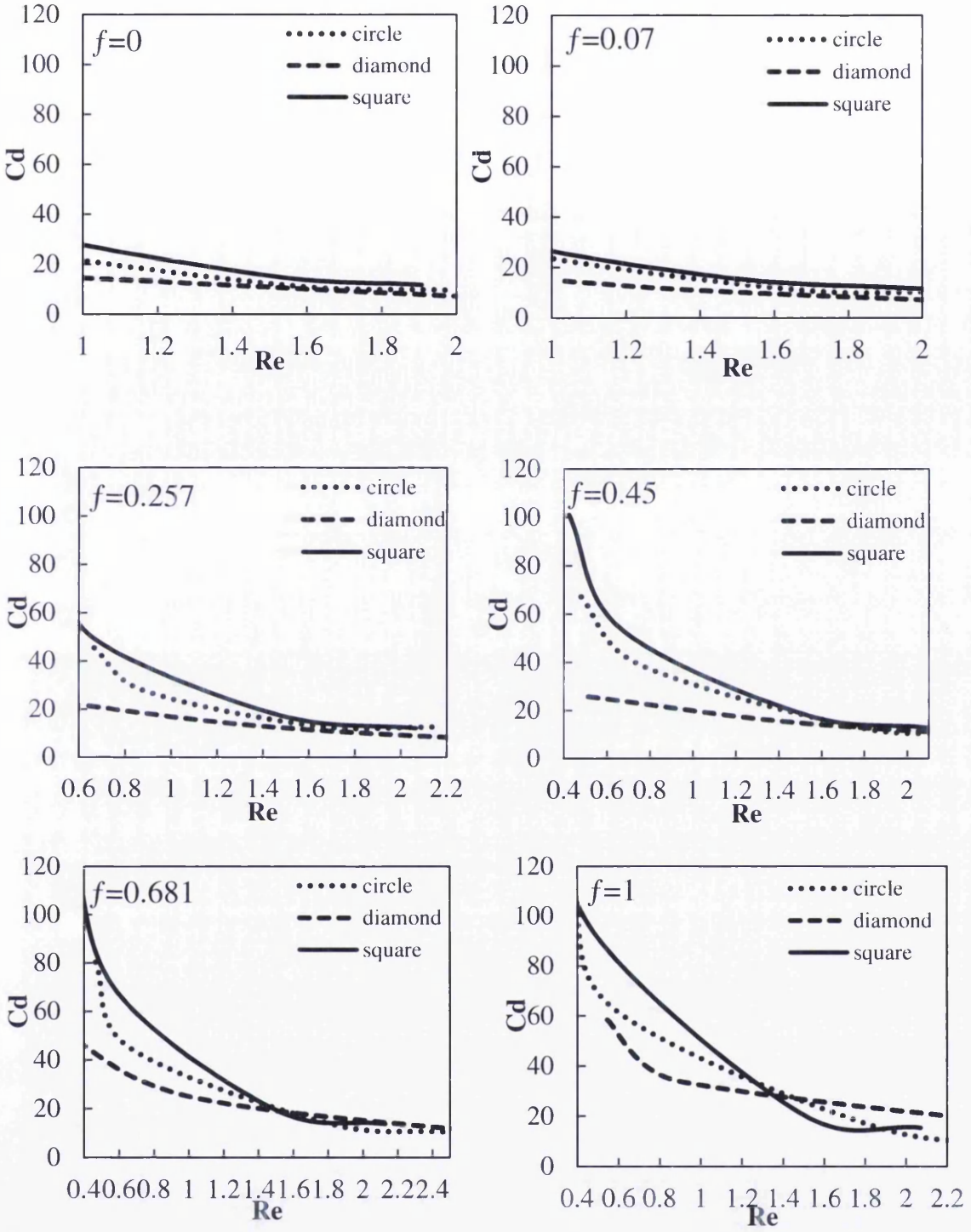

Figure 4.22. Drag coefficient variation with respect to Reynolds number for circular, diamond and square shaped cylinders. The graphs are shown for different surface roughness value.

The pressure contour plots shown Appendix A4.2 show that for smooth circular cylinder ($f = 0$) does not interfere with the pressure gradients around the cylinder for acceleration values up to 50 m/s^2 i.e. Reynolds number 1.5. The results are not

expected to be similar to the analytical solution derived from the continuum calculations (Lagree, 2013) at this Reynolds number flow. However, these are compared in Figure 4.23 as a matter of curiosity. Interestingly the pattern is similar however the magnitude of the drag coefficient is significantly different for a given Reynolds number.

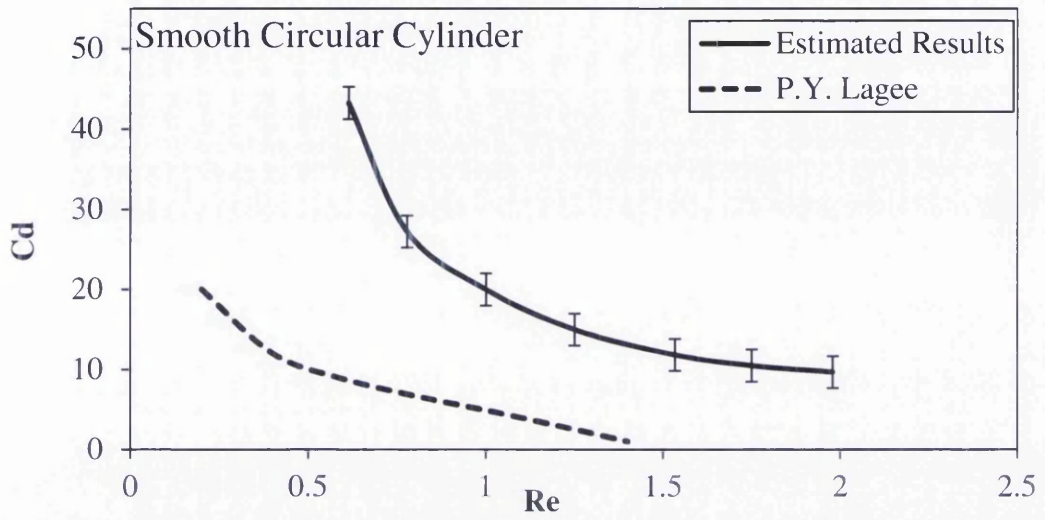

Figure 4.23. Comparison of drag coefficient variation with Reynolds number for the proposed molecular dynamics simulation with continuum based analytical solutions (Lagree, 2013).

4.5 Conclusions

A detailed mathematical formulation, based on first principles, is proposed to predict drag coefficients for a molecular flow over different shaped cylindrical geometries confined within parallel walls. The molecular flow is induced by altering individual molecular velocity by applying a constant acceleration value, which is a small percentage of molecular acceleration, at each time step. The number of molecules, volume and the total thermal or kinetic energy (NVT) of the system is conserved using a Gaussian thermostat. An array of two dimensional MLS nodes is introduced along with an algorithm to average instantaneous molecular velocities and pressures over all time steps in order to predict macroscopic properties at each MLS node. The formulation was verified with number of tests e.g. comparing instantaneous molecular velocity distributions with Maxwell distributions and comparing the

calculated pressure value at a point with the assumed pressure value e.g. 40MPa. The number density used in the simulation assumed that the pressure value is 40MPa. This is discussed in detail in Chapter 2.

The formulation for modelling a continuum wall, as presented in Chapter 3, is used and results are compared with an equivalent molecular wall. It was discovered that pressure calculations are sensitive to the molecular or continuum wall assumptions. However, the difference in the force values was approximately constant and hence, the resulting coefficients of drag were similar. The drag coefficient variation with respect to Reynolds number, under various conditions such as cylinder shape and surface roughness, is studied.

It is discussed in Chapter 2, the Knudson number for a methane flow at 300K, 40MPa through a 8nm slit pore is 0.0214, and as shown in Figure 2.8, the region of interest is close to the continuum limit. A comparison with an analytical expression, based on continuum assumptions, highlighted that the drag coefficients resulting from molecular flows are significantly higher and hence, it is concluded that the molecular contribution may not be ignored even for small Knudson number flows that are close to the continuum limit. In order to realise and optimise the potential applications as reviewed in Chapter 2, new experimental techniques need to be devised to measure forces at 50-100 nm scale so that the simulation codes can be verified and optimal design and operating conditions discovered.

4.6 Appendix: A4.1

Velocity and pressure contours for flow past a diamond shaped cylinder for roughness values (0, 0.7, 0.257, 0.45, 0.68 and 1) and acceleration values (0, 6, 10, 50, 100 (m/s^2)).

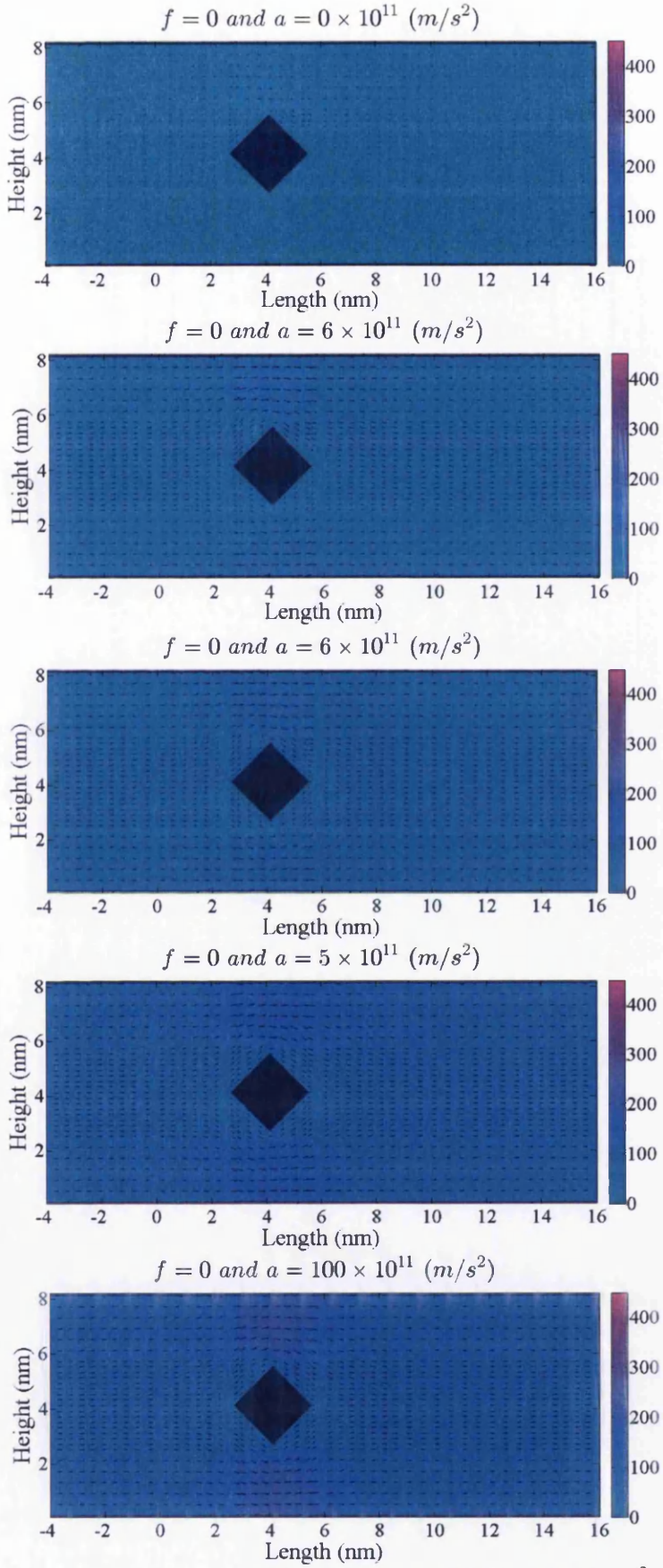

Figure 4.24. Velocity contours for f=0 and accelerations 0,6,10,50,100 (m/s^2)

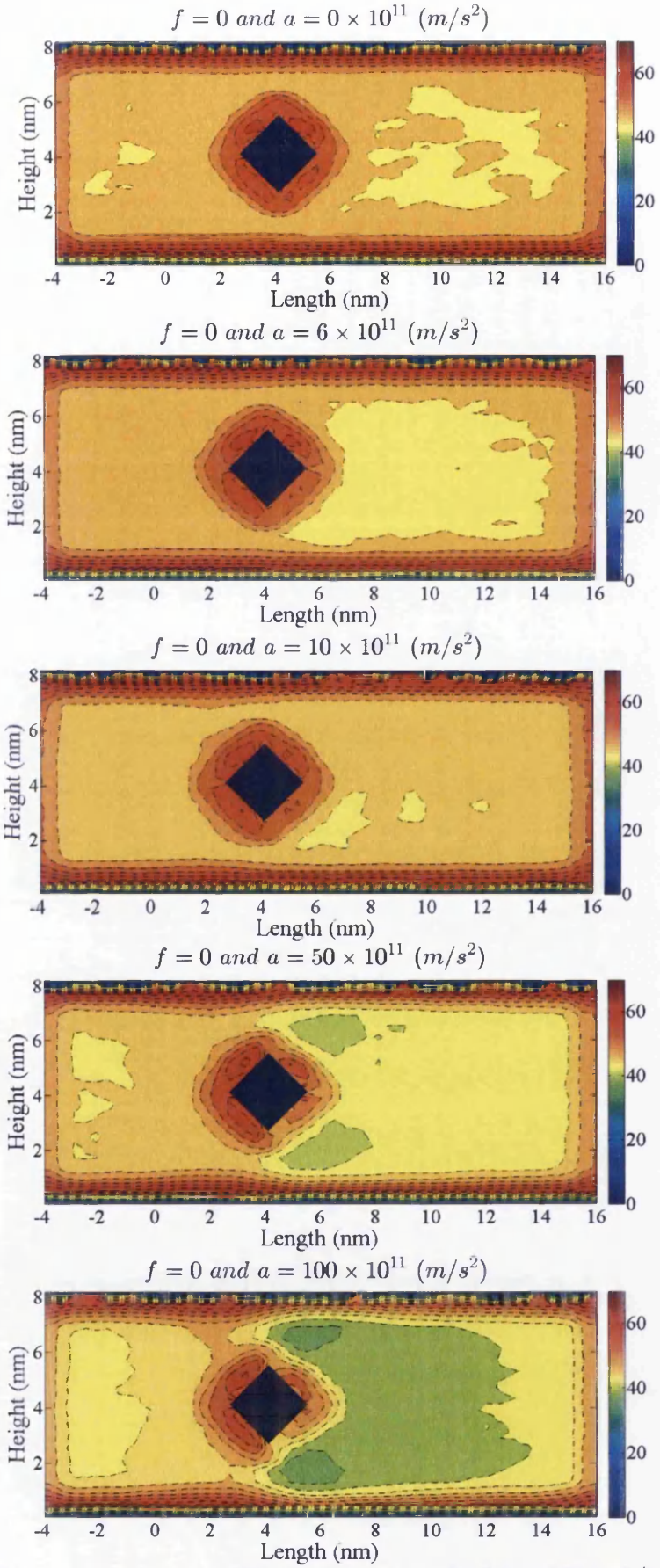

Figure 4.25. Pressure contours for f=0 and accelerations 0,6,10,50,100 (m/s^2)

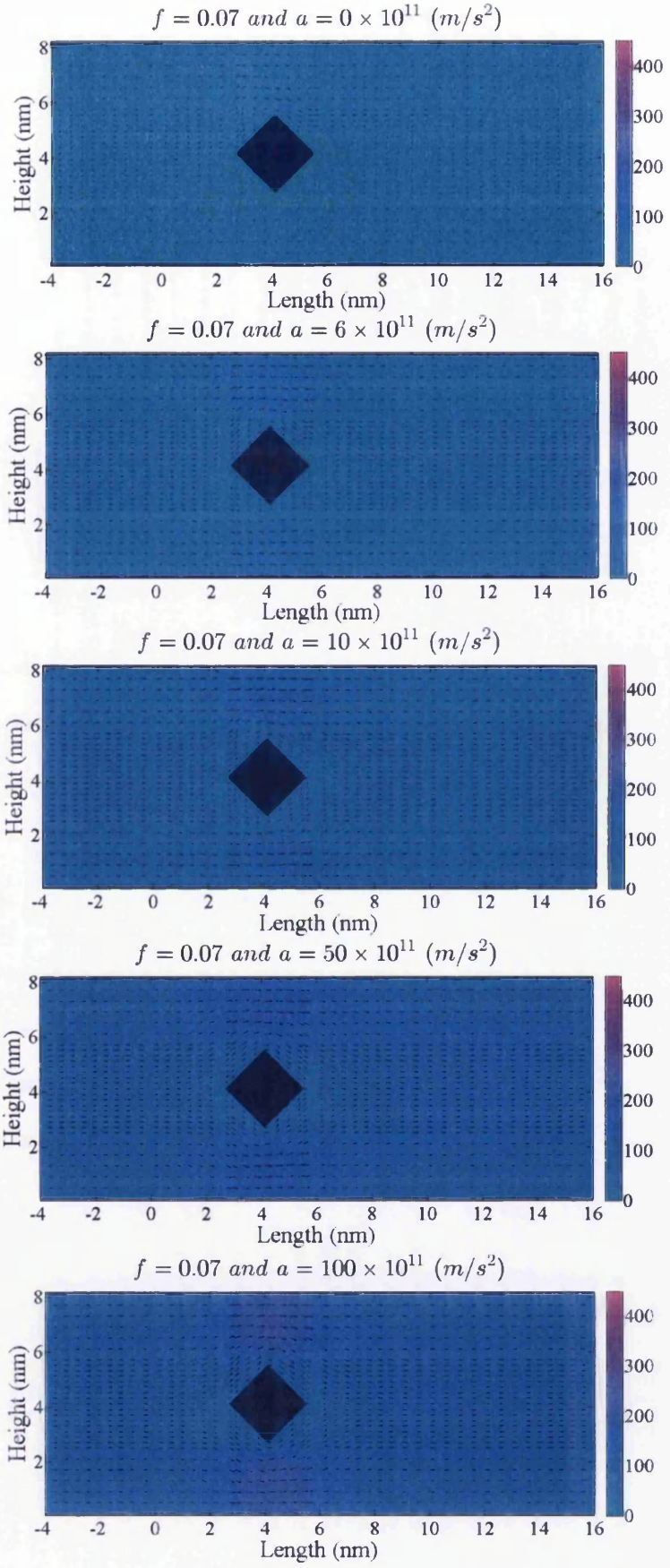

Figure 4.26. Velocity contours for f=0.07 and accelerations 0,6,10,50,100 (m/s^2)

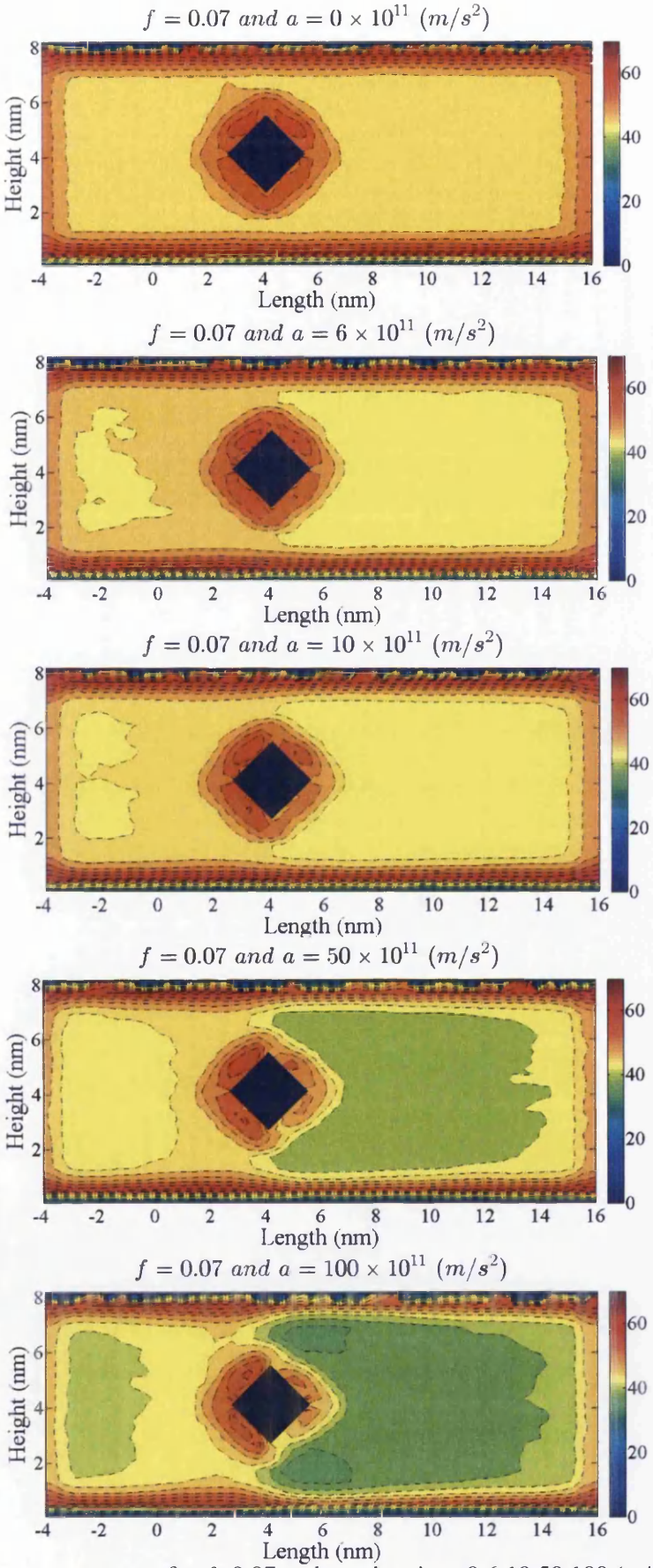

Figure 4.27. Pressure contours for f=0.07 and accelerations 0,6,10,50,100 (m/s^2)

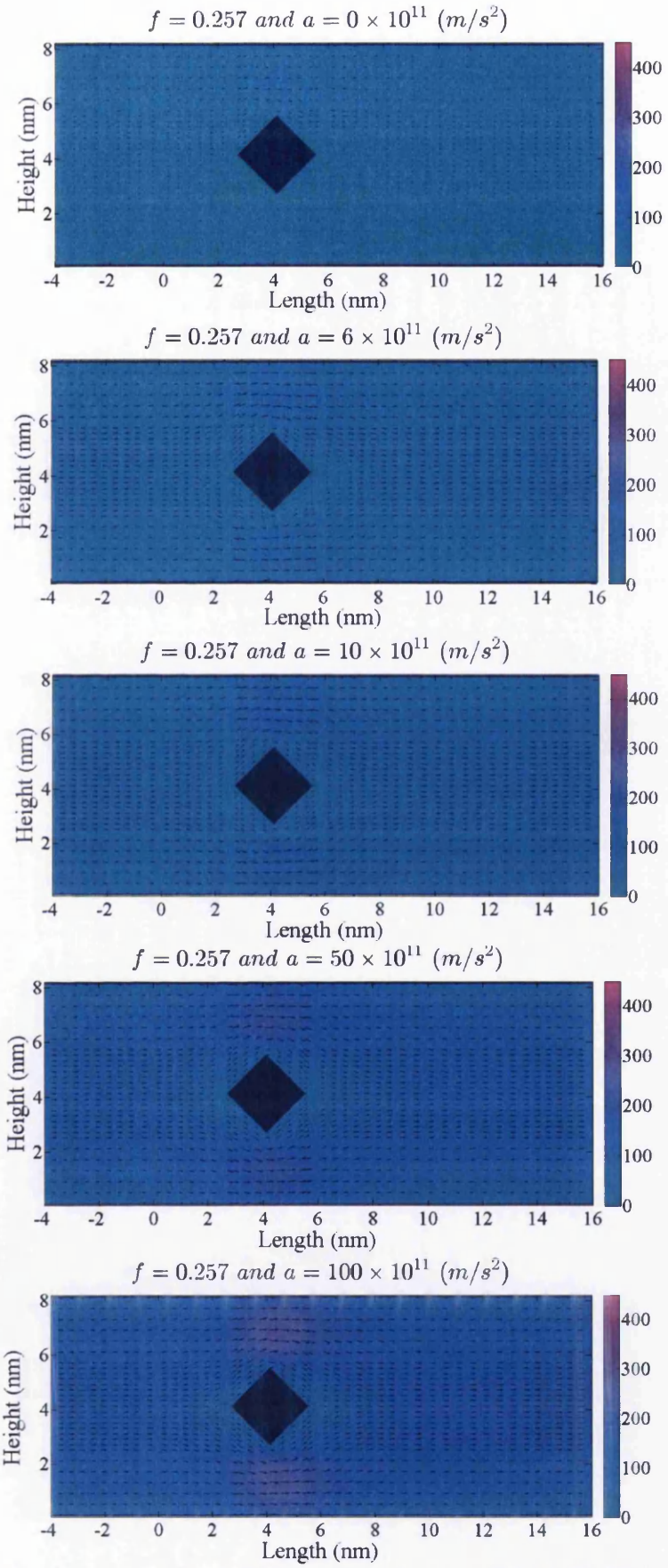

Figure 4.28. Velocity contours for f=0.257 and accelerations 0,6,10,50,100 (m/s^2).

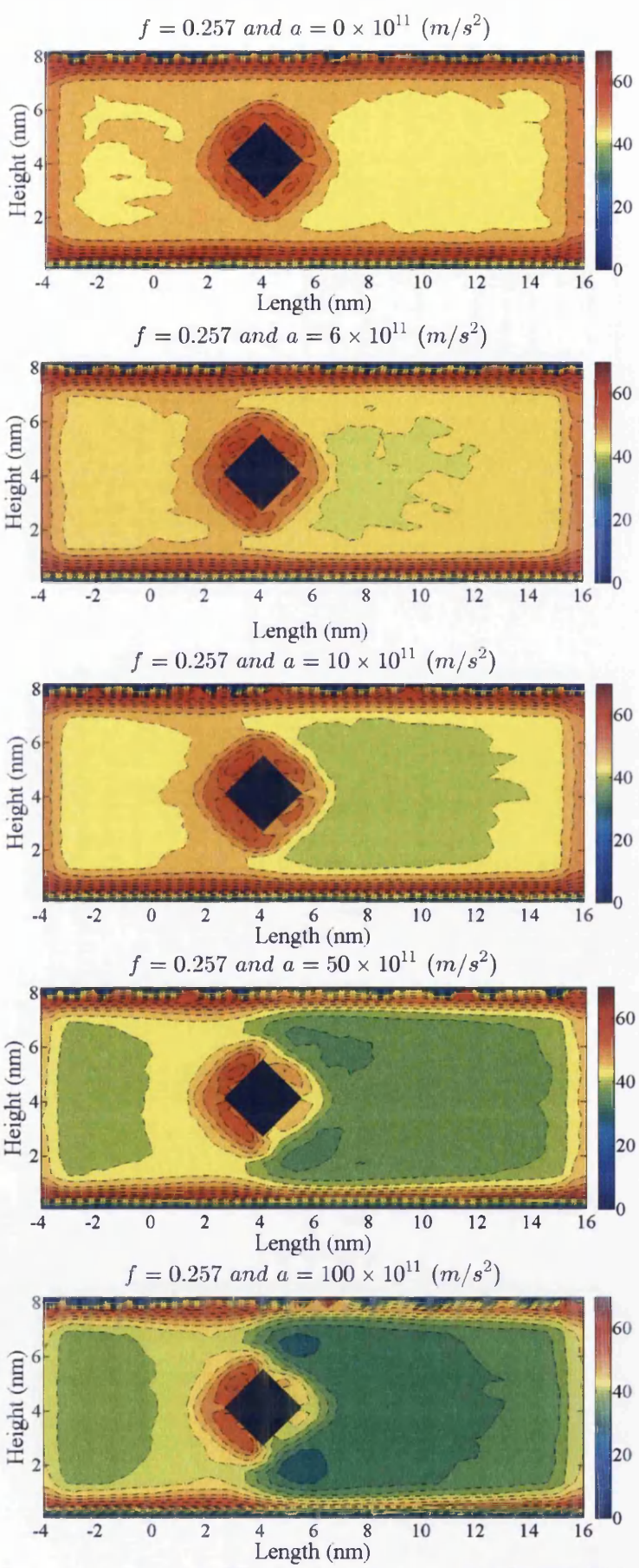

Figure 4.29. Pressure contours for f=0.257 and accelerations 0,6,10,50,100 (m/s^2)

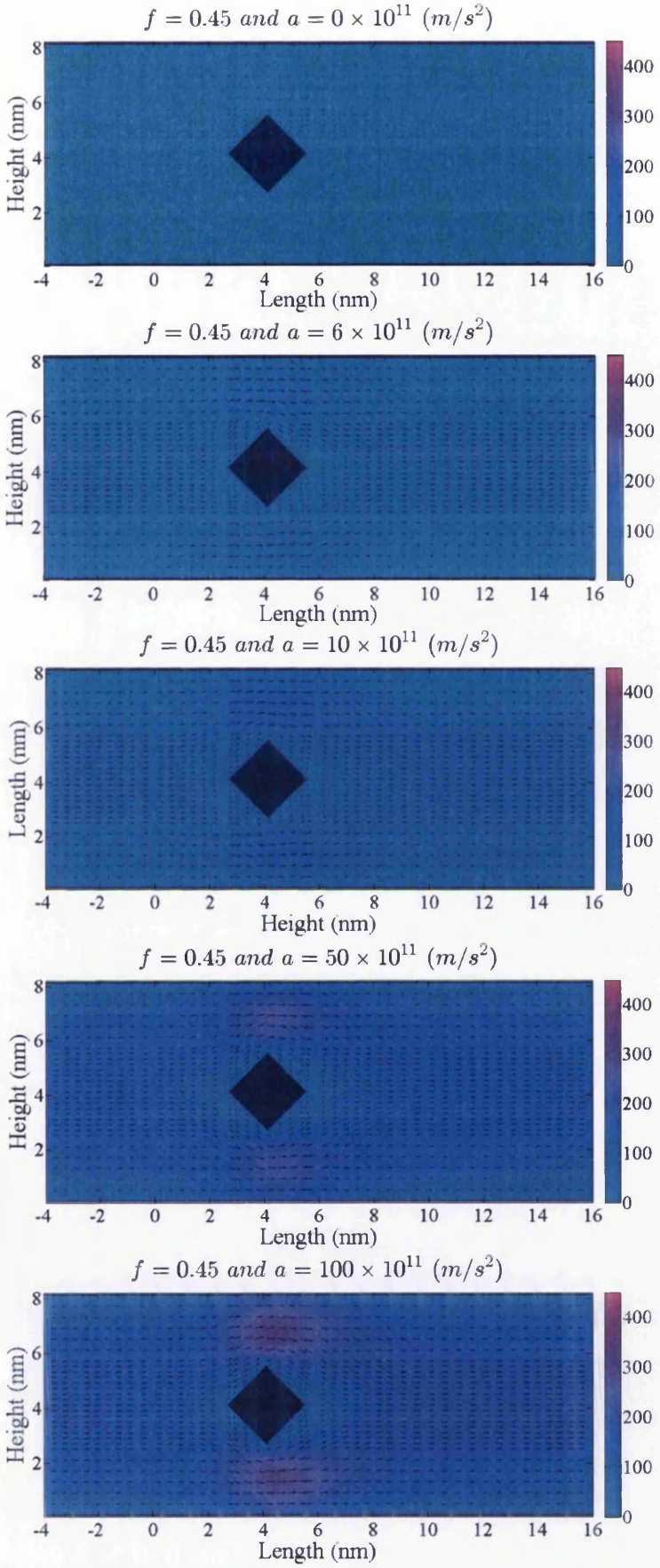

Figure 4.30. Velocity contours for f=0.45 and accelerations 0,6,10,50,100 (m/s^2)

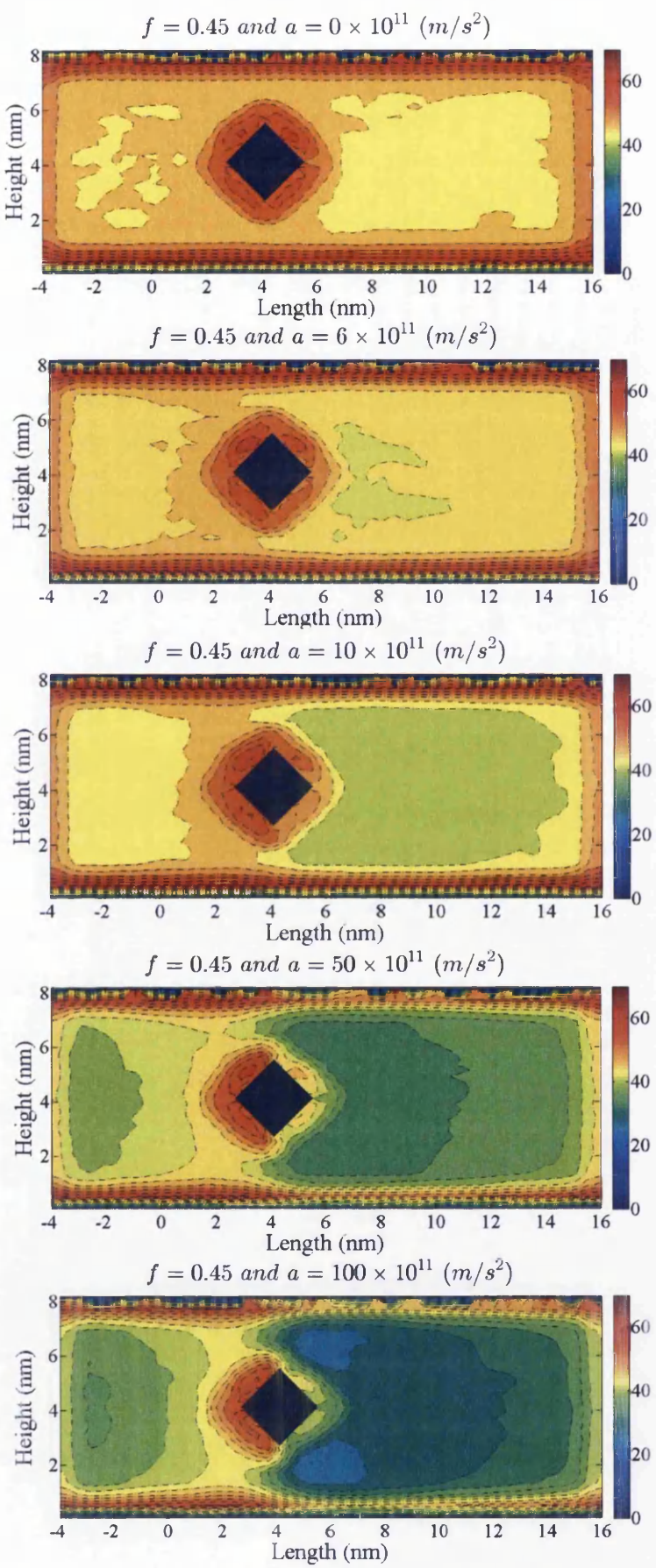

Figure 4.31. Pressure contours for f=0.45 and accelerations 0,6,10,50,100 (m/s^2)

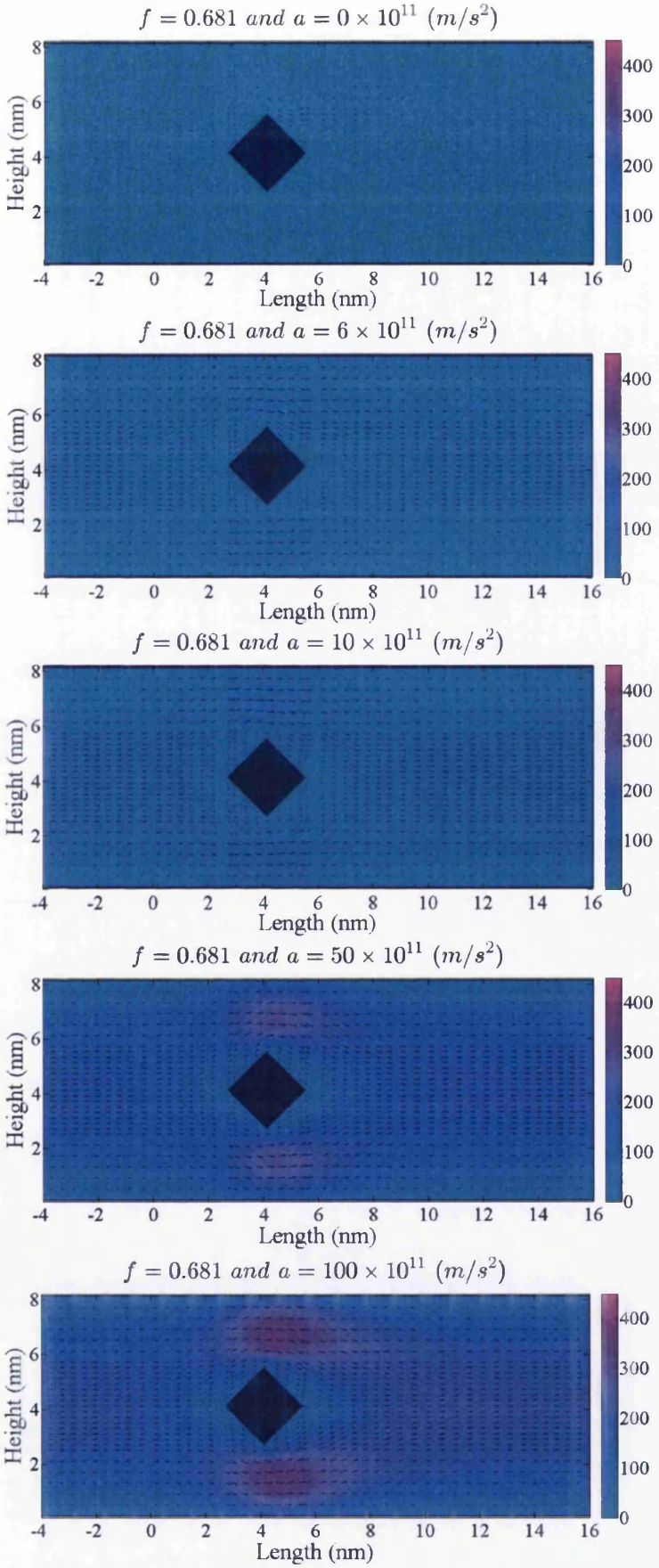

Figure 4.32. Velocity contours for f=0.681 and accelerations 0,6,10,50,100 (m/s^2)

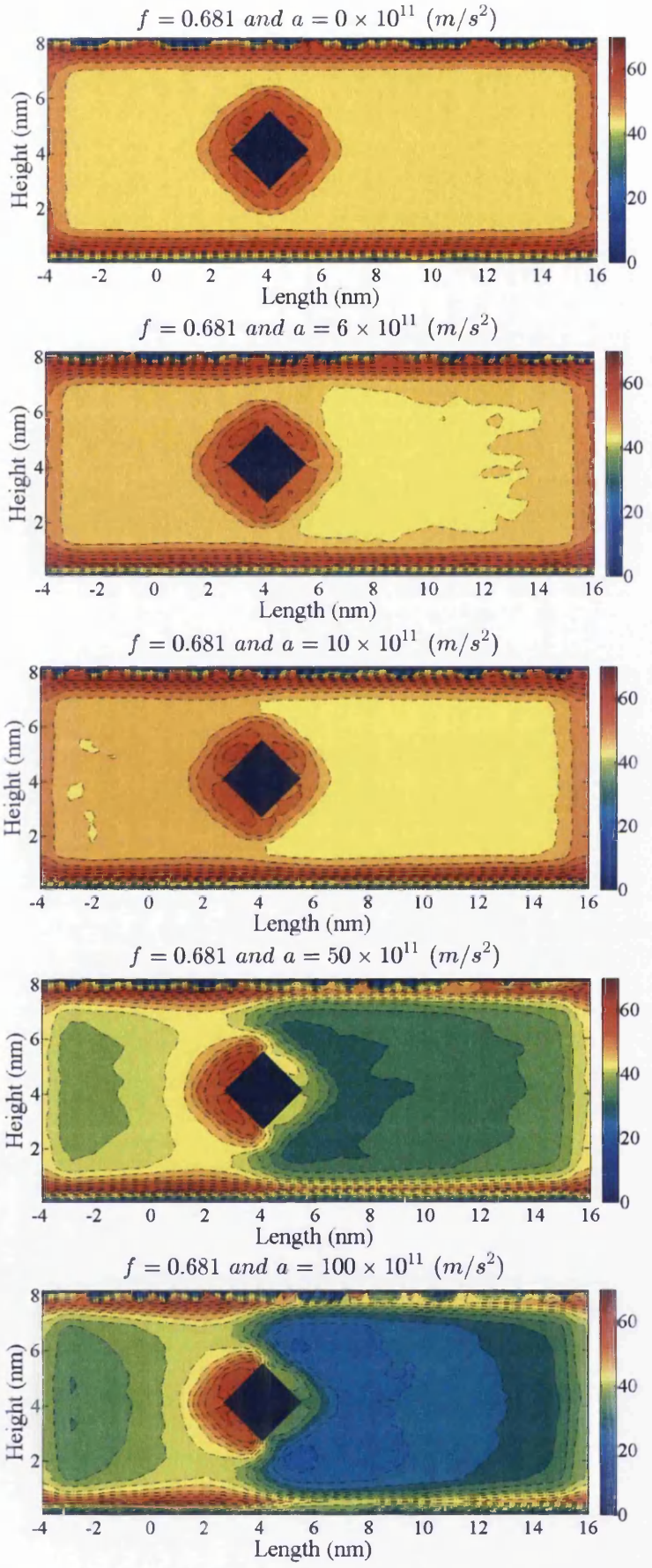

Figure 4.33. Velocity contours for f=0.681 and accelerations 0,6,10,50,100 (m/s^2)

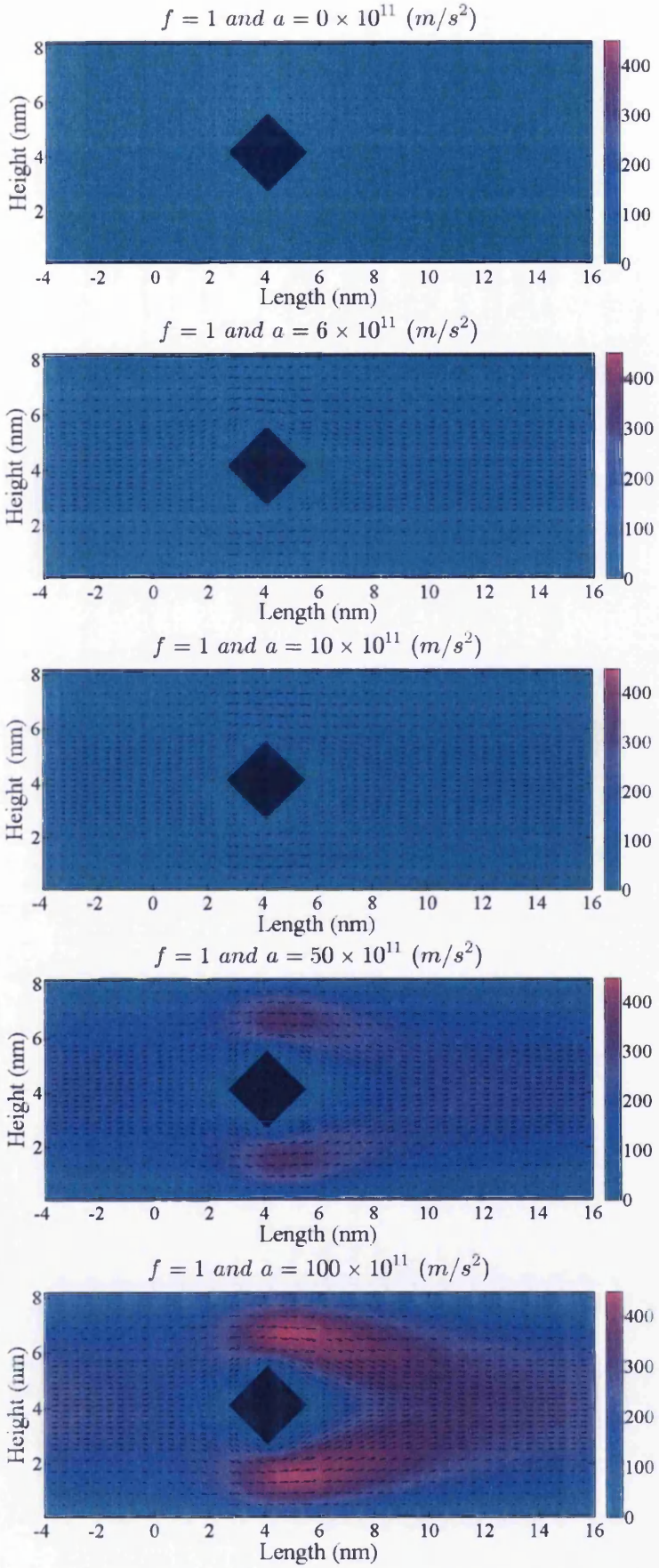

Figure 4.34. Velocity contours for f=1 and accelerations 0,6,10,50,100 (m/s^2)

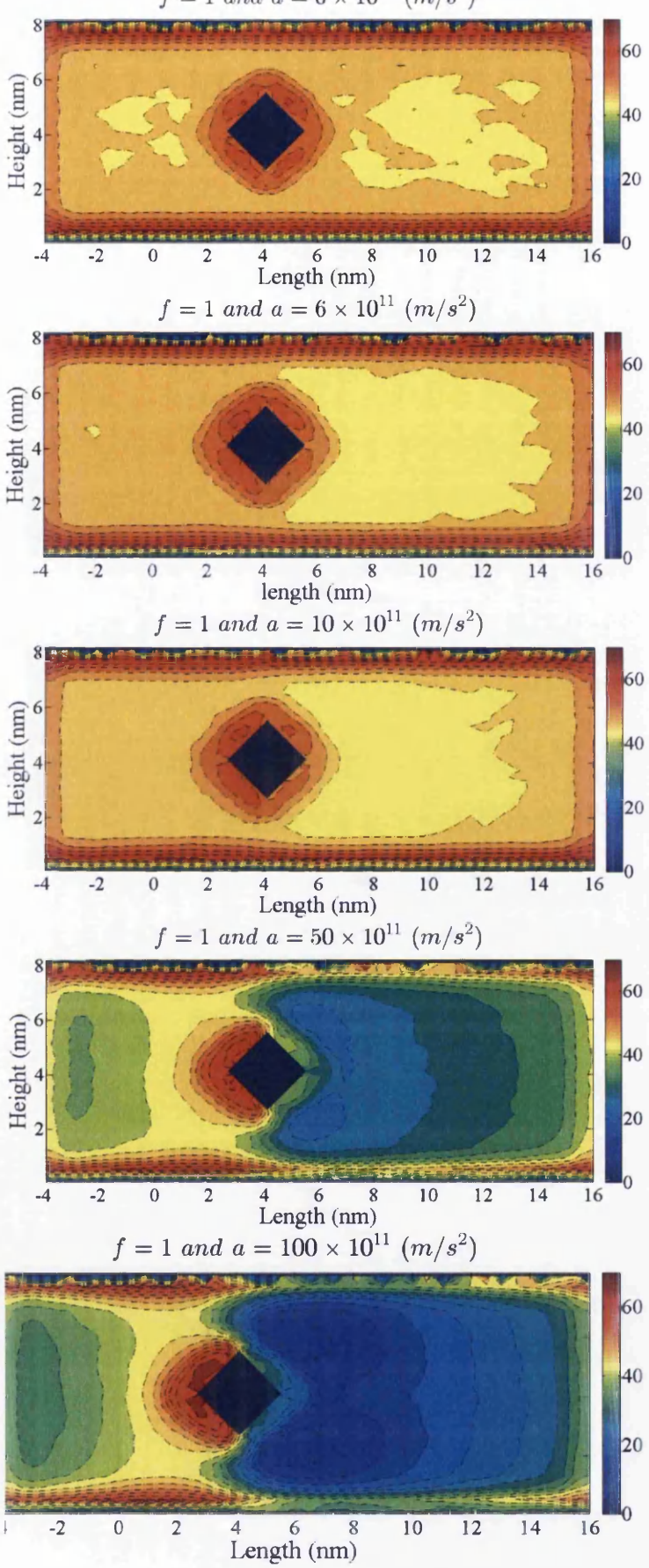

Figure 4.35. Pressure contours for f=1 and accelerations 0,6,10,50,100 (m/s^2)

4.7 Appendix: A4.2

Velocity and pressure contours for flow past a circular shaped cylinder for roughness values (0, 0.7, 0.257, 0.45, 0.68 and 1) and acceleration values (0, 6, 10, 50, 100 (m/s^2)).

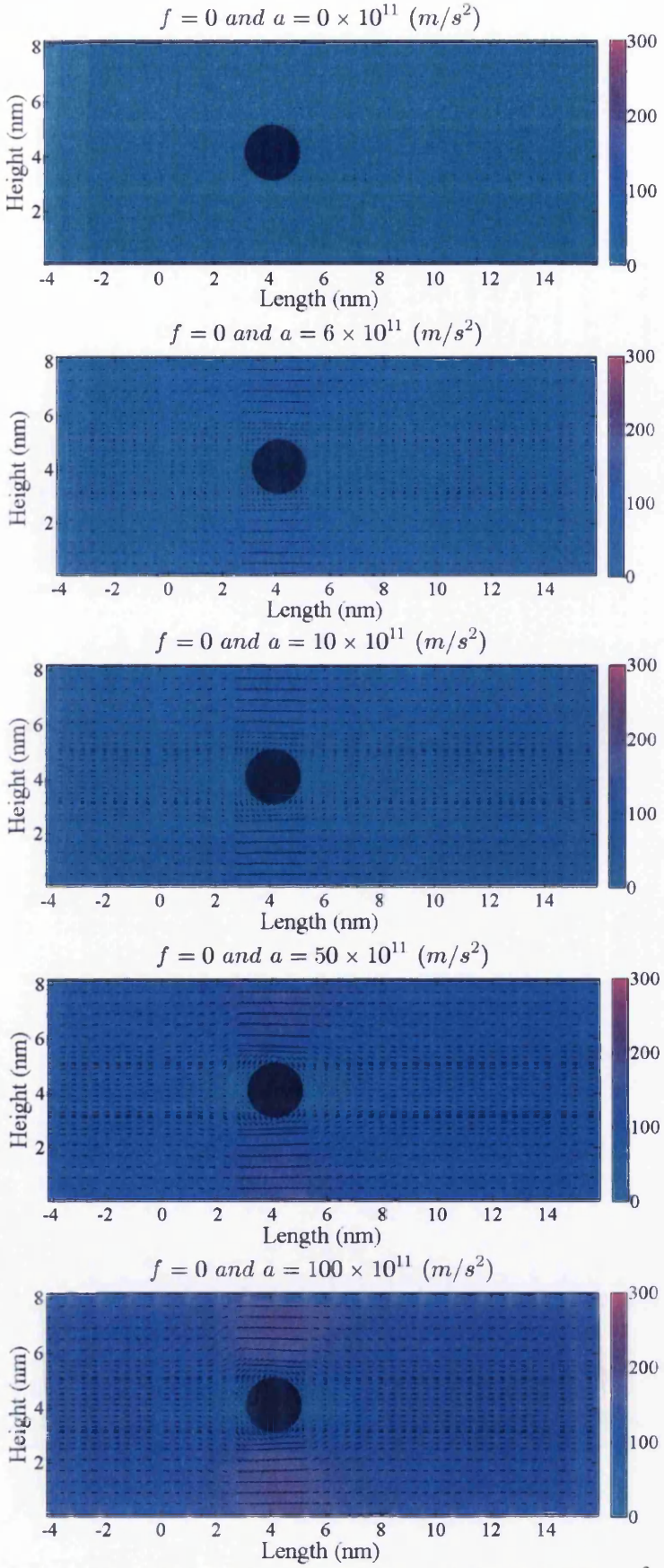

Figure 4.36. Velocity contours for f=0 and accelerations 0,6,10,50,100 (m/s^2)

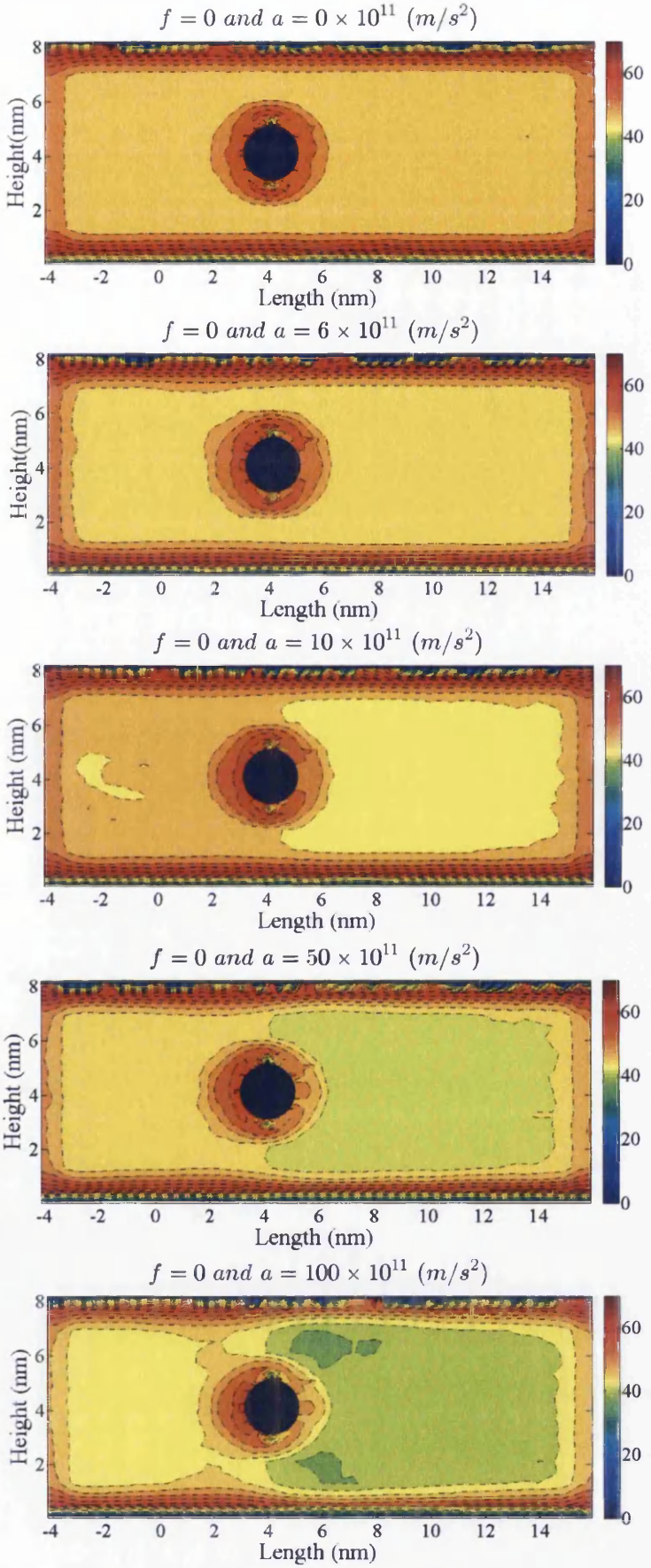

Figure 4.37.Pressure contours for f=0 and accelerations 0,6,10,50,100 (m/s^2)

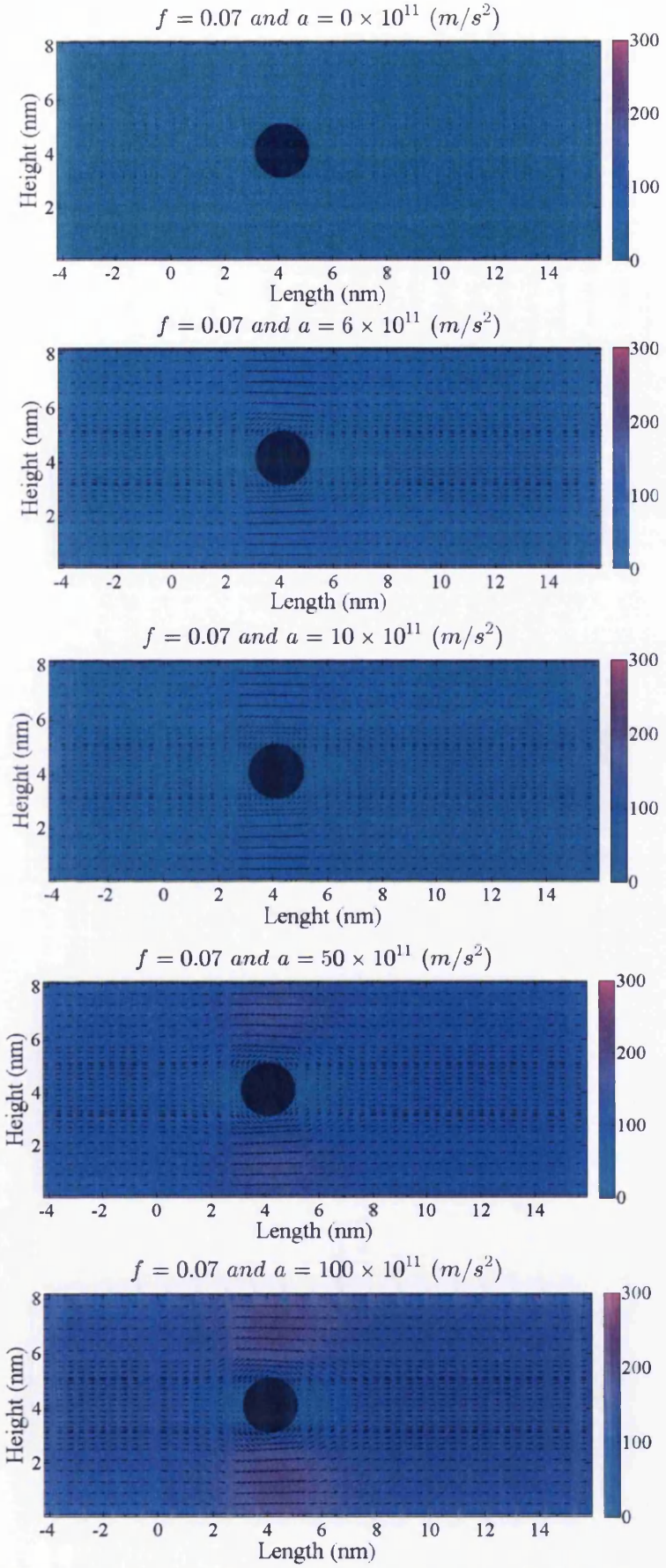

Figure 4.38. Velocity contours for f=0.07 and accelerations 0,6,10,50,100 (m/s^2)

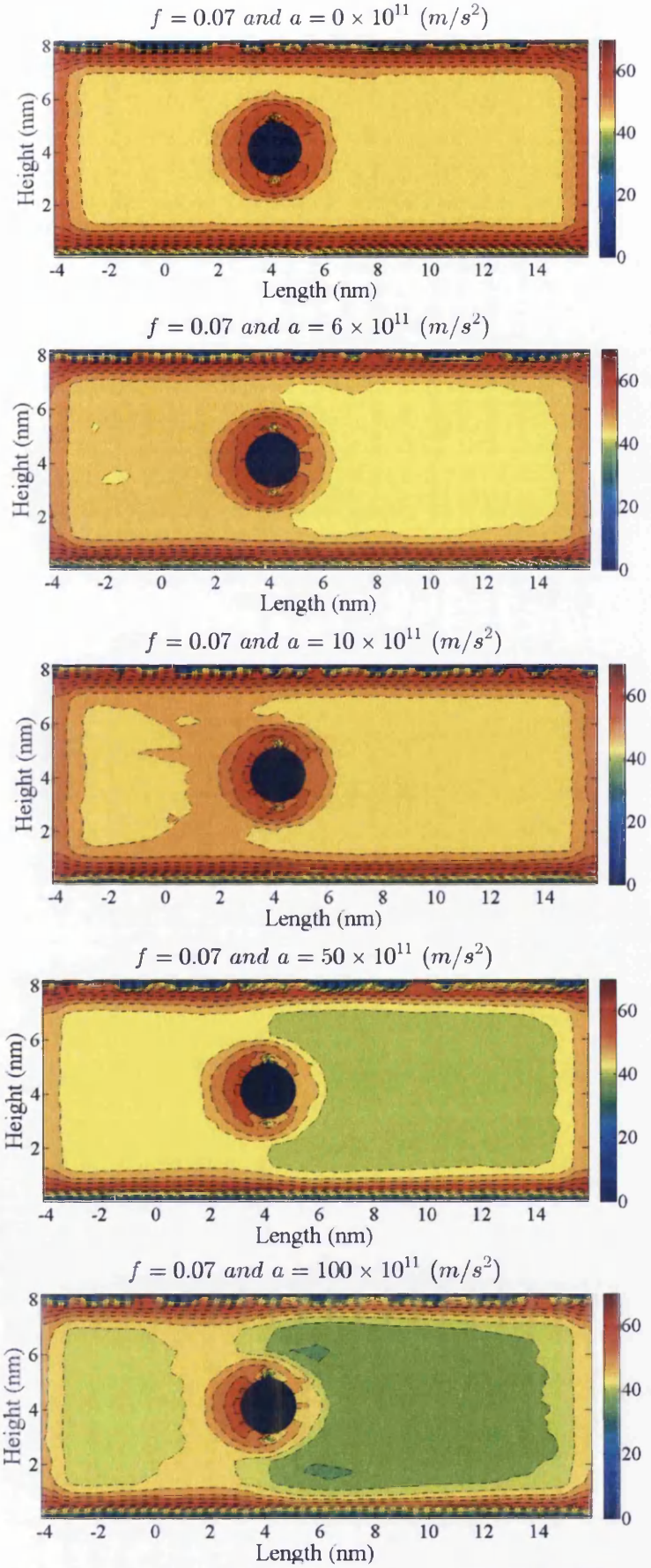

Figure 4.39. Pressure contours for f=0.07 and accelerations 0,6,10,50,100 (m/s^2)

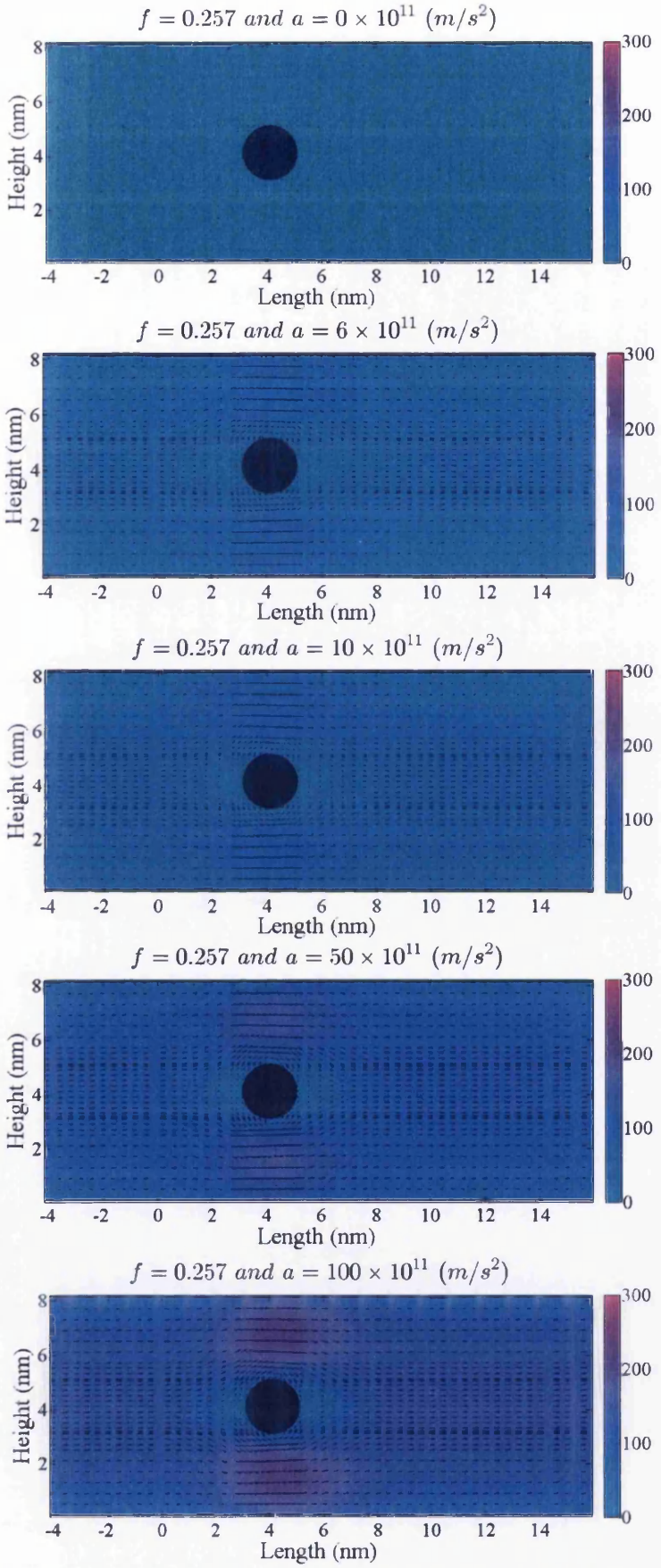

Figure 4.40. Velocity contours for f=0.257 and accelerations 0,6,10,50,100 (m/s^2)

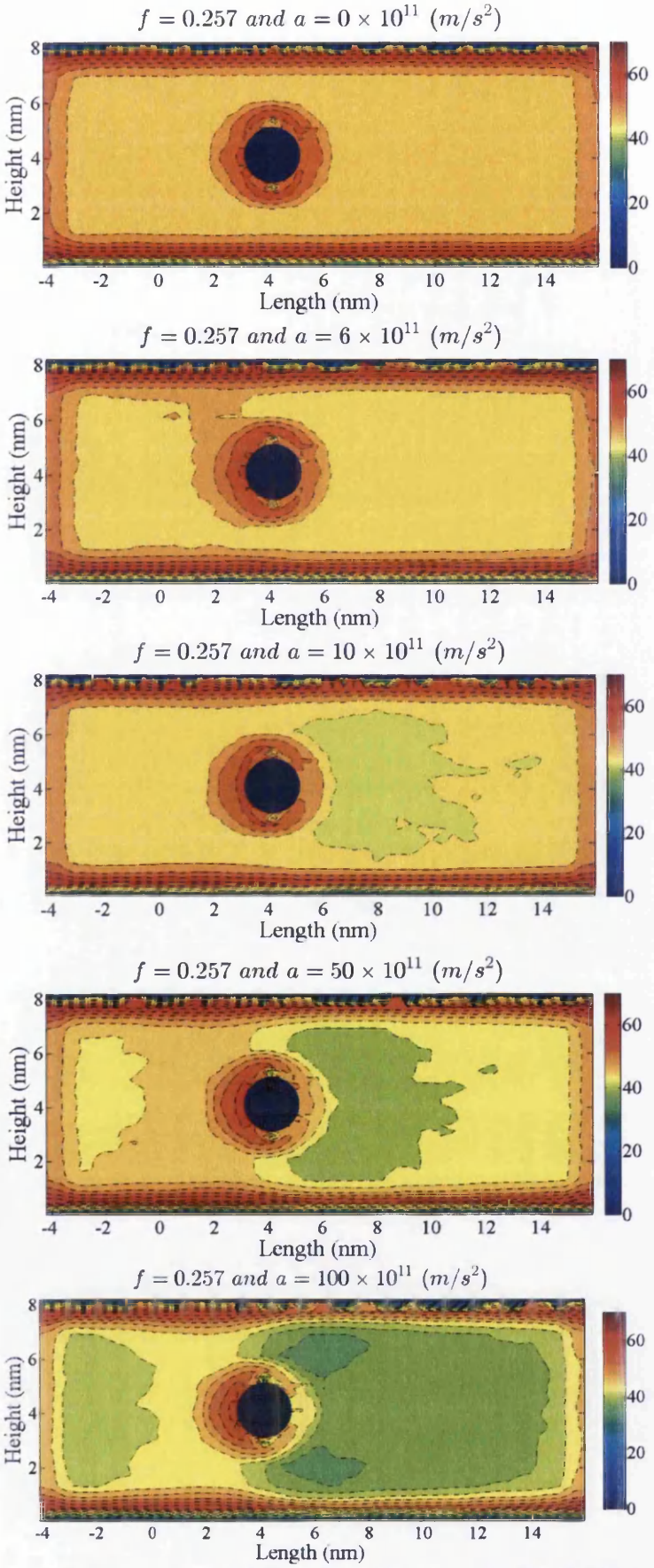

Figure 4.41. Pressure contours for f=0.257 and accelerations 0,6,10,50,100 (m/s^2)

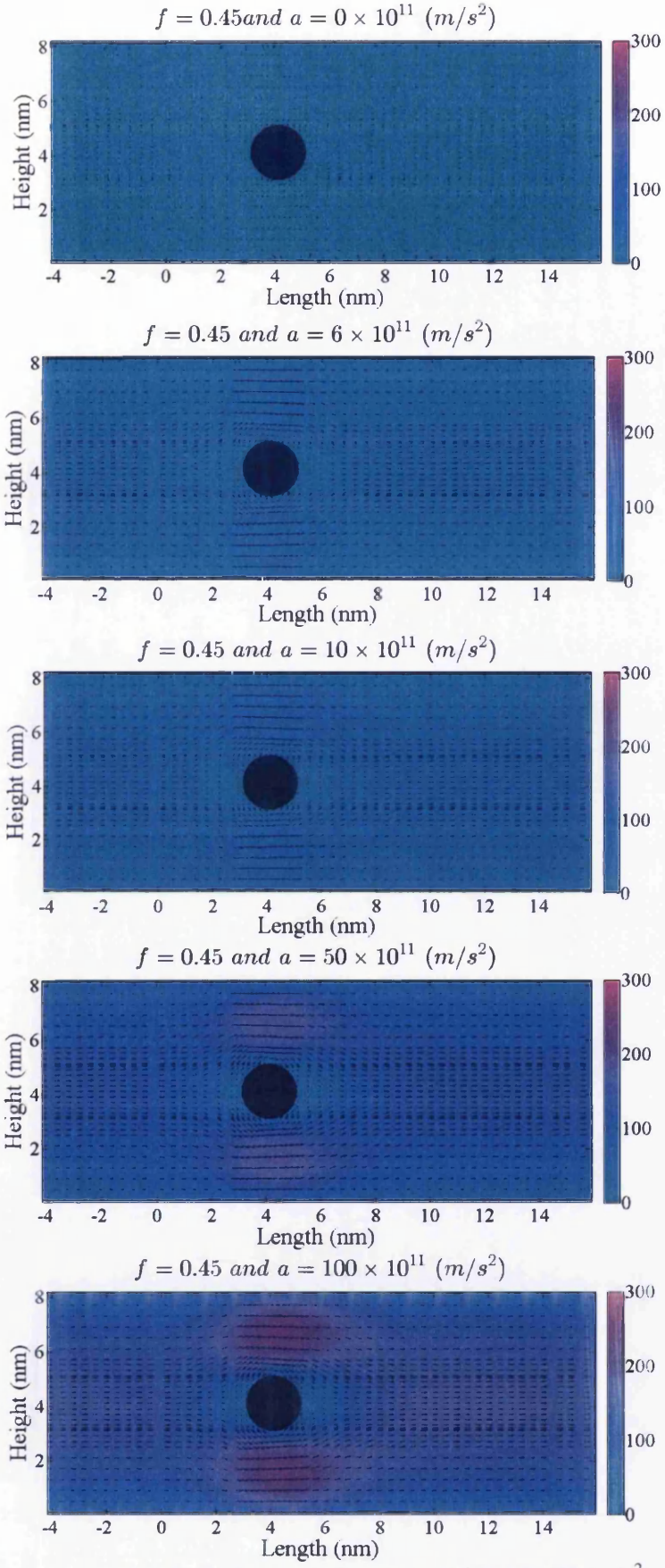

Figure 4.42. Velocity contours for f=0.45 and accelerations 0,6,10,50,100 (m/s^2)

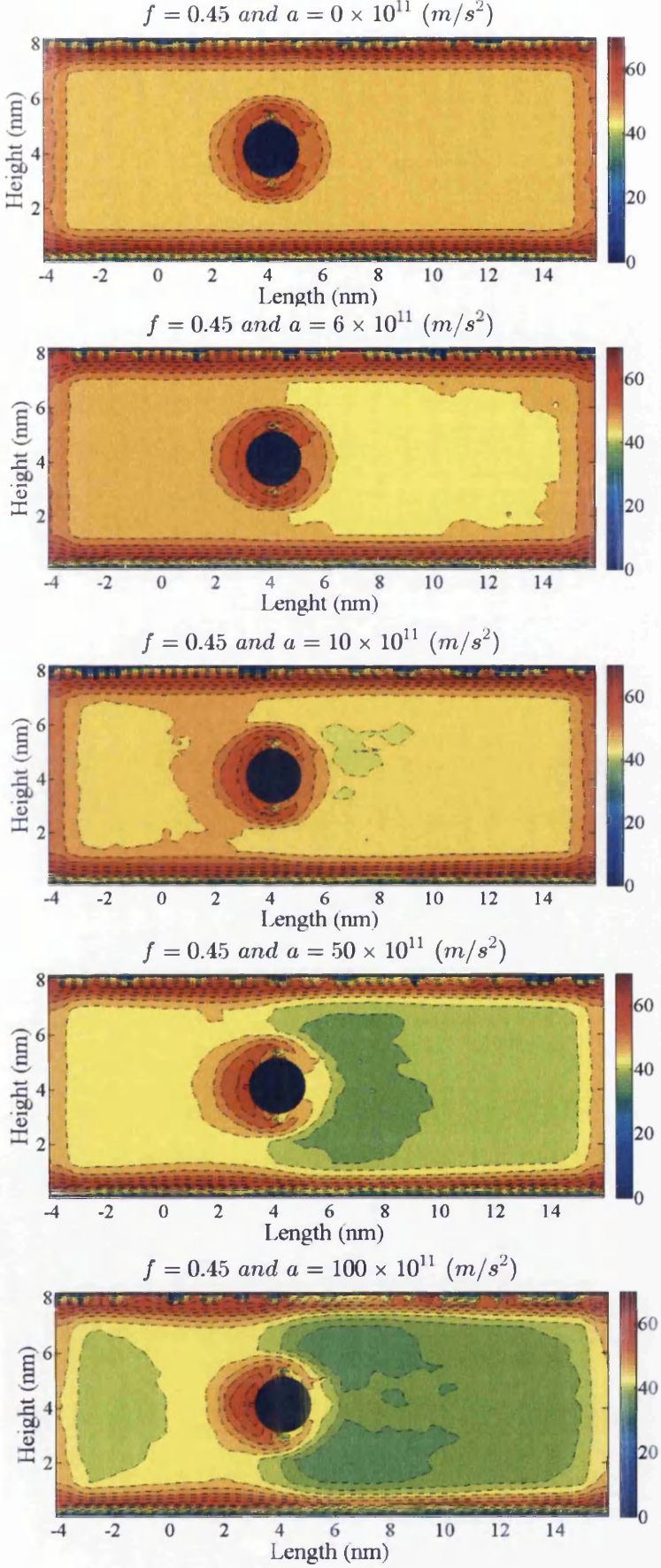

Figure 4.43. Pressure contours for f=0.45 and accelerations 0,6,10,50,100 (m/s^2)

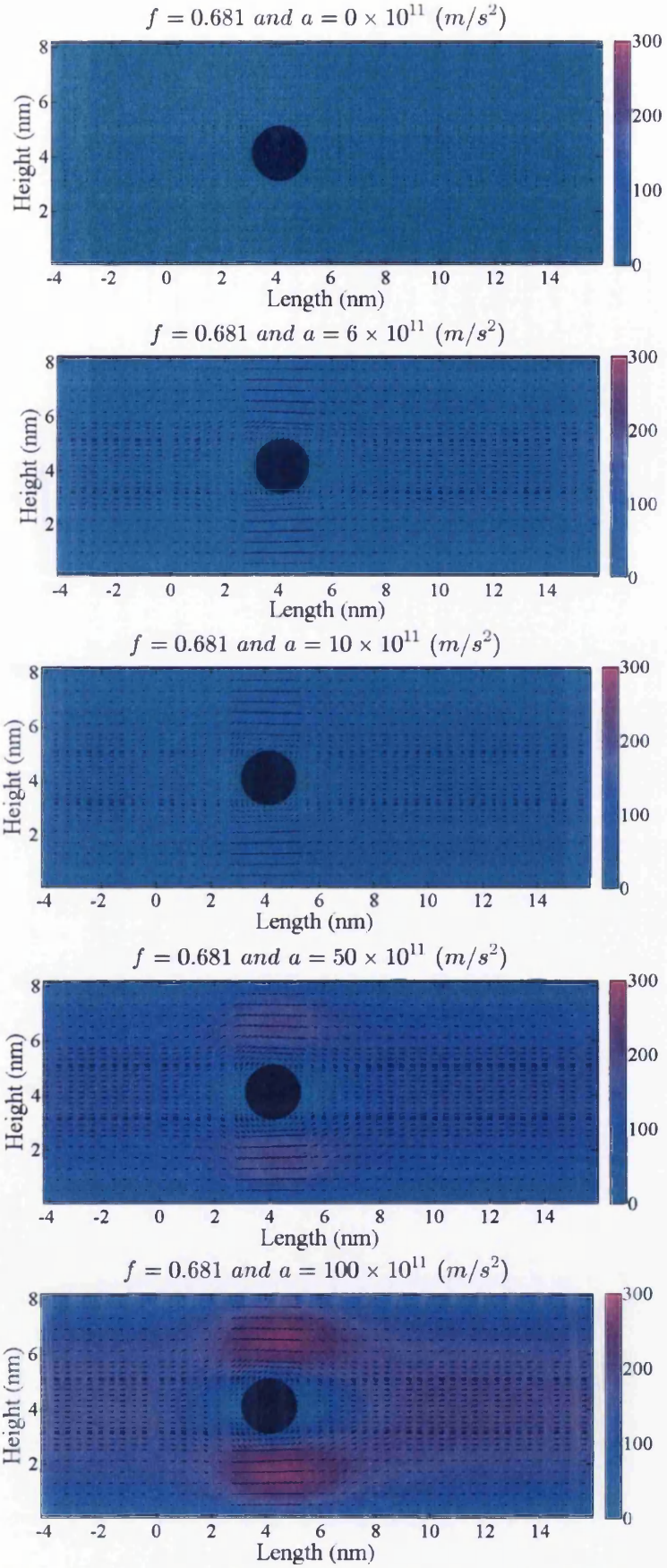

Figure 4.44. Velocity contours for f=0.681 and accelerations 0,6,10,50,100 (m/s^2)

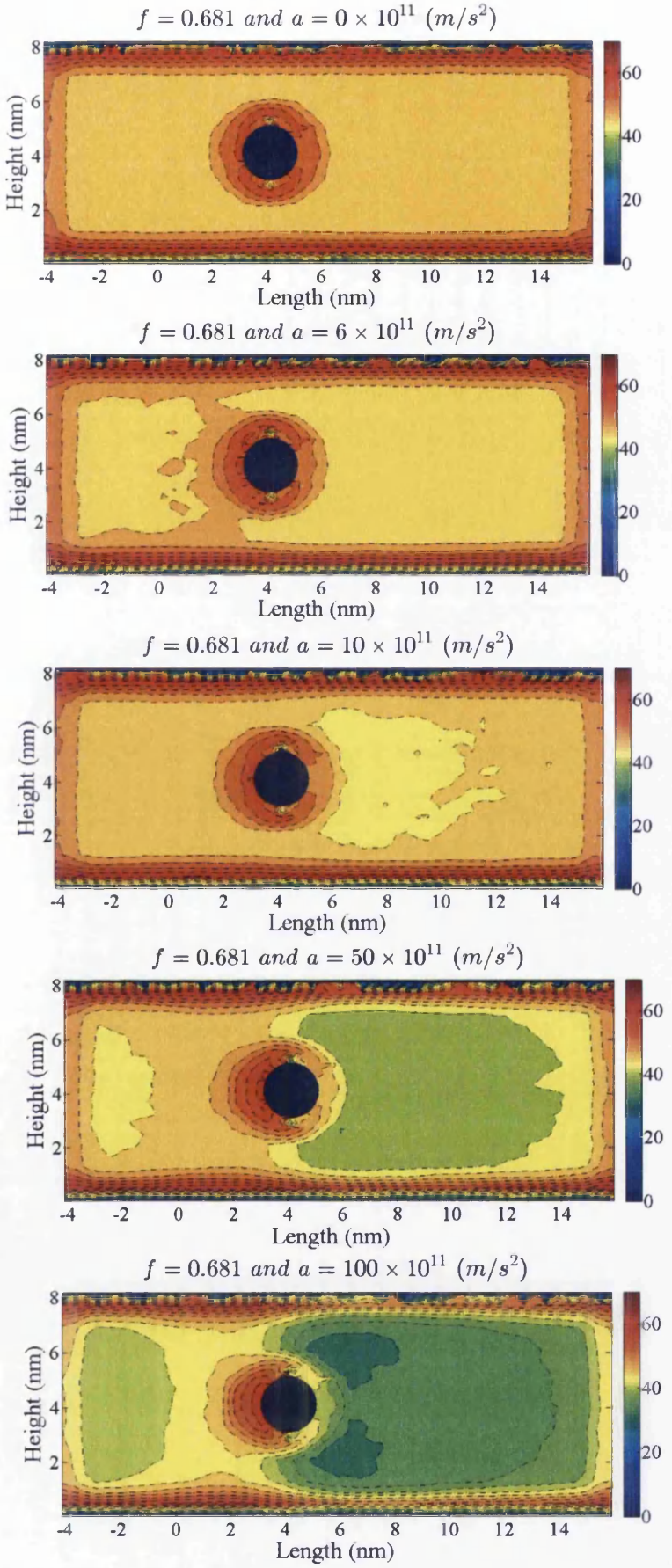

Figure 4.45. Pressure contours for f=0.681 and accelerations 0,6,10,50,100 (m/s^2)

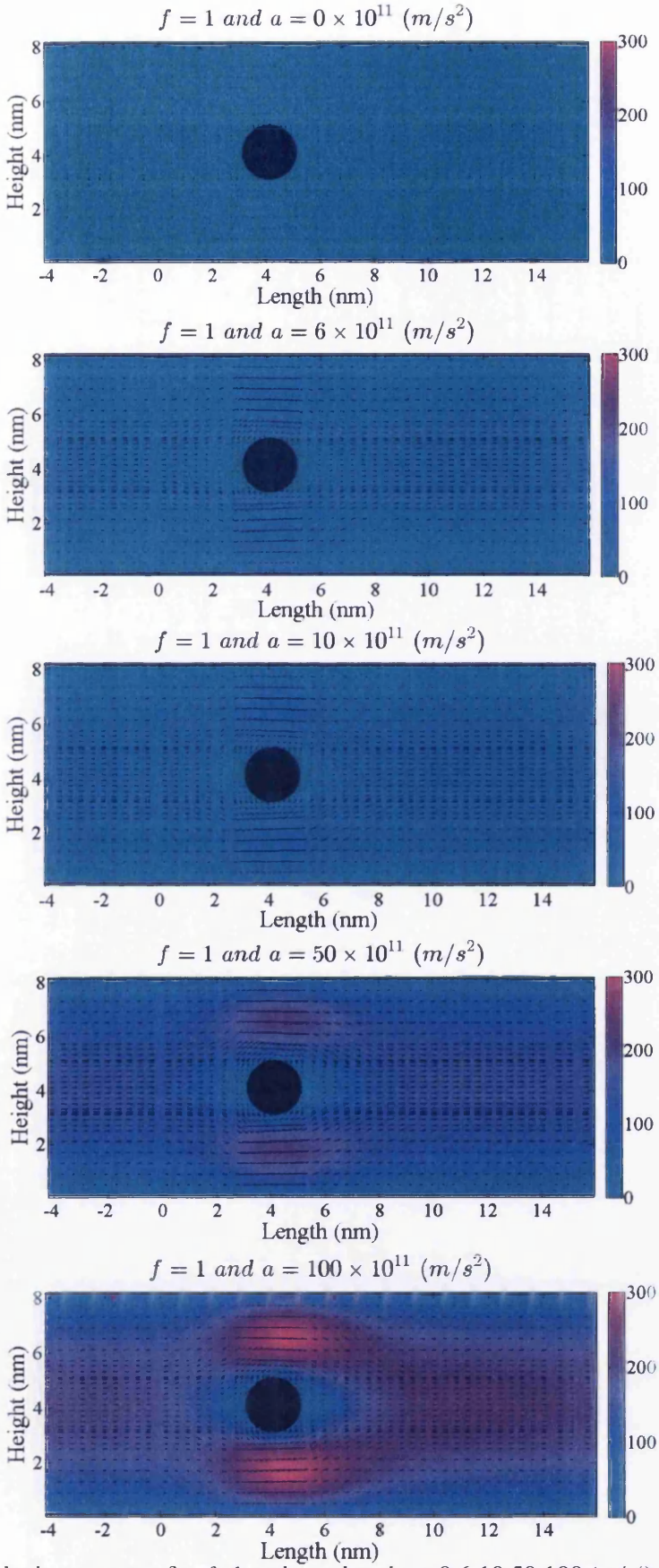

Figure 4.46. Velocity contours for f=1 and accelerations 0,6,10,50,100 (m/s^2)

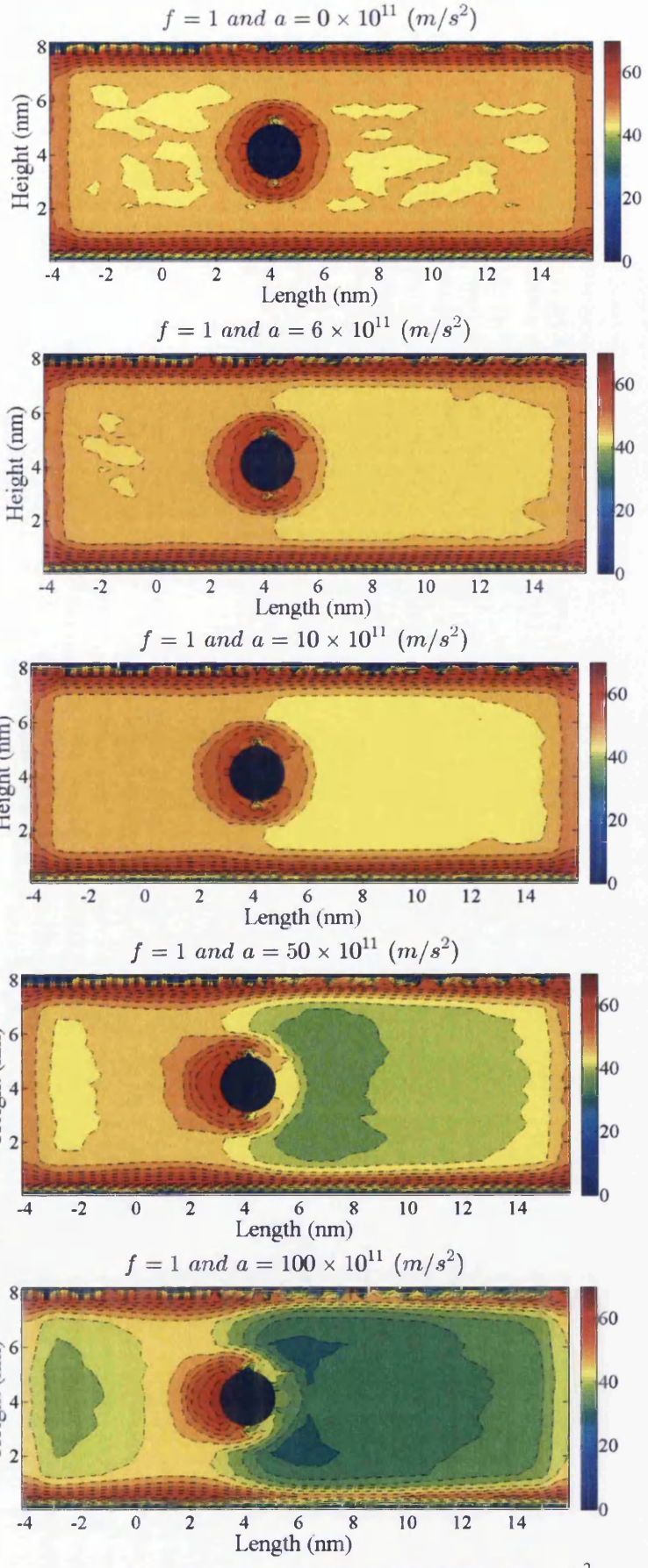

Figure 4.47. Pressure contours for f=1 and accelerations 0,6,10,50,100 (m/s^2)

4.8 Appendix: A4.3

Velocity and pressure contours for flow past a square shaped cylinder for roughness values (0, 0.7, 0.257, 0.45, 0.68 and 1) and acceleration values (0, 6, 10, 50, 100 (m/s^2)).

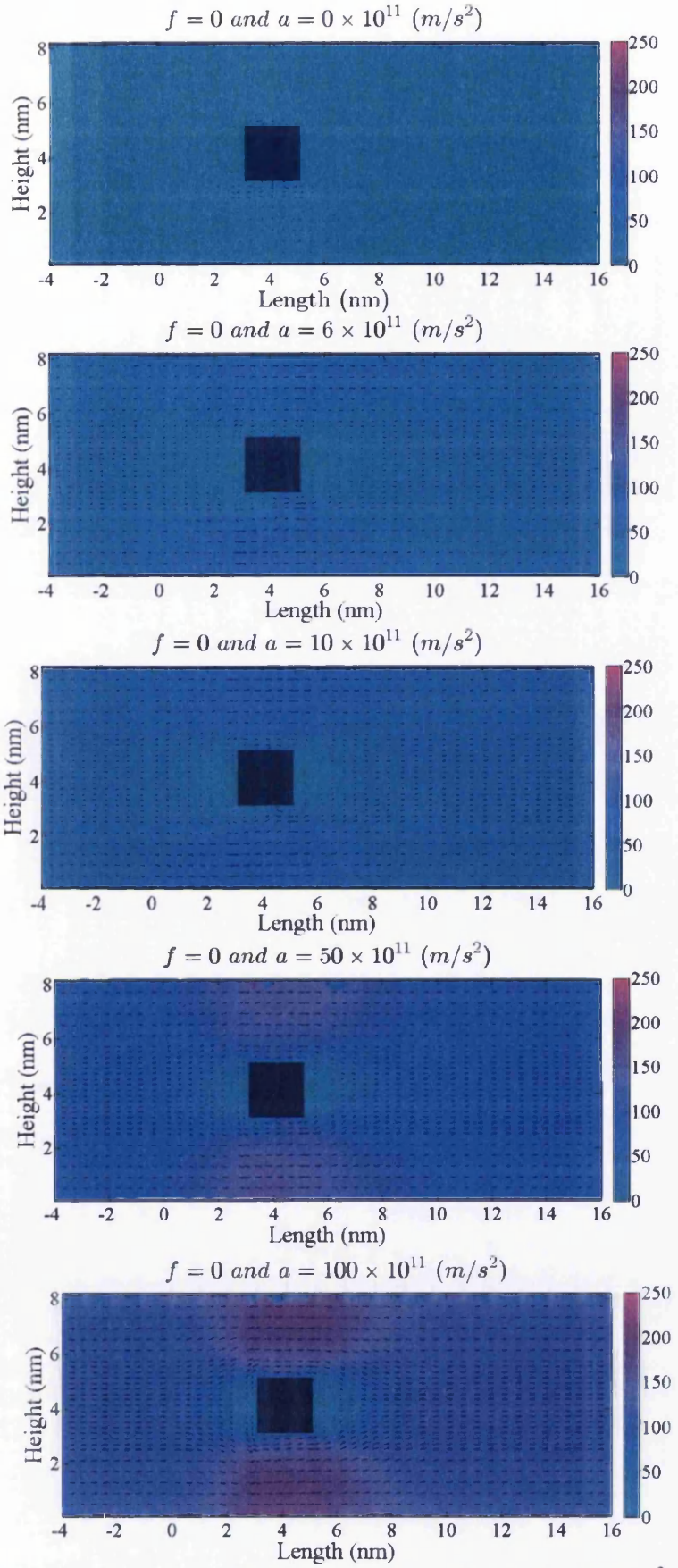

Figure 4.48. Velocity contours for f=0 and accelerations 0,6,10,50,100 (m/s^2)

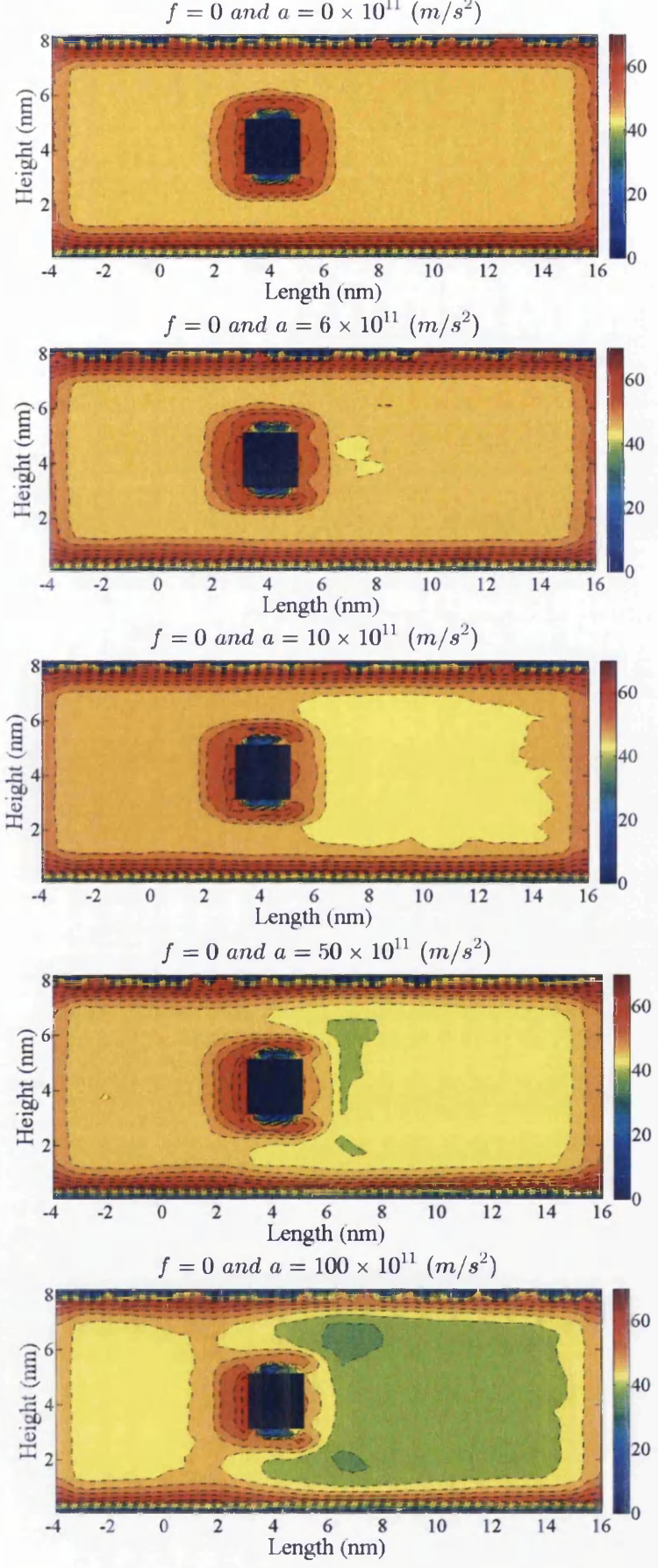

Figure 4.49. Pressure contours for f=0 and accelerations 0,6,10,50,100 (m/s^2)

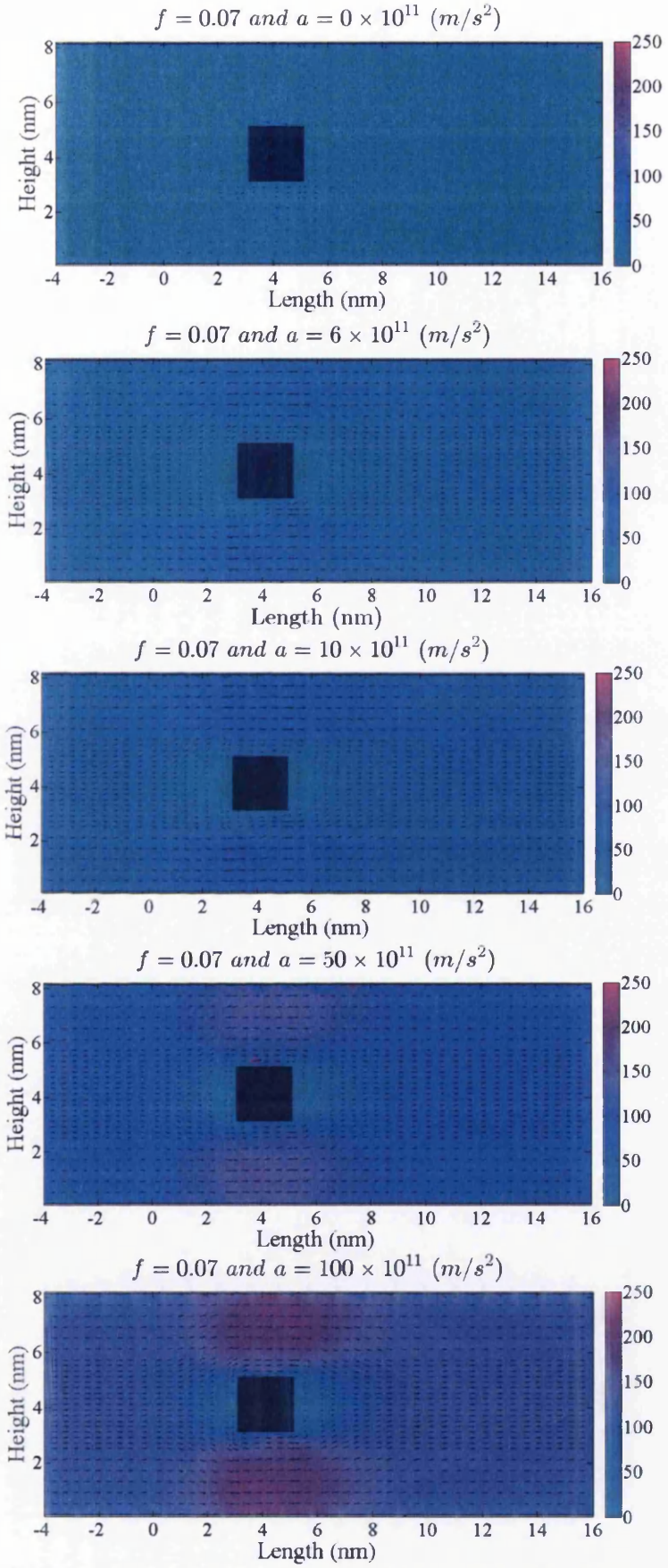

Figure 4.50. Velocity contours for f=0.07 and accelerations 0,6,10,50,100 (m/s^2)

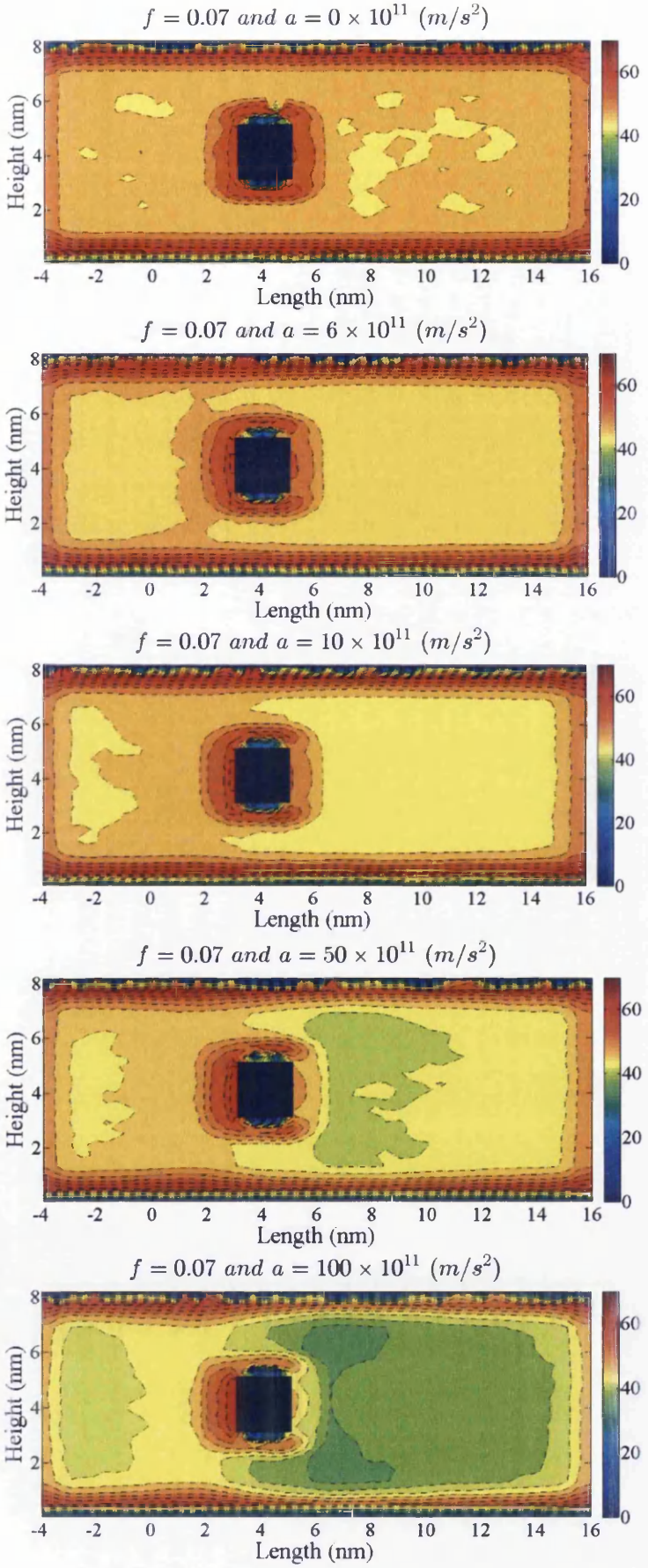

Figure 4.51. Pressure contours for f=0.07 and accelerations 0,6,10,50,100 (m/s^2)

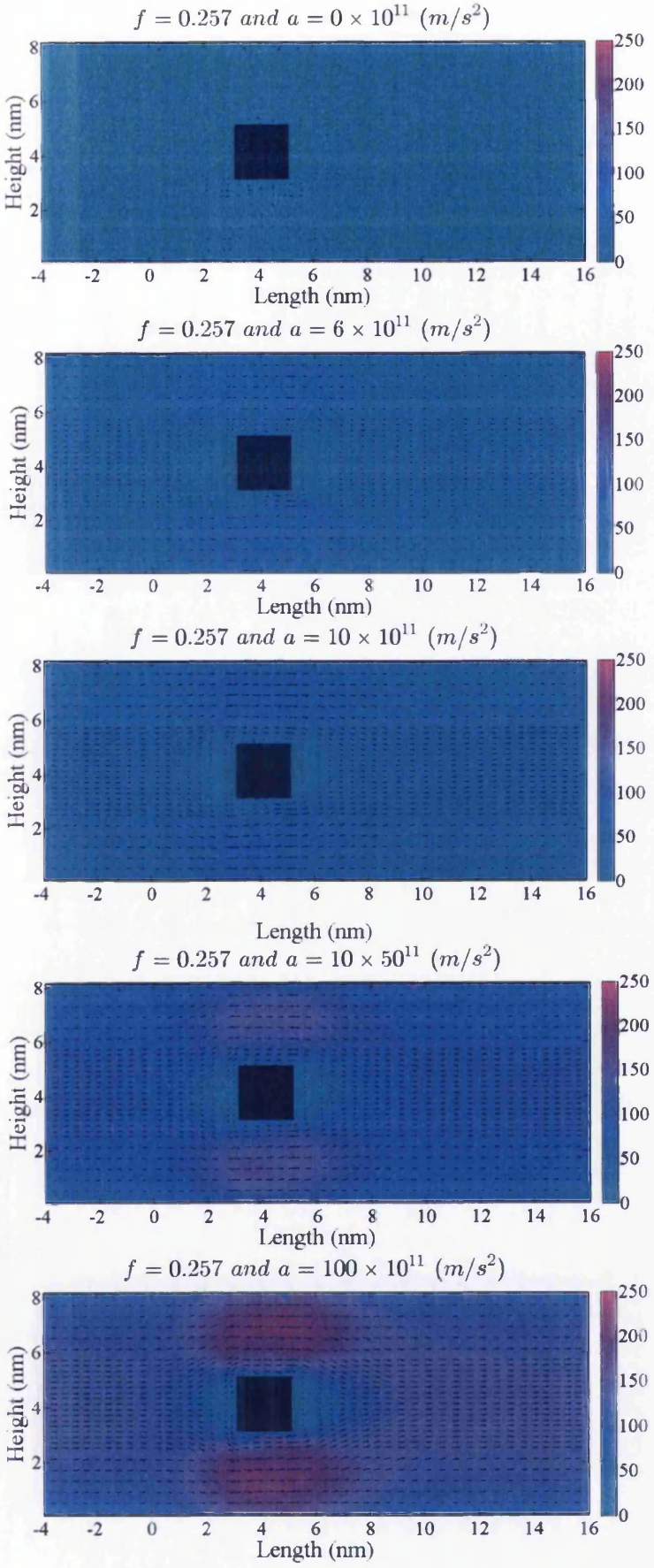

Figure 4.52. Velocity contours for f=0.257 and accelerations 0,6,10,50,100 (m/s^2)

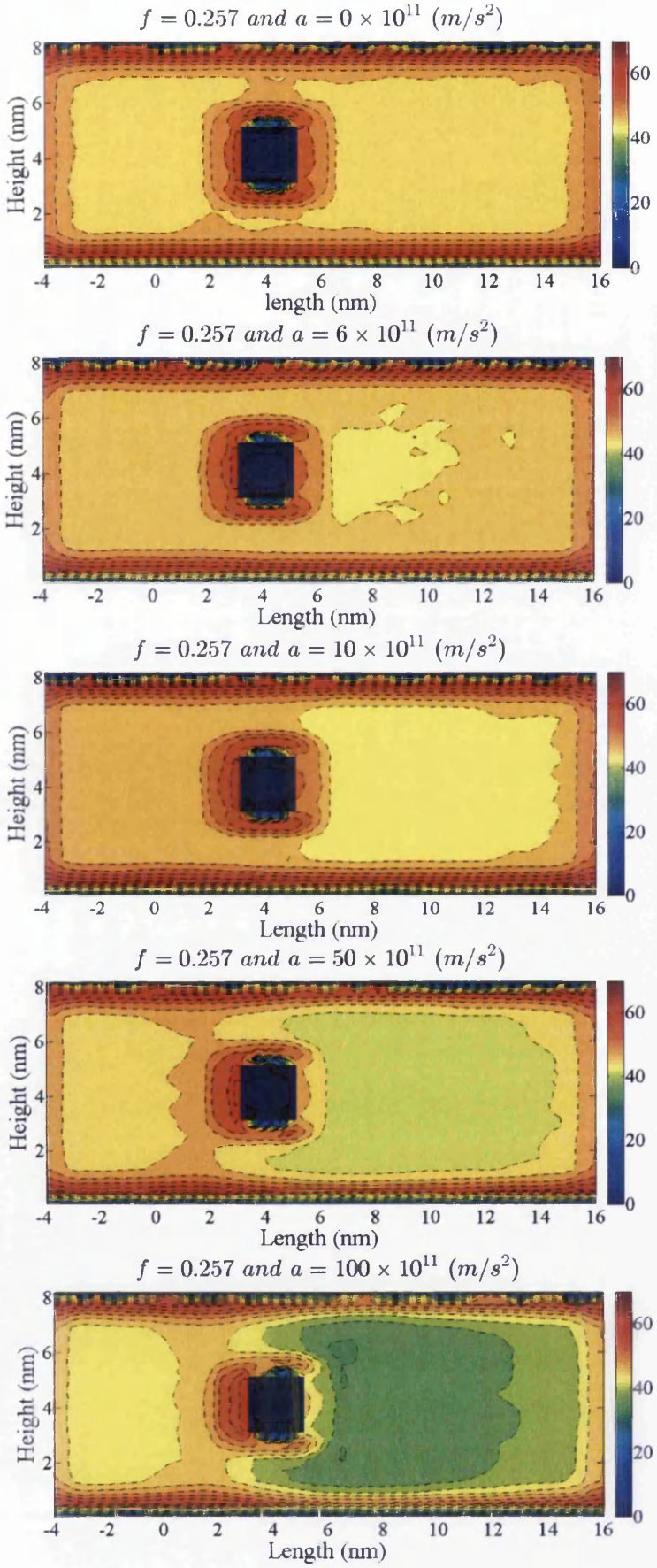

Figure 4.53. Pressure contours for f=0.257 and accelerations 0,6,10,50,100 (m/s^2)

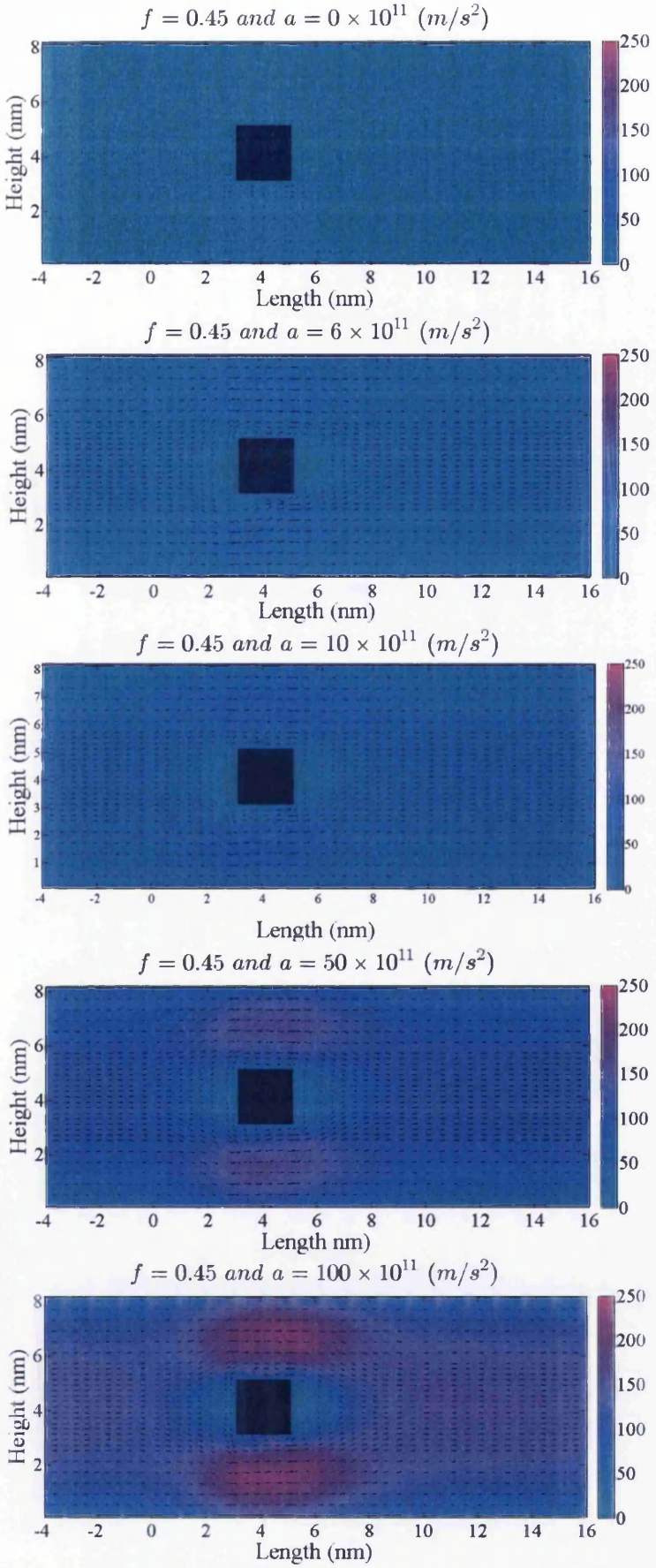

Figure 4.54. Velocity contours for f=0.45 and accelerations 0,6,10,50,100 (m/s^2)

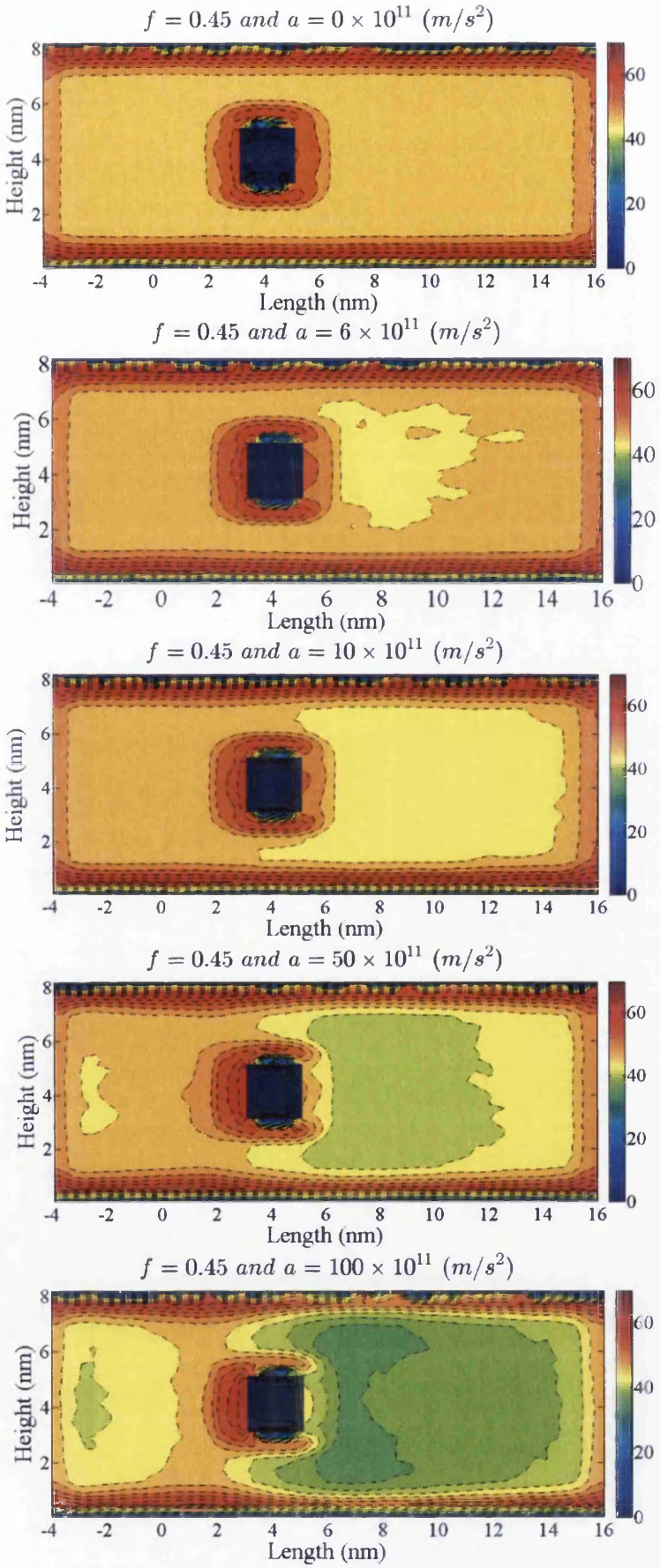

Figure 4.55. Pressure contours for f=0.45 and accelerations 0,6,10,50,100 (m/s^2)

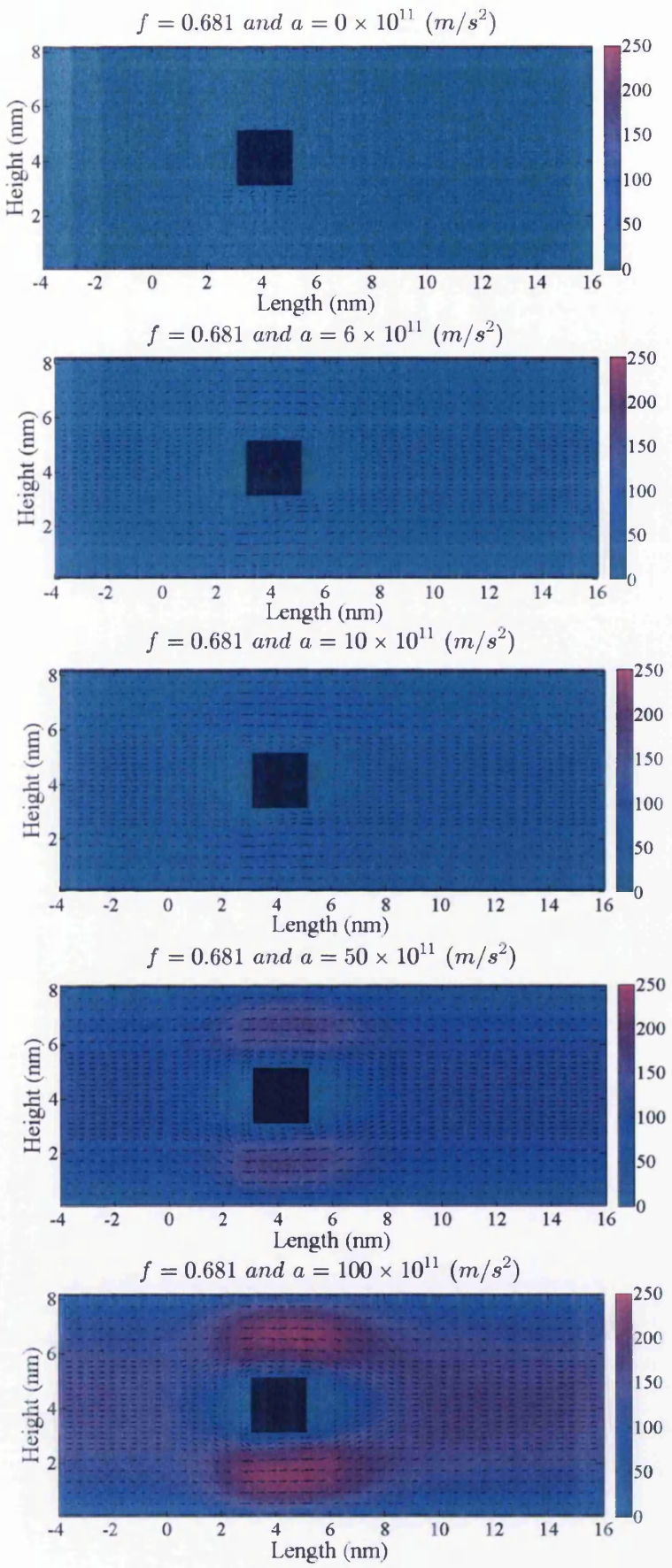

Figure 4.56. Velocity contours for f=0.681 and accelerations 0,6,10,50,100 (m/s^2)

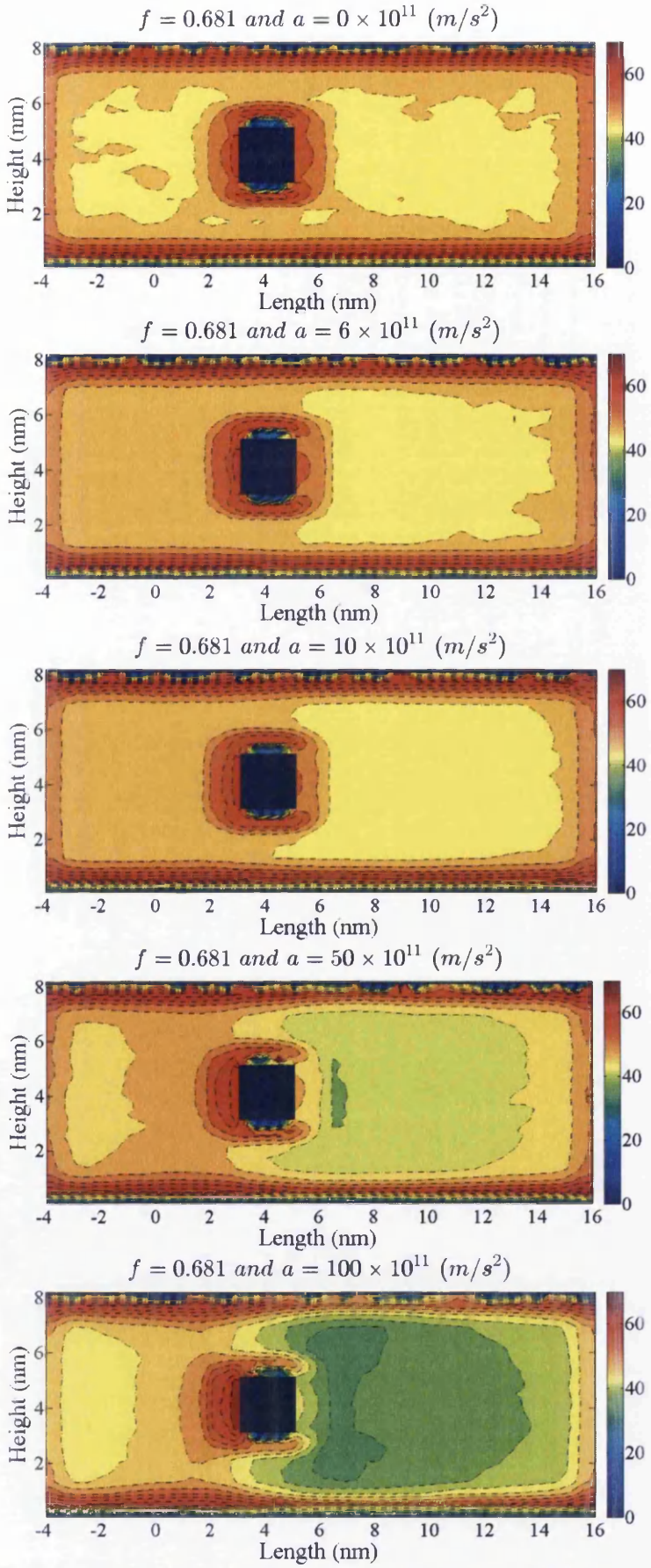

Figure 4.57. Pressure contours for f=0.681 and accelerations 0,6,10,50,100 (m/s^2)

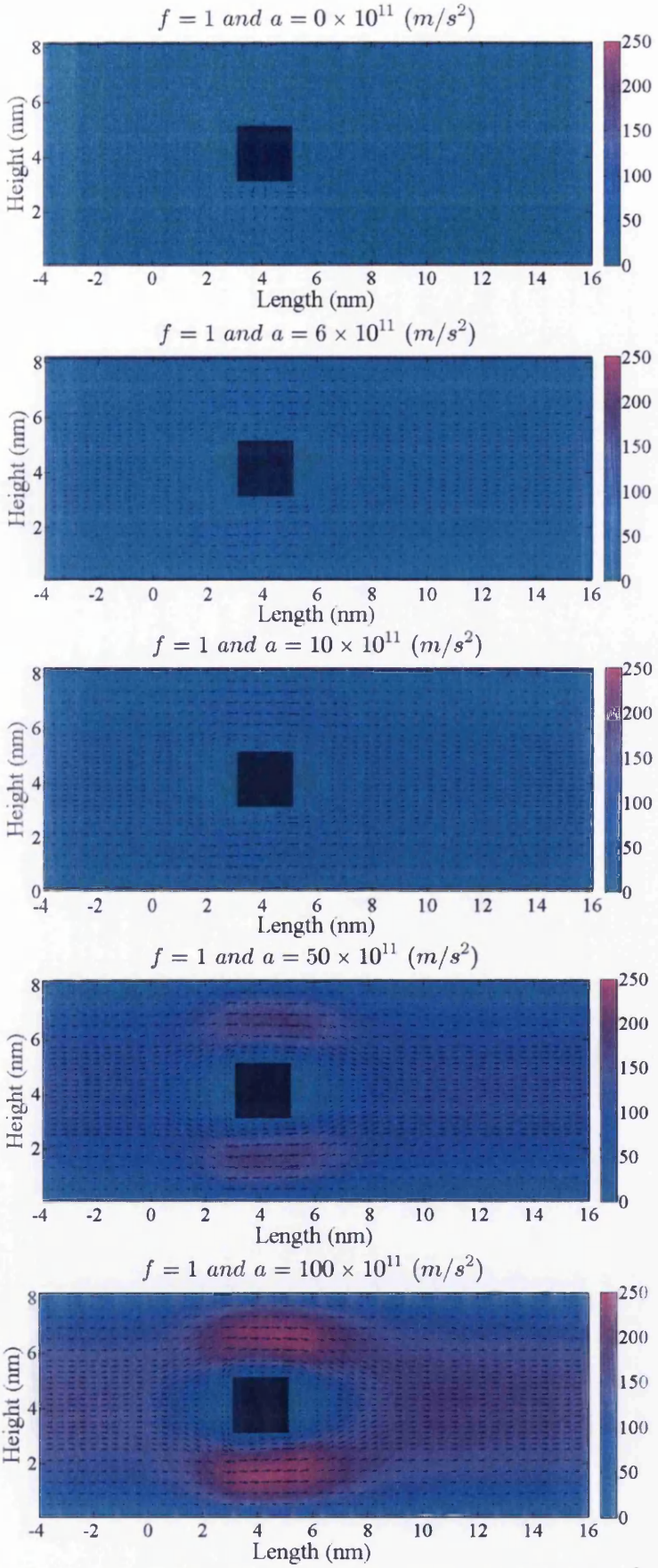

Figure 4.58. Velocity contours for f=1 and accelerations 0,6,10,50,100 (m/s^2)

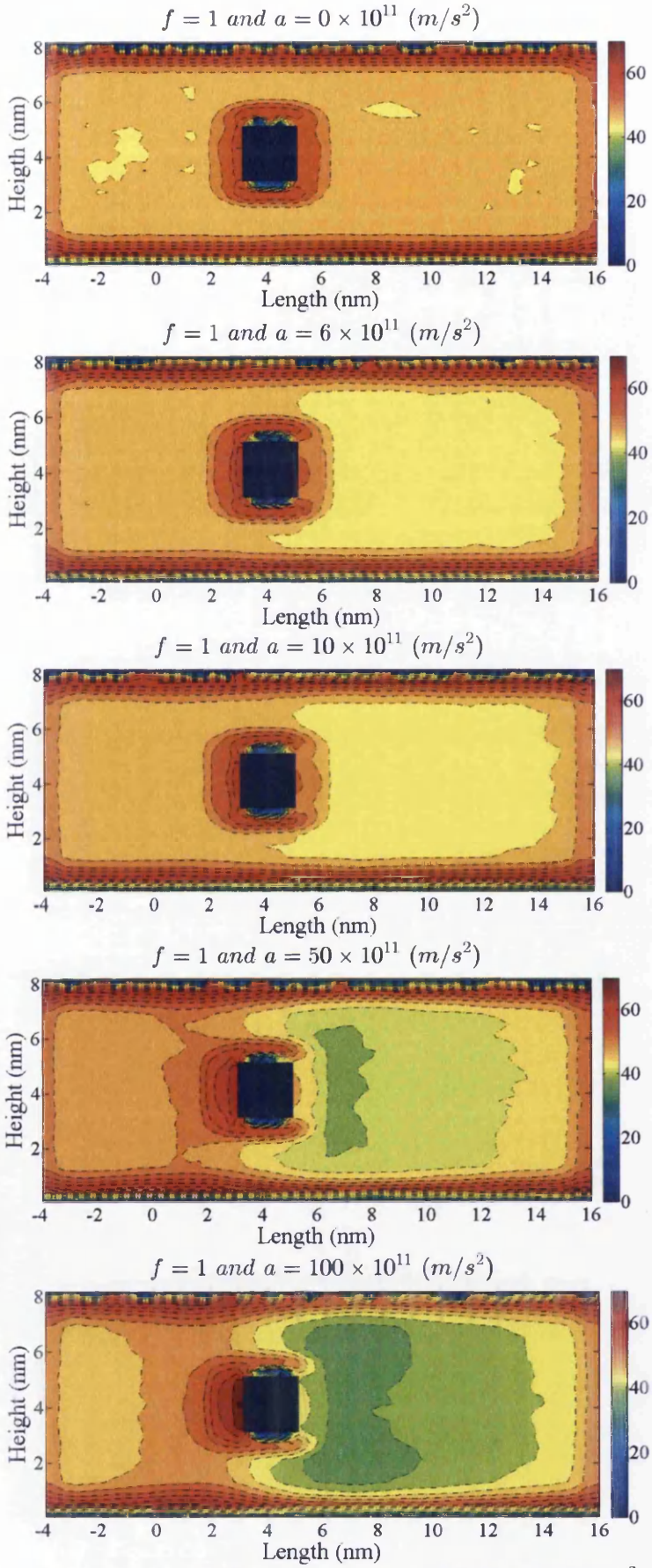

Figure 4.59. Pressure contours for f=1 and accelerations 0,6,10,50,100 (m/s^2)

Chapter 5 Conclusion and Future Work

5.1 Conclusion

The emergence of nano-devices in drug delivery applications and cleaning of nano-surfaces has made the fundamental research on predicting fluid structure interaction at nano-scale justifiable and necessary. The prediction of macroscopic properties at fluid-structure interfaces, such as development of a boundary layer, macroscopic velocity profiles and drag forces during a pressure driven molecular flow, is still an open area of research with research publications providing alternative routes for averaging molecular properties in order to predict macroscopic properties.

The first chapter of this thesis has put the perceived meaning of the nano-scale research into context. Due to the computational limitations, the algorithms have been tested on an 8nm by 20nm channel, however, it is expected that the proposed formulation is useful for modelling interaction of molecular flow around continuum or molecular objects such as circular, squared or diamond shaped nano-cylinders at scales around 100-500nm. The potential applications that may require knowledge of drag forces at nano-scales, and are published in peer reviewed journals, are summarised in Chapter 2. It is observed that the nano-scale research is still at the fundamental stage with most prototypes currently being developed at micron scales. However, it is also noted in Chapter 2 that the requirement of knowledge of drag forces for molecular flows over surfaces at 50-100nm scale is a realistic expectation. Various computational approaches have also been discussed in the same chapter and the molecular dynamics approach was selected as it was desired to be able to predict drag forces for a pressure driven molecular flow from first principles under NVT assumptions. For a given pressure and temperature value, the effect of compressibility factor was studied and a corresponding value of the number density, and molecular specific volume, was assumed.

A soft sphere molecular model has been proposed in Chapter 3 with a modified formulation for defining collision with a wall and the subsequent thermalisation. The collision is defined as per the previous work (Dyson, 2006) when molecules within a cut off region from the wall change the direction in the normal component of velocity. In the proposed model, the molecules that have been collided with the wall maintain the same normal component of the velocity after the collision irrespective

of whether they have been thermalized by the wall or not. If the molecules are thermalized by the wall then the parallel component of velocity is replaced randomly with a corresponding velocity component selected from the Maxwell velocity distribution corresponding to the wall temperature. It was observed that the molecules followed the corresponding Gaussian distribution in each dimension and the resulting three dimensional speed distribution was a Maxwell Boltzmann distribution whether it was a smooth or very rough wall with a low or high acceleration value applied to molecules. This observation increased the confidence in the formulation and the code.

Surface roughness is a macroscopic concept. With recent advances in atomic force microscopy (AFM) techniques, a smooth nano-scale surface measured in Swansea's nano-scale laboratory is shown in Figure 5.1. As mentioned in the literature review of Chapter 3, the attempt to model the roughness by modifying the molecular wall is considered as unrealistic. However, as also commonly used in the literature, an accommodation coefficient is used to model the effect of surface roughness. The Chapter 3 also discusses the guidelines on using accommodation coefficient values.

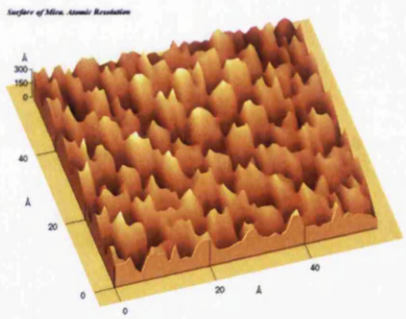

Figure 5.1. Nano-scale surface of mica (smooth surface) at nano-scale. Courtesy: Professor Nidal's research group, Swansea University, UK.

A Moving Least Square (MLS) method is used in this thesis and is extended to two dimensions with a circular cut off for each MLS node to determine macroscopic properties averaged over space and time from the molecular dynamics code. The circular cut off can be further extended to a spherical cut off if the variation in the z direction (i.e. along the breadth of the channel, the width of the channel is the distance between the parallel walls) becomes important. In order to increase computational efficiency , an innovative look up table strategy has been proposed to input experimentally, or computationally determined, wall forces to a computational

model based on an equivalent continuum wall. The proposed formulation has been tested on both molecular and equivalent continuum walls. It was observed that macroscopic velocity profiles are less sensitive to the molecular or continuum wall assumptions. However, as shown in Chapter 4, the pressure values around the wall are highly dependent and sensitive to the continuum or molecular wall assumption. The drag coefficient values for flows around cylinders were similar to each other irrespective of the choice of the wall.

The proposed formulation has been verified in the following way:

(i) Comparison of results with those obtained by using molecular walls (Chapter 3);

(ii) Observations of parabolic velocity distributions for confined flows within parallel plates and its dependence on the surface roughness value (Chapter 3);

(iii) Comparing instantaneous velocity distributions with corresponding Gaussian distributions (Chapters 3 and 4);

(iv) Observation of the development of a linear temperature gradient with correspondingly lower and higher wall temperatures for slit pore walls (Chapter 3); and

(v) For a special case with no walls and a zero applied acceleration value, prediction of the same pressure value that was used in calculating the molecular specific volume at a given temperature (Chapter 4).

The dependence of geometry (stepped, inclined and slit pore geometry for Chapter 3 and square, circular and diamond shaped cylinders placed within a slit pore geometry for Chapter 4), temperature, surface roughness values (accommodation coefficient), and molecular acceleration applied has been discussed in detail and the results (variation of velocity contours, total average velocity values, pressure contours and drag coefficient values) commented upon. The Chapter 4 also attempts to show the drag coefficient results with reference to the Reynolds number variation and highlights the difference in values predicted via the molecular route with reference to an analytical solution based on continuum assumptions.

5.2 Future Work

The proposed work has successfully extended the previous work (Dyson, 2006) in a robust way, to be able to calculate the drag and lift coefficients on bodies resulting from molecular flows. The work has opened new opportunities for research in order to make further advances in the research on nano-scale drug delivery and other applications as outlined in Chapter 2. Some of the research opportunities that have generated from this research or are beneficial for this research direction are summarised below:

- Need for an advancement in experimental research to measure pressure values (and/or drag/lift forces) on bodies at 50-100nm scale under various conditions simulated in this research.
- Extension of the proposed formulation to non-periodic boundary conditions. Different formulations with reference to thermostats for the conservation of energy and momentum.
- Extension of the formulation for 3D geometries (Figure 5.2b). The existing slit pore geometries are assumed as 2.5 D (Figure 5.2a) as there is no change in the z direction.

Figure 5.2. (a) 2.5 D representation of a square shaped cylinder with infinite length is placed between parallel walls. (b) in a corresponding 3D representation, the cylinder length is small and contained within the control volume e.g. a cube as shown.

- Potential coupling of this formulation with Dissipative Particle Dynamics (DPD) methods so that the molecular scale information can be scaled up to the micron scale.

- The possibility of embedding the proposed formulation in the large scale and highly parallelised open source codes such as LAMMPS[1] or DL_POLY/DL_MESO[2] in order to extend of the formulation for a fluid mixture with more than one fluid particles or simulation of nano-scale (up to 100 nm) particles suspended in a fluid medium and model its interaction with a wall.

[1] http://lammps.sandia.gov

[2] http://www.stfc.ac.uk/cse/25526.aspx

References

LAMMPS Molecular Dynamics Simulator [Online]. LAMMPS Available: http://lammps.sandia.gov [Accessed 11/03 2014].

Tiny, implantable medical device can propel itself through bloodstream [Online]. Available: https://engineering.stanford.edu/news/implantable-wirelessly-powered-self-propelled-medical-device [Accessed 20/02 2014].

ADISA, O. O. 2012. *Modelling gas storage in molecular nanosystems.* The University of Adelaide.

AHMADI, G. & GUO, S. 2007. Bumpy Particle Adhesion and Removal in Turbulent Flows Including Electrostatic and Capillary Forces. *The Journal of Adhesion,* 83, 289-311.

ALDER, B. J. & WAINWRIGHT, T. E. 1957. Phase Transition for a Hard Sphere System. *The Journal of Chemical Physics,* 27, 1208-1209.

ARRUEBO, M., FERNÁNDEZ-PACHECO, R., IBARRA, M. R. & SANTAMARÍA, J. 2007. Magnetic nanoparticles for drug delivery. *Nano Today,* 2, 22-32.

ARYA, G., CHANG, H.-C. & MAGINN, E. J. 2003. Molecular Simulations of Knudsen Wall-slip: Effect of Wall Morphology. *Molecular Simulation,* 29, 697-709.

BAO, G. 2009. Protein Mechanics: A New Frontier in Biomechanics. *Exp Mech,* 49, 153-164.

BAO, G., KAMM, R. D., THOMAS, W., HWANG, W., FLETCHER, D. A., GRODZINSKY, A. J., ZHU, C. & MOFRAD, M. R. 2010. Molecular Biomechanics: The Molecular Basis of How Forces Regulate Cellular Function. *Mol Cell Biomech,* 3, 91-105.

BARISIK, M. & BESKOK, A. 2011. Equilibrium molecular dynamics studies on nanoscale-confined fluids. *Microfluidics and Nanofluidics,* 11, 269-282.

BASAGAOGLU, H. & SUCCI, S. 2010. Lattice-Boltzmann simulations of repulsive particle-particle and particle-wall interactions: coughing and choking. *J Chem Phys,* 132, 3374685.

BAWA, R. 2008. Nanoparticle-based Therapeutics in Humans: A Survey. *Nanotechnology Law & Business,* 5, 135-155.

BEAN, A. J. 2006. *Protein Trafficking in Neurons*, Elsevier Science.

BERG, H. C. 2004. *E. coli in Motion*, Springer-Verlag New York.

BHUSHAN, B. 2007. Nanotribology and nanomechanics of MEMS/NEMS and BioMEMS/BioNEMS materials and devices. *Microelectronic Engineering,* 84, 387-412.

BOWLING, R. A. 1985. An Analysis of Particle Adhesion on Semiconductor Surfaces. *Journal of The Electrochemical Society,* 132, 2208-2214.

BROWER-TOLAND, B. D., SMITH, C. L., YEH, R. C., LIS, J. T., PETERSON, C. L. & WANG, M. D. 2002. Mechanical disruption of individual nucleosomes reveals a reversible multistage release of DNA. *Proc Natl Acad Sci U S A,* 99, 1960-5.

BUSNAINA, A. A. & ELSAWY, T. 2000. The Effect of Relative Humidity on Particle Adhesion and Removal. *The Journal of Adhesion,* 74, 391-409.

BUSNAINA, A. A. & HONG, L. Year. Physical removal of nano-scale defects from surfaces. *In:* Advanced Semiconductor Manufacturing 2002 IEEE/SEMI Conference and Workshop, 2002 2002. 272-277.

DOBSON, J. 2006. Magnetic micro- and nano-particle-based targeting for drug and gene delivery. *Nanomedicine,* 1, 31-7.

DOYLE, P. & UNDERHILL, P. 2005. Brownian Dynamics Simulations of Polymers and Soft Matter. *In:* YIP, S. (ed.) *Handbook of Materials Modeling.* Springer Netherlands.

DUTTA, A. 2009. *MULTICOMPONENT GAS DIFFUSION AND ADSORPTION IN COALS FOR ENHANCED METHANE RECOVERY.* MSc, STANFORD UNIVERSITY.

DYSON, P. 2006. *Numerical Computation of Fluid Properties at Nano/Meso Scales.* PhD, University of Wales, Swansea.

DYSON, P., RANSING, R., WILLIAMS, P. & WILLIAMS, P. 2008. *Fluid Properties at Nano-meso Scale: A Numerical Treatment.*

EDBERG, R., EVANS, D. J. & MORRISS, G. P. 1986. Constrained molecular dynamics: Simulations of liquid alkanes with a new algorithm. *The Journal of Chemical Physics,* 84, 6933-6939.

ERIC LAUGA, M. P. B. A. H. A. S. 2005. Microfluidics: The No-Slip Boundary Condition.

ERMAK, D. L. & MCCAMMON, J. A. 1978. Brownian dynamics with hydrodynamic interactions. *The Journal of Chemical Physics,* 69, 1352-1360.

EVANS, D. J., HOOVER, W. G., FAILOR, B. H., MORAN, B. & LADD, A. J. C. 1983. Nonequilibrium molecular dynamics via Gauss's principle of least constraint. *Physical Review A,* 28, 1016-1021.

FAN, X.-J., PHAN-THIEN, N., YONG, N. T. & DIAO, X. 2002. Molecular dynamics simulation of a liquid in a complex nano channel flow. *Physics of Fluids (1994-present),* 14, 1146-1153.

FANUN, M. 2010. *Colloids in Drug Delivery*, Taylor and Francis Group, LLC.

FRENKEL, D. & SMIT, B. 2001. *Understanding Molecular Simulation: From Algorithms to Applications*, Elsevier Science.

GALE, G. W. & BUSNAINA, A. A. 1999. ROLES OF CAVITATION AND ACOUSTIC STREAMING IN MEGASONIC CLEANING. *Particulate Science and Technology,* 17, 229-238.

GIJS, M. M. 2004. Magnetic bead handling on-chip: new opportunities for analytical applications. *Microfluidics and Nanofluidics,* 1, 22-40.

GODDARD, W. A., BRENNER, D., LYSHEVSKI, S. E. & IAFRATE, G. J. 2007. *Handbook of Nanoscience, Engineering, and Technology, Second Edition*, Taylor & Francis.

GRONEBERG, D. A., RABE, K. F. & FISCHER, A. 2006. Novel concepts of neuropeptide-based drug therapy: Vasoactive intestinal polypeptide and its receptors. *European Journal of Pharmacology,* 533, 182-194.

GROOT, R. D. & WARREN, P. B. 1997. Dissipative particle dynamics: Bridging the gap between atomistic and mesoscopic simulation. *The Journal of Chemical Physics,* 107, 4423-4435.

GUPTA, R. B. & KOMPELLA, U. B. 2006. *Nanoparticle Technology for Drug Delivery*, Taylor & Francis.

HANASAKI, I., NAKATANI, A. & KITAGAWA, H. 2003. Molecular dynamics study of Ar flow and He flow inside carbon nanotube junction as a molecular nozzle and diffuser *Science and Technology of Advanced Materials,* 5, 107-113.

HARTKAMP, R., GHOSH, A., WEINHART, T. & LUDING, S. 2012. A study of the anisotropy of stress in a fluid confined in a nanochannel. *J Chem Phys,* 137, 4737927.

HESS, H. & VOGEL, V. 2001. Molecular shuttles based on motor proteins: active transport in synthetic environments. *J Biotechnol,* 82, 67-85.

HILBERS, P. A. J., NEDEA, S. V., MARKVOORT, A. J., TEN EIKELDER, H. M. M. & SPIJKER, P. 2008. Implicit particle wall boundary condition in molecular dynamics. *Proceedings of the Institution of Mechanical Engineers, Part C: Journal of Mechanical Engineering Science,* 222, 855-864.

HOWARD, J. 2001. *Mechanics of Motor Proteins and the Cytoskeleton*, Sinauer Associates, Incorporated.

HUANG, C., CHOI, P. Y., NANDAKUMAR, K. & KOSTIUK, L. W. 2008. Investigation of entrance and exit effects on liquid transport through a cylindrical nanopore. *Phys Chem Chem Phys,* 10, 186-92.

HUANG, Y., GUO, D., LU, X. & LUO, J. 2011. Mechanisms for nano particle removal in brush scrubber cleaning. *Applied Surface Science,* 257, 3055-3062.

IRVING, J. H. & KIRKWOOD, J. G. 1950. The Statistical Mechanical Theory of Transport Processes. IV. The Equations of Hydrodynamics. *The Journal of Chemical Physics,* 18, 817-829.

IVANCEVIC, V. G. & IVANCEVIC, T. T. 2006. *Unified Modelling Approach to Physics, Control, Biomechanics, Neurodynamics and Psycho-Socio-Economical Dynamics*, Springer.

JABBARZADEH, A. 2010. Molecular Dynamics Simulations of Flow over a Nano-cylinder in a Rectangular Nano-channel *NANOTECH,* 2, 733-736

JABBARZADEH, A. & TANNER, R. I. 2006. Molecular dynamics simulation and its application to nano-rheology. *The British Society of Rheology*, 165 - 216.

KAMALI, R. & KHARAZMI, A. 2011. Molecular dynamics simulation of surface roughness effects on nanoscale flows. *International Journal of Thermal Sciences,* 50, 226-232.

KARNIADAKIS, G., BESKOK, A. & ALURU, N. 2005. *Microflows and Nanoflows: Fundamentals and Simulation*, Springer.

KASITEROPOULOU, D., KARAKASIDIS, T. E. & LIAKOPOULOS, A. 2011. Dissipative Particle Dynamics investigation of parameters affecting planar nanochannel flows. *Materials Science and Engineering: B,* 176, 1574-1579.

KASITEROPOULOU, D., KARAKASIDIS, T. E. & LIAKOPOULOS, A. 2012. A dissipative particle dynamics study of flow in periodically grooved nanochannels. *International Journal for Numerical Methods in Fluids,* 68, 1156-1172.

KEAVENY, E. E., PIVKIN, I. V., MAXEY, M. & EM KARNIADAKIS, G. 2005. A comparative study between dissipative particle dynamics and molecular dynamics for simple- and complex-geometry flows. *J Chem Phys,* 123, 104107.

KIM, T. H., BUSNAINA, A., PARK, J.-G. & KIM, D. 2012. Nanoscale Particle Removal Using Wet Laser Shockwave Cleaning. *Journal of Solid State Science and Technology,* 1, 70-77.

KINGSLEY, J. D., DOU, H., MOREHEAD, J., RABINOW, B., GENDELMAN, H. E. & DESTACHE, C. J. 2006. Nanotechnology: a focus on nanoparticles as a drug delivery system. *J Neuroimmune Pharmacol,* 1, 340-50.

KIPP, J. E. 2004. The role of solid nanoparticle technology in the parenteral delivery of poorly water-soluble drugs. *International Journal of Pharmaceutics,* 284, 109-122.

KOELMAN, J. M. V. A. & HOOGERBRUGGE, P. J. 1993. Dynamic Simulations of Hard-Sphere Suspensions Under Steady Shear. *EPL (Europhysics Letters),* 21, 363.

KOLAHI, K. S. & MOFRAD, M. R. 2008. Molecular mechanics of filamin's rod domain. *Biophys J,* 94, 1075-83.

KRUPP, H. 1967. *Particle Adhesion: Theory and Experiment*, Advan. Colloid Interface Sci. 1 (1967), 111-239.

LAGREE, P. Y. 2013. *Small Re flows* [Online]. Paris: Institut Jean Le Rond Alembert, . Available: http://www.lmm.jussieu.fr/~lagree/COURS/M2MHP/petitRe.pdf [Accessed].

LARSON, R. G. 2005. The rheology of dilute solutions of flexible polymers: Progress and problems. *Journal of Rheology (1978-present),* 49, 1-70.

LEES, A. W. & EDWARDS, S. F. 1972. The computer study of transport processes under extreme conditions. *Journal of Physics C: Solid State Physics,* 5, 1921.

LEY, B. 1999. *Diameter of a Human Hair* [Online]. Available: http://www.webcitation.org/mainframe.php [Accessed 20/02 2014].

LI, A. & AHMADI, G. 1992. Dispersion and Deposition of Spherical Particles from Point Sources in a Turbulent Channel Flow. *Aerosol Science and Technology,* 16, 209-226.

LI, Y., XU, J. & LI, D. 2010. Molecular dynamics simulation of nanoscale liquid flows. *Microfluidics and Nanofluidics,* 9, 1011-1031.

LIANG, Y., HILAL, N., LANGSTON, P. & STAROV, V. 2007. Advances in colloid and Interface Science 151-157.

LION, T. W. & ALLEN, R. J. 2012. Computing the local pressure in molecular dynamics simulations. *J Phys Condens Matter,* 24, 0953-8984.

LIPKOWITZ, K. B. 2010. *Reviews in Computational Chemistry*, Wiley.

LOEB, L. B. 2004. *The Kinetic Theory of Gases,* New York, Corier Dover Publications.

LOPEZ, R. 2007. *Blood Rheology Using a Brownian Dynamics Simulation of Bead Spring Ring with a Constant Area*, University of Illinois at Chicago.

MANDELKERN, M., ELIAS, J. G., EDEN, D. & CROTHERS, D. M. 1981. The dimensions of DNA in solution. *Journal of Molecular Biology,* 152, 153-161.

MARTEL, S., MATHIEU, J. B., FELFOUL, O., CHANU, A., ABOUSSOUAN, E., TAMAZ, S., POUPONNEAU, P., YAHIA, L., BEAUDOIN, G., SOULEZ, G. & MANKIEWICZ, M. 2008. A computer-assisted protocol for endovascular target interventions using a clinical MRI system for controlling untethered microdevices and future nanorobots. *Comput Aided Surg,* 13, 340-52.

MATHIEU, J. B. & MARTEL, S. 2007. Magnetic microparticle steering within the constraints of an MRI system: proof of concept of a novel targeting approach. *Biomed Microdevices,* 9, 801-8.

MAXWELL, J. C. 1878. On Stresses in Rarefied Gases Arising from Inequalities of Temperature. *Proceedings of the Royal Society of London,* 27, 304-308.

MERTENS, P. W. & PARTON, E. 2002. Sub-100 nm technologies drive single wafer cleaning. *Solid State Technology,* 45.

MICKEL, W., JOLY, L. & BIBEN, T. 2011. Transport, phase transitions, and wetting in micro/nanochannels: A phase field/DDFT approach. *The Journal of Chemical Physics,* 134, 094105.

MISRA, R. D. K. 2008. Magnetic nanoparticle carrier for targeted drug delivery: perspective, outlook and design. *Materials Science and Technology,* 24, 1011-1019.

NAGAYAMA, G. & CHENG, P. 2004. Effects of interface wettability on microscale flow by molecular dynamics simulation. *International Journal of Heat and Mass Transfer,* 47, 501-513.

OULD-OUALI, L., NOPPE, M., LANGLOIS, X., WILLEMS, B., TE RIELE, P., TIMMERMAN, P., BREWSTER, M. E., ARIËN, A. & PRÉAT, V. 2005. Self-assembling PEG-p(CL-co-TMC) copolymers for oral delivery of poorly water-soluble drugs: a case study with risperidone. *Journal of Controlled Release,* 102, 657-668.

PAN, W. 2010. *Single Particle DPD: Algorithms and Applications.* PhD, Brown University.

PODCZECK, F., NEWTON, J. M. & JAMES, M. B. 1997. Variations in the adhesion force between a drug and carrier particles as a result of changes in the relative humidity of the air. *International Journal of Pharmaceutics,* 149, 151-160.

PURCELL, E. M. 1977. Life at Low Reynolds Number. *American Journal of Physics,* 45, 3-11.

QUESNEL, D. J., RIMAI, R. S. & SHARPE, L. H. 2002. *Particle Adhesion: Applications and Advances*, Taylor & Francis.

RAHMAN, A. 1964. Correlations in the Motion of Atoms in Liquid Argon. *Physical Review,* 136, A405-A411.

ROTHMAN, D. H. & ZALESKI, S. 1997. *Lattice-Gas Cellular Automata: Simple Models of Complex Hydrodynamics*, Cambridge University Press.

SANTANGELO, P., NITIN, N. & BAO, G. 2006. Nanostructured probes for RNA detection in living cells. *Ann Biomed Eng,* 34, 39-50.

SATOH, A. 2010. *Introduction to Practice of Molecular Simulation: Molecular Dynamics, Monte Carlo, Brownian Dynamics, Lattice Boltzmann and Dissipative Particle Dynamics*, Elsevier Science.

SCHAAF, S. A. & CHAMBRE, P. L. 1961. *Flow of Rarefied Gases*, Princeton University Press.

SIPERSTEIN, F., MYERS, A. L. & TALU, O. 2002. Long range corrections for computer simulations of adsorption. *Molecular Physics,* 100, 2025-2030.

SIRK, T. 2006. *Numerical Simulation of Nanoscale Flow: A Molecular Dynamics Study of Drag.* MSc.

SOFOS, F., KARAKASIDIS, T. & LIAKOPOULOS, A. 2012. Surface wettability effects on flow in rough wall nanochannels. *Microfluidics and Nanofluidics,* 12, 25-31.

SOFOS, F., KARAKASIDIS, T. E. & LIAKOPOULOS, A. 2010. Effect of wall roughness on shear viscosity and diffusion in nanochannels. *International Journal of Heat and Mass Transfer,* 53, 3839-3846.

SOKHAN, V. P., NICHOLSON, D. & QUIRKE, N. 2001. Fluid flow in nanopores: An examination of hydrodynamic boundary conditions. *The Journal of Chemical Physics,* 115, 3878-3887.

SQUIRES, T. M. & QUAKE, S. R. 2005. Microfluidics: Fluid physics at the nanoliter scale. *Reviews of Modern Physics,* 77, 977-1026.

STILLINGER, F. H. & RAHMAN, A. 1974. Improved simulation of liquid water by molecular dynamics. *The Journal of Chemical Physics,* 60, 1545-1557.

SUCCI, S. 2001. *The Lattice Boltzmann Equation: For Fluid Dynamics and Beyond*, Clarendon Press.

SUN, J., HE, Y., TAO, W., YIN, X. & WANG, H. 2012. Roughness effect on flow and thermal boundaries in microchannel/nanochannel flow using molecular dynamics-continuum hybrid simulation. *International Journal for Numerical Methods in Engineering,* 89, 2-19.

SURI, S. S., FENNIRI, H. & SINGH, B. 2007. Nanotechnology-based drug delivery systems. *J Occup Med Toxicol,* 2, 16.

TAN, J., SHAH, S., THOMAS, A., OU-YANG, H. D. & LIU, Y. 2013. The influence of size, shape and vessel geometry on nanoparticle distribution. *Microfluid Nanofluidics,* 14, 77-87.

TATA-MOTORS. *Tata Nano* [Online]. Available: http://www.tatanano.com/technical-specifications.html [Accessed 20/02 2014].

TO, Q. D., PHAM, T. T., LAURIAT, G. & LÉONARD, C. 2012. Molecular Dynamics Simulations of Pressure-Driven Flows and Comparison with Acceleration-Driven Flows. *Advances in Mechanical Engineering,* 2012, 1-10.

TOGHRAIE SEMIROMI, D. & AZIMIAN, A. R. 2010. Nanoscale Poiseuille flow and effects of modified Lennard–Jones potential function. *Heat and Mass Transfer,* 46, 791-801.

TOSENBERGER, A., SALNIKOV, V., BESSONOV, N., BABUSHKINA, E. & VOLPERT, V. 2011. Particle Dynamics Methods of Blood Flow Simulations. *Mathematical Modelling of Natural Phenomena,* 6, 320-332.

TURGEON, M. L. 2005. *Clinical Hematology Theory and Procedures*, Lippincott Williams & Wilkins.

UHRICH, K. E., CANNIZZARO, S. M., LANGER, R. S. & SHAKESHEFF, K. M. 1999. Polymeric systems for controlled drug release. *Chem Rev,* 99, 3181-98.

VARTHOLOMEOS, P., FRUCHARD, M., FERREIRA, A. & MAVROIDIS, C. 2011. MRI-guided nanorobotic systems for therapeutic and diagnostic applications. *Annu Rev Biomed Eng,* 13, 157-84.

VARTHOLOMEOS, P. & MAVROIDIS, C. Year. Simulation platform for self-assembly structures in MRI-guided nanorobotic drug delivery systems. *In:* Robotics and Automation (ICRA), 2010 IEEE International Conference on, 3-7 May 2010 2010. 5594-5600.

VOLKOVA, E. I., SUYETIN, M. V. & VAKHRUSHEV, A. V. 2009. Temperature Sensitive Nanocapsule of Complex Structural Form for Methane Storage. *Nanoscale Research Letters,* 5, 205-210.

WAGNER, A. J. 2008. *A Practical Introduction to the Lattice Boltzmann Method.* North Dakota State University.

WORLD, C., GARIN, G. & BERK, B. 2006. Vascular shear stress and activation of inflammatory genes. *Current Atherosclerosis Reports,* 8, 240-244.

YANG, S. C. 2006. Effects of surface roughness and interface wettability on nanoscale flow in a nanochannel. *Microfluidics and Nanofluidics,* 2, 501-511.

YANG, X. & ZHENG, Z. C. 2010. Effects of Channel Scale on Slip Length of Flow in Micro/Nanochannels. *Journal of Fluids Engineering,* 132, 061201-061201.

ZHANG, H., ZHANG, Z. & YE, H. 2011. Molecular dynamics-based prediction of boundary slip of fluids in nanochannels. *Microfluidics and Nanofluidics,* 12, 107-115.